

RADC-TR-82-308
Final Technical Report
December 1982



ADA126207

INFRARED DETECTION OF MICROWAVE INDUCED SURFACE CURRENTS ON FLAT PLATES

United States Air Force Academy

Ronald M. Sega

APPROVED FOR PUBLIC RELEASE; DISTRIBUTION UNLIMITED

DTIC
ELECTE
MAR 31 1983

ROME AIR DEVELOPMENT CENTER
Air Force Systems Command
Griffiss Air Force Base, NY 13441

DTIC FILE COPY

83 03 30 053

This report has been reviewed by the RADC Public Affairs Office (PA) and is releasable to the National Technical Information Service (NTIS). At NTIS it will be releasable to the general public, including foreign nations.

RADC-TR-82-308 has been reviewed and is approved for publication.

APPROVED:



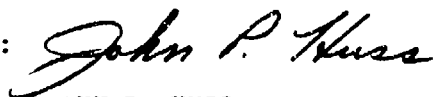
JACOB SCHIERER
Project Engineer

APPROVED:



EDMUND J. WESTCOTT
Technical Director
Reliability & Compatibility Division

FOR THE COMMANDER:



JOHN P. HUSS
Acting Chief, Plans Office

If your address has changed or if you wish to be removed from the RADC mailing list, or if the addressee is no longer employed by your organization, please notify RADC (RBCT) Griffiss AFB NY 13441. This will assist us in maintaining a current mailing list.

Do not return copies of this report unless contractual obligations or notices on a specific document requires that it be returned.

UNCLASSIFIED

SECURITY CLASSIFICATION OF THIS PAGE (When Data Entered)

REPORT DOCUMENTATION PAGE		READ INSTRUCTIONS BEFORE COMPLETING FORM
1. REPORT NUMBER RADC-TR-82-308	2. GOVT ACCESSION NO. AD-A126 207	3. RECIPIENT'S CATALOG NUMBER
4. TITLE (and Subtitle) INFRARED DETECTION OF MICROWAVE INDUCED SURFACE CURRENTS ON FLAT PLATES		5. TYPE OF REPORT & PERIOD COVERED Final Technical Report
7. AUTHOR(s) Ronald M. Sega		6. PERFORMING ORG. REPORT NUMBER N/A
9. PERFORMING ORGANIZATION NAME AND ADDRESS United States Air Force Academy Colorado Springs CO 80840		8. CONTRACT OR GRANT NUMBER(s) N/A
11. CONTROLLING OFFICE NAME AND ADDRESS Rome Air Development Center (RBCT) Griffiss AFB NY 13441		10. PROGRAM ELEMENT, PROJECT, TASK AREA & WORK UNIT NUMBERS 62702F 23380403
14. MONITORING AGENCY NAME & ADDRESS (if different from Controlling Office) Same		12. REPORT DATE December 1982
		13. NUMBER OF PAGES 372
		15. SECURITY CLASS. (of this report) UNCLASSIFIED
		15a. DECLASSIFICATION/DOWNGRADING SCHEDULE N/A
16. DISTRIBUTION STATEMENT (of this Report) Approved for public release; distribution unlimited.		
17. DISTRIBUTION STATEMENT (of the abstract entered in Block 20, if different from Report) Same		
18. SUPPLEMENTARY NOTES RADC Project Engineer: Jacob Scherer (RBCT)		
19. KEY WORDS (Continue on reverse side if necessary and identify by block number) Infrared Surface Currents Conductive Bodies Infrared Detection RF Currents Measurements Infrared Measurements EM Currents Electric Currents Electromagnetic Radiation		
20. ABSTRACT (Continue on reverse side if necessary and identify by block number) The surface currents induced by electromagnetic radiation incident on conductive bodies produce joule heating measurable by infrared techniques. Qualitative studies have shown that surface current amplitude information can be determined from the surface heating pattern. A quantitative analysis, via infrared techniques, of surface current amplitude distributions on the flat plates is presented, and the results are compared to actual current distributions determined from electromagnetic computer code calcu-		

DD FORM 1 JAN 73 1473

EDITION OF 1 NOV 65 IS OBSOLETE

UNCLASSIFIED

SECURITY CLASSIFICATION OF THIS PAGE (When Data Entered)

UNCLASSIFIED

SECURITY CLASSIFICATION OF THIS PAGE(When Data Entered)

↓
lations and probe measurements. This correlation study on flat plates is an essential step toward the infrared measurement of current amplitude distributions on more complex shapes.

UNCLASSIFIED

SECURITY CLASSIFICATION OF THIS PAGE(When Data Entered)

ACKNOWLEDGEMENT

The author owes many thanks to several friends and colleagues for their help and encouragement during the completion of this paper. They include Major Vic Martin, Major Don Warmuth, Capt Allan J. Briding, and Professor John Jackson. To Mrs. Lee Seitenbecher who perservered in typing the original manuscript. Thanks go to the Physics Department of the United States Air Force Academy, headed by Colonel John May, which provided the laboratory space and research time for the project and the Frank J. Seiler Research Laboratory. The Rome Air Development Center (RADC) was also instrumental in providing the much needed support, in particular, Mr. Jacob Scherer and Capt Gary Brock. Finally, a very special thanks to Professor Robert W. Burton who provided the skillful guidance, insightful counsel, and continual encouragement required to complete this work.



Accession For	
NTIS GRA&I	<input checked="" type="checkbox"/>
DTIC TAB	<input type="checkbox"/>
Unannounced	<input type="checkbox"/>
Justification	
By	
Distribution	
Availability Codes	
Avail and/or	
Dist	Special
A	

CONTENTS

CHAPTER

I. INTRODUCTION	1
II. THEORETICAL DETERMINATION OF CURRENTS ON FLAT PLATES	11
Circular Flat Plate (Disk).....	12
Square Flat Plate	68
III. INFRARED/MICROWAVE LABORATORY	71
Microwave Radiation	75
Infrared Detection	84
Thermograph Equipment	84
Digitizing the Thermovision Output.	87
Thermovision Calibration	93
Targets	98
IV. MAGNETIC FIELD PROBE	102
Experimental Considerations	106
Calibration	117
V. PROBE MEASUREMENT OF SURFACE CURRENTS...	141
Procedure	141
Results	143

VI. IR MEASUREMENT OF SURFACE CURRENTS	154
Technique	154
Results	160
VII. CORRELATION	213
Disk Components	214
Relative Current	228
VIII. CONCLUSIONS	241
BIBLIOGRAPHY	245
APPENDIX	
A. WAVE DEMONSTRATOR	249
B. BODY OF REVOLUTION INPUT DATA	270
C. BODY OF TRANSLATION SQUARE PLATE RESULTS	265
D. COMPUTER PROGRAMS	294
E. HORIZONTAL MAGNETIC FIELD PROBE RESULTS	320
F. EMISSIVITY DEPENDENCE ON ANGLE	329

FIGURES

Figure		Page
1	Defining the position vectors.....	4
2	Coordinate system for the disk.....	13
3	Data from an analytic solution (Bouwkamp) for the .15 wavelength circular disk.....	26
4	Plot of J_ρ and J_ϕ current components at $\phi = 0^\circ$ and $\phi = 90^\circ$ for the .15 wavelength circular disk (analytic solution).....	27
5	Polynomial fit for the J_ρ current component at $\phi = 0^\circ$ for the .15 wavelength circular disk (analytic solution).....	28
6	Plot of the J_ρ current component at $\phi = 0^\circ$ for the .15 wavelength circular disk (analytic solution).....	29
7	Polynomial fit for the J_ϕ current component at $\phi = 90^\circ$ for the .15 wavelength circular disk (analytic solution).....	30
8	Plot for the J_ϕ current component at $\phi = 90^\circ$ for the .15 wavelength circular disk (analytic solution).....	31
9	Data from the Body of Revolution Code for the .15 wavelength circular disk.....	33
10	Plot of J_ρ and J_ϕ current components at $\phi = 0^\circ$ and $\phi = 90^\circ$ for the .15 wavelength circular disk.....	34
11	Polynomial fit for the J_ρ current component at $\phi = 0^\circ$ for the .15 wavelength circular disk.....	35
12	Plot of the J_ρ current component at $\phi = 0^\circ$ for the .15 wavelength circular disk.....	36
13	Polynomial fit for the J_ϕ current component at $\phi = 90^\circ$ for the .15 wavelength circular disk.....	37

14	Plot for the J_ϕ current component at $\phi = 90^\circ$ for the .15 wavelength circular disk.....	38
15	Data from the Body of Revolution Code for the 3.0 wavelength circular disk.....	40
16	Plot of J_ρ and J_ϕ current components at $\phi = 0^\circ$ and $\phi = 90^\circ$ on the 3.0 wavelength circular disk.....	41
17	Theoretical result for 3.0 wavelength circular disk	42
18	Theoretical solution for the disk.....	43
19	Data from the Body of Revolution Code for the .38 wavelength circular disk.....	44
20	Plot of J_ρ and J_ϕ current components at $\phi = 0^\circ$ and $\phi = 90^\circ$ on the .38 wavelength circular disk.....	45
21	Polynomial fit for the J_ρ current component at $\phi = 0^\circ$ on the .38 wavelength circular disk.....	46
22	Plot of the J_ρ current component at $\phi = 0^\circ$ for the .38 wavelength circular disk.....	47
23	Polynomial fit for the J_ϕ current component at $\phi = 90^\circ$ for the .38 wavelength circular disk.....	48
24	Plot for the J_ϕ current component at $\phi = 90^\circ$ for the .38 wavelength circular disk.....	49
25	Data from the Body of Revolution Code for the .50 wavelength circular disk.....	50
26	Plot of J_ρ and J_ϕ current components at $\phi = 0^\circ$ and $\phi = 90^\circ$ on the .50 wavelength circular disk.....	51
27	Polynomial fit for the J_ρ current component at $\phi = 0^\circ$ for the .50 wavelength circular disk.....	52

28	Plot of the J_ρ current component at $\phi = 0^\circ$ for the .50 wavelength circular disk.....	53
29	Polynomial fit for the J_ϕ current component at $\phi = 90^\circ$ for the .50 wavelength circular disk.....	54
30	Plot for the J_ϕ current component at $\phi = 90^\circ$ for the .50 wavelength circular disk.....	55
31	Data from the Body of Revolution Code for the 1.0 wavelength circular disk.....	56
32	Plot of J_ρ and J_ϕ current components at $\phi = 0^\circ$ and $\phi = 90^\circ$ for the 1.0 wavelength circular disk.....	57
33	Polynomial fit for the J_ρ current component at $\phi = 0^\circ$ for the 1.0 wavelength circular disk.....	58
34	Plot of the J_ρ current component at $\phi = 0^\circ$ for the 1.0 wavelength circular disk.....	59
35	Polynomial fit for the J_ϕ current component at $\phi = 90^\circ$ for the 1.0 wavelength circular disk.....	60
36	Plot for the J_ϕ current component at $\phi = 90^\circ$ for the 1.0 wavelength circular disk.....	61
37	Data from the Body of Revolution Code for the 1.3 wavelength circular disk.....	62
38	Plot of J_ρ and J_ϕ current components at $\phi = 0^\circ$ and $\phi = 90^\circ$ for the 1.3 wavelength circular disk.....	63
39	Polynomial fit for the J_ρ current component at $\phi = 90^\circ$ for the 1.3 wavelength circular disk.....	64
40	Plot of the J_ρ current component at $\phi = 0^\circ$ for the 1.3 wavelength circular disk.....	65

41	Polynomial fit for the J_ϕ current component at $\phi = 90^\circ$ for the 1.3 wavelength circular disk.....	66
42	Plot for the J_ϕ current component at $\phi = 90^\circ$ for the 1.3 wavelength circular disk.....	67
43	Theoretical result for the .15 wavelength square plate.....	69
44	Theoretical result for the 1.0 wavelength square plate.....	69
45	Theoretical result for 1.2 wavelength square plate.....	70
46	Experimental Arrangement.....	72
47	Infrared/Microwave Laboratory.....	74
48	Block diagram of the microwave propagation apparatus.....	76
49	Microwave sources.....	77
50	Antenna reflectors.....	79
51	90° Corner Reflector.....	83
52	Infrared detection equipment.....	86
53	Early infrared results for a .50 wavelength square plate above the ground plane (aquadac on epoxy).....	91
54	Early infrared results for a 1.3 wavelength square plate above the ground plane (aquadac on epoxy).....	92
55	Published calibration curve for the Thermovision 680 (ISU vs Temp).....	94
56	Experimentally derived calibration curve for the Thermovision 680 (ISU vs Temp).....	97
57	Targets - Aquadac on plexiglass.....	100
58	Targets - Carbon/paraffin over metal.....	101

59	Photograph of a Magnetic Field Probe - Semirigid Coaxial Cable Construction.....	107
60	Drawing of a Magnetic Field Probe - Semirigid Coaxial Cable Construction.....	107
61	Photograph of the Vertical Magnetic Field Probe.....	108
62	Drawing of the Vertical Magnetic Field Probe.....	108
63	Photograph of the Horizontal Magnetic Field Probe.....	109
64	Drawing of the Horizontal Magnetic Field Probe.....	109
65	Magnetic field probe - chamber orientation.....	111
66	Magnetic field probe recording equipment...	113
67	Circuit diagram of the magnetic field probe pre-amplifier.....	114
68	Experimental arrangement for horizontal and vertical probe positioning.....	115
69	Measured gain response of the magnetic field probe.....	118
70	Microwave power meters	119
71	Correlation of microwave source power indication to free field power measured at target location (937 MHz).....	121
72	Plot of source power vs free field power (937 MHz).....	122
73	Correlation of microwave source power indication to free field power measured at target location (2.45 GHz).....	123
74	Plot of source power vs free field power (2.45 GHz).....	124
75	Correlation of magnetic field probe response to source power (937 MHz).....	125

76	Plot of magnetic field probe response vs source power (937 MHz).....	126
77	Correlation of magnetic field probe response to source power (2.45 GHz).....	127
78	Plot of magnetic field probe response va source power (2.45 GHz).....	128
79	Correlation of magnetic field probe response to the square root of source power (937 MHz).....	129
80	Plot of magnetic field probe response vs square root of source power (937 MHz).....	130
81	Correlation of magnetic field probe response to the square root of source power (2.45 GHz).....	131
82	Plot of magnetic field probe response vs square root of source power (2.45 GHz).....	132
83	Correlation of magnetic field probe response to input power (937 MHz).....	133
84	Plot of magnetic field probe response vs input power (937 MHz).....	134
85	Correlation of magnetic field probe response to input power (2.45 GHz).....	135
86	Plot of magnetic field probe response vs input power (2.45 GHz).....	136
87	Correlation of magnetic field probe response to square root of input power (937 MHz).....	137
88	Plot of magnetic field probe response vs square root of input power (937 MHz).....	138
89	Correlation of magnetic field probe response to square root of input power (2.45 GHz)...	139

90	Plot of magnetic field probe response vs square root of input power (2.45 GHz)...	140
91	Magnetic field probe in front of a metal target.....	142
92	Vertical Magnetic Field Probe Measurements for the free field at 3/4 and 1 3/4 inches above ground plane.....	144
93	Vertical Magnetic Field Probe Measurements for the .38 wavelength circular disk.....	145
94	Vertical Magnetic Field Probe Measurements for the .38 wavelength square plate.....	146
95	Vertical Magnetic Field Probe Measurements for the .50 wavelength circular disk.....	147
96	Vertical Magnetic Field Probe Measurements for the .50 wavelength square plate.....	148
97	Vertical Magnetic Field Probe Measurements for the free field at 3/4 and 1 3/4 inches above ground plane.....	149
98	Vertical Magnetic Field Probe Measurements for the 1.0 wavelength circular disk.....	150
99	Vertical Magnetic Field Probe Measurements for the 1.0 wavelength square plate.....	151
101	Vertical Magnetic Field Probe Measurements for the 1.3 wavelength circular disk.....	152
101	Vertical Magnetic Field Probe Measurements for the 1.3 wavelength square plate.....	153
102	Circuit for relating current and temperature.....	155
103	Experimental arrangement for relating current density and temperature.....	155
104	Quadratic curve fit for empirical J vs T (carbon/paraffin over metal).....	158

105	Quadratic curve fit for empirical J vs T (aquadac on plexiglass).....	159
106	Thermogram for an illuminated .38 wave- length circular disk - carbon/paraffin over metal.....	162
107	Digitized thermovision data for .38 wave- length circular disk - carbon/paraffin over metal.....	162
108	Thermovision data profiles for .38 wave- length circular disk - carbon/paraffin over metal.....	163
109	Temperature profiles for .38 wavelength circular disk - carbon/paraffin over metal.....	164
110	Infrared obtained current profiles for .38 wavelength circular disk - carbon/paraffin over metal.....	165
111	Thermogram for an illuminated .38 wavelength square plate - carbon/paraffin over metal.....	166
112	Digitized thermovision data for .38 wave- length square plate - carbon/paraffin over metal.....	166
113	Thermovision data profiles for .38 wave- length square plate - carbon/paraffin over metal.....	167
114	Temperature profiles for .38 wavelength square plate - carbon/paraffin over metal.....	168
115	Infrared obtained current profiles for .38 wavelength square plate - carbon/paraffin on metal.....	169
116	Thermogram for an illuminated .50 wavelength circular disk - carbon/paraffin over metal.....	170

117	Digitized thermovision data for .50 wavelength circular disk - carbon/paraffin over metal.....	170
118	Thermovision data profiles for .50 wavelength circular disk - carbon/paraffin over metal.....	171
119	Temperature profiles for .50 wavelength circular disk - carbon/paraffin over metal.....	172
120	Infrared obtained current profiles for .50 wavelength circular disk - carbon/paraffin over metal.....	173
121	Thermogram for an illuminated .50 wavelength circular disk - aquadac on plexiglass.....	174
122	Digitized thermovision data for .50 wavelength circular disk - aquadac on plexiglass.....	174
123	Thermovision data profiles for .50 wavelength circular disk - aquadac on plexiglass.....	175
124	Temperature profiles for .50 wavelength circular disk - aquadac on plexiglass.....	176
125	Infrared obtained current profiles for .50 circular disk - aquadac on plexiglass.....	177
126	Thermogram for an illuminated .50 wavelength square plate - carbon/paraffin over metal.....	178
127	Digitized thermovision data for .50 wavelength square plate - carbon/paraffin over metal.....	178
128	Thermovision data profiles for .50 wavelength square plate - carbon/paraffin over metal.....	179
129	Temperature profiles for .50 wavelength square plate - carbon/paraffin over metal.....	180

130	Infrared obtained current profiles for .50 wavelength square plate - carbon/paraffin over metal.....	181
131	Thermogram for an illuminated .50 wavelength square plate - aquadac on plexiglass.....	182
132	Digitized thermovision data for .50 wavelength square plate - aquadac on plexiglass.....	182
133	Thermovision data profiles for .50 wavelength square plate - aquadac on plexiglass.....	183
134	Temperature profiles for .50 wavelength square plate - aquadac on plexiglass.....	184
135	Infrared obtained current profiles for .50 wavelength square plate - aquadac on plexiglass.....	185
136	Thermogram for an illuminated 1.0 wavelength circular disk - carbon/paraffin over metal.....	186
137	Digitized thermovision data for 1.0 wavelength circular disk - carbon/paraffin over metal.....	186
138	Thermovision data profiles for 1.0 wavelength circular disk - carbon/paraffin over metal.....	187
139	Temperature profiles for 1.0 wavelength circular disk - carbon/paraffin on metal.....	188
140	Infrared obtained current profiles for 1.0 wavelength circular disk - carbon/paraffin on metal.....	189
141	Thermogram for an illuminated 1.0 wavelength circular disk - aquadac on plexiglass.....	190
142	Digitized thermovision data for 1.0 wavelength circular disk - aquadac on plexiglass.....	190

143	Thermovision data profiles for 1.0 wavelength circular disk - aquadac on plexiglass.....	191
144	Temperature profiles for 1.0 wavelength circular disk - aquadac on plexiglass.....	192
145	Infrared obtained current profiles for 1.0 wavelength circular disk - aquadac on plexiglass.....	193
146	Thermogram for an illuminated 1.0 wavelength square plate - carbon/paraffin over metal.....	194
147	Digitized thermovision data for 1.0 wavelength square plate - carbon/paraffin over metal.....	194
148	Temperature matrix for 1.0 wavelength square plate - carbon/paraffin over metal.....	195
149	Current matrix for 1.0 wavelength square plate - carbon/paraffin over metal.....	195
150	Thermovision data matrix profile for 1.0 wavelength square plate - carbon/paraffin over metal.....	196
151	Temperature matrix profile for 1.0 wavelength square plate - carbon/paraffin over metal.....	196
152	Infrared obtained current matrix profile for 1.0 wavelength square plate - carbon/paraffin over metal.....	197
153	Thermovision data profiles for 1.0 wavelength square plate - carbon/paraffin over metal.....	198
154	Temperature profiles for 1.0 wavelength square plate - carbon/paraffin over metal..	199
155	Infrared obtained current profiles for 1.0 wavelength square plate - carbon/paraffin over metal.....	200

156	Thermogram for an illuminated 1.0 wavelength square plate - aquadac on plexiglass.....	201
157	Digitized thermovision data for 1.0 wavelength square plate - aquadac on plexiglass.....	201
158	Thermovision data profiles for 1.0 wavelength square plate - aquadac on plexiglass.....	202
159	Temperature profiles for 1.0 wavelength square plate - aquadac on plexiglass.....	203
160	Infrared obtained current profiles for 1.0 wavelength square plate - aquadac on plexiglass.....	204
161	Thermogram for an illuminated 1.3 wavelength circular disk - carbon/paraffin over metal.....	205
162	Digitized thermovision data for 1.3 wavelength circular disk - carbon/paraffin over metal.....	205
163	Thermovision data profiles for 1.3 wavelength circular disk - carbon/paraffin over metal.....	206
164	Temperature profiles for 1.3 wavelength circular disk - carbon/paraffin over metal.....	207
165	Infrared obtained current profiles for 1.3 wavelength circular disk - carbon/paraffin over metal.....	208
166	Thermogram for an illuminated 1.3 wavelength square plate - carbon/paraffin over metal.....	209
167	Digitized thermovision data for 1.3 wavelength square plate - carbon/paraffin over metal.....	209

168	Thermovision data profiles for 1.3 wavelength square plate - carbon/paraffin over metal.....	210
169	Temperature profiles for 1.3 wavelength square plate - carbon/paraffin over metal.....	211
170	Infrared obtained current profiles for 1.3 wavelength square plate - carbon/paraffin over metal.....	213
171	Plot of current components for the .38 wavelength circular disk (lower scan).....	216
172	Plot of current components for the .38 wavelength circular disk (middle scan).....	217
173	Plot of current components for the .38 wavelength circular disk (upper scan).....	218
174	Plot of current components for the .50 wavelength circular disk (lower scan).....	219
175	Plot of current components for the .50 wavelength circular disk (middle scan).....	220
176	Plot of current components for the .50 wavelength circular disk (upper scan).....	221
177	Plot of current components for the 1.0 wavelength circular disk (lower scan).....	222
178	Plot of current components for the 1.0 wavelength circular disk (middle scan).....	223
179	Plot of current components for the 1.0 wavelength circular disk (upper scan).....	224
180	Plot of current components for the 1.3 wavelength circular disk (lower scan).....	225
181	Plot of current components for the 1.3 wavelength circular disk (middle scan).....	226
182	Plot of current components for the 1.3 wavelength circular disk (upper scan).....	227

183	Correlation of theoretical, probe, and IR results for the .38 wavelength circular disk (lower scan).....	229
184	Correlation of theoretical, probe, and IR results for the .38 wavelength circular disk (middle scan).....	230
185	Correlation of theoretical, probe, and IR results for the .38 wavelength circular disk (upper scan).....	231
186	Correlation of magnetic field probe and IR results for the .38 wavelength square plate (lower scan).....	232
187	Correlation of the magnetic field probe and IR results for the .38 wavelength square plate (middle scan).....	233
188	Correlation of the magnetic field probe and IR results for the .38 wavelength square plate (upper scan).....	234
189	Correlation of theoretical, probe, and IR results for the 1.0 wavelength square plate (carbon/paraffin on metal).....	236
190	Correlation of theoretical, probe, and IR results for the 1.0 wavelength square plate (aquadac on plexiglass).....	237
191	Correlation of theoretical, probe, and IR results for the .50 wavelength square plate (carbon/paraffin over metal).....	238
192	Correlation of theoretical, probe, and IR results for the .50 wavelength square plate (aquadac on plexiglass).....	239
193	Theoretical comparison of Body of Transluation Computer Code for the 1.0 wavelength square plate.....	240

TABLES

Table		Page
1	Microwave Equipment	78
2	Flat Plate Size	98

CHAPTER I

INTRODUCTION

The objective of this study is to determine the extent to which infrared techniques measure the actual amplitude distribution of induced surface currents on flat plates with given surface preparations. Measurements of currents induced on complex shapes by time varying electromagnetic fields is, in general, a time-consuming and costly job. The reason is that many point-by-point current measurements must be taken in order to characterize the induced current distribution on a given target. Yet, knowledge of such current distributions is essential to many research programs such as electromagnetic pulse interactions with aircraft systems, radar cross-section optimization, etc.

The importance of knowledge of surface currents in electromagnetic problems can be illustrated with a simplified approach to finding the electric (\vec{E}) and magnetic (\vec{H}) fields starting from Maxwell's Equations.

$$\text{Ampere's Law} \quad \vec{\nabla} \times \vec{H} = \epsilon \frac{\partial \vec{E}}{\partial t} + \vec{J} \quad (1)$$

$$\text{Faraday's Law} \quad \vec{\nabla} \times \vec{E} = -\mu \frac{\partial \vec{H}}{\partial t} \quad (2)$$

$$\text{Gauss' Law for Electric Fields} \quad \vec{\nabla} \cdot \vec{E} = \frac{\rho}{\epsilon} \quad (3)$$

Gauss' Law -- Magnetic Fields $\vec{\nabla} \cdot \vec{B} = 0$ (4)

The relationship between current density (\vec{J}) and charge density (ρ) is found in the equation of continuity:

$$\vec{\nabla} \cdot \vec{J} = -\frac{\partial \rho}{\partial t} \quad (5)$$

From equation (4), the vector relation of the divergence of a curl of vector is equal to zero ($\vec{\nabla} \cdot \vec{\nabla} \times \vec{A} = 0$), and the constituent relation, $\vec{B} = \mu \vec{H}$, a vector potential \vec{A} can be defined as follows:

$$\mu \vec{H} = \vec{\nabla} \times \vec{A} \quad (6)$$

Now, substituting equation (6) into (2) we obtain

$$\vec{\nabla} \times \vec{E} = -\frac{\partial}{\partial t} (\vec{\nabla} \times \vec{A}) \quad (7)$$

With the spatial and time coordinates treated independently, equation (7) can be rearranged as

$$\vec{\nabla} \times (\vec{E} + \dot{\vec{A}}) = 0 \quad (8)$$

From the vector identity, curl of a gradient of a scalar is zero, from equation (8) one defines a scalar potential V as

$$\vec{E} + \dot{\vec{A}} = -\vec{\nabla} V \quad (9)$$

Rearranging,

$$\vec{E} = -\vec{\nabla} V - \dot{\vec{A}} \quad (10)$$

Thus, the electric and magnetic fields are expressed in terms of potentials. We can now derive differential equations for the potential function in terms of the sources \vec{J} and ρ .

Substituting (6) and (10) into equation (1), we have

$$\frac{1}{\mu} (\vec{\nabla} \times \vec{\nabla} \times \vec{A}) = -\epsilon \ddot{\vec{A}} - \epsilon \vec{\nabla} V + \vec{J} \quad (11)$$

Applying the vector identity $\nabla \times \nabla \times \vec{A} = \nabla \nabla \cdot \vec{A} - \nabla^2 \vec{A}$ to equation (11) yields

$$\nabla^2 \vec{A} - \mu \epsilon \ddot{\vec{A}} = -\mu \vec{J} + \mu \epsilon \nabla \dot{V} + \nabla \nabla \cdot \vec{A} \quad (12)$$

Substituting (10) into (3),

$$\nabla^2 V + \nabla \cdot \dot{\vec{A}} = -\frac{\rho}{\epsilon} \quad (13)$$

Now, equations (11) and (13) can be decoupled using the Lorentz gauge condition.

$$\nabla \cdot \vec{A} = -\mu \epsilon \dot{V} \quad (14)$$

Wave equations in terms of a single potential and source terms follows the substitution of (14) into (11) and (13)

$$\nabla^2 \vec{A} - \mu \epsilon \ddot{\vec{A}} = -\mu \vec{J} \quad (15)$$

$$\nabla^2 V - \mu \epsilon \ddot{V} = -\frac{\rho}{\epsilon}$$

Finally, the solutions to the wave equations are of the form

$$\vec{A}(\vec{r}, t) = \frac{\mu}{4\pi} \int \frac{\vec{J}(\vec{r}', t - \frac{R}{v})}{R} dv' \quad (16)$$

$$V(\vec{r}, t) = \frac{1}{4\pi\epsilon} \int \frac{\rho(\vec{r}', t - \frac{R}{v})}{R} dv' \quad (17)$$

where \vec{r} locates the field point of interest \vec{r}' locates a source element, R is the distance between source element and field point, $t - \frac{R}{v}$ is the retarded time correcting for the finite velocity, v , of the electromagnetic wave, and the integration is performed over the volume containing the source elements.

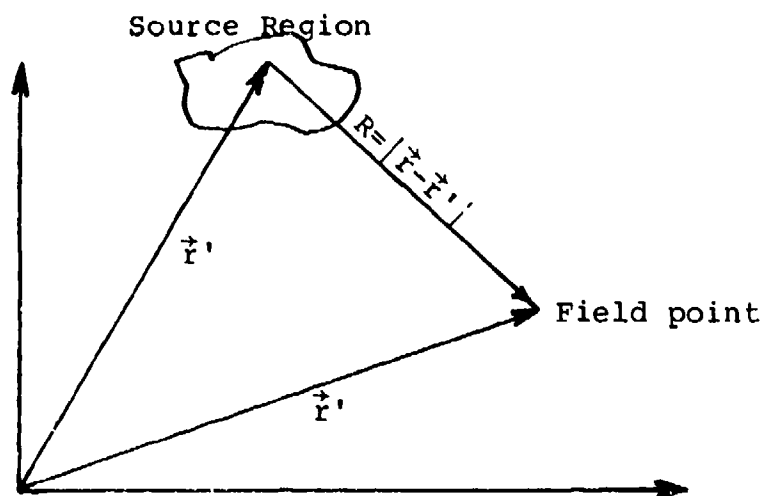


Figure 1.

Defining the position vectors.

Therefore, knowing the magnitude, direction and phase of the vector quantity \vec{J} at all source points, we can, in principle, calculate the vector potential \vec{A} . Knowing the vector potential, the scalar potential can be found through the Lorentz condition, equation (14). With the vector and scalar potentials, we can now solve for the electric and magnetic fields at an arbitrary point in space. In this study, only the magnitude of microwave induced current density on flat plates will be investigated. At the microwave frequencies used in this work the current density is confined near the surface for highly conductive objects and is generally called a surface current.

This report represents a necessary step toward refining a technique which shows much promise in characterizing induced surface current patterns with a single measurement. The technique is based on the fact that when current flows in a conductor of finite resistivity, I^2R heating occurs. When the surface temperature rises to roughly 0.1° K or higher above ambient, the induced temperature distribution over the surface (which corresponds to induced currents in that surface), can be detected by a thermographic system via emitted thermal radiation.

Thermography, as applied to this study, is the heat detection process displayed in both a color code representation and a numeric array of intensity values. The science of infrared detection has been advanced over the past two decades by the AGA Corporation in Sweden. The basis of operation is a scanning scheme of infrared prisms and a photovoltaic cell from which voltage inputs are processed. Applications of thermography have spanned the areas of medicine, building construction, transmission line problems, blast furnace operations, etc.

At the Naval Postgraduate School, Burton and associates advanced the horizon of applications to include the detection of surface currents produced by incident electromagnetic plane waves on objects, and by observing heating patterns on resistive paper produced by antennas (1). The incident electromagnetic wave, interacting with objects of appropriate size, produces standing wave patterns, detectable in the infrared region due to the I^2R heating effects. In the laboratory environment, the qualitative comparison of current distributions present on antennas of various configurations were also made (2). Further results demonstrated a good qualitative comparison of induced currents on flat plates and cylinders with values measured at Harvard. The results appeared in a color photograph representation such that ten colors are displayed corresponding to a temperature range whereby each color represented roughly one-tenth of that range. The results were encouraging and would obviously be of benefit if applied to complex structures such as aircraft that could be scaled down for laboratory examination. This work indicated that a necessary step in the extension of the IR results to various applications was the quantifying of the obtained data. Once this data was obtained in this more workable format, an examination to determine, as accurately as possible,

the correspondence between actual surface currents and those determined with IR techniques was needed. For simple geometries, currents have been calculated analytically (22,26) or utilizing numerical techniques (23), and verified experimentally. For the comparison study, square and circular flat plates were logical candidates owing to their high symmetry.

The theoretical determination of surface currents induced on the perfect electric conducting flat plates with normally incident plane electromagnetic wave has been developed by previous investigators. Results for circular flat plates of electrical size of largest dimension .38, .50, 1.0, and 1.3 wavelengths are presented. The analytic solution for the electrically small circular flat plate (disk) will be outlined. The perfectly conducting, vanishing thin disk is computed through the first six terms for the .15 wavelength disk and the results are presented and compared to the solution obtained from an \vec{E} -field solution for a conducting body of revolution developed by Joseph R. Mautz and Roger F. Harrington of Syracuse University (33). The 3.0 wavelength solution from the Body of Revolution (BOR) Code is also compared with an analytic result obtained by Andrejewski (2). Disks of electrical size .38, .50, 1.0, and 1.3 are then

solved using this computer code. The flat plate solution using a body of translation electromagnetic computer code developed for the Rome Air Development Center is presented and compared with results from the literature.

An infrared/microwave facility was designed, constructed, and equipped in a converted storage room at the United States Air Force Academy. The available microwave apparatus dictated the size of anechoic chamber and the frequencies of 2.45 GHz and 937 MHz. Investigations of chamber characteristics using various reflector arrangements with a quarter wave monopole on a ground plane were carried out using a ripple-tank two dimensional modeling apparatus, a crossed-dipole power probe, and a time-varying magnetic field detector. Corner reflectors and cylindrical parabolic reflectors were experimentally positioned to direct maximum power while still achieving a "plane" wave over a sixteen centimeter target. The nucleus of infrared detection equipment was a AGA Thermovision 680 System. An interface for digitization was developed such that correction to the received Thermovision data could be applied on a point by point basis. An infrared measurement technique including a seven frame average of the illuminated matrices to reduce

random error influences on the final result was developed. The averaged matrix in ISU units was then corrected for camera calibration resulting in a determination of temperature increase due to the incident microwave. To obtain surface currents from temperature, a functional relationship was empirically determined by applying various levels of DC current through the coating and recording the corresponding temperature rise.

The verification of surface currents on metal plates illuminated with an optimized plane electromagnetic wave required the design and fabrication of a loop detector. The induced voltage is related to the magnitude of the time varying magnetic field through Faraday's Law and hence to surface current. Consideration of shielding from stray RF coupling as well as electric field coupling were found to be critical to obtain accurate measured values.

Finally, current values obtained from theory, probe measurement, and IR detection are compared. The comparison procedure developed should be reapplied for future coating schemes using higher resolution infrared detection systems. Data gained through correlation studies on simple shapes will then permit an extension to more complex shapes.

Supplemental studies in wave interaction modeling and emissivity dependence on angle were also conducted and are summarized in the Appendices.

CHAPTER II

THEORETICAL DETERMINATION OF CURRENTS ON
FLAT PLATES

The solution to the metallic plate or even the perfectly conducting plate is not trivial as emphasized in a paper given by Professor T. B. A. Senior in May 1982 (45) in which recent approaches to solve the integro-differential equations for arbitrary flat plates given in a 1977 IEEE publication were found to be in error as the plate shape varied from the elliptic case. For perfectly conducting disks of largest largest electrical dimension .38, .50, 1.0, and 1.3 wavelengths, a Body of Revolution electromagnetics code was used for their respective solution at normal incidence. Since the disk has been solved analytically, the numerical approach of the computer code was compared, at both extremes of the experimental dimensions, to an analytical treatment. Analytic solutions developed by C. J. Bouwkamp (7) and W. Andrejewski (2) were used for the .15 and 3.0 wavelength circular disks, respectively. The code results showed good agreement with the analytic solutions. For the perfectly conducting square plates, solutions from the literature

are presented in the range of the experimental sizes. An additional Body of Translation electro-magnetics computer code solution is found in Appendix C for the plate sizes used in this report.

Circular Flat Plate (Disk)

The general formulation for this problem begins with the requirement that the electromagnetic field must obey Maxwell's equations. At the surface, the boundary conditions must be satisfied. In the perfectly conducting case, the tangential component of the electric field and the normal component of the magnetic field must vanish. For flat objects the special situation at the edges must also be considered. If one observes that current or charge can reside at an edge and that the electric field varies as $1/r$, one at first would allow, on a theoretical basis, for the electric fields and current to approach infinity at the edge. A generally accepted conservation of energy argument dealing with the order of this mathematical singularity is stated by Josef Meixner as follows (34):

The edge condition states that the electromagnetic energy density must be integrable over any finite domain even if this domain contains singularities of the electromagnetic field. In other words, the electromagnetic energy in any finite domain must be finite. In the case of a

perfectly conducting surface with an edge, one concludes from this condition that near the edge the singular components of the electric and magnetic field vectors are of the order $\rho^{-1/2}$, where ρ is the distance from the edge, while the components of the electric and magnetic field strengths parallel to the edge are always finite.

The following discussion is taken from Bouwkamp (7) to illustrate the solution process for the simplest case, that of an electrically small, perfectly conducting circular disk illuminated by a plane wave at normal incidence. The disk is taken to be of unit radius and centered on the origin of rectangular coordinates x, y, z so that the rims of the disk is defined by $z = 0, x^2 + y^2 = 1$ (see Figure 2).

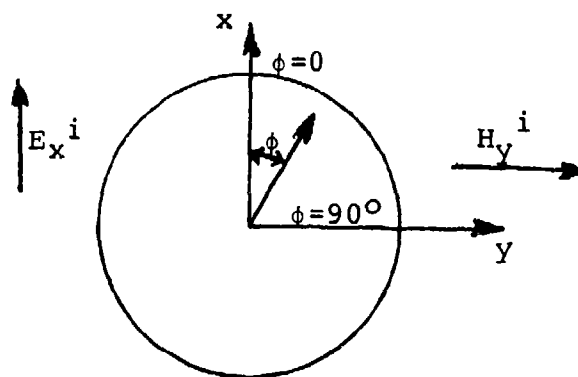


Figure 2. Coordinate system for the disk.

The incident wave is plane polarized with the electric field along the X axis, the magnetic field aligned with the Y axis, and thus the wave is moving in the positive Z direction. This solution is restricted to $ka < 1$ where k is the wave number and a is the radius of the disk. The general expressions relating the field vectors with the scalar and vector potentials (equations 6 and 10) and the general expression for the vector potential in terms of current density serve as a starting point. The scattered field can then be written in rectangular coordinates in terms of the vector potential as

$$H_x^S = - \frac{\partial A_y}{\partial z} \quad (18)$$

$$H_y^S = \frac{\partial A_x}{\partial z} \quad (19)$$

$$H_z^S = \frac{\partial A_y}{\partial x} - \frac{\partial A_x}{\partial y} \quad (20)$$

$$E_x^S = ikA_x - \frac{1}{ik} \frac{\partial}{\partial x} \left(\frac{\partial A_x}{\partial x} + \frac{\partial A_y}{\partial y} \right) \quad (21)$$

$$E_y^S = ikA_y - \frac{1}{ik} \frac{\partial}{\partial y} \left(\frac{\partial A_x}{\partial x} + \frac{\partial A_y}{\partial y} \right) \quad (22)$$

$$E_z^S = - \frac{1}{ik} \frac{\partial}{\partial z} \left(\frac{\partial A_x}{\partial x} + \frac{\partial A_y}{\partial y} \right) \quad (23)$$

The boundary conditions for a perfectly conducting, and thus perfectly reflecting, disk are that the total tangential electric field and the total normal magnetic field must vanish at the surface. The total field is simply the incident plus the scattered field. Thus, at the surface ($X^2+Y^2 \leq 1$)

$$E_x^s = - E_x^i \quad (24)$$

$$E_y = 0 \quad (25)$$

$$H_z = 0. \quad (26)$$

Now from the scattered field expressions and the stated boundary conditions, the following simultaneous system of equations can be written as follows:

$$\frac{\partial A_y}{\partial y} = \frac{\partial A_x}{\partial x} \quad (27)$$

$$\frac{\partial^2 A_x}{\partial x^2} + \frac{\partial^2 A_x}{\partial y^2} + k^2 A_x = ik \quad (28)$$

$$\frac{\partial^2 A_y}{\partial x^2} + \frac{\partial^2 A_y}{\partial y^2} + k^2 A_y = 0 \quad (29)$$

with

$$A_x = \frac{1}{c} \int \frac{J_x e^{ikr}}{r} ds \quad (30)$$

$$A_y = \frac{1}{c} \int J_y \frac{e^{ikr}}{r} ds \quad (31)$$

These are the integro-differential equations that must be solved to obtain the rectangular components of the

current density. Now, Bouwkamp reduces this simultaneous system to that of an ordinary system by using symmetry and normal incidence argument to eliminate the functions J_y and A_y . What is left is set of integro-differential equations in only J_x .

The conditions on the edge of the disk must be considered. From a combination of physical and mathematical arguments stated earlier, order functions are obtained. These state, that near the rim, as the distance to the rim goes to zero, the current component on the surface of the disk that is normal to the edge will decrease with the square of the distance and the current component on the surface that is tangential to the edge will increase as the reciprocal of the square root of the distance.

To take advantage of the symmetry in this situation, the incident wave is considered in terms of cylindrical coordinates. Functions depending on the radius (ρ) are then introduced along with azimuthal angle dependence of the current. The current components are then written as:

$$\frac{1}{c} J_x = \frac{A(\rho) + B(\rho) \cos 2\phi}{\pi^2 \sqrt{1-\rho^2}} \quad (31)$$

$$\frac{1}{c} J_y = \frac{B(\rho) \sin 2\phi}{\pi^2 \sqrt{1-\rho^2}} \quad (32)$$

where J_x and J_y are related to each other by

$$J_y = - \frac{1}{2} \frac{\partial J_x}{\partial \phi} = \frac{1}{2} (y \frac{\partial J_x}{\partial x} - x \frac{\partial J_x}{\partial y}) \quad (33)$$

The functions A and B must also satisfy the conditions that on the rim their sum is zero and at the center of the disk the value of B is zero.

Now, solutions for equations (31) and (32) eventually reduce to being able to solve the following integral equation:

$$\int_0^{2\pi} d\phi' \int_0^1 \rho' d\rho' \frac{A(\rho') + B(\rho') \cos 2\phi'}{\pi^2 \sqrt{1-\rho'^2}} \frac{e^{ikr}}{r} = - \frac{1}{ik} - \rho J_0(k\rho) + \rho J_2(k\rho) \cos 2\phi \quad (34)$$

for 3 unknowns ρ , A, B

over $0 \leq \rho \leq 1$ and $0 \leq \phi \leq 2\pi$

$$\text{where } r^2 = \rho^2 - 2\rho\rho' \cos(\phi - \phi') + \rho'^2$$

$A(\rho')$ and $B(\rho')$ are uniformly bounded on the interval and J_0 and J_2 are Bessel functions of argument $k\rho$ and of order 0 and 2 respectively.

From a power series solution of equation (34) are found series solutions of $A(\rho)$ and $B(\rho)$ from equations (31) and (32). For the first six terms,

$$\begin{aligned} A(\rho) &= \sum_{n=1}^6 A_n(ik)^n \\ &= \frac{1}{3} (-4+3\rho^2) ik + \pi 0 + \\ &+ \frac{1}{90} (56-40\rho^2+5\rho^4) (ik)^3 \end{aligned}$$

$$\begin{aligned}
& + \frac{4\pi}{9} (2-\rho^2) (ik)^4 + \\
& + \frac{1}{12600} (-2656 + 2408\rho^2 - 448\rho^4 + 21\rho^6) (ik)^5 \\
& + \frac{2}{675} (-296 + 192\rho^2 - 15\rho^4) (ik)^6 + O(A_7) \quad (35)
\end{aligned}$$

$$\begin{aligned}
\text{and } B(\rho) &= \sum_{n=1}^6 B_n (ik)^n \\
&= \frac{1}{3} \rho^2 (ik) + O(\pi) + \\
&+ \frac{1}{30} \rho^2 (-8 + \rho^2) (ik)^3 + \\
&- \frac{4\pi}{9} \rho^2 (ik)^4 + \\
&+ \frac{1}{2520} \rho^2 (200 - 68\rho^2 + 3\rho^4) (ik)^5 + \\
&+ \frac{2\pi}{675} \rho^2 (134 - 15\rho^2) (ik)^6 + O(B_7) \quad (36)
\end{aligned}$$

Simplifying,

$$\begin{aligned}
A(\rho) &= k \left\{ \frac{j}{3} \left[-4 + 3 \left(\frac{\rho}{a} \right)^2 \right] + \right. \\
&- \frac{jk^2}{90} \left[56 - 40 \left(\frac{\rho}{a} \right)^2 + 5 \left(\frac{\rho}{a} \right)^4 \right] \\
&+ \frac{4\pi k^2}{9} \left[2 - \left(\frac{\rho}{a} \right)^2 \right] \\
&+ \frac{jk^4}{12600} \left[-2656 + 2408 \left(\frac{\rho}{a} \right)^2 - 488 \left(\frac{\rho}{a} \right)^4 - 21 \left(\frac{\rho}{a} \right)^6 \right] \\
&- \frac{2\pi k^5}{675} \left[-296 + 192 \left(\frac{\rho}{a} \right)^2 - 15 \left(\frac{\rho}{a} \right)^4 \right] + O \left. \right\} \quad (37) \\
B(\rho) &= k \left\{ \frac{j}{3} \left(\frac{\rho}{a} \right)^2 - \frac{jk^2}{30} \left(\frac{\rho}{a} \right)^2 \left[-8 + \left(\frac{\rho}{a} \right)^2 \right] \right. \\
&- \frac{4\pi k^2}{9} \left(\frac{\rho}{a} \right)^2 + \frac{jk^4}{2520} \left(\frac{\rho}{a} \right)^2 \left[200 - 68 \left(\frac{\rho}{a} \right)^2 + 3 \left(\frac{\rho}{a} \right)^4 \right]
\end{aligned}$$

$$- \frac{2\pi k^5}{675} \left(\frac{\rho}{a}\right)^2 \left[134 - 15 \left(\frac{\rho}{a}\right)^2 \right] + 0 \} \quad (38)$$

Now, Bouwkamp assumes in the initial development that

$$\frac{E}{H} = 1. \text{ However, } \frac{E}{H} = \sqrt{\frac{\mu_0}{\epsilon_0}} = 377 \text{ and therefore,}$$

J_x, J_y must include $\frac{1}{377}$ factor.

To find the magnitude of the current components we will simplify by separating the real and imaginary parts

$$| J_x | = \sqrt{J_x J_x^*} \quad (39)$$

$$| J_x | = \frac{ck}{377\pi^2 \sqrt{1 - \left(\frac{\rho}{a}\right)^2}} \left\{ [A(\rho) + B(\rho) \cos 2\phi] [A(\rho) + B(\rho) \cos 2\phi]^* \right\} \quad (40)$$

$$\begin{aligned} J_x = & \frac{ck}{377\pi^2 \sqrt{1 - \left(\frac{\rho}{a}\right)^2}} \left\{ \frac{4\pi k}{9} \left[2 - \left(\frac{\rho}{a}\right)^2 \right] - \frac{2\pi k^5}{675} \right. \\ & \left. [-296 + 192 \left(\frac{\rho}{a}\right)^2 - 15 \left(\frac{\rho}{a}\right)^4] \right\} + j \left\{ \frac{1}{3} [-4 + 3 \left(\frac{\rho}{a}\right)^2] - \frac{k^2}{90} \right. \\ & \left. [56 - 40 \left(\frac{\rho}{a}\right)^2 + 5 \left(\frac{\rho}{a}\right)^4] + \frac{k^4}{12600} [-2656 + 2408 \left(\frac{\rho}{a}\right)^2 \right. \right. \\ & \left. \left. - 448 \left(\frac{\rho}{a}\right)^4 + 21 \left(\frac{\rho}{a}\right)^6] \right\} + \left\{ \frac{4\pi k^3}{9} \left(\frac{\rho}{a}\right) - \frac{2\pi k^5}{675} \left(\frac{\rho}{a}\right)^2 \right. \\ & \left. [134 - 15 \left(\frac{\rho}{a}\right)^2] \right\} \cos 2\phi + j \cos 2\phi \left\{ \frac{1}{3} \left[\left(\frac{\rho}{a}\right)^2 \right] \right. \\ & \left. - \frac{k^2}{30} \left(\frac{\rho}{a}\right)^2 [-8 + \left(\frac{\rho}{a}\right)^2] + \frac{k^4}{2520} \left(\frac{\rho}{a}\right)^2 [200 - 68 \left(\frac{\rho}{a}\right)^2 \right. \right. \\ & \left. \left. + 3 \left(\frac{\rho}{a}\right)^4] \right\} \right\} \quad (41) \end{aligned}$$

$$J_x = \frac{c2\pi}{377\pi^2\lambda \sqrt{1-(\frac{\rho}{a})^2}} [a_1 + ja_2) + (b_1\cos 2\phi + jb_2\cos 2\phi)] \quad (42)$$

where

a_1 = real part of $A(\rho)$

a_2 = imaginary part of $A(\rho)$

b_1 = real part of $B(\rho)$

b_2 = imaginary part of $B(\rho)$

Simplifying further, $c = 3.00 \times 10^8$ m/sec

$$\begin{aligned} |J_x| &= \frac{5.05 \times 10^5}{\lambda \sqrt{1-(\frac{\rho}{a})^2}} \left\{ [(a_1+b_1\cos 2\phi + j(a_2+b_2\cos 2\phi)) \right. \\ &\quad \left. ((a_1+b_1\cos 2\phi) - j(a_2+b_2\cos 2\phi))]^{\frac{1}{2}} \right\} \\ &= \frac{5.05 \times 10^5}{\lambda \sqrt{1-(\frac{\rho}{a})^2}} [(a_1+b_1\cos 2\phi)^2 + (a_2+b_2\cos 2\phi)^2]^{\frac{1}{2}} \quad (43) \end{aligned}$$

Similarly,

$$\begin{aligned} |J_y| &= (J_y J_y^*)^{\frac{1}{2}} \\ &= \left| \frac{c2\pi \sin 2\phi}{377\pi^2\lambda \sqrt{1-(\frac{\rho}{a})^2}} (B(\rho) B(\rho)^*)^{\frac{1}{2}} \right| \\ &= \left| \frac{5.05 \times 10^5 \sin 2\phi}{\lambda \sqrt{1-(\frac{\rho}{a})^2}} (b_1^2 + b_2^2)^{\frac{1}{2}} \right| \quad (44) \end{aligned}$$

Now, let the total current be J_t which is given by the following expression:

$$|J_t| = (|J_x|^2 + |J_y|^2)^{\frac{1}{2}} \quad (45)$$

Consider the term $\sqrt{1-(\frac{\rho}{a})^2}$ in the denominator of J_x and J_y . As ρ approaches the radius a , the currents tend to infinity. The calculations based on equations (44) and (45) will be restricted to $\rho \leq .95a$.

It was advantageous to transform from cylindrical coordinates to rectangular coordinates using the following substitutions:

$$\rho = \sqrt{x^2 + y^2}$$

$$\sin 2\phi = \frac{2 \tan \phi}{1 + \tan^2 \phi}$$

$$\cos 2\phi = \frac{1 - \tan^2 \phi}{1 + \tan^2 \phi}$$

$$\text{where } \tan \phi = \frac{y}{x}$$

It follows that

$$\sin 2\phi = \frac{2xy}{x^2 + y^2}$$

$$\cos 2\phi = \frac{x^2 - y^2}{x^2 + y^2}$$

The latter equations were then programmed on an HP9845 minicomputer and the results for a $.075\lambda$ radius disk are given. With a vertically polarized incident plane wave, the total current density along the horizontal and vertical axis can be computed. Curve fits for the results follow a discussion of the program used.

The regression curve fits were done using a Hewlett Packard software package on the 9845B mini-computer. The program takes a set of points (X, Y) and fits various types of curves to them using least square methods. An analysis of variance table is also computed and this information is printed in the text that follows. The input parameters (X_i, Y_i) are loaded into full-precision one-dimensional arrays of N elements each with N being at least 3. The output variables are also full precision and are defined as follows:

Regression

Df - regression degrees of freedom
(degree for polynomial model)

SS - regression sum of squares

MS - regression mean squares

Residual

Df - residual degrees of freedom $(N-2)$

SS - residual sum of squares

MS - residual mean squares

Total

Df - total degrees of freedom (regression
and residual)

SS - total sum of squares

F - the F statistic (regression mean squares/
residual mean squares)

The F ratio is an indication of how good the curve fit is and, in general, is optimized by the highest possible F ratio. In the general outputs that follow, a blank space for an F ratio implies an exact fit such that all points fall on the curve. It should also be noted that several factors enter the goodness of fit such as the number of data points, the number of coefficients, etc. For data sets in this paper, only the linear and polynomial models were found to be appropriate. For n data points (X_i, Y_i) the method and formulae used by the program are as follows (24):

For the linear model $y = a + bx$:

$$a = \frac{\sum Y_i}{n} - b \frac{\sum X_i}{n}$$

$$b = \frac{\frac{\sum X_i Y_i}{n} - \frac{\sum X_i \sum Y_i}{n^2}}{\frac{\sum X_i^2}{n} - \frac{(\sum X_i)^2}{n^2}}$$

$$\text{Total sum of squares} = \sum Y_i^2 - \frac{(\sum Y_i)^2}{n}$$

$$\text{Regression sum of squares} = \frac{[\sum x_i y_i - \frac{\sum x_i \sum y_i}{n}]^2}{\sum x_i^2 - \frac{(\sum x_i)^2}{n}}$$

$$\text{Residual Sum of Squares} = \text{Total SS} - \text{REG SS}$$

$$\text{Regression Mean Squares} = \text{REG SS}$$

$$\text{Residual Mean Squares} = \frac{\text{RES SS}}{n-2}$$

$$F \text{ Ratio} = \frac{\text{RES MS}}{\text{RES MS}}$$

For the polynomial model

$$y = a_m x^m + a_{m-1} x^{m-1} + \dots + a_1 x + a_0$$

m = degree of the desired polynomial

$(x_i, f(x_i))$ = set of tabulated points $((x_i, y_i))$ in the other models

$$g_j(x_i) = x_i^j \text{ for } i = 0, 1, \dots, n$$

$$\alpha_{kj} = \sum_{i=0}^n g_k(x_i) g_j(x_i) \quad \text{for } k = 0, 1, 2, \dots, m$$

$$j = 0, 1, 2, \dots, m$$

A system of simultaneous equations is then written in terms of α 's as follows

$$\alpha_{m0} a_m + \alpha_{m-10} a_{m-1} + \dots + \alpha_{00} a_0 = \sum_{i=0}^n f(x_i) g_0(x_i)$$

$$\alpha_{m1} a_m + \alpha_{m-11} a_{m-1} + \dots + \alpha_{01} a_0 = \sum_{i=0}^n f(x_i) g_1(x_i)$$

$$\begin{array}{ccccccc}
 \alpha_{m2} a_m + \alpha_{m-12} a_{m-1} + \dots + \alpha_{02} a_0 & = & \sum_{i=0}^n f(x_i) g_2(x_i) \\
 \vdots & & \vdots & & \vdots \\
 \alpha_{mm} a_m + \alpha_{m-1m} a_{m-1} + \dots + \alpha_{0m} a_0 & = & \sum_{i=0}^n f(x_i) g_m(x_i)
 \end{array}$$

which can be solved to find the coefficients

$$a_0, a_1, a_2, \dots, a_m$$

$$\bar{y} = \frac{\sum y_i}{n}$$

$$\hat{y}_i = a_m x_i^m + a_{m-1} x_i^{m-1} + \dots + a_1 x_i + a_0$$

$$\text{Total Sum of Squares} = \sum (y_i - \bar{y})^2$$

$$\text{Regression Sum of Squares} = \sum (\hat{y}_i - \bar{y})^2$$

$$\text{Residual Sum of Squares} = \text{Total SS} - \text{REG SS}$$

$$\text{Regression Mean Squares} = \frac{\text{REG SS}}{m}$$

$$\text{Residual Mean Squares} = \frac{\text{RES SS}}{n-1-m}$$

DATA

Point #1:	X=0	Y=5.45
Point #2:	X=1	Y=5.41
Point #3:	X=2	Y=5.46
Point #4:	X=3	Y=5.34
Point #5:	X=4	Y=5.48
Point #6:	X=5	Y=5.22
Point #7:	X=6	Y=5.5
Point #8:	X=7	Y=5.5
Point #9:	X=8	Y=5.54
Point #10:	X=9	Y=4.83
Point #11:	X=10	Y=5.59
Point #12:	X=11	Y=4.56
Point #13:	X=12	Y=5.67
Point #14:	X=13	Y=4.21
Point #15:	X=14	Y=5.81
Point #16:	X=15	Y=3.77
Point #17:	X=16	Y=6.04
Point #18:	X=17	Y=3.21
Point #19:	X=18	Y=6.47
Point #20:	X=19	Y=2.44
Point #21:	X=20	Y=7.46
Point #22:	X=21	Y=1.16
Point #23:	22	Y=11.3

Figure 3: Data from an analytic solution (Bouwkamp) for the .15 wavelength circular disk.

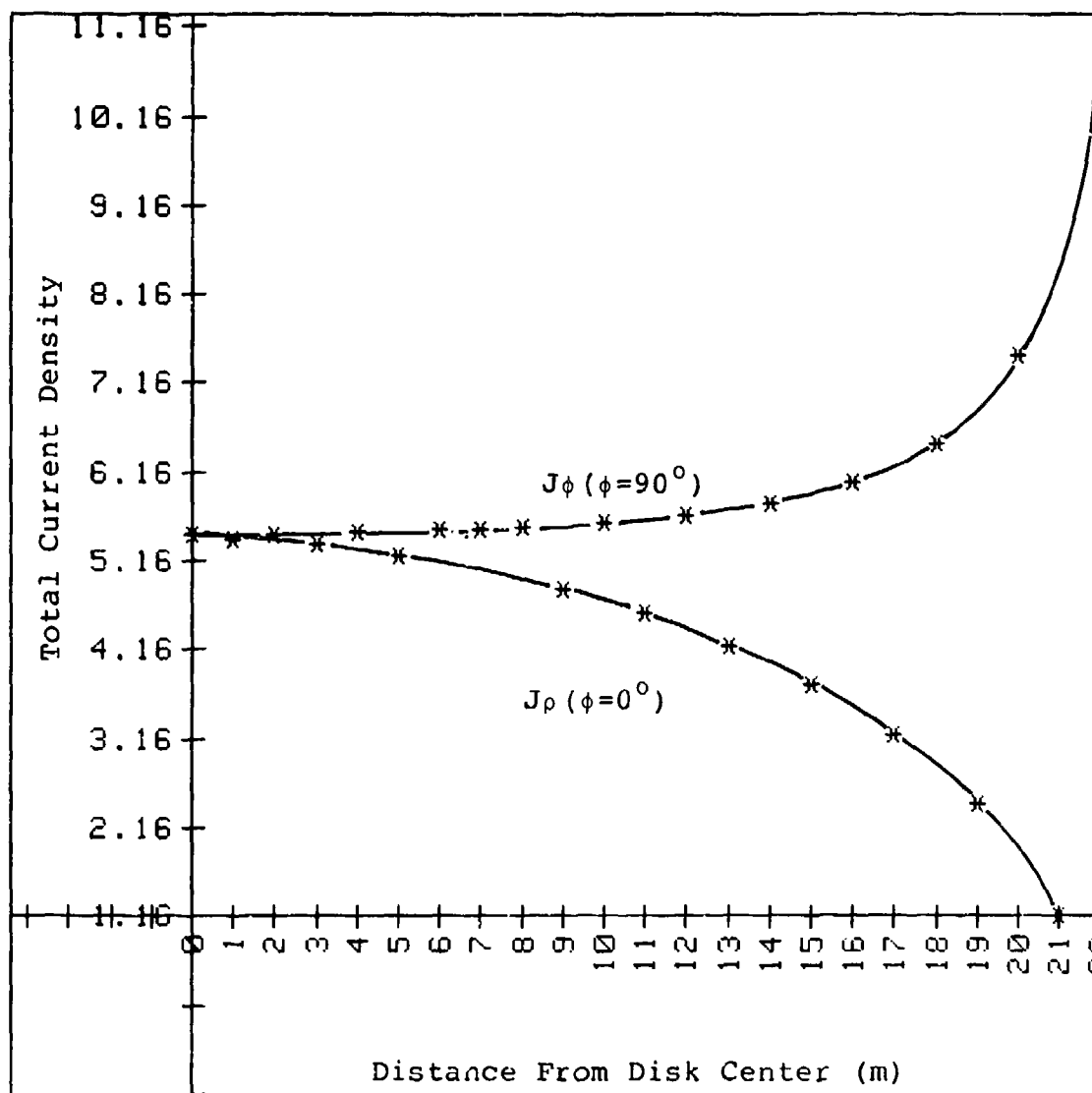


Figure 4: Plot of J_ρ and J_ϕ current components at $\phi = 0^\circ$ and $\phi = 90^\circ$ for the .15 wavelength circular disk (analytic solution).

DATA

Point #1:	X=0	Y=5.45
Point #2:	X=1	Y=5.41
Point #3:	X=2	Y=5.34
Point #4:	X=3	Y=5.22
Point #5:	X=4	Y=5.05
Point #6:	X=5	Y=4.83
Point #7:	X=6	Y=4.56
Point #8:	X=7	Y=4.21
Point #9:	X=8	Y=3.77
Point #10:	X=9	Y=3.21
Point #11:	X=10	Y=2.44
Point #12:	X=11	Y=1.16

POLYNOMIAL MODEL: $Y=A(M)*X^M+A(M-1)*X^{(M-1)}+...+A(1)*X+A(0)$

Coefficients:

$A(0)=5.454547487$
 $A(1)=-.07842408$
 $A(2)=.03991346$
 $A(3)=-.019131686$
 $A(4)=.0024157556$
 $A(5)=-.00011274502$

Source	Df	SS	MS	F
Regression	5	20.113	4.023	
12702.7636366 M4D.3D				
Residual	6	.002	.000	
Total	11	20.115		

Figure 5: Polynomial fit for the J_p current component at $\phi = 0^\circ$ for the .15 wavelength circular disk (analytic solution).

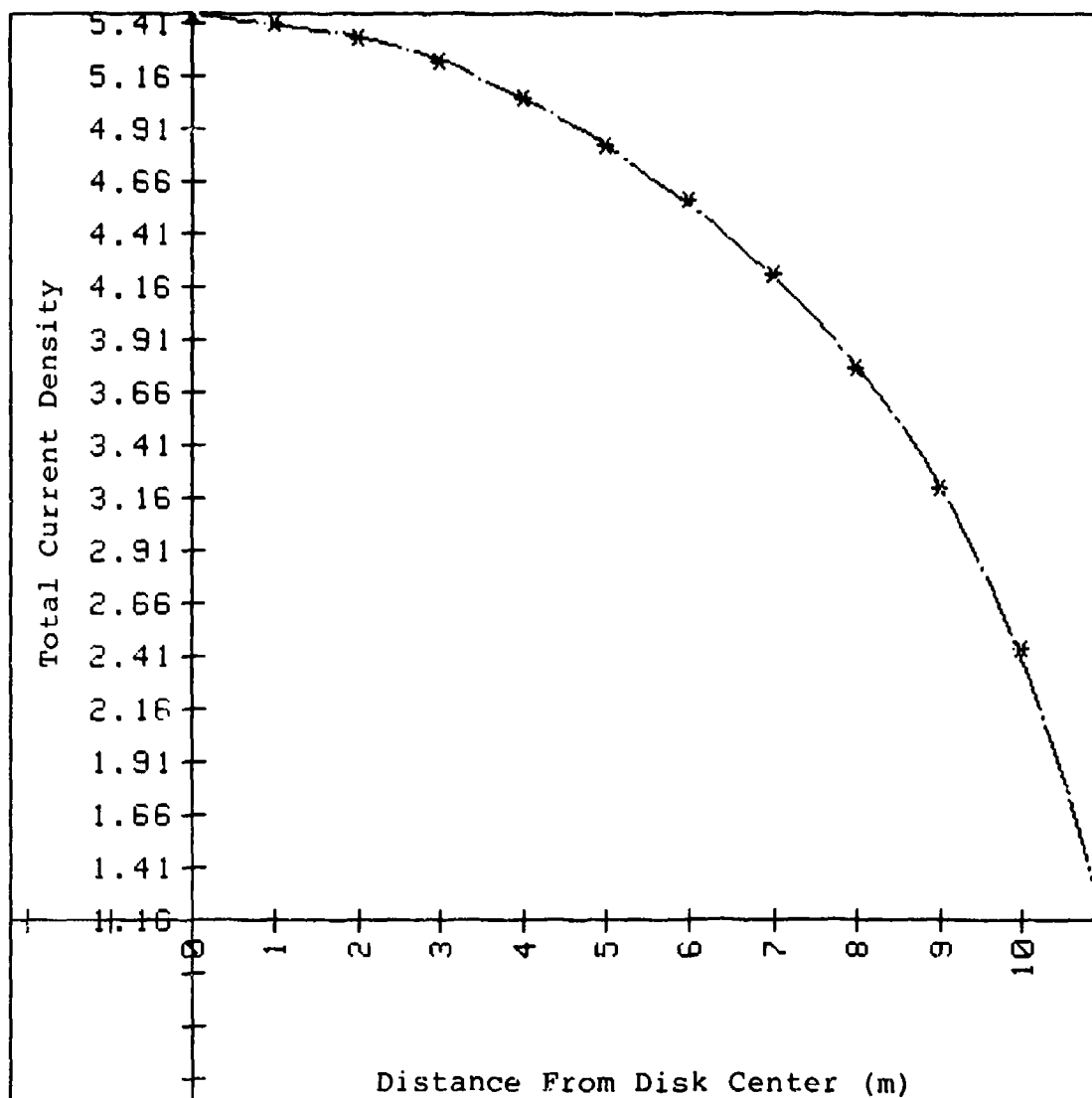


Figure 6: Plot of the J_0 current component at $\phi = 0^\circ$ for the .15 wavelength circular disk (analytic solution).

DATA

Point #1:	X=0	Y=5.45
Point #2:	X=1	Y=5.46
Point #3:	X=2	Y=5.48
Point #4:	X=3	Y=5.5
Point #5:	X=4	Y=5.54
Point #6:	X=5	Y=5.59
Point #7:	X=6	Y=5.67
Point #8:	X=7	Y=5.81
Point #9:	X=8	Y=6.04
Point #10:	X=9	Y=6.47
Point #11:	X=10	Y=7.46

POLYNOMIAL MODEL: $Y=A(M)*X^M+A(M-1)*X^{(M-1)}+...+A(1)*X+A(0)$

Coefficients:

$A(0)=5.445332077$
 $A(1)=.07520403$
 $A(2)=-.06801385$
 $A(3)=.02502269$
 $A(4)=-.003571543$
 $A(5)=.00018750039$

Source	Df	SS	MS	F
Regression	5	3.779	.756	2194.413
Residual	5	.002	.000	
Total	10	3.780		

Figure 7: Polynomial fit for the $J\phi$ current component at $\phi = 90^\circ$ for the .15 wavelength circular disk (analytic solution).

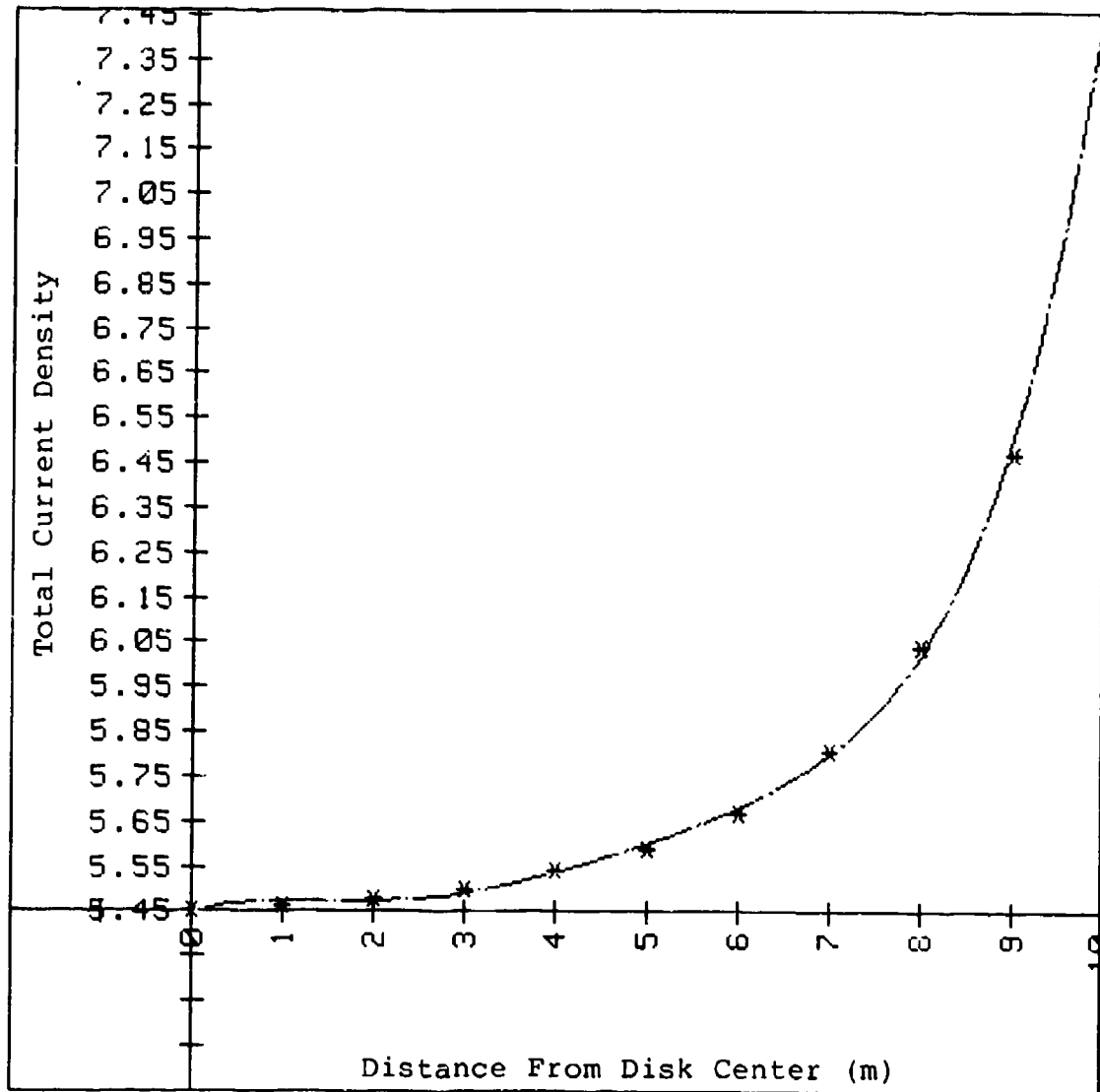


Figure 8: Plot for the J_ϕ current component at $\phi = 90^\circ$ for the .15 wavelength circular disk (analytic solution).

Now, Bouwkamp's solution is limited to $ka < 1$ where $k = \frac{2\pi}{\lambda}$ and a is the radius of the disk. To obtain theoretical solutions on the disks of experimental interest, a Body of Revolution electromagnetics computer code developed by J. R. Mautz and R. F. Harrington (33) was used with the input data appearing in Appendix B. In the figures that immediately follow for the .15 wavelength circular plate, the correlation with the solution of Bouwkamp is good.

In all data plots for the J_ϕ current component it should be noted that the point nearest to the rim departs significantly from the neighboring interior point. The polynomial modeling was unable to follow this departure from a relatively smooth curve. The last point was therefore deleted from the polynomial fit to the J_ϕ component throughout this text. This edge point deletions should be recalled in Chapter VII that there exists a very high edge current associated with the maximum value of J_ϕ , though not depicted.

DATA

Point #1:	X=.001	Y=.8792
Point #2:	X=.002	Y=.8768
Point #3:	X=.003	Y=.872
Point #4:	X=.004	Y=.8637
Point #5:	X=.005	Y=.8731
Point #6:	X=.006	Y=.8464
Point #7:	X=.007	Y=.8741
Point #8:	X=.008	Y=.8224
Point #9:	X=.009	Y=.8776
Point #10:	X=.01	Y=.7911
Point #11:	X=.011	Y=.8821
Point #12:	X=.012	Y=.7514
Point #13:	X=.013	Y=.8923
Point #14:	X=.014	Y=.7021
Point #15:	X=.015	Y=.9091
Point #16:	X=.016	Y=.641
Point #17:	X=.017	Y=.9409
Point #18:	X=.018	Y=.5645
Point #19:	X=.019	Y=1.007
Point #20:	X=.02	Y=.4656
Point #21:	X=.021	Y=1.121
Point #22:	X=.022	Y=.334
Point #23:	X=.023	Y=2.208

Figure 9: Data from the Body of Revolution
Code for the .15 wavelength
circular disk.

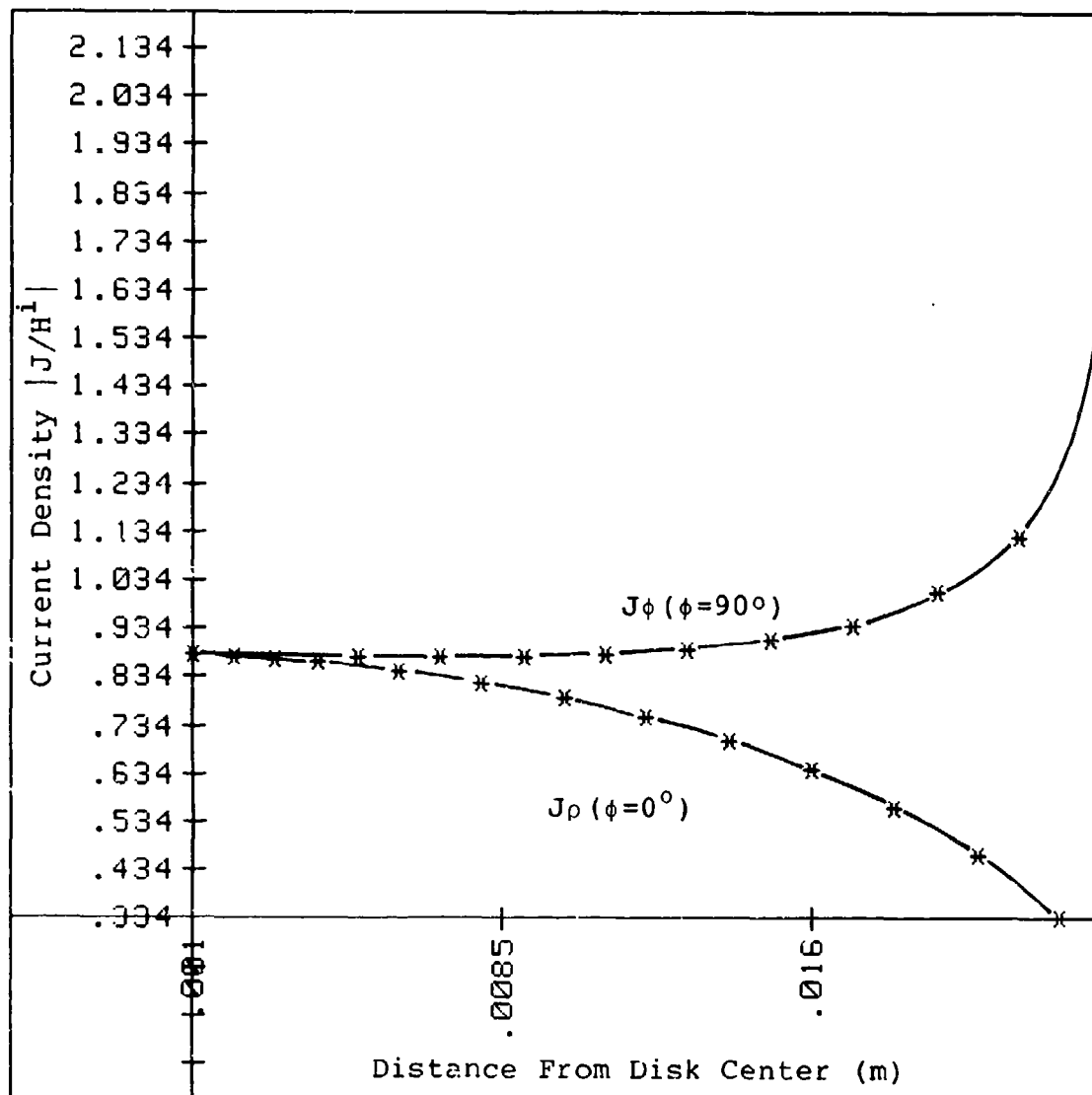


Figure 10: Plot of J_ρ and J_ϕ current components at $\phi = 0^\circ$ and $\phi = 90^\circ$ for the .15 wavelength circular disk.

DATA

Point #1:	X=.002	Y=.8768
Point #2:	X=.004	Y=.8637
Point #3:	X=.006	Y=.8464
Point #4:	X=.008	Y=.8224
Point #5:	X=.01	Y=.7911
Point #6:	X=.012	Y=.7514
Point #7:	X=.014	Y=.7021
Point #8:	X=.016	Y=.641
Point #9:	X=.018	Y=.5645
Point #10:	X=.02	Y=.4656
Point #11:	X=.022	Y=.334

POLYNOMIAL MODEL: $Y=A(M)*X^M+A(M-1)*X^{(M-1)}+\dots+A(1)*X+A(0)$
Coefficients:
 $A(0)=.89003945$
 $A(1)=-7.65403$
 $A(2)=839.877$
 $A(3)=-176413.9$
 $A(4)=8980760$
 $A(5)=-197817300$

Source	Df	SS	MS	F
Regression	5	.316	.063	
-20431.5213247 M4D.3D				
Residual	5	-.000	-.000	
Total	10	.316		

Figure 11: Polynomial fit for the J_p current component at $\phi = 0^\circ$ for the .15 wavelength circular disk.

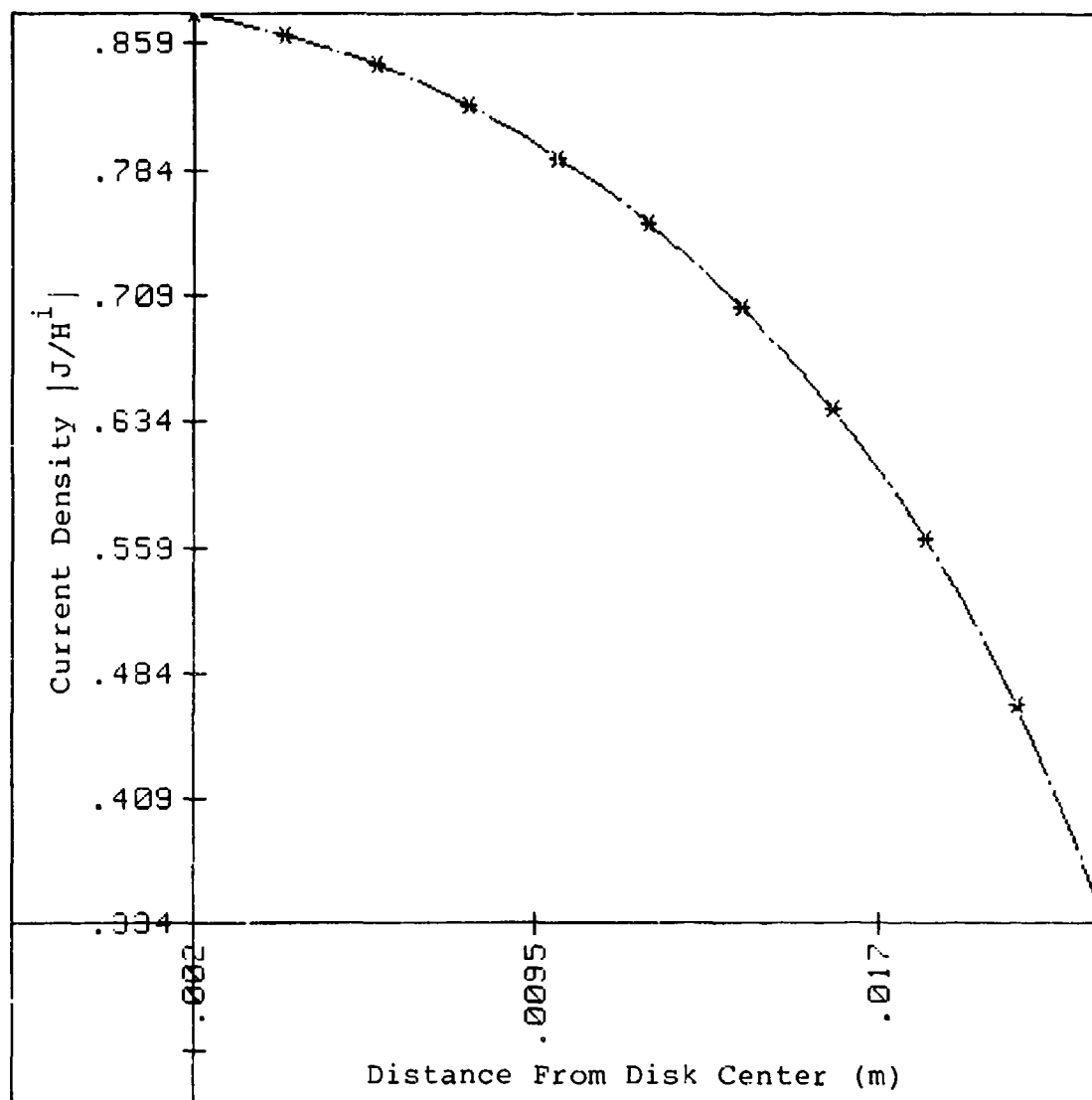


Figure 12: Plot of the J_ρ current component at $\phi = 0^\circ$ for the .15 wavelength circular disk.

DATA

Point #1:	X=.001	Y=.8792
Point #2:	X=.003	Y=.872
Point #3:	X=.005	Y=.8731
Point #4:	X=.007	Y=.8741
Point #5:	X=.009	Y=.8776
Point #6:	X=.011	Y=.8821
Point #7:	X=.013	Y=.8923
Point #8:	X=.015	Y=.9091
Point #9:	X=.017	Y=.9409
Point #10:	X=.019	Y=1.007
Point #11:	X=.021	Y=1.121

POLYNOMIAL MODEL: $Y=A(M)*X^M+A(M-1)*X^{(M-1)}+...+A(1)*X+A(0)$

Coefficients:

$A(0)=.884230915$
 $A(1)=-6.09513$
 $A(2)=816.735$
 $A(3)=1125.7$
 $A(4)=-4909480$
 $A(5)=232369100$

Source	Df	SS	MS	F
Regression	5	.061	.012	
17032.4362827 M4D.3D				
Residual	5	.000	.000	
Total	10	.061		

Figure 13: Polynomial fit for the J_ϕ current component at $\phi = 90^\circ$ for the .15 wavelength circular disk.

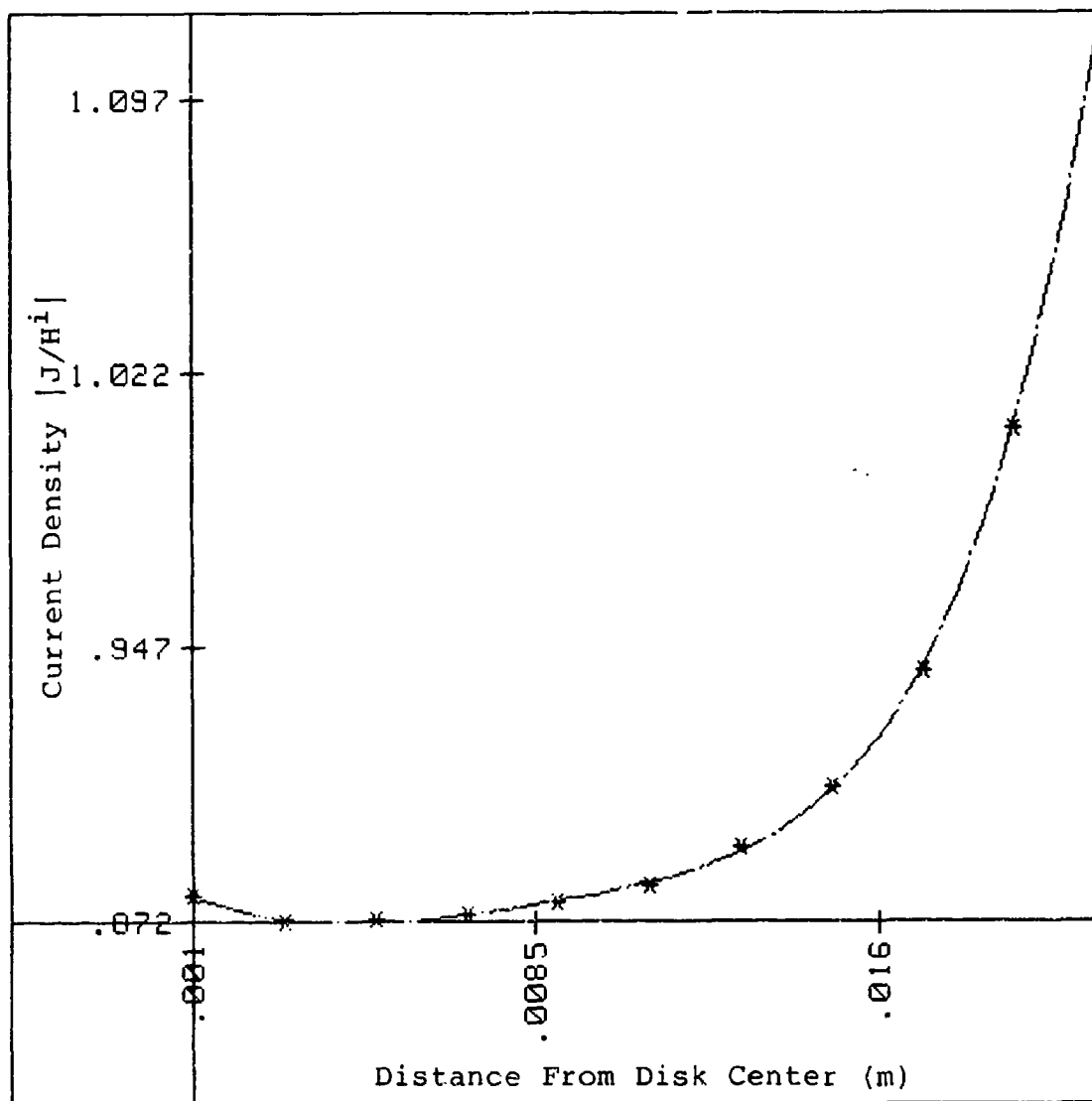


Figure 14: Plot for the J_ϕ current component at $\phi = 90^\circ$ for the .15 wavelength circular disk.

To confirm that the code is reasonable at the longer wavelengths, a 3.0 wavelength disk was run and compared to the analytic solution of Andrejewski (2) which immediately follows the plot from the code (Figure 17). The correlation is again quite good. After the summary graphs (Figure 19) are found, the polynomial fits for the maximum J_ρ and J_ϕ current components for the experimental circular disks of diameters .38, .50, 1.0, and 1.3 wavelengths are given.

DATA

Point #1:	X=.0063	Y=3.441
Point #2:	X=.0122	Y=3.285
Point #3:	X=.0185	Y=3.106
Point #4:	X=.0245	Y=2.667
Point #5:	X=.0307	Y=2.906
Point #6:	X=.0367	Y=1.953
Point #7:	X=.0429	Y=2.627
Point #8:	X=.049	Y=1.29
Point #9:	X=.0551	Y=2.358
Point #10:	X=.0612	Y=.8748
Point #11:	X=.0673	Y=2.125
Point #12:	X=.0734	Y=.8345
Point #13:	X=.0795	Y=1.967
Point #14:	X=.0857	Y=1.149
Point #15:	X=.0917	Y=1.886
Point #16:	X=.0979	Y=1.706
Point #17:	X=.1039	Y=1.875
Point #18:	X=.1102	Y=2.343
Point #19:	X=.1161	Y=1.899
Point #20:	X=.1224	Y=2.869
Point #21:	X=.1283	Y=1.925
Point #22:	X=.1346	Y=3.115
Point #23:	X=.1405	Y=1.918
Point #24:	X=.1469	Y=2.989
Point #25:	X=.1527	Y=1.866
Point #26:	X=.1591	Y=2.4585
Point #27:	X=.1649	Y=1.778
Point #28:	X=.1714	Y=1.667
Point #29:	X=.1771	Y=2.898

Figure 15: Data from the Body of Revolution
Code for the 3.0 wavelength
circular disk.

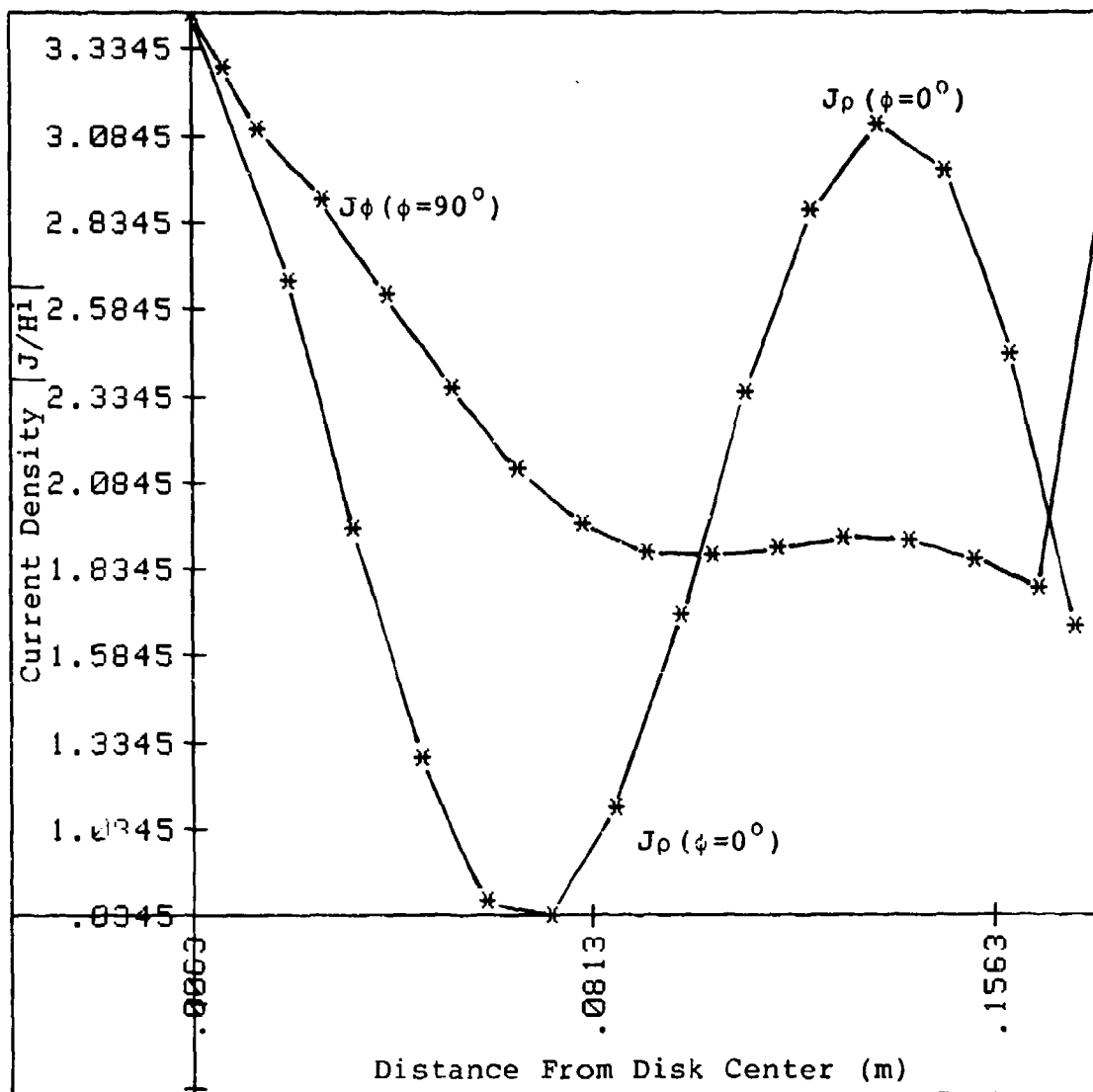


Figure 16: Plot of J_ρ and J_ϕ current components at $\phi = 0^\circ$ and $\phi = 90^\circ$ on the 3.0 wavelength circular disk.

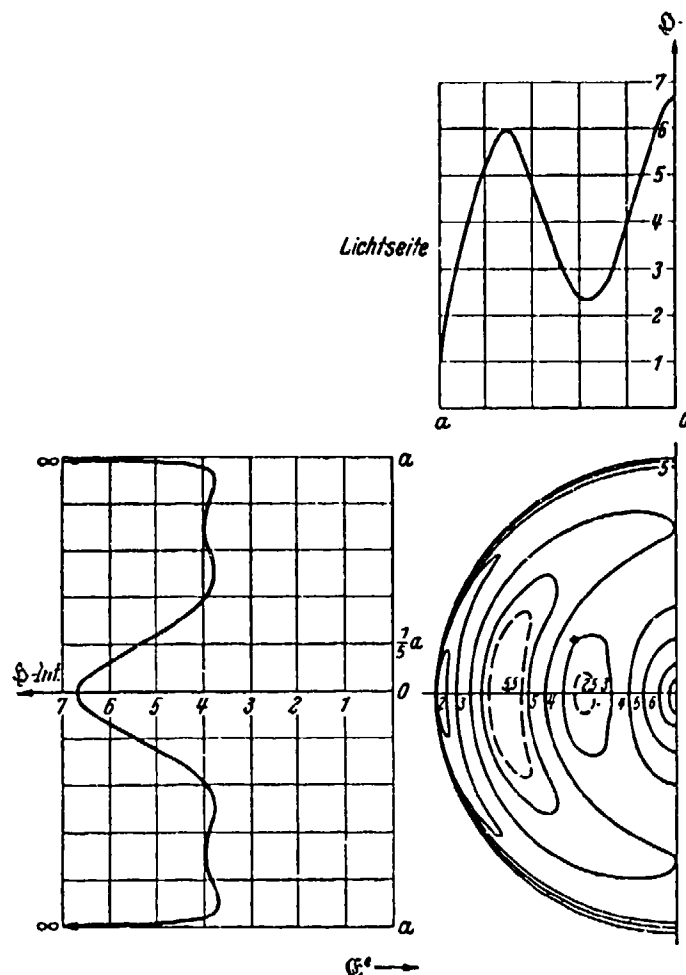
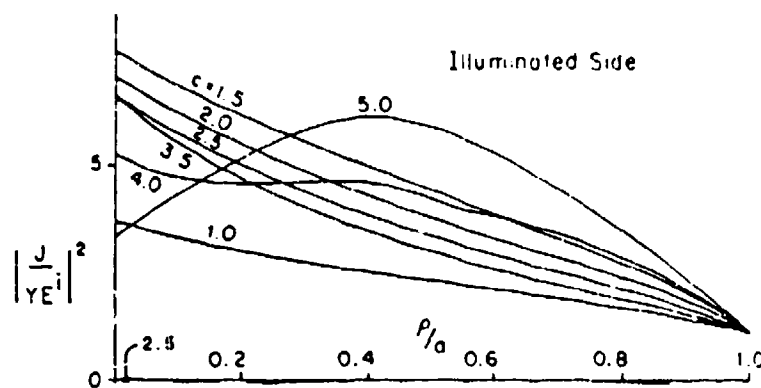


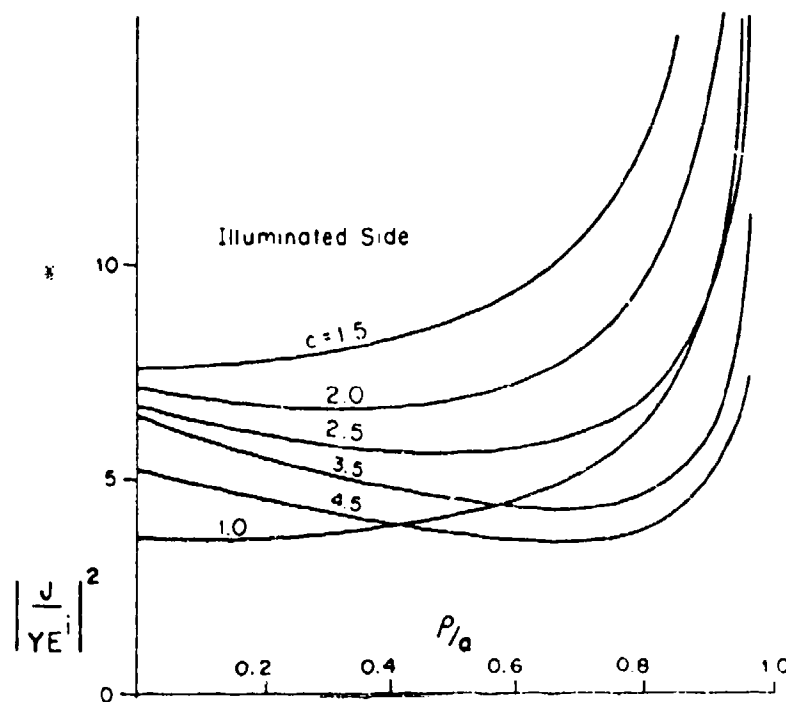
Figure 17: Theoretical result for 3.0 wavelength circular disk (2).

In this figure is shown the illuminated side of a disk of approximate diameter of 3.0 wavelengths. The top graph corresponds to J_0 at $\phi = 0^\circ$ and the left graph corresponds to J_ϕ at $\phi = 90^\circ$.

In Figure 19 are summary graphs for the perfectly conducting disk in which $C = ka$. Note that at approximately 1.2 wavelengths in diameter that the J_0 component begins to depart from the case of the small disk.



(a) J_ρ component at $\phi = 0$.



(b) J_ϕ component at $\phi = 90^\circ$.

Figure 18: Theoretical solution for the disk (9).

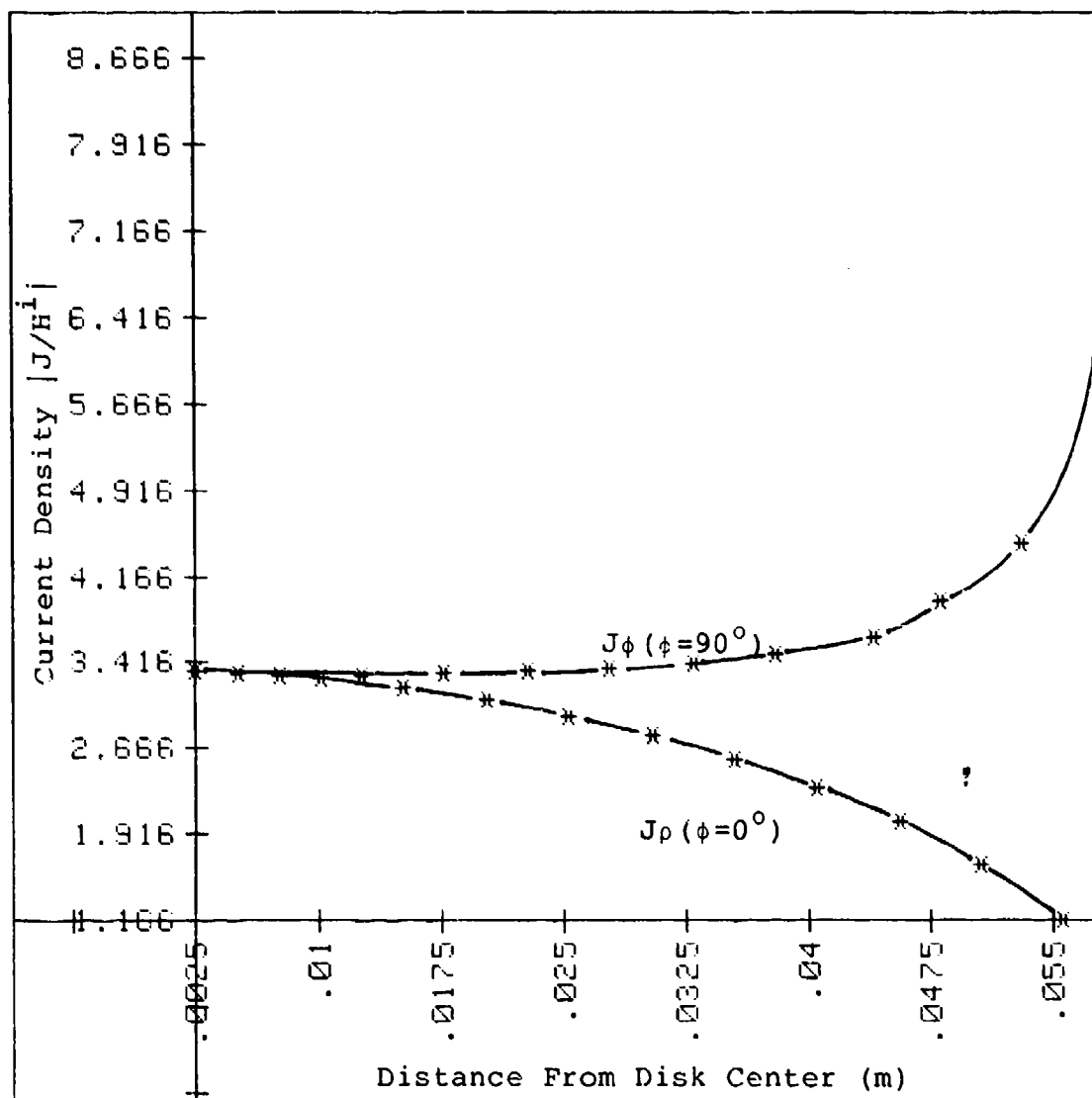


Figure 19: Plot of J_ρ and J_ϕ current components at $\phi = 0^\circ$ and $\phi = 90^\circ$ on the .38 wavelength circular disk.

DATA

Point #1:	X=.0025	Y=3.338
Point #2:	X=.0051	Y=3.327
Point #3:	X=.0076	Y=3.308
Point #4:	X=.0101	Y=3.27
Point #5:	X=.0126	Y=3.311
Point #6:	X=.0152	Y=3.191
Point #7:	X=.0177	Y=3.317
Point #8:	X=.0203	Y=3.084
Point #9:	X=.0228	Y=3.339
Point #10:	X=.0253	Y=2.95
Point #11:	X=.0278	Y=3.359
Point #12:	X=.0304	Y=2.78
Point #13:	X=.0329	Y=3.41
Point #14:	X=.0355	Y=2.572
Point #15:	X=.038	Y=3.495
Point #16:	X=.0405	Y=2.326
Point #17:	X=.044	Y=3.64
Point #18:	X=.0456	Y=2.023
Point #19:	X=.0481	Y=3.944
Point #20:	X=.0507	Y=1.643
Point #21:	X=.0532	Y=4.457
Point #22:	X=.0557	Y=1.166
Point #23:	X=.0582	Y=9.06

Figure 20: Data from the Body of the Revolution Code for the .38 wavelength circular disk.

DATA

Point #1:	X=.0051	Y=3.327
Point #2:	X=.0101	Y=3.27
Point #3:	X=.0152	Y=3.191
Point #4:	X=.0203	Y=3.084
Point #5:	X=.0253	Y=2.95
Point #6:	X=.0304	Y=2.78
Point #7:	X=.0355	Y=2.572
Point #8:	X=.0405	Y=2.326
Point #9:	X=.0456	Y=2.023
Point #10:	X=.0507	Y=1.643
Point #11:	X=.0557	Y=1.166

POLYNOMIAL MODEL: $Y=A(M)*X^M+A(M-1)*X^{(M-1)}+...+A(1)*X+A(0)$

Coefficients:

$A(0)=3.402624814$

$A(1)=-13.5166622$

$A(2)=87.090219$

$A(3)=-10076.8948$

Source	Df	SS	MS	F
Regression	3	5.089	1.696	
13340.7291375 M4D.3D				
Residual	7	.001	.000	
Total	10	5.090		

Figure 21: Polynomial fit for the J_0 current component at $\phi = 0^\circ$ on the .38 wavelength circular disk.

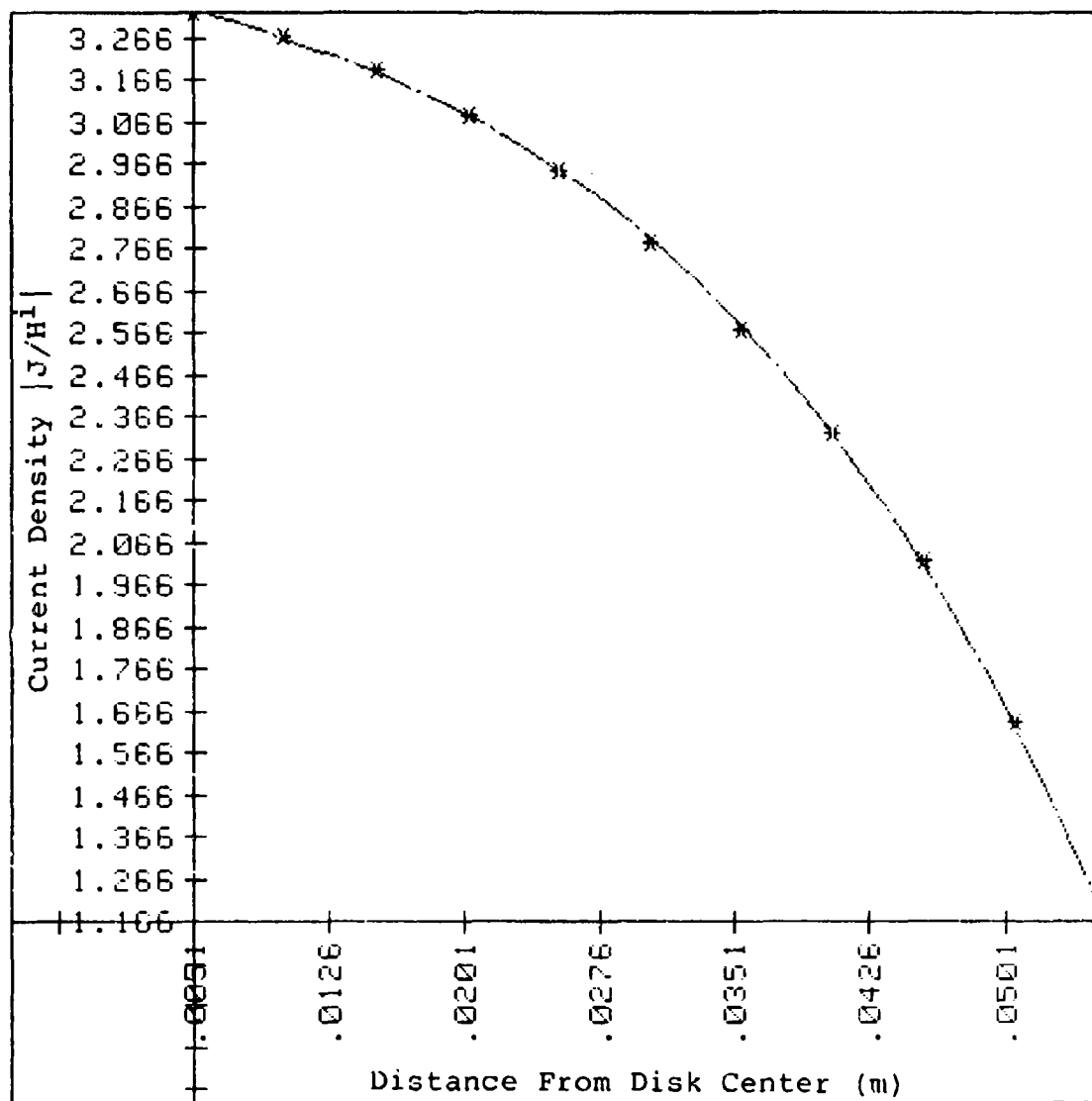


Figure 22: Plot of the J_ϕ current component at $\phi = 0^\circ$ for the .38 wavelength circular disk.

DATA

Point #1:	X=.0025	Y=3.338
Point #2:	X=.0076	Y=3.308
Point #3:	X=.0126	Y=3.311
Point #4:	X=.0177	Y=3.317
Point #5:	X=.0228	Y=3.339
Point #6:	X=.0278	Y=3.359
Point #7:	X=.0329	Y=3.41
Point #8:	X=.038	Y=3.495
Point #9:	X=.044	Y=3.64
Point #10:	X=.0481	Y=3.944
Point #11:	X=.0532	Y=4.457

POLYNOMIAL MODEL: $Y=A(M)*X^M+A(M-1)*X^{(M-1)}+\dots+A(1)*X+A(0)$

Coefficients:

$A(0)=3.395325482$
 $A(1)=-26.378934$
 $A(2)=2360.5108$
 $A(3)=-78558.199$
 $A(4)=950222.7$

Source	Df	SS	MS	F
Regression	4	1.301	.325	850.187
Residual	6	.002	.000	
Total	10	1.303		

Figure 23: Polynomial fit for the $J\phi$ current component at $\phi = 90^\circ$ for the .38 wavelength circular disk.

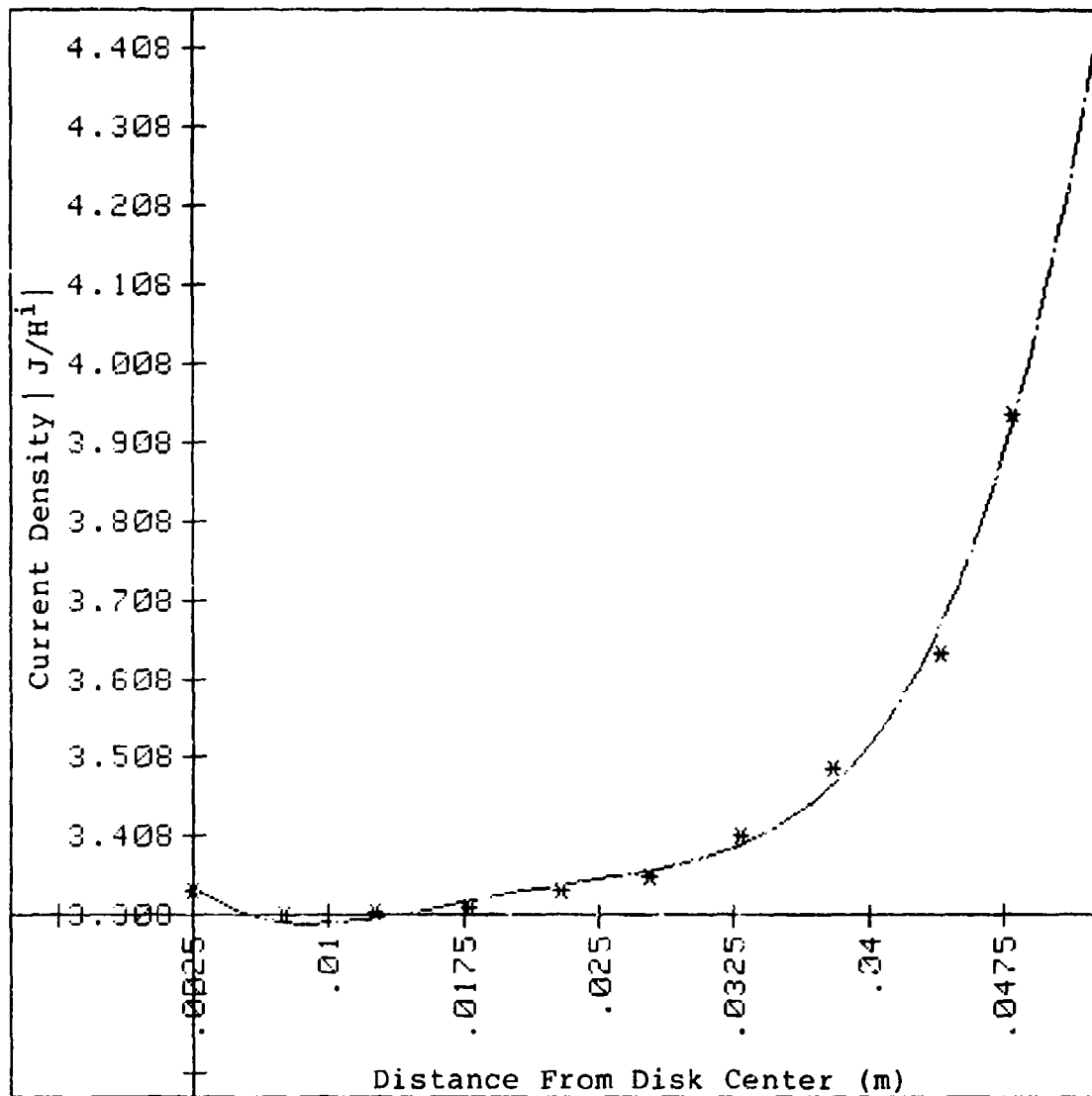


Figure 24: Plot for the J_ϕ current component at $\phi = 90^\circ$ for the .38 wavelength circular disk.

DATA

Point #1:	X=.0033	Y=3.745
Point #2:	X=.0067	Y=3.731
Point #3:	X=.01	Y=3.704
Point #4:	X=.0133	Y=3.658
Point #5:	X=.0167	Y=3.7
Point #6:	X=.02	Y=3.558
Point #7:	X=.0233	Y=3.696
Point #8:	X=.0267	Y=3.423
Point #9:	X=.03	Y=3.704
Point #10:	X=.0333	Y=3.254
Point #11:	X=.0367	Y=3.708
Point #12:	X=.04	Y=3.044
Point #13:	X=.0433	Y=3.746
Point #14:	X=.0466	Y=2.797
Point #15:	X=.05	Y=3.808
Point #16:	X=.0533	Y=2.5
Point #17:	X=.0567	Y=3.948
Point #18:	X=.06	Y=2.15
Point #19:	X=.0633	Y=4.253
Point #20:	X=.0666	Y=1.731
Point #21:	X=.07	Y=4.789
Point #22:	X=.0733	Y=1.204
Point #23:	X=.0767	Y=9.794

Figure 25: Data from the Body of Revolution
Code for the .50 wavelength circular
disk.

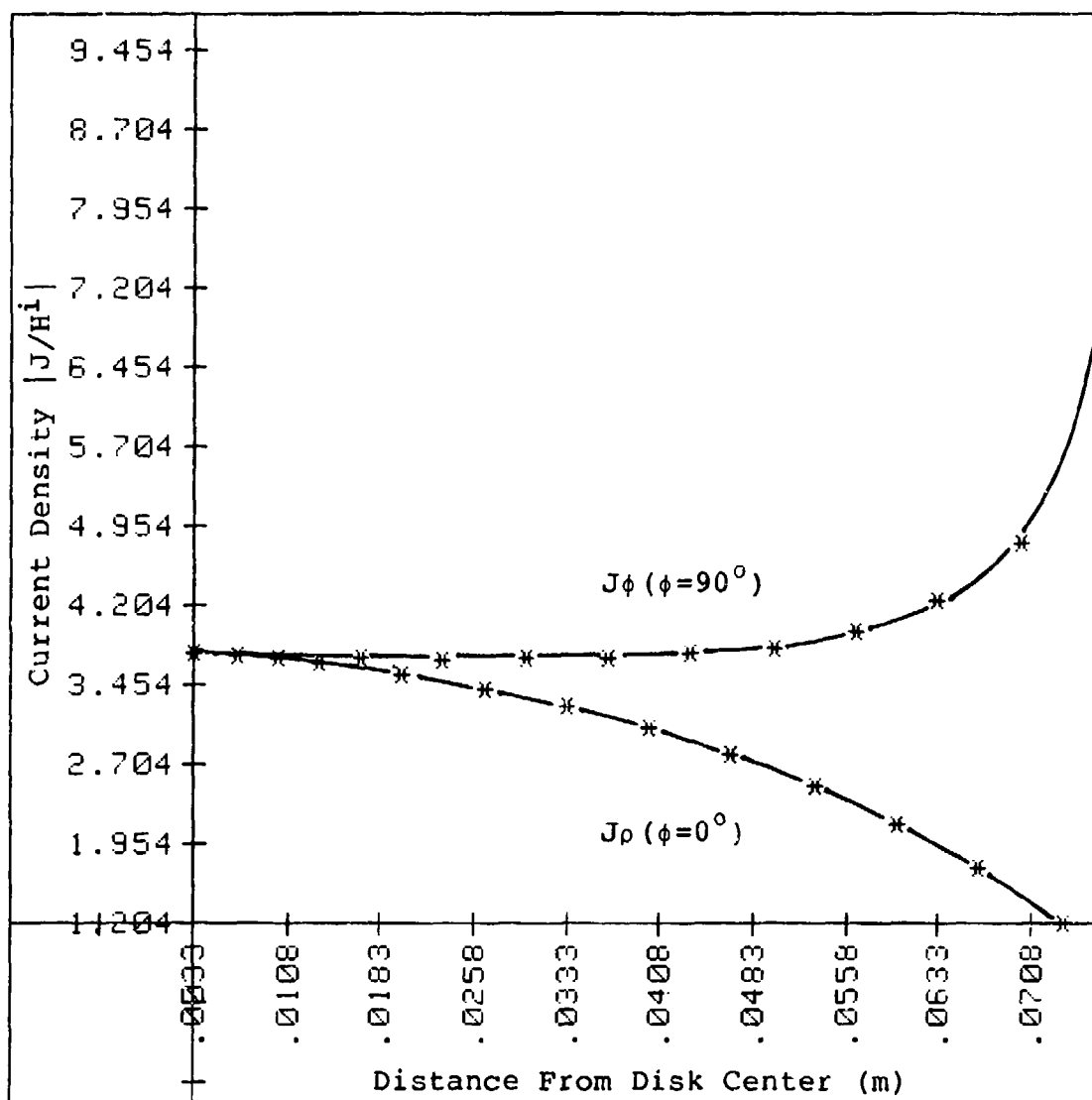


Figure 26: Plot of J_ρ and J_ϕ current components at $\phi = 0^\circ$ and $\phi = 90^\circ$ on the .50 wavelength circular disk.

DATA

Point #1:	X=.0067	Y=3.731
Point #2:	X=.0133	Y=3.658
Point #3:	X=.02	Y=3.558
Point #4:	X=.0267	Y=3.423
Point #5:	X=.0333	Y=3.254
Point #6:	X=.04	Y=3.044
Point #7:	X=.0466	Y=2.797
Point #8:	X=.0533	Y=2.5
Point #9:	X=.06	Y=2.15
Point #10:	X=.0666	Y=1.731
Point #11:	X=.0733	Y=1.204

POLYNOMIAL MODEL: $Y=A(M)*X^M+A(M-1)*X^{(M-1)}+...+A(1)*X+A(0)$

Coefficients:

A(0)=3.808547119

A(1)=-9.9410142

A(2)=-76.172458

A(3)=-3694.9184

Source	Df	SS	MS	F
Regression	3	7.027	2.342	
22102.2789119 M4D.3D				
Residual	7	.001	.000	
Total	10	7.028		

Figure 27: Polynomial fit for the J_0 current component at $\phi = 0^\circ$ for the .50 wavelength circular disk.

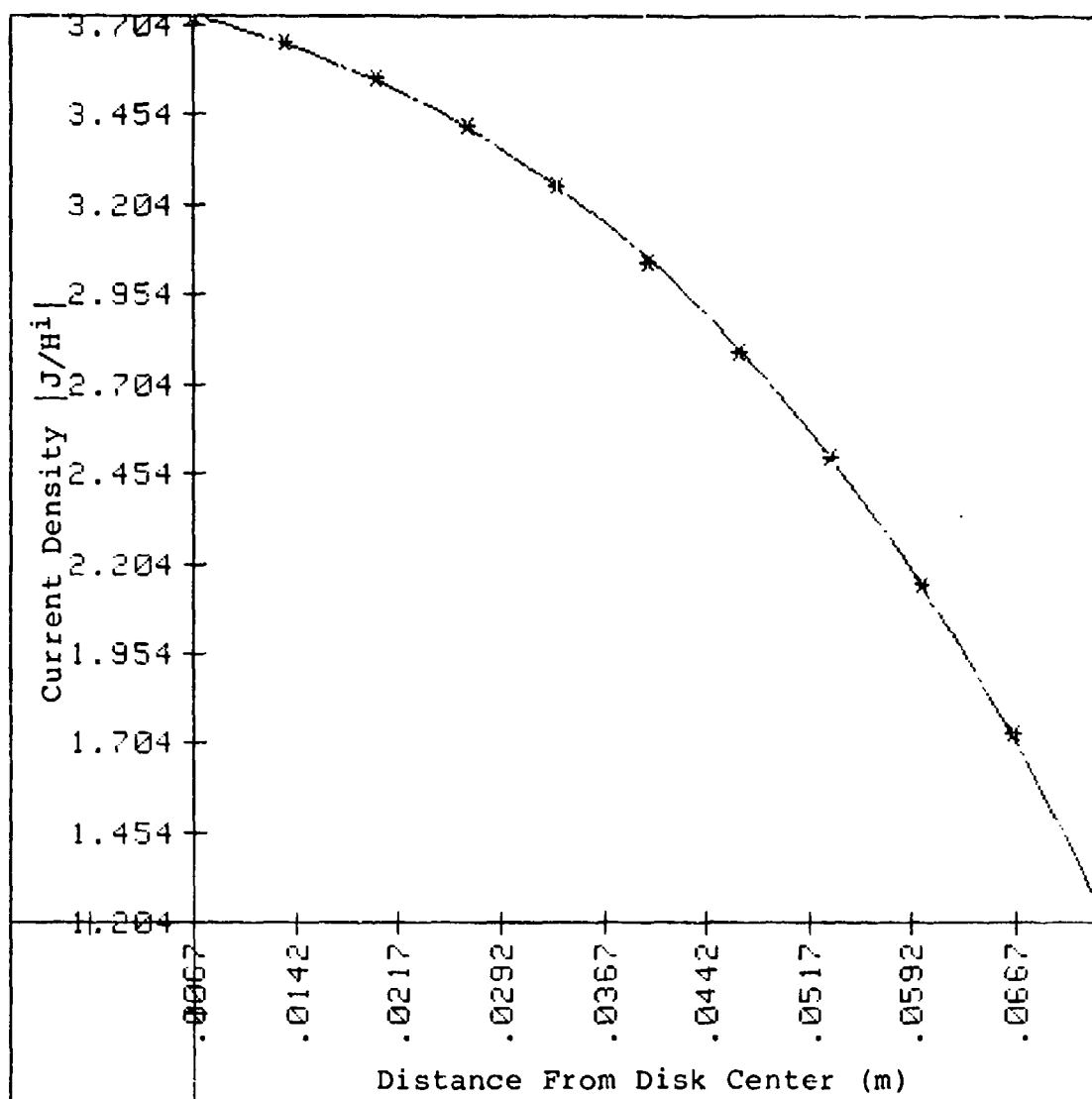


Figure 28: Plot of the J_0 current component at $\phi = 0^\circ$ for the .50 wavelength circular disk.

DATA

Point #1:	X=.0033	Y=3.745
Point #2:	X=.01	Y=3.704
Point #3:	X=.0167	Y=3.7
Point #4:	X=.0233	Y=3.696
Point #5:	X=.03	Y=3.704
Point #6:	X=.0367	Y=3.708
Point #7:	X=.0433	Y=3.746
Point #8:	X=.05	Y=3.808
Point #9:	X=.0567	Y=3.948
Point #10:	X=.0633	Y=4.253
Point #11:	X=.07	Y=4.789

POLYNOMIAL MODEL: $Y=A(M)*X^M+A(M-1)*X^{(M-1)}+...+A(1)*X+A(0)$

Coefficients:

$A(0)=3.7749465$
 $A(1)=-10.77588$
 $A(2)=454.693$
 $A(3)=-4183.87$
 $A(4)=-126590.5$
 $A(5)=2389217$

Source	Df	SS	MS	F
Regression	5	1.168	.234	6969.584
Residual	5	.000	.000	
Total	10	1.168		

Figure 29: Polynomial fit for the J_ϕ current component at $\phi = 90^\circ$ for the .50 wavelength circular disk.

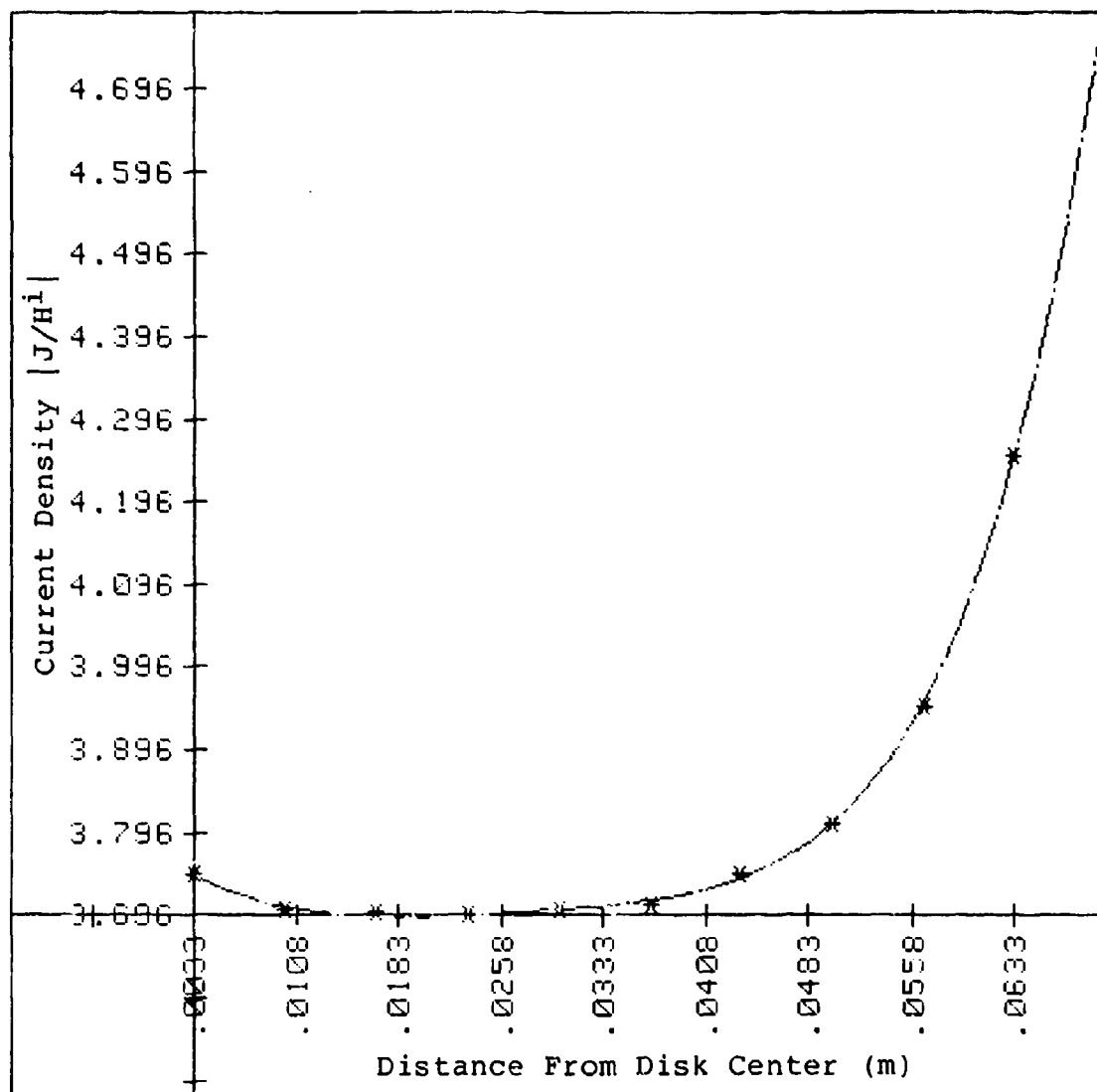


Figure 30: Plot for the J_ϕ current component at $\phi = 90^\circ$ for the .50 wavelength circular disk.

DATA		
Point #1:	X=.0015	Y=3.153
Point #2:	X=.0031	Y=3.146
Point #3:	X=.0046	Y=3.13
Point #4:	X=.0061	Y=3.109
Point #5:	X=.0076	Y=3.108
Point #6:	X=.0092	Y=3.053
Point #7:	X=.0107	Y=3.082
Point #8:	X=.0122	Y=2.982
Point #9:	X=.0137	Y=3.045
Point #10:	X=.0153	Y=2.89
Point #11:	X=.0168	Y=2.995
Point #12:	X=.0184	Y=2.782
Point #13:	X=.0199	Y=2.948
Point #14:	X=.0214	Y=2.663
Point #15:	X=.0229	Y=2.883
Point #16:	X=.0245	Y=2.527
Point #17:	X=.026	Y=2.821
Point #18:	X=.0275	Y=2.385
Point #19:	X=.029	Y=2.748
Point #20:	X=.0306	Y=2.23
Point #21:	X=.0321	Y=2.674
Point #22:	X=.0337	Y=2.069
Point #23:	X=.0352	Y=2.604
Point #24:	X=.0367	Y=1.909
Point #25:	X=.0382	Y=2.531
Point #26:	X=.0398	Y=1.741
Point #27:	X=.0413	Y=2.472
Point #28:	X=.0428	Y=1.576
Point #29:	X=.0443	Y=2.422
Point #30:	X=.0459	Y=1.403
Point #31:	X=.0474	Y=2.403
Point #32:	X=.049	Y=1.224
Point #33:	X=.0505	Y=2.437
Point #34:	X=.052	Y=1.041
Point #35:	X=.0535	Y=2.582
Point #36:	X=.0551	Y=.8284
Point #37:	X=.0566	Y=2.895
Point #38:	X=.0581	Y=.5831
Point #39:	X=.0596	Y=6.03

Figure 31: Data from the Body of Revolution
Code for the 1.0 wavelength
circular disk.

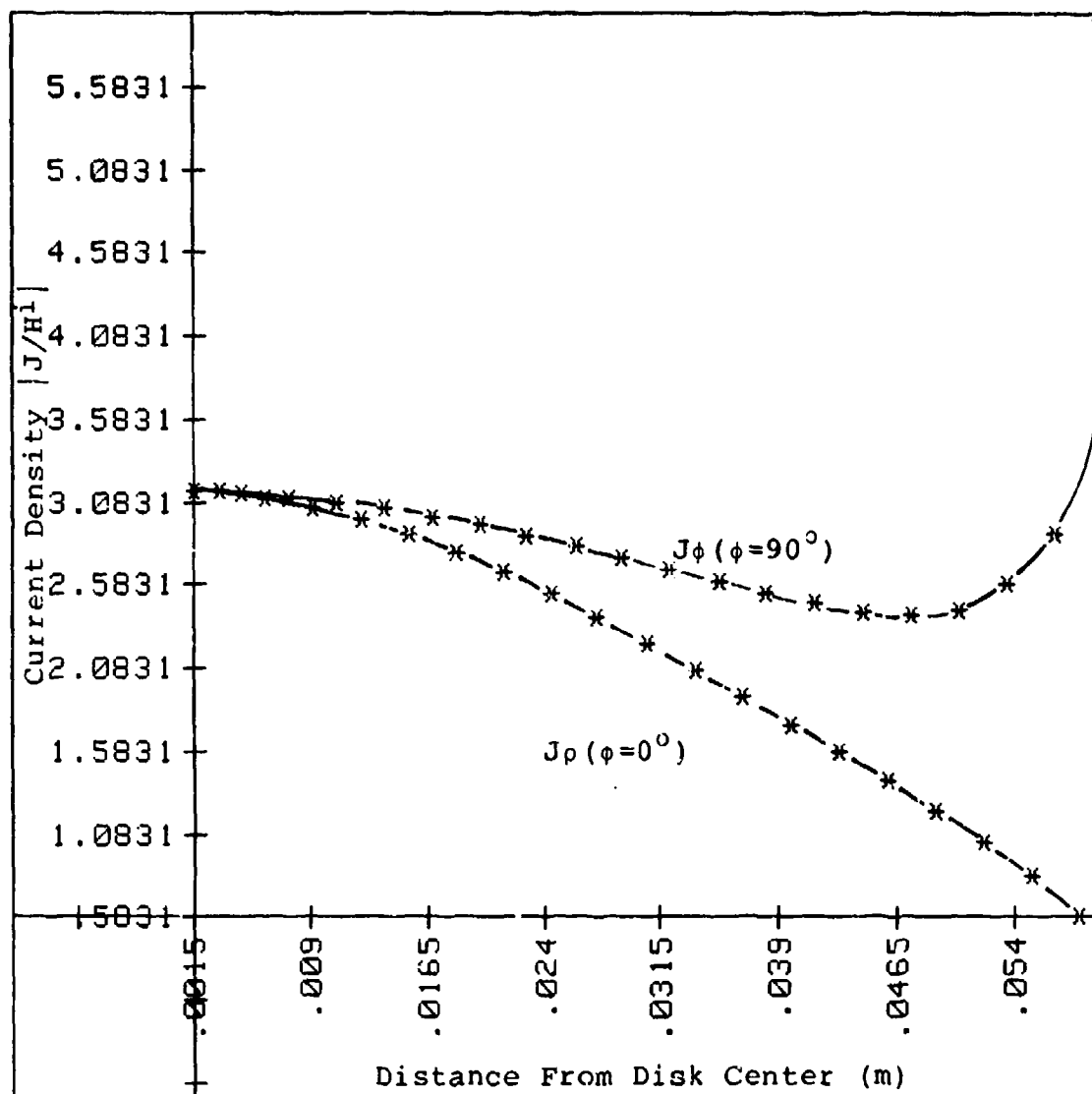


Figure 32: Plot of J_ρ and J_ϕ current components at $\phi = 0^\circ$ and $\phi = 90^\circ$ for the 1.0 wavelength circular disk.

DATA

Point #1:	X=.0031	Y=3.146
Point #2:	X=.0061	Y=3.109
Point #3:	X=.0092	Y=3.053
Point #4:	X=.0122	Y=2.982
Point #5:	X=.0153	Y=2.89
Point #6:	X=.0184	Y=2.782
Point #7:	X=.0214	Y=2.663
Point #8:	X=.0245	Y=2.527
Point #9:	X=.0275	Y=2.385
Point #10:	X=.0306	Y=2.23
Point #11:	X=.0337	Y=2.069
Point #12:	X=.0367	Y=1.909
Point #13:	X=.0398	Y=1.741
Point #14:	X=.0428	Y=1.576
Point #15:	X=.0459	Y=1.403
Point #16:	X=.049	Y=1.224
Point #17:	X=.052	Y=1.041
Point #18:	X=.0551	Y=.8284
Point #19:	X=.0581	Y=.5831

POLYNOMIAL MODEL: $Y=A(M)*X^M+A(M-1)*X^{(M-1)}+\dots+A(1)*X+A(0)$

Coefficients:

A(0)=3.1943401455

A(1)=-8.2680791

A(2)=-883.671313

A(3)=4536.71457

Source	Df	SS	MS	F
Regression	3	12.211	4.070	
13136.0954293 M4D.3D				
Residual	15	.005	.000	
Total	18	12.215		

Figure 33: Polynomial fit for the J_p current component at $\phi = 0^\circ$ for the 1.0 wavelength circular disk.

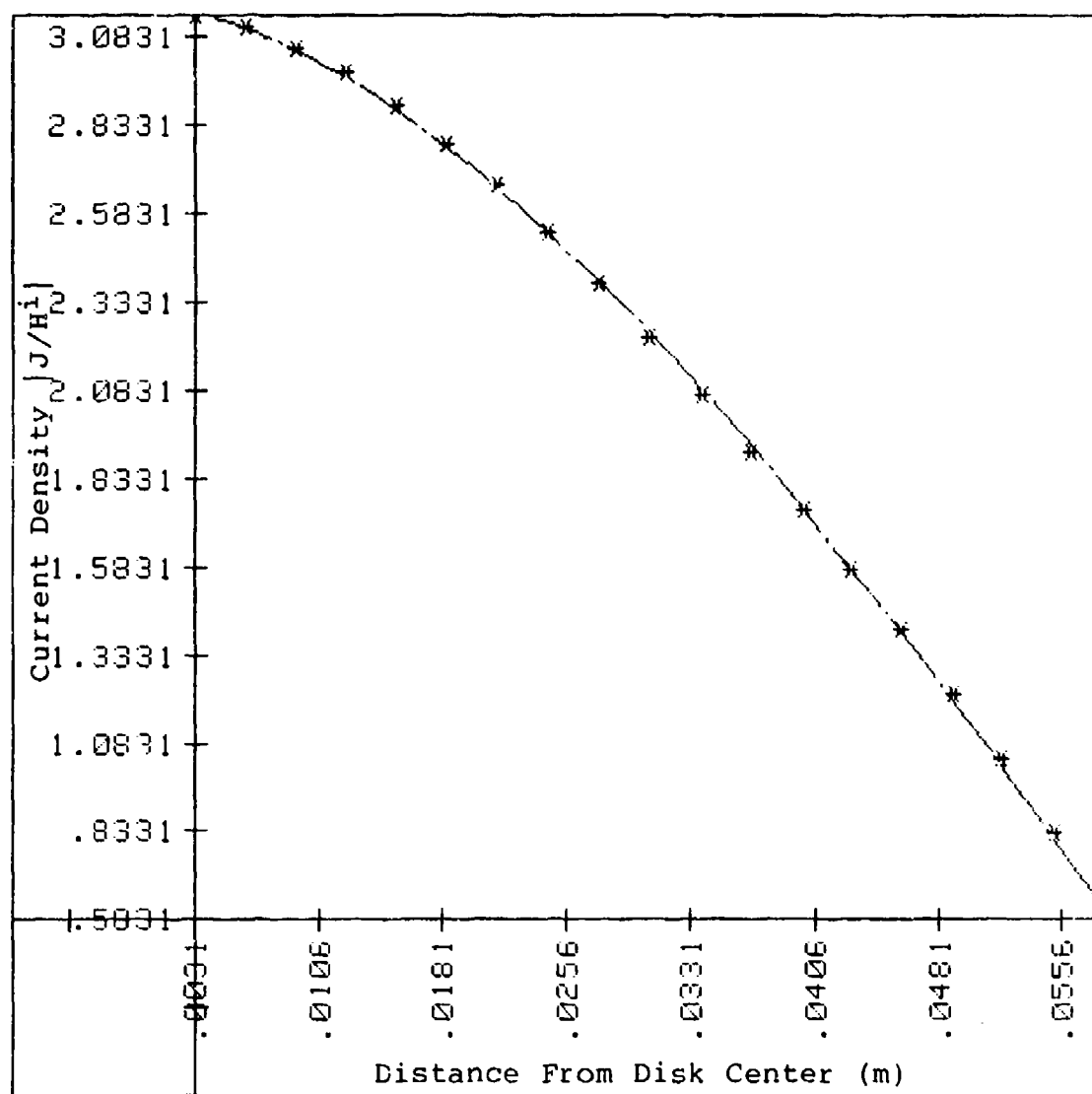


Figure 34: Plot of the J_0 current component at $\phi = 0^\circ$ for the 1.0 wavelength circular disk.

DATA

Point #1:	X=.0015	Y=3.153
Point #2:	X=.0046	Y=3.13
Point #3:	X=.0076	Y=3.168
Point #4:	X=.0107	Y=3.082
Point #5:	X=.0137	Y=3.045
Point #6:	X=.0168	Y=2.995
Point #7:	X=.0199	Y=2.948
Point #8:	X=.0229	Y=2.883
Point #9:	X=.026	Y=2.821
Point #10:	X=.029	Y=2.748
Point #11:	X=.0321	Y=2.674
Point #12:	X=.0352	Y=2.604
Point #13:	X=.0382	Y=2.531
Point #14:	X=.0413	Y=2.472
Point #15:	X=.0443	Y=2.422
Point #16:	X=.0474	Y=2.403
Point #17:	X=.0505	Y=2.437
Point #18:	X=.0535	Y=2.582
Point #19:	X=.0566	Y=2.895

POLYNOMIAL MODEL: $Y=A(M)*X^M+A(M-1)*X^{(M-1)}+\dots+A(1)*X+A(0)$
 Coefficients:

$A(0)=3.17569475$
 $A(1)=-17.25378$
 $A(2)=2264.259$
 $A(3)=-203305.9$
 $A(4)=7448120$
 $A(5)=-130549100$
 $A(6)=903319000$

Source	Df	SS	MS	F
Regression	6	1.257	.210	
-15629.6659251 M4D.3D				
Residual	12	-.000	-.000	
Total	18	1.257		

Figure 35: Polynomial fit for the J_ϕ current component at $\phi = 90^\circ$ for the 1.0 wavelength circular disk.

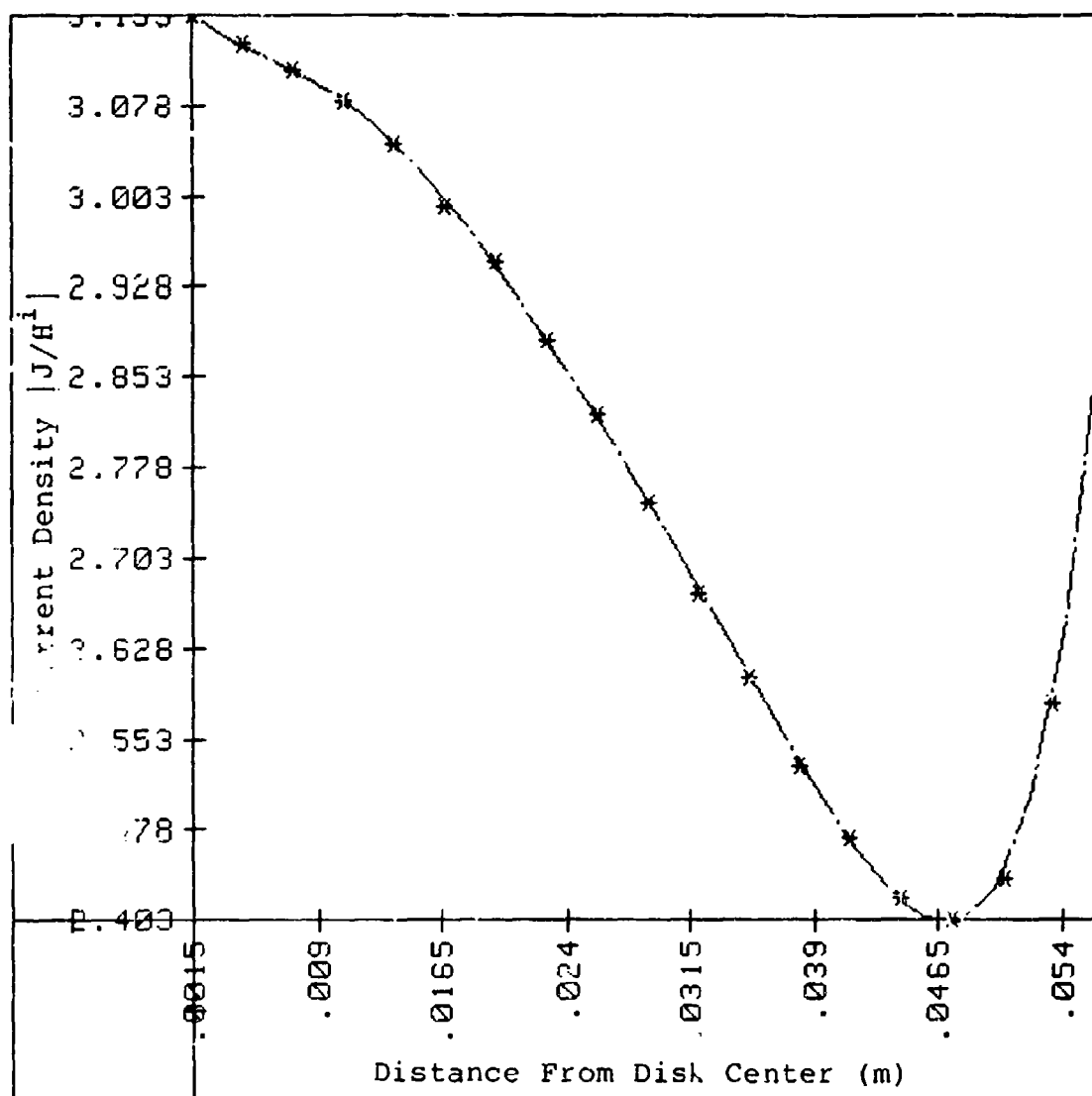


Figure 36: Plot for the $J\phi$ current component at $\phi = 90^\circ$ for the 1.0 wavelength circular disk.

DATA		
Point #1:	X=.002	Y=3.081
Point #2:	X=.004	Y=3.072
Point #3:	X=.006	Y=3.058
Point #4:	X=.008	Y=3.023
Point #5:	X=.01	Y=3.031
Point #6:	X=.0119	Y=2.952
Point #7:	X=.0139	Y=2.987
Point #8:	X=.0159	Y=2.857
Point #9:	X=.0179	Y=2.934
Point #10:	X=.0199	Y=2.744
Point #11:	X=.0219	Y=2.865
Point #12:	X=.0239	Y=2.62
Point #13:	X=.0259	Y=2.793
Point #14:	X=.0278	Y=2.497
Point #15:	X=.0298	Y=2.708
Point #16:	X=.0318	Y=2.373
Point #17:	X=.0338	Y=2.617
Point #18:	X=.0358	Y=2.259
Point #19:	X=.0378	Y=2.522
Point #20:	X=.0398	Y=2.158
Point #21:	X=.0418	Y=2.424
Point #22:	X=.0438	Y=2.072
Point #23:	X=.0458	Y=2.328
Point #24:	X=.0477	Y=2
Point #25:	X=.0497	Y=2.235
Point #26:	X=.0517	Y=1.931
Point #27:	X=.0537	Y=2.148
Point #28:	X=.0557	Y=1.857
Point #29:	X=.0577	Y=2.071
Point #30:	X=.0597	Y=1.768
Point #31:	X=.0617	Y=2.018
Point #32:	X=.0636	Y=1.652
Point #33:	X=.0656	Y=2.001
Point #34:	X=.0676	Y=1.487
Point #35:	X=.0696	Y=2.072
Point #36:	X=.0716	Y=1.25
Point #37:	X=.0736	Y=2.285
Point #38:	X=.0756	Y=.9054
Point #39:	X=.0776	Y=4.718

Figure 37: Data from the Body of Revolution Code for the 1.3 wavelength circular disk.

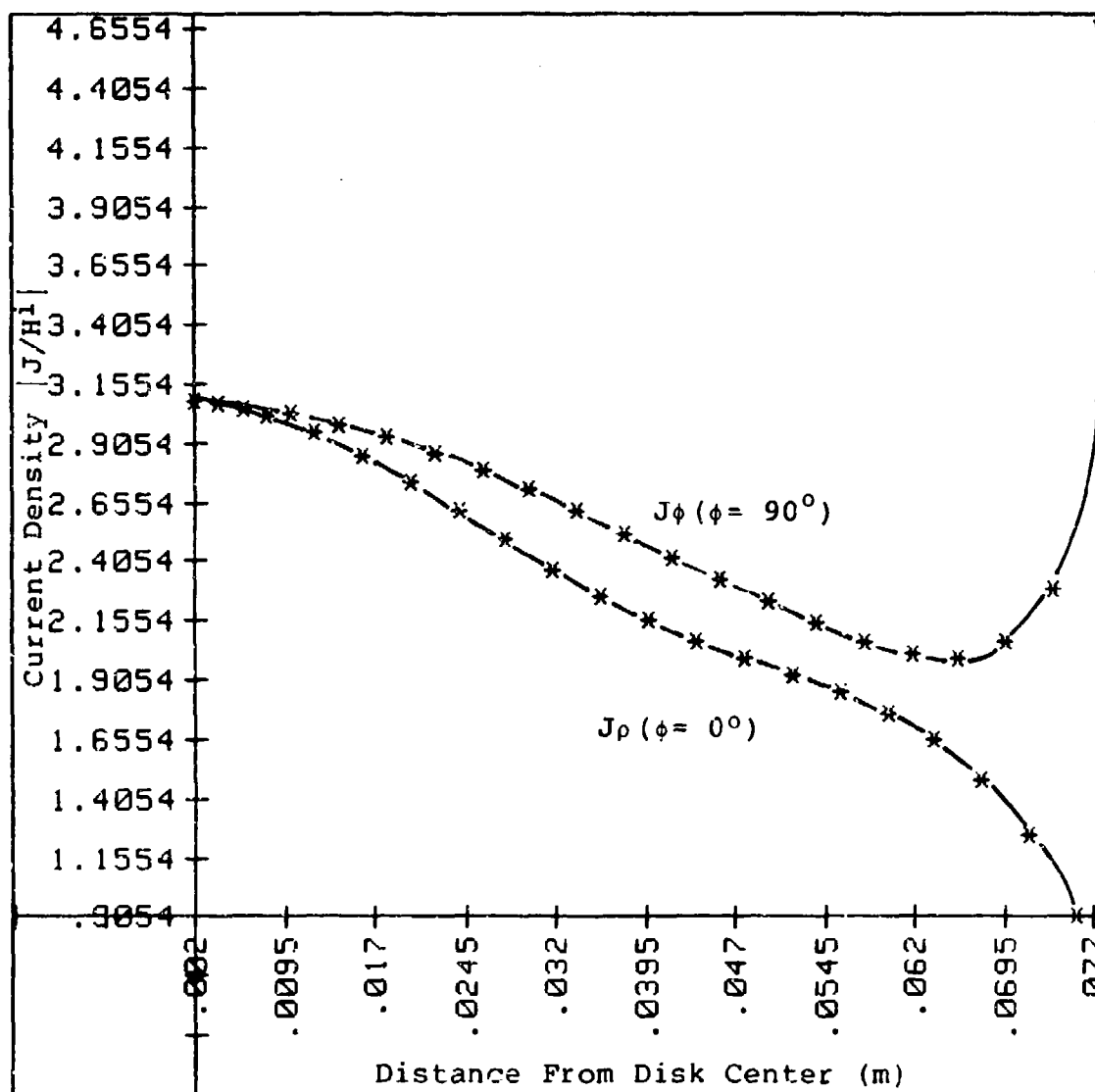


Figure 38: Plot of J_ρ and J_ϕ current components at $\phi = 0^\circ$ and $\phi = 90^\circ$ for the 1.3 wavelength circular disk.

DATA

Point #1:	X=.004	Y=3.072
Point #2:	X=.008	Y=3.023
Point #3:	X=.0119	Y=2.952
Point #4:	X=.0159	Y=2.857
Point #5:	X=.0199	Y=2.744
Point #6:	X=.0239	Y=2.62
Point #7:	X=.0278	Y=2.497
Point #8:	X=.0318	Y=2.373
Point #9:	X=.0358	Y=2.259
Point #10:	X=.0398	Y=2.158
Point #11:	X=.0438	Y=2.072
Point #12:	X=.0477	Y=2
Point #13:	X=.0517	Y=1.931
Point #14:	X=.0557	Y=1.857
Point #15:	X=.0597	Y=1.768
Point #16:	X=.0636	Y=1.652
Point #17:	X=.0676	Y=1.487
Point #18:	X=.0716	Y=1.25
Point #19:	X=.0756	Y=.9054

POLYNOMIAL MODEL: $Y=A(M)*X^M+A(M-1)*X^{(M-1)}+...+A(1)*X+A(0)$

Coefficients:

A(0)=3.008052927

A(1)=22.5225579

A(2)=-2844.32076

A(3)=60469.0732

A(4)=-418319.823

Source	Df	SS	MS	F
Regression	4	6.844	1.711	
15893.1909279 M4D.3D				
Residual	14	.002	.000	
Total	18	6.845		

Figure 39: Polynomial fit for the J_0 current component at $\phi = 90^\circ$ for the 1.3 wavelength circular disk.

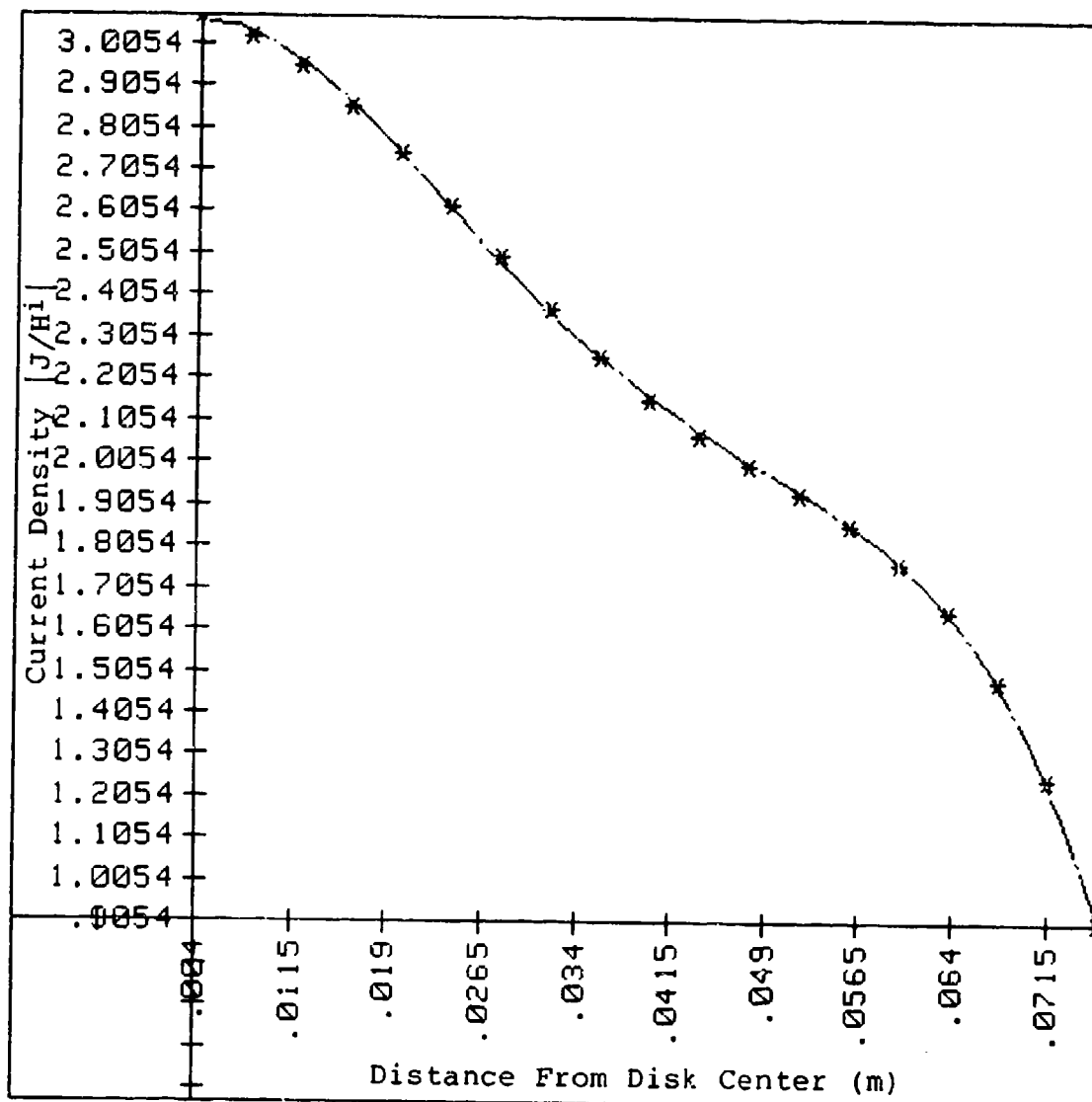


Figure 40: Plot of the J_0 current component at $\phi = 0^\circ$ for the 1.3 wavelength circular disk.

DATA

Point #1:	X=.002	Y=3.081
Point #2:	X=.006	Y=3.058
Point #3:	X=.01	Y=3.031
Point #4:	X=.0139	Y=2.987
Point #5:	X=.0179	Y=2.934
Point #6:	X=.0219	Y=2.865
Point #7:	X=.0259	Y=2.793
Point #8:	X=.0298	Y=2.708
Point #9:	X=.0338	Y=2.617
Point #10:	X=.0378	Y=2.522
Point #11:	X=.0418	Y=2.424
Point #12:	X=.0458	Y=2.328
Point #13:	X=.0497	Y=2.235
Point #14:	X=.0537	Y=2.148
Point #15:	X=.0577	Y=2.071
Point #16:	X=.0617	Y=2.018
Point #17:	X=.0656	Y=2.001
Point #18:	X=.0696	Y=2.072
Point #19:	X=.0736	Y=2.285

POLYNOMIAL MODEL: $Y=A(M)*X^M+A(M-1)*X^{(M-1)}+\dots+A(1)*X+A(0)$

Coefficients:

$A(0)=3.10093991$
 $A(1)=-10.89312$
 $A(2)=989.22$
 $A(3)=-84386.8$
 $A(4)=2455025$
 $A(5)=-32841490$
 $A(6)=170852500$

Source	Df	SS	MS	F
Regression	6	2.732	.455	6819.542
Residual	12	.001	.000	
Total	18	2.733		

Figure 41: Polynomial fit for the J_ϕ current component at $\phi \approx 90^\circ$ for the 1.3 wavelength circular disk.

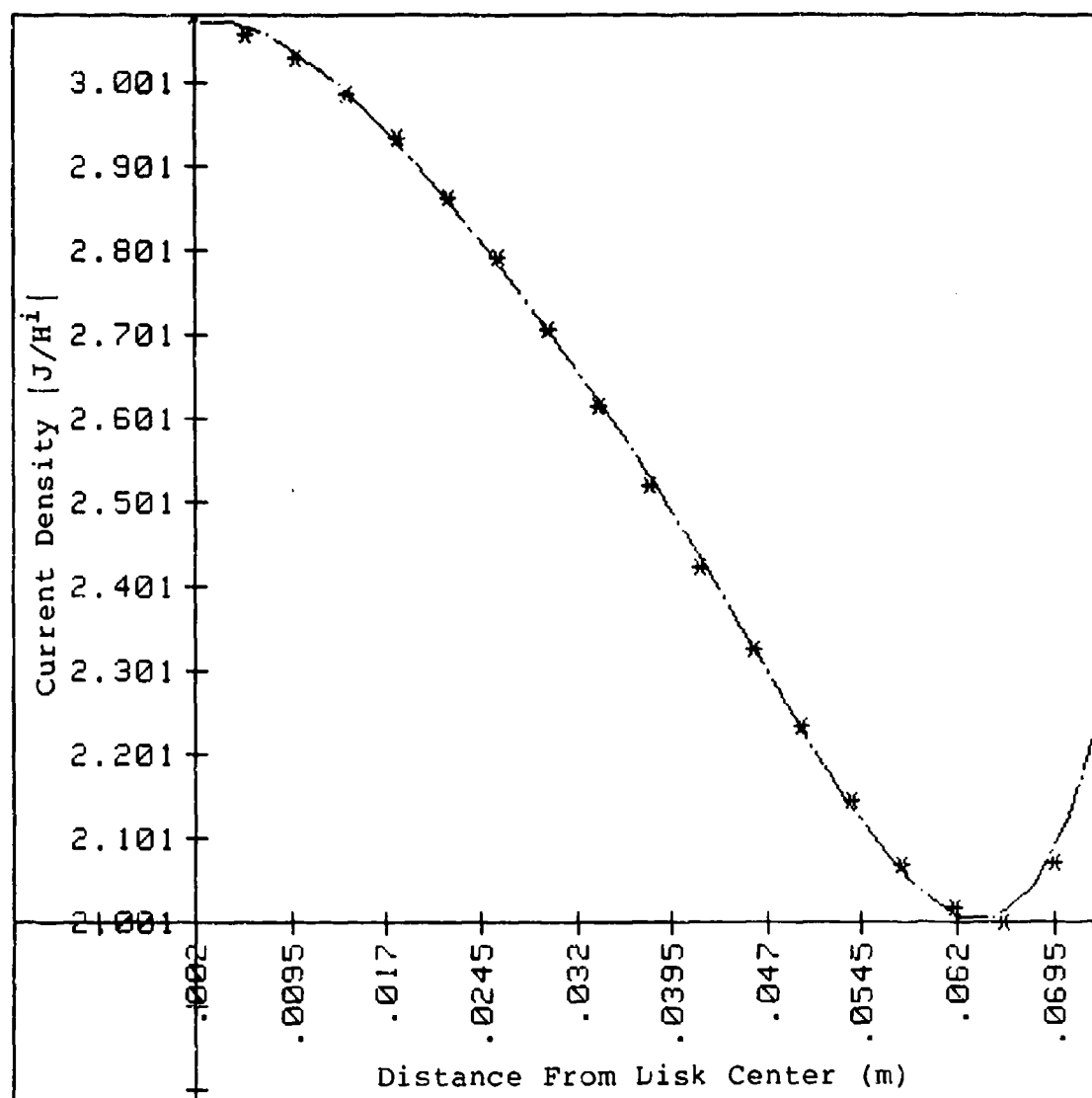


Figure 42: Plot for the J_ϕ current component at $\phi = 90^\circ$ for the 1.3 wavelength circular disk.

Square Flat Plate

The square flat plate is not solvable analytically. A Body of Translation electromagnetic computer code solution was run at the Rome Air Development Center and data results were then collated into tables for total current for the top half of the square plate and contour plots were drawn. These appear in Appendix C along with the current components at the horizontal bisecting line of a 1.0 wavelength square plate. This data differs from that of other codes such as the ones that appear in the next three figures. The square plates are of electrical sizes .15, 1.0, and 1.2 wavelengths and the dominant current component is vertical if we consider the incident \vec{E} -field to also be oriented vertically. It should be noted that the plates are assumed to be perfectly conducting and that the form of the current density plots do not vary significantly from .15 to 1.2 wavelengths. Only a slight rise in current is observed near the midpoint of 1.0 and 1.2 wavelength plate unlike the case of the .15 wavelength plate. Also, shown in Figure 45 is the current on a resistive plate depicted by a dashed line.

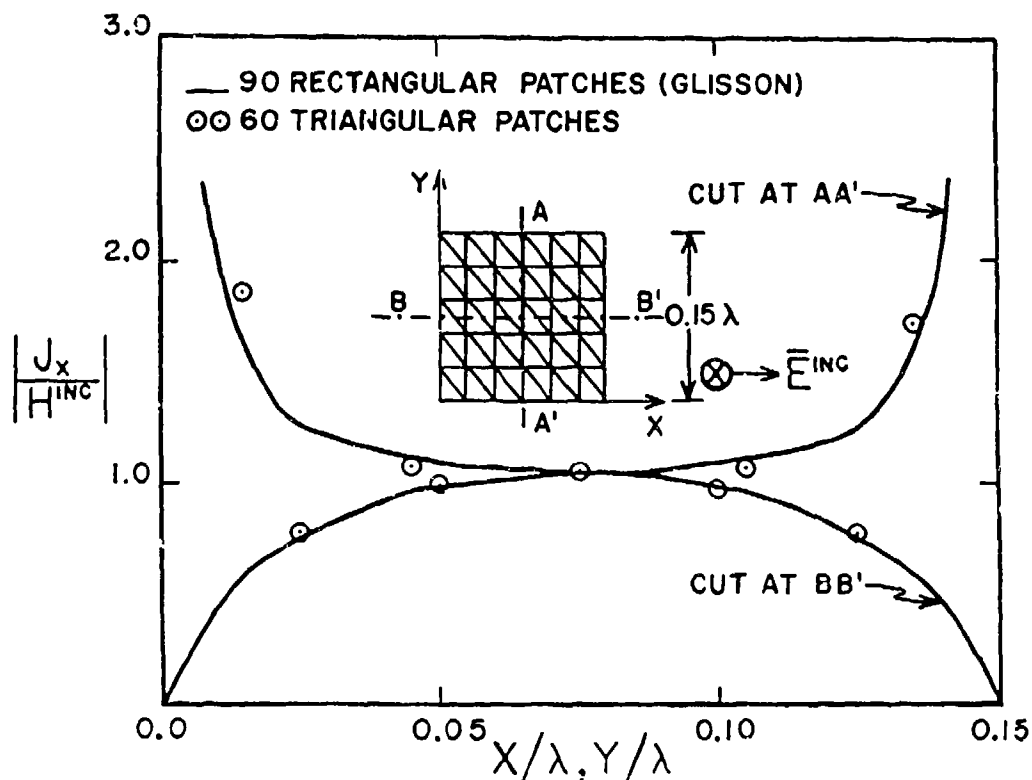


Figure 43: Theoretical result for the .15 wavelength square plate (51).

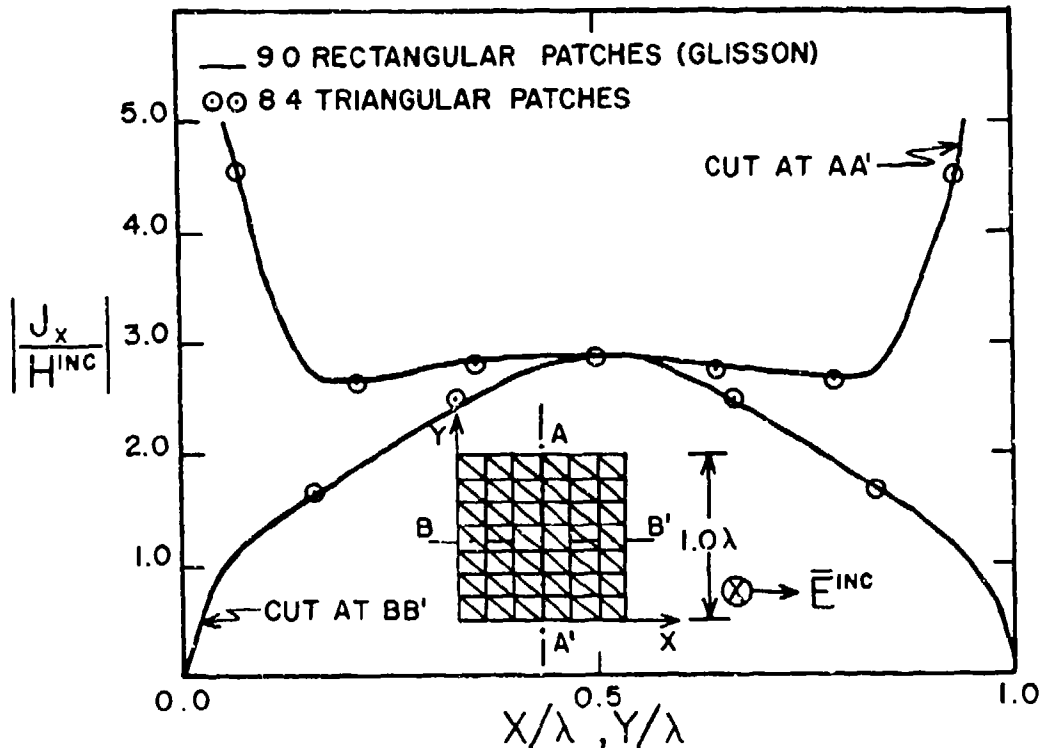


Figure 44: Theoretical result for the 1.0 wavelength square plate (51).

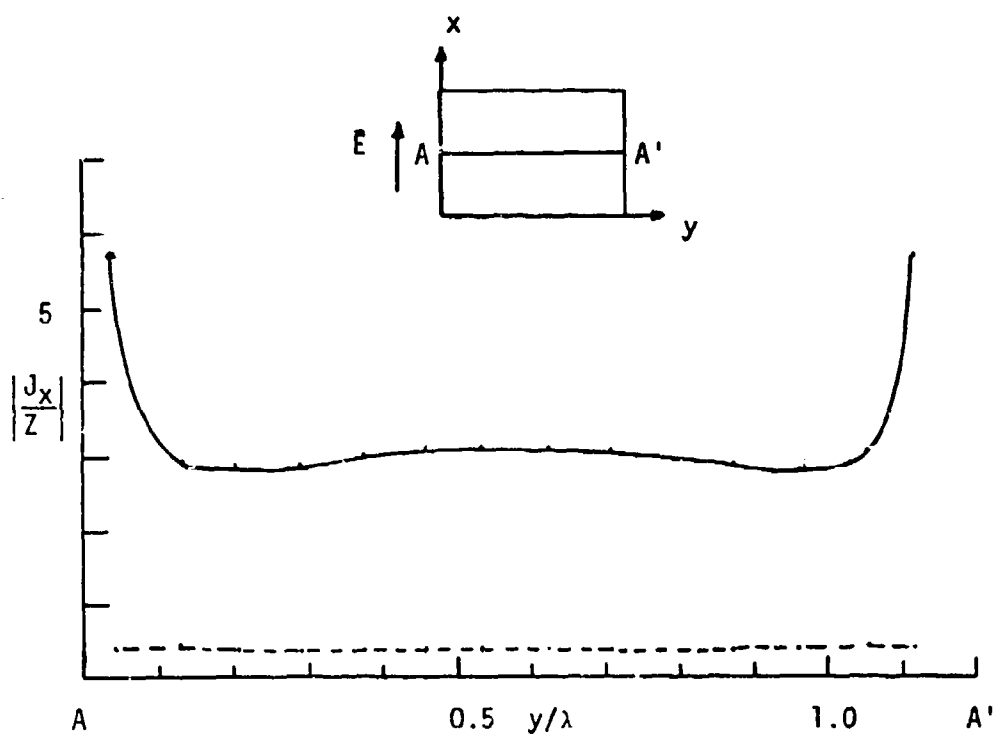


Figure 45: Theoretical result for 1.2 wavelength square plate (45).

CHAPTER III

INFRARED/MICROWAVE LABORATORY

To conduct an experiment for detecting microwave induced surface current through an infrared approach, it was necessary to design and construct a facility where none had previously existed. For a "proof of principle" goal, flexibility was highly valued as unforeseen problems were bound to occur. Time and financial constraints dictated that available resources be used to the maximum extent possible. To observe heating effects on relatively preliminary coating schemes, the highest microwave levels possible from available sources were to be obtained, thus safety considerations were also paramount. The basic experimental arrangement is seen on the following page (Figure 46).

The antenna, metal parabolic and corner reflectors, and target object were mounted on a 12' x 4' aluminum ground plane which was encased by absorbing cones forming an anechoic chamber. The electromagnetic wave propagates from the antenna/reflector configuration to the target. The wave interaction with the target creates surface currents which in turn

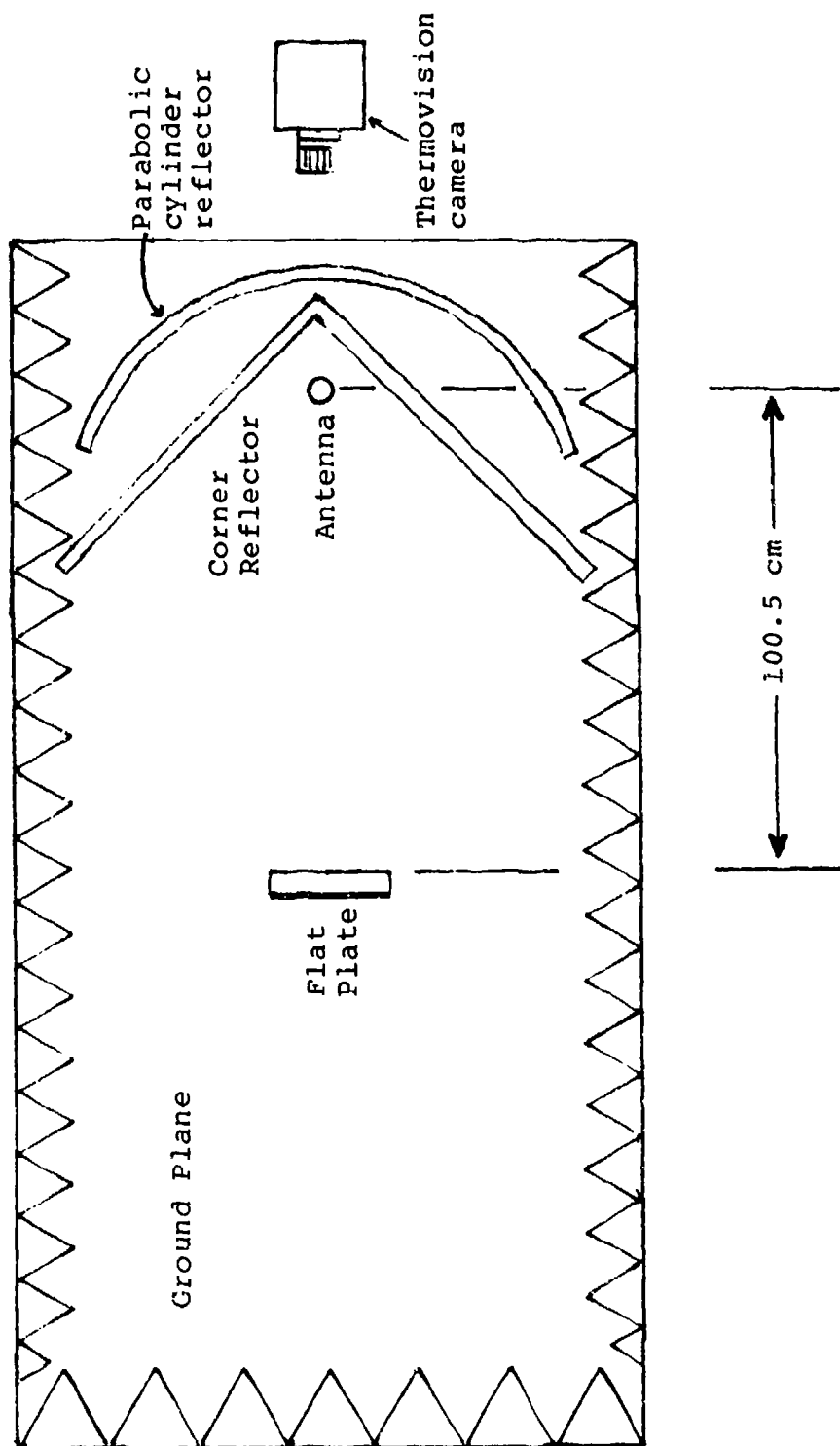


Figure 46: Experimental Arrangement.

produce joule heating detectable by the Thermovision camera located behind the reflectors. The camera was maintained at normal incidence from the target surface.

The basic setup is seen in the following photograph (Figure 47). Located to the left of the chamber on a cart is the apparatus for recording position and induced voltage from a magnetic field probe which was developed to detect surface currents. The magnetic field probe will be discussed in detail in Chapter IV. The cones on the side walls are eight inches from base to tip, constructed of a carbon impregnated urethane material, and mounted on plywood with contact cement. The first horizontal section of the left side wall (6' x 4') was designed and constructed with guides on the top and bottom which allowed forward and back movement or entire removal of the plywood/cone side wall. The chamber was on two bakelite covered work benches. The aluminum ground plane was elevated from the workbench base with 2x4 boards to provide a space for probe telemetry as well as coaxial cable and couplings for the antenna mounted vertically in the ground plane. Leveling of the ground plane was accomplished with shims and adjustment of the support legs.



Figure 47: Infrared/Microwave Laboratory

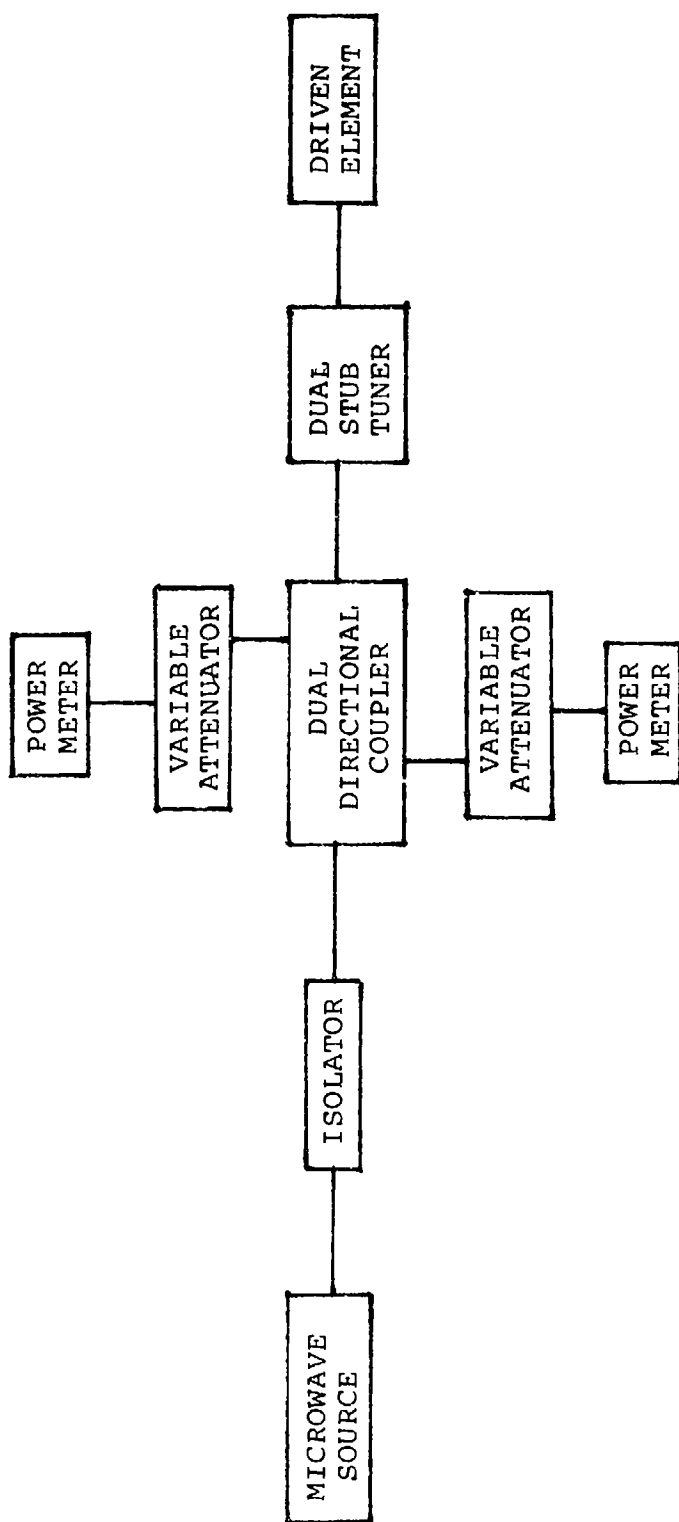


Figure 48: Block diagram of the microwave propagation apparatus.

The following discussion includes the equipment involved in the propagation of the EM wave, detection of the IR, and the particular targets of interest in this report.

Microwave Radiation

Continuous wave sources at frequencies of 937 MHz and 2.45 GHz were used. The experimental arrangement is shown in a block diagram in Figure 48 and a photograph in Figure 49. Table 1 provides further information on the equipment. As is standard practice, tuning was accomplished so as to maximize transmitted power and minimize reflected power. Maximum source power was 80 watts and 120 watts for the 937 MHz and 2.45 GHz sources respectively. A Hewlett Packard spectrum analyzer (Model 8555A) was used to confirm that the output frequencies were 937 MHz and 2.45 GHz for the respective microwave sources. The reasons for selecting 937 MHz included remaining down slightly from the limit of the device, it had been used at Monterey, and it provided a significantly different wavelength than that of the 2.45 GHz single frequency source. In Figure 50 is shown a variable aperture, corner reflector, and a parabolic cylinder reflector depicted with a quarter-wave monopole.

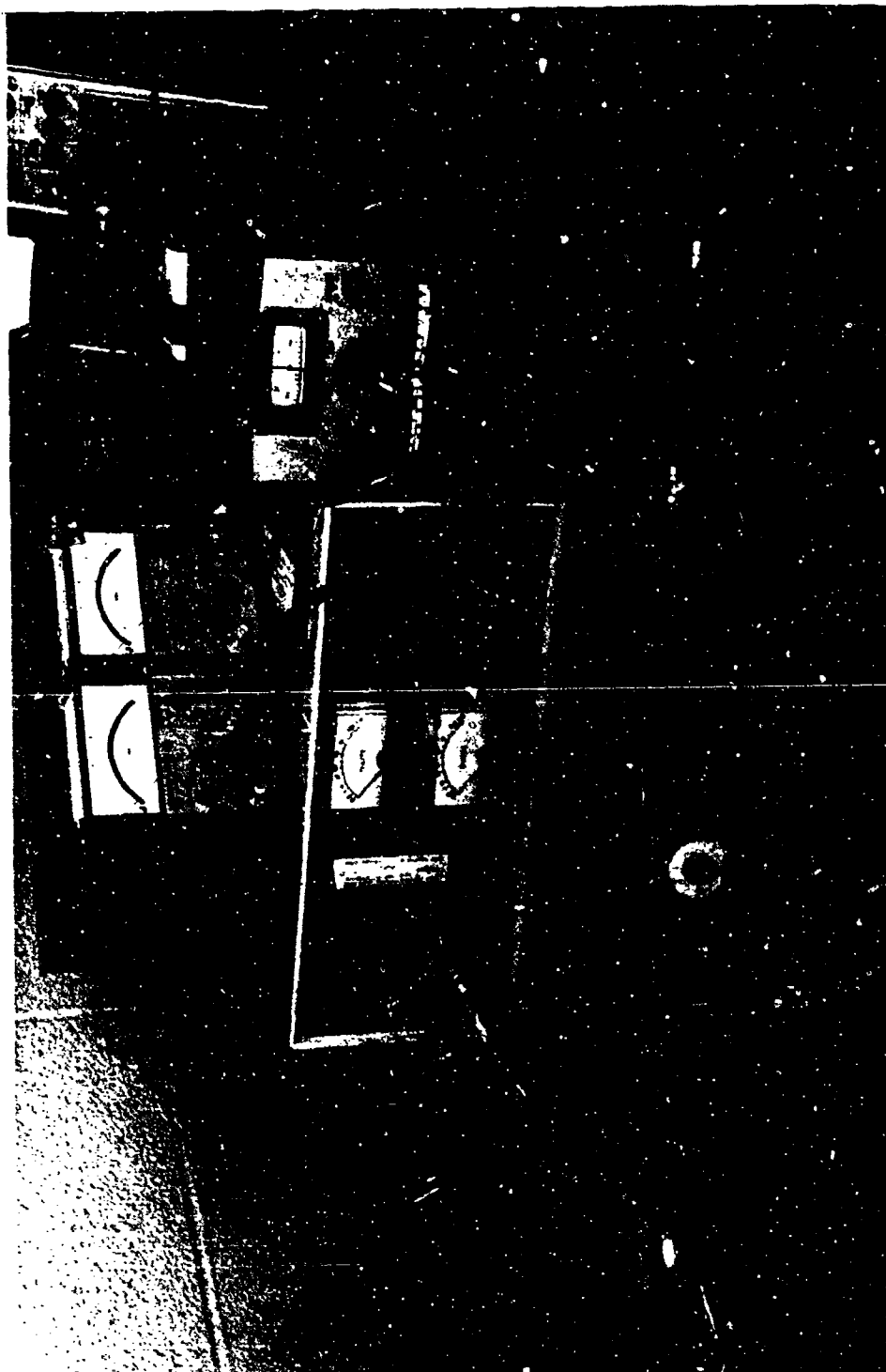
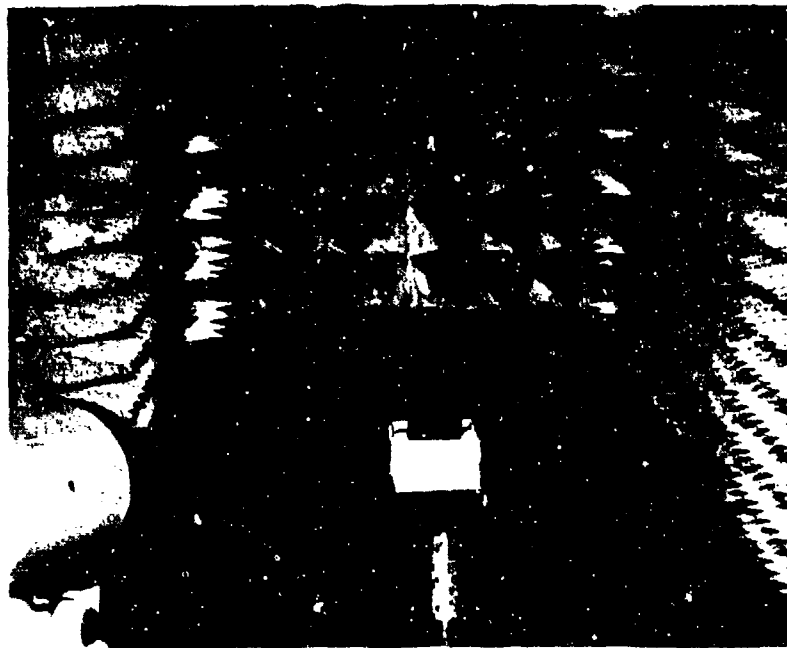


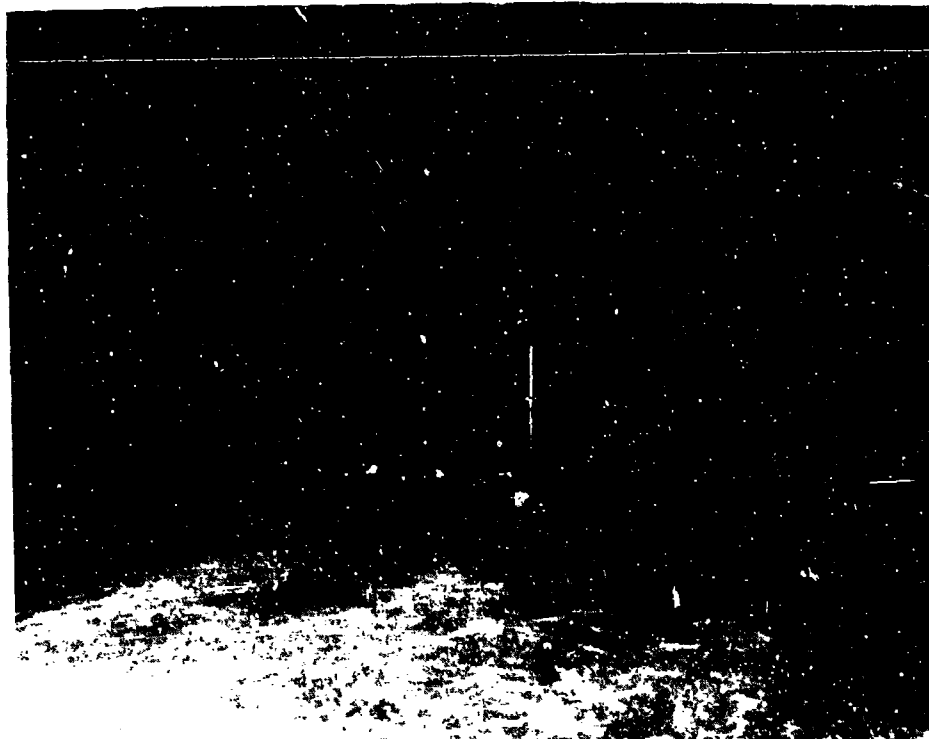
Figure 49: Microwave Sources

Table 1
Microwave Equipment

<u>Nomenclature</u>	<u>Identification</u>
Microwave Sources	Microwave Power Generator Model MPG 4M KIVA Instrument Corporation Rockville, MD (2.45 GHz) Power Signal Source Sierra Electronics Division Model 476A-1000 Philco Corporation, USA (.5-1.0 GHz)
Isolator	Ferrite Isolator Micro-mega Model RL-146
Dual Directional Coupler	Hewlett Packard Model 765D (450-945 MHz)
Attenuators	Variable Attenuators Microlab/FXR Model No. AJ-310N (.5-6.0 GHz) Coaxial Attenuators Merrimac Type AU10A (.5-12 GHz)
Dual Stub Tuners	Microlab S 2-05 N (Used at 937 MHz) Microlab/FXR Model N 800 A
Power Meters	Hewlett Packard Model 432A Thermister Mount Model 478A
Coaxial Cable	Plastoid Corporation RG-214U



(a) Adjustable corner reflector (2.45 GHz)



(b) Parabolic cylinder reflector (2.45 GHz)

Figure 50: Antenna reflectors

The driven elements were quarter-wave monopoles mounted on a ground plane. The current distribution on the antenna is modeled through image theory as that of a center fed half wave dipole in free space with one half of the radiation resistance. The antennas were made from .32 cm diameter brass rods and threaded so as to be easily interchangeable and to fit into a connector mounted into the ground plane from below. The interior line in the coaxial cable was connected to the antenna and maintained in a rigid position with a Teflon spacer which fit firmly in mounted opening in the ground plane. The accepted value of .95 was applied to the electrical quarter wave length to yield an antenna height of 7.6 cm and 2.9 cm above the ground plane for frequencies of 937 MHz and 2.45 GHz respectively (29). With vertically oriented antennas on a horizontal ground plane, it is clear that the incident field at a target would be nearly vertically polarized, \vec{E} vertical and \vec{H} horizontal.

To increase power at the target and thus increase perceptible heating effects, greater gain from the antenna was required. Additionally, a plane wave was also required if correlations were to be reasonably made with theoretical studies which

assumed an incident plane wave. Corner reflectors and parabolic cylinder reflectors were logically choices. It was also recognized that a chamber width of only four feet could result in reflection problems and thus difficulty in achieving a "quiet zone" at the target. A hinged, variable aperture corner reflector was designed and constructed using empirically determined optimum dimensions from work by Cottony and Wilson (14). Antenna to apex spacing consideration were originally discussed in 1940 by Krauss (29). It is well known that corner reflection with aperture angles such as 180° , 90° , 60° , 45° etc., that result when 360° is evenly divided by an integer can be modeled through image theory to readily give the far field pattern of interest. Also, apex to antenna spacing can be varied to give a maximum lobe on the centerline, a null on centerline or a transition situation between these extremes (27). However, the problem remained essentially an empirical one due to the complicating "small" anechoic chamber, particularly in the case of 937 MHz. A ripple tank study of two dimensional modeling of wave interactions, varying reflectors and apex to antennas spacing in a "small" chamber was conducted and a summary appears in Appendix A.

The far field or Fraunhofer condition requires that the distance of the scattering object from an exciting source (D) be related as

$$D > \frac{2L^2}{\lambda} \quad (46)$$

where

λ is the wavelength and

L is the characteristic length which in the case of a corner reflector is simply twice the apex to antenna distance (See Figure 51). A 90° corner reflector was eventually used for the 937 MHz case ($\lambda=32$ cm) such that

$$S = .32\lambda$$

which implies

$$L = 2S = .64\lambda \quad (47)$$

and therefore

$$D > \frac{2(.64\lambda)^2}{\lambda} = .82\lambda$$

$$D > 26.2 \text{ cm}$$

The target was actually in the chamber 100.5 cm from the antenna with $S = 10.2$ cm implying that $D = 110.7$ cm which is in the far field.

The positioning of a parabolic cylinder reflector for the 2.45 GHz case was again empirically arrived at after having started with situation where

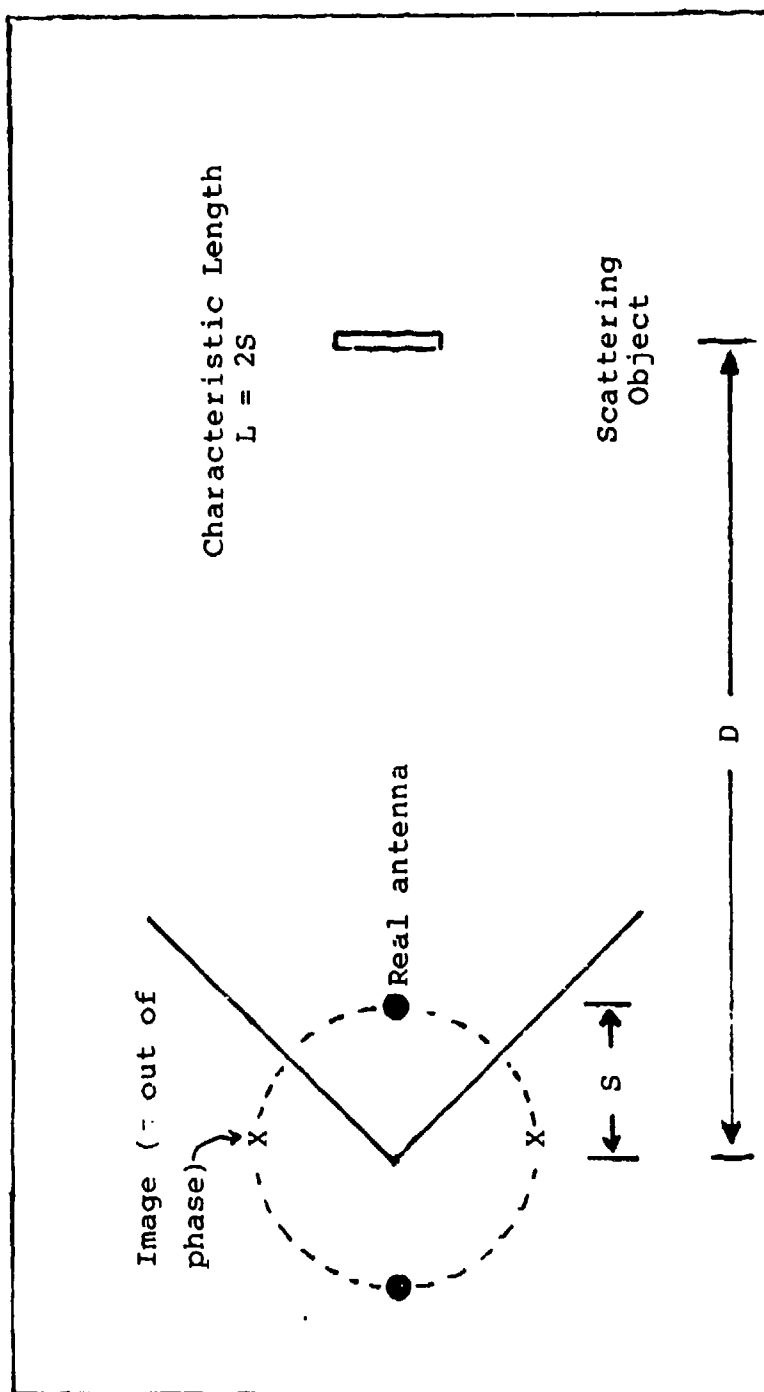


Figure 51: 90° Corner Reflector.

the antenna was at the focal point and the antenna was roughly in the plane of the aperture. Final antenna to reflector spacing was 15.3 cm. Free field plots for both frequencies across 20 cm at the target location for 3/4 and 1 3/4 inches off the ground plane are found in Chapter V.

Infrared Detection

This work extends efforts performed at the Naval Postgraduate School under Dr. Robert W. Burton where qualitative studies were carried out on non-metallic surfaces.

Thermography Equipment

The system used in all of our measurements was an AGA 680 camera operating in the 2-5.6 μm spectral region. This device has an 8° lens with a 1.3 mr instantaneous field of view. The detector is made of indium antimonide (InSb) and cooled to 77 K with liquid nitrogen with a limiting sensitivity of $.1^\circ\text{K}$. Since the detector is a semi-conductor, it is a photon detector rather than an energy detector. This is significant since the number of photons a blackbody emits is proportional to T^3 rather than T^4 as is the case for the total energy radiated. The AGA 680 is a

line scanning system that forms a 128 x 128 array of its 8° square window. One complete scan or "frame" takes 1/16 second and is comprised of 64 rows having 128 elements in each row. It detects the number of photons emitted from each element per unit time and then assigns it a level from 1 to 10 based on the number of photons received. These levels are graphically displayed in the form of ten discrete colors on a CRT display. The system's sensitivity is discretely variable in the form of fixed isotherm unit (ISU) windows which, in other words, determine the temperature "band width" that the camera will be capable of detecting. It also contains a threshold adjustment which determines where on the temperature scale the temperature window will be located. In Figure 52 the AGA 680 Thermovision System is seen with the black and white monitor to the left of an Hewlett Packard 9845B minicomputer, and the color monitor to the left of the black and white monitor. The camera is in the foreground and was adequate for this phase of the overall project but would not provide the flexibility of placement near a target object due to its size and field perturbing effects in chamber. Initial work was required on the system in the spring and summer of 1980 as a faulty video



Figure 52: Infrared detection equipment.

amplification board and "chopper" adjustments were located and corrected. However, even with a properly functioning 680 system the results were still in gray levels on the black and white display and ten color levels on the color display. As will become clear, a photographic display was not adequate to explore the surface current problem.

Digitizing the Thermovision Output

For the required quantitative analysis, such as the point-by-point correction for emissivity variations, and determination of surface current densities, computer support was necessary. Unfortunately, the data from the Thermovision camera was too fast for direct input to a reasonably compact computer. The required interface between the camera and the computer was designed specifically for the present needs of the project. The interface stores one frame of data at camera speeds and then off-loads the data at computer speeds (interface built by Major Warmuth).

The AGA Thermovision 680 camera scans from left to right at a rate of $0.625 \mu\text{sec}$ per line. It uses approximately 64 lines (from top to bottom) to produce one frame, and interlaces seven frames per picture. The first frame illuminates dots in lines one, three, five, etc. The second frame illuminates

dots in lines two, four, six, etc. The TV uses the standard electrical power frequency to control vertical movement. Therefore, it produces sixty frames and thirty pictures per second. The thermovision produces about 16 frames and 2.3 pictures per second.

The interface reads 128 samples per scan line, digitizes the temperature level, and stores the results for one frame. This yields approximately 8200 pieces of data in 62 msec. The data is then transferred into a Hewlett Packard 9845B desk-top computer. Once the data is in the computer, it may be manipulated through normal matrix techniques.

The computer signals the interface when a frame of data is to be taken; the interface then waits for a vertical sync pulse from the camera. The vertical sync pulse aligns all circuitry in the Thermovision system at the upper left-hand corner of the display. When the interface receives the vertical sync, it acknowledges the computer's request and begins digitizing and storing the video data. A very fast 16K by 8 bit memory board was locally available; therefore, design of a new storage device was not required. Digitizing initially to ten levels was

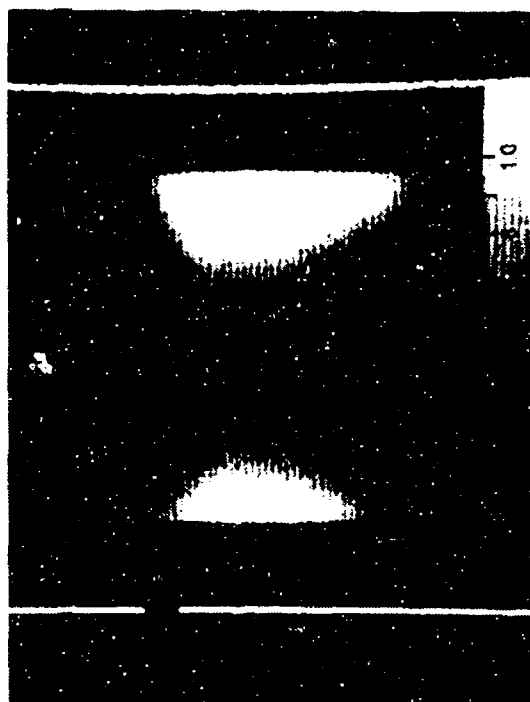
appropriate in the original system since the Thermovision color display depicts only ten levels.

The interface uses an onboard clock running at 277 KHz. This clock provides 173 samples per line, but about 25% of the line is a right-edge bar and horizontal blanking which provides no useful information. Thus, only the first 128 words are stored. The counter which controls word storage is reset at 128 and enabled by a horizontal sync pulse generated by the Thermovision camera. The horizontal sync pulse aligns the Thermovision system at the left-hand edge of the display. The output of the counter is used to determine the least significant eight bits of the address to the memory where the current digitized value of the video signal is to be stored. The most significant six bits of the address are determined by counting the number of horizontal sync pulses since the last vertical sync pulse. The interface continues digitizing and storing data until it sees a second vertical sync pulse.

The second vertical sync pulse shuts down the data collection portion of the interface and forces the system to notify the computer that a frame of data has been captured. When the computer receives

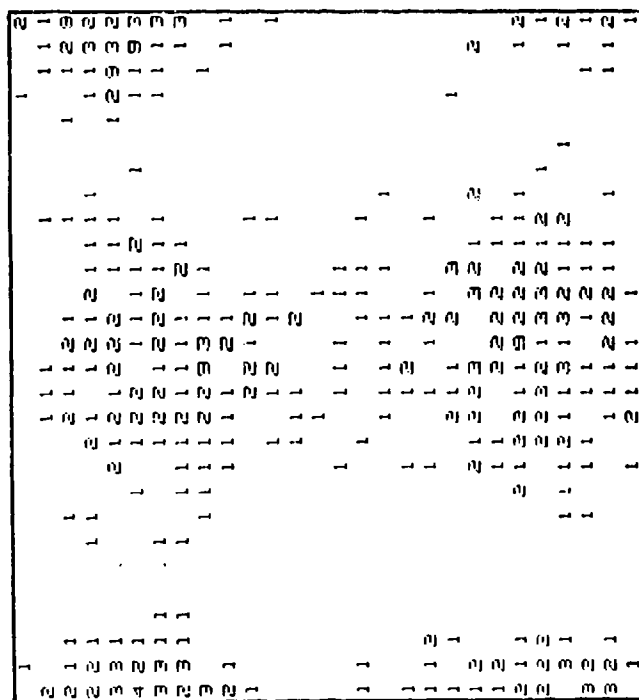
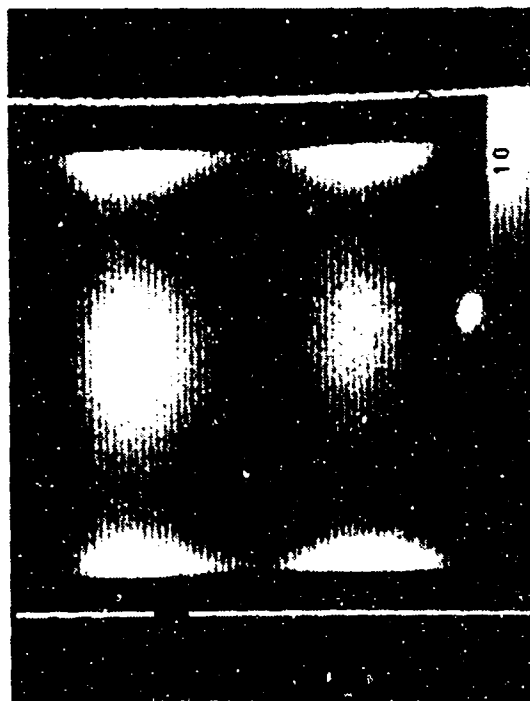
this notification, it takes control of the interface and the associated memory. The computer transfers the first address to the memory, requests the data stored there, and places it in its internal memory. After restoring the data, it goes to the second address, and so on. When the entire frame of data has been moved to the internal memory, the operator is notified so data manipulation may begin. For data manipulation considerations and the resolution constraint of taking only one frame at a time, the 128 words per row were reduced to 64 by taking only every other one. Therefore, the working matrix was 64 x 64.

In Figures 53 and 54 are shown two early efforts involving the microwave illumination of square plates and the digitization of the results. The square plate was a boron-epoxy substrate with a carbon-based paint for a coating. The frequency was changed from 937 MHz to 2.45 GHz such that the electrical size of plate changed from .50 to 1.3 wavelength. The accompanying patterns also changed as is clear from the figures.

[illegible]

(b) Ditized Output.

Figure 53: Early infrared results for a .50 wavelength square plate above the ground plane (aquadac on epoxy).



(a) Thermogram. (b) Ditized Output.

Figure 54: Early infrared results for a 1.3 wavelength square plate above the ground plane (aquadac on epoxy).

Thermovision Calibration

With Thermovision data in digital form the next task is to transform this data in isotherm units to that of temperature which will later be shown to be related to current. Calibration curves for the AGA Thermovision 680 may be modeled by

$$I = \frac{p}{e^{\frac{q}{T}} - 1} \quad (48)$$

where

I = Isotherm unit corresponding to T

T = Absolute temperature ($^{\circ}\text{K}$)

p, q = Aperature constaints

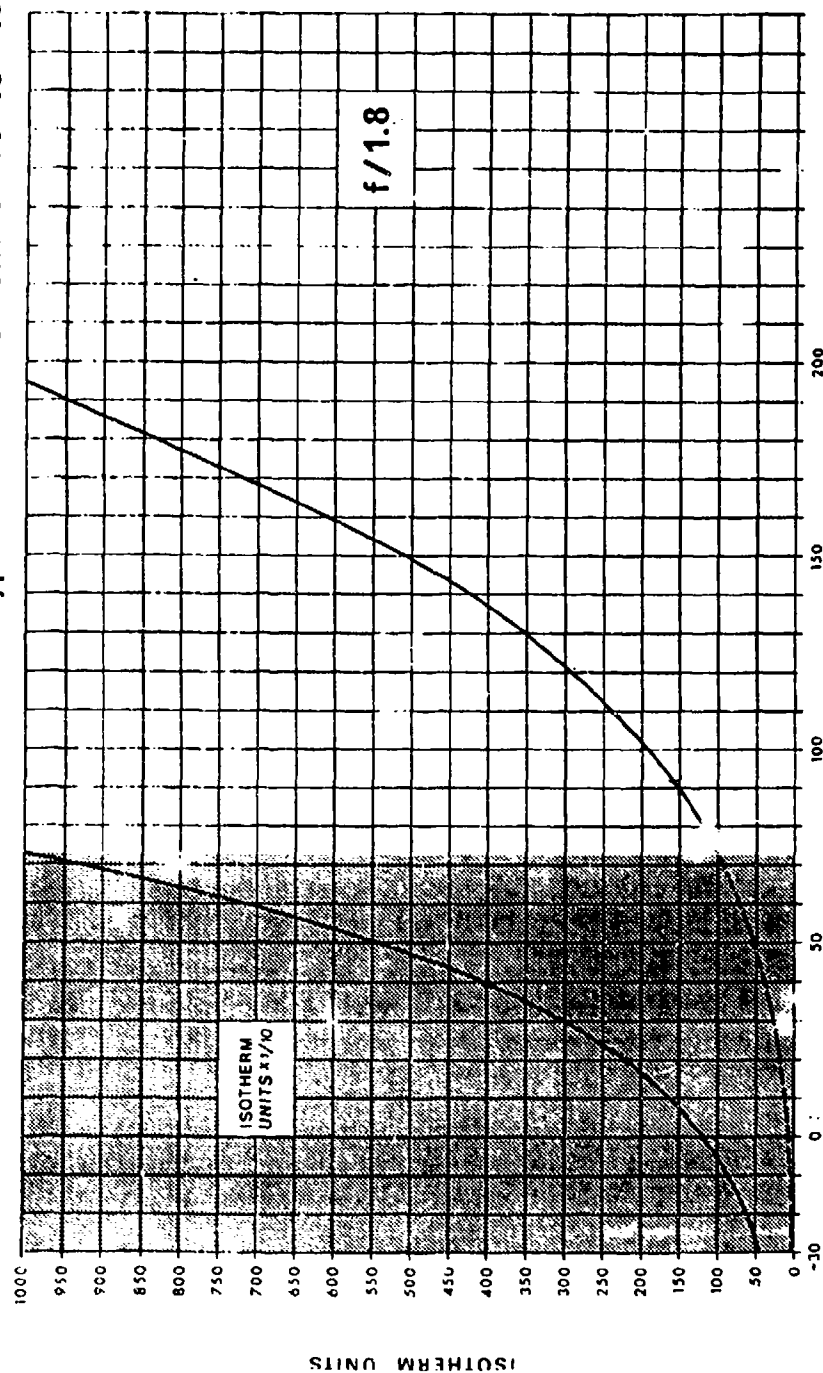
A typical calibration taken from 680 manual is given in Figure 55. By measuring two values on the curve (i.e., T_1, I_1 and T_2, I_2) and substituting individually in equation (48), the result is a system of two equations in two unknowns. Thus taking two measurements using a suitable temperature source can yield the calibration unknowns p and q .

From equation (48) and the two measured values, the following expressions are obtained.

$$p = I_1 \left(e^{\frac{q}{T_1}} - 1 \right) \quad (49)$$

$$q = T_2 \ln \left(\frac{p}{I_2} + 1 \right) \quad (50)$$

AGA THERMOVISION[®] SYSTEM 680
Typical calibration chart -30° to +190°C



AGA

Figure 55: Published calibration curve for the Thermovision 680 (IS" vs Temp).

Substituting equation (49) for p into equation (50) for q , the result is the following transcendental equation.

$$q = T_2 \ln \frac{I_1}{I_2} (e^{\frac{q}{T_1}} - 1) + 1 \quad (51)$$

Typically, q is much larger than T_1 so that

$$\frac{I_1}{I_2} (e^{\frac{q}{T_1}} - 1) + 1 \approx \frac{I_1}{I_2} e^{\frac{q}{T_1}} \quad (52)$$

and therefore

$$q \approx \frac{T_1 T_2}{T_1 - T_2} \ln \frac{I_1}{I_2} \quad (53)$$

An example of the relative magnitude of q and T_1 is found by taking two points from the graph in Figure 55, $T_1 = 90^\circ \text{ C} = 363^\circ \text{ K}$, $I_1 = 150 \text{ ISU}$, $T_2 = 190^\circ \text{ C} = 463^\circ \text{ K}$, and $I_2 = 950^\circ$ and solving for p and q . The resulting expression defining the curve is

$$I = \frac{771,348}{\frac{3102}{e^{\frac{q}{T}} - 1}}$$

where

$$p = 771,348 \text{ and}$$

$$q = 3102$$

A more general solution to the transcendental equation is found in computer program named 'CAMCAL' in Appendix D using the Newton's approximation. This

iterative technique allows the user to select the convergence criterion and uses the following function.

$$f(q) = T_2 \ln \frac{I_1}{I_2} (e^{\frac{q}{T_1}-1} + 1) - q \quad (54)$$

its derivative

$$f'(q) = \left[\frac{T_2}{\frac{I_1}{I_2} (e^{\frac{q}{T_1}-1} + 1)} \right] \frac{I_1}{I_2 T_1} e^{\frac{q}{T_1}-1} - 1 \quad (55)$$

and the standard recursion relation.

$$q_{n+1} = q_n - \frac{f(q_n)}{f'(q_n)} \quad (56)$$

The values of p and q used in all calculations in this paper were determined to be

$$p = 772600.6 \text{ and}$$

$$q = 3102.6$$

which yield the calibration curve in Figure 56. Note that for ambient temperature and for small changes in temperature, the relationship between isotherm units and degrees of temperature is nearly linear.

P=772600.6

Q=3102.6

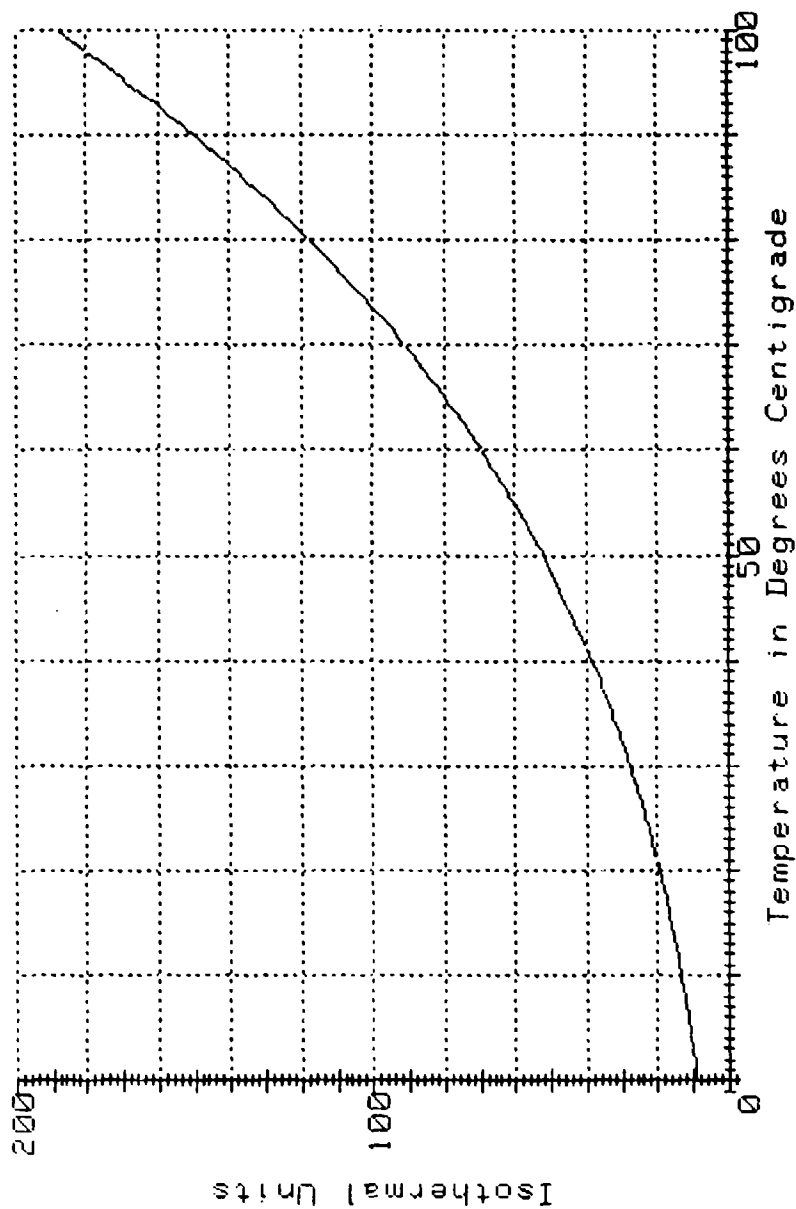


Figure 56: Experimentally derived calibration curve for the Thermovision 680 (ISU vs Temp).

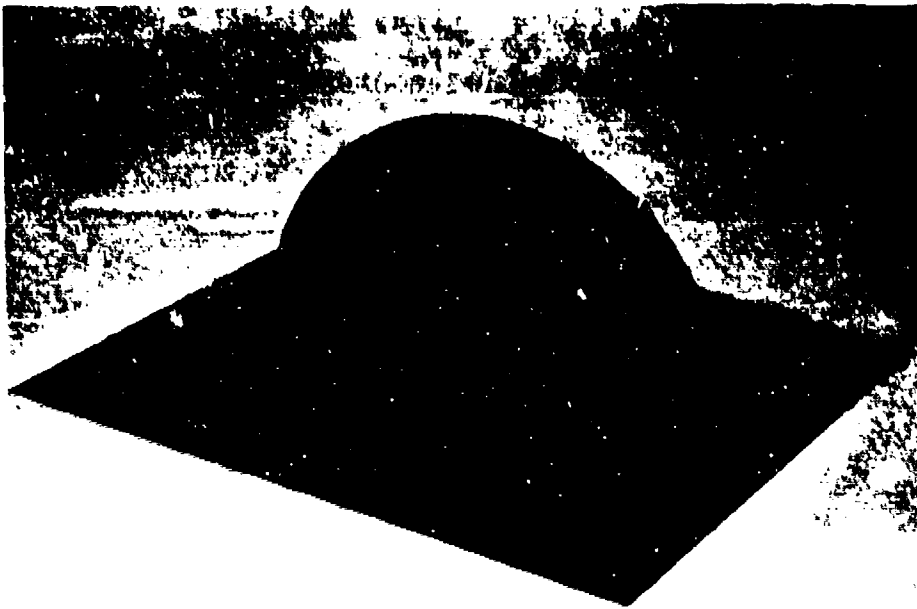
Targets

Several considerations were involved in the selection of flat plate electrical and physical sizes. The minimum focal distance for the AGA Thermovision 680 is 1.7 m which was used in data collection. Thus the object size was reasonably restricted to greater than 10 cm along the largest physical dimension to obtain a sufficient number IR elements to distinguish current patterns. For the electrical dimension, chamber size considerations reasonably restricted a "quiet zone" to approximately 20 cm for the maximum horizontal direction. One must recall that objects in contact with a ground plane will have an electrical image such that an electrical square plate will physically appear as a rectangular plate having a horizontal dimension twice that of the vertical dimension. Additionally, the investigation of current patterns should include resonant and nonresonant sizes. The following physical and electrical sizes were chosen.

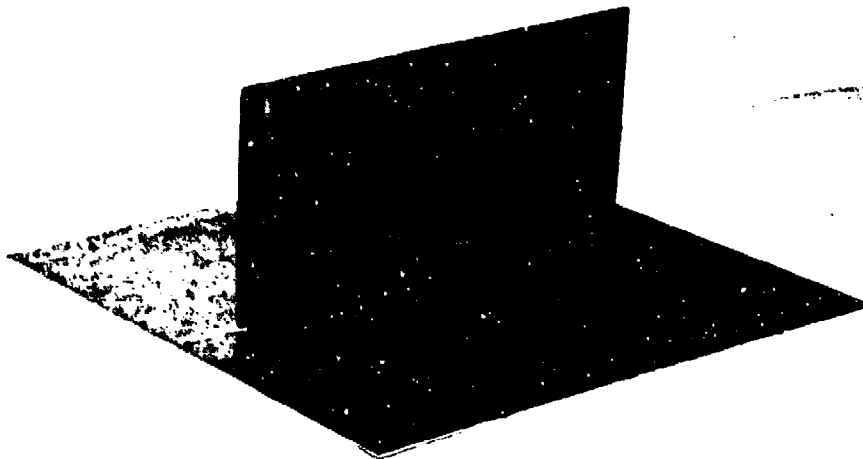
Table 2

Largest physical dimension (cm)	<u>Flat Plate Size</u>	
	2.45 GHz (Wavelengths)	937 MHz (Wavelengths)
16	1.333	.50
12.24	1.0	.3825

Three material compositions were used. The first was 1/16 inch plexiglass coated on one side with a carbon based paint known commercially as Television Tube Kote (aquadac). The thickness of several sprayed on coats was 59 μm and the conductivity of the aquadac was measured by Major Vic Martin to be 315 mhos/m. To achieve a good electrical contact with the ground plane, the plates were first mounted on square 1/32 inch thick aluminum sheet with silver conducting point as seen in Figure 57. When placed in the chamber the mounting aluminum sheet was taped to the ground plane with copper tape. The second composition was again developed by Martin. A 2 mm thick coating of carbon/paraffin mixture with a measured conductivity of 1 mho/m was placed on a 1/2 inch thick sheet of styrofoam which in turn was attached with double-stick material to a 1/16 inch thick aluminum plate. A sampling of this composition is seen in Figure 58. The third type was simply 1/4 inch thick aluminum plates that were sanded to remove a factory coating and used for the probe measurement study.



(a) Circular disk.



(b) Square flat plate.

Figure 57: Targets - Aquadac on plexiglass.

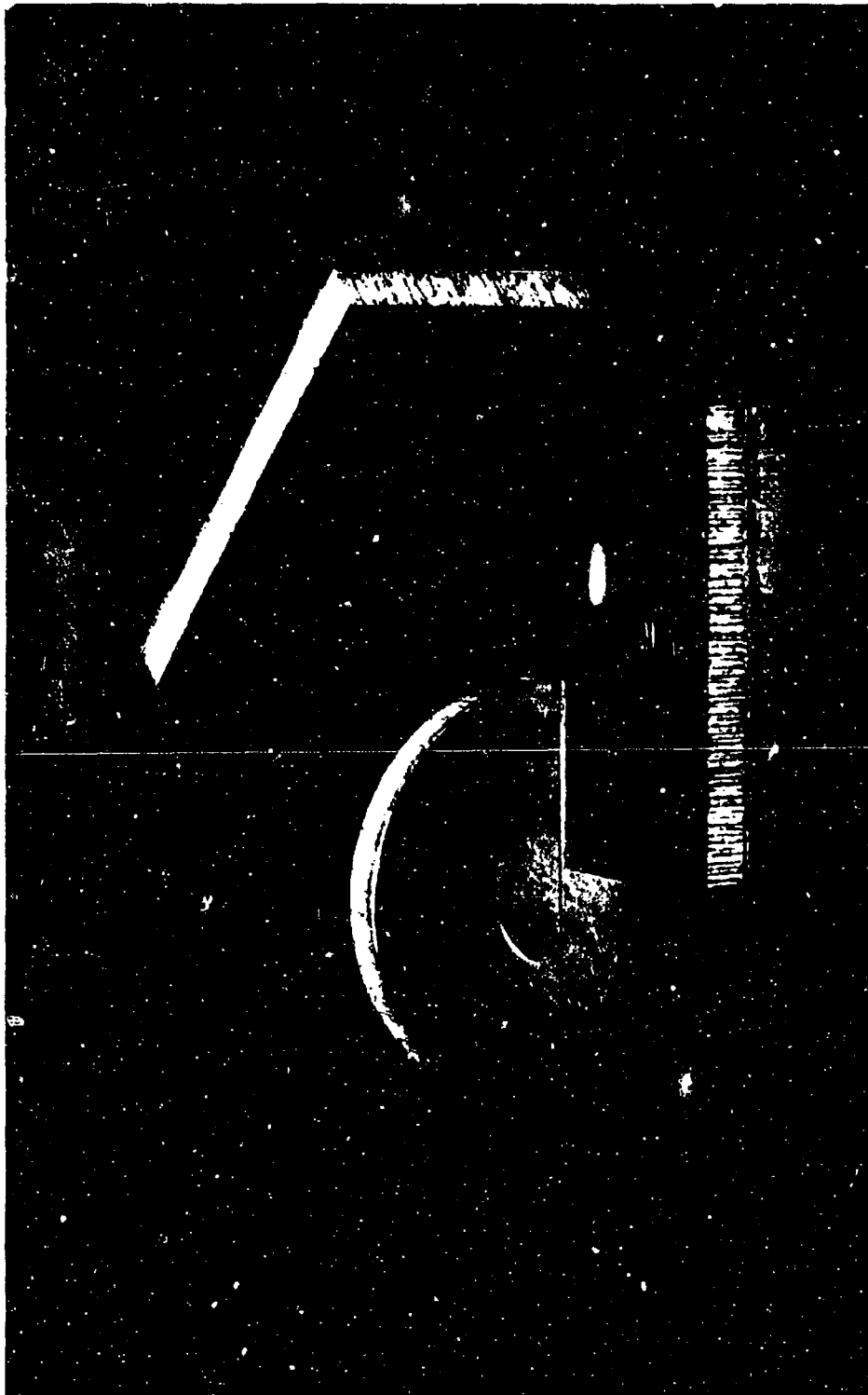


Figure 58: Targets - Carbon/paraffin over metal.

CHAPTER IV

MAGNETIC FIELD PROBE

The classic technique for measuring surface currents is with a loop antenna (50). In most cases, the objects are metallic with a structure which is convenient for shielding the probe telemetry from the incident and scattered EM field. It was not clear during the work on this project that the target would be restricted to metal. A magnetic field probe was therefore developed that could scan along any material surface or be used as a free field probe.

The basis of operation of a magnetic field or "current" probe is Faraday's Law. Stated roughly, the induced voltage in the loop will be equal to the time rate of change of the magnetic field through the loop assuming permeability and area of the loop are constant. Most exactly, the line integral of the electric field around the perimeter of a loop is equal to the integral of the time rate-of-change of the magnetic induction over the area of the loop.

$$\oint \vec{E} \cdot d\vec{l} = - \frac{d}{dt} \int \vec{B} \cdot d\vec{S} \quad (57)$$

where \vec{E} is the electric field intensity in volts per meter, and \vec{B} is the magnetic flux density in teslas. The left side of equation is simply the induced voltage (V) in the loop. The right side can be simplified by assuming that \vec{B} is constant over the area S. Assuming a sinusoid field, the greatest dimension for any probe in this report is .64 cm compared with the smallest wavelength of 12.24 cm implies that the variation of \vec{H} over the area will be no larger than five percent. Therefore, the component of \vec{B} parallel to $d\vec{S}$ can be considered spatially independent of $d\vec{S}$ over the loop and the area is independent of time such that equation (57) reduces to

$$V = - S \frac{dB}{dt} \quad (58)$$

where B now is the component perpendicular to the plane of the loop. Applying the constituent relation $\vec{B} = \mu \vec{H}$ to the case of the probe in free space ($\mu = \mu_0 =$ permeability of free space), we have

$$V = - \mu_0 S \frac{dH}{dt} \quad (59)$$

or

$$V = - j\omega\mu_0 SH \quad (60)$$

for an $e^{j\omega t}$ time variation of the magnetic field.

V_{rms} is actually the measured quantity. Now, a magnetic field probe can be used to measure surface current density since the magnetic field over a conductive sheet is related to the surface current density by Ampere's Law:

$$\oint_L \vec{H} \cdot d\vec{l} = \int_S \vec{J}_t \cdot d\vec{s} , \quad (61)$$

where

H = magnetic field intensity in amperes
per meter

$d\ell$ = incremental length on a closed contour
in meters

J_t = conduction current density plus the
displacement current density in amperes
per meter

ds = incremental area on the contour in
square meters.

For the case of metallic sheets, the conduction current density dominates the displacement current density and the magnetic flux does not appreciably penetrate the sheet. Therefore, Ampere's Law reduces to

$$H = J_s \quad (62)$$

where J_s is the surface current density in amperes per meter.

For metal plates, the assumptions associated with a small probe and a good conductor allow one to see quite simply that output voltage from a magnetic field sensing probe positioned at the surface of a conductor is linear with surface current density.

If there is appreciable penetration of the magnetic field through the object surface the simplifying assumptions should be checked for validity. In this report, the probe will only be used on a high conductive aluminum surface in a high frequency (gigahertz) range which implies a very small skin depth (δ) which is the depth in the conductive sheet where the current density is $1/e = .368$ of its value at the surface. The skin depth is given by

$$\delta = \left(\frac{2}{\omega \mu \sigma} \right)^{\frac{1}{2}} \quad (63)$$

An important property of a field probe is that it is an integrating device. That is, the contributing current density source for the magnetic field and, hence the induced voltage, is not a "point" source, but rather an area in the vicinity of the probe. A generally accepted figure for probe integration area is 1.5 times the loop area. This integrating property is particularly evident at plate edges where it should be understood that the

current sources are not present throughout the integrating area of the probe as would be the case in the center of the plate. Experimental values of current will be diminished somewhat from the anticipated higher edge current values due predominantly to this effect.

Experimental Considerations

Receiving and recording the induced voltage in a high frequency (EM) field presents many experimental problems. The only excitation source that is desired is the time varying magnetic field at the probe. The potential coupling of the electric field to the probe and potential coupling of both \vec{E} and \vec{H} to the telemetry must be overcome. The recording device must be capable of either receiving at the driving frequency or the signal must be converted to D.C. The strength of the incident field and the sophistication of equipment dictated the minimum reasonable probe size and therefore the minimum integrating area.

Three probes were developed with varying degrees of success and are shown in the following three figures. The AC semirigid coaxial approach (Figure 59) utilized the cable from Uniform Tubes

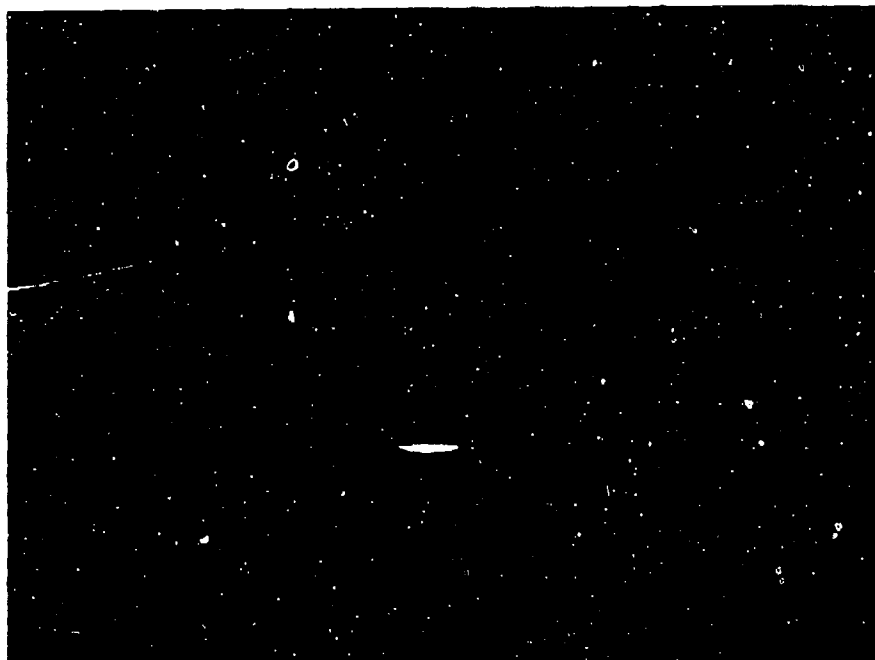


Figure 59: Photograph of a Magnetic Field Probe - Semirigid Coaxial Cable Construction.

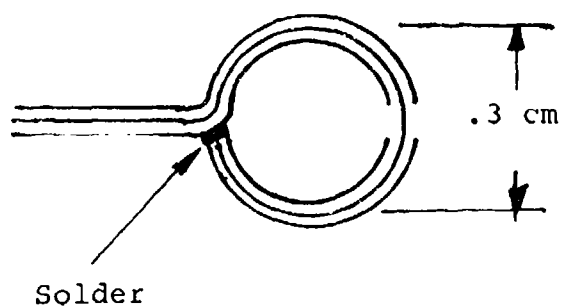


Figure 60: Drawing of a Magnetic Field Probe - Semirigid Coaxial Cable Construction.

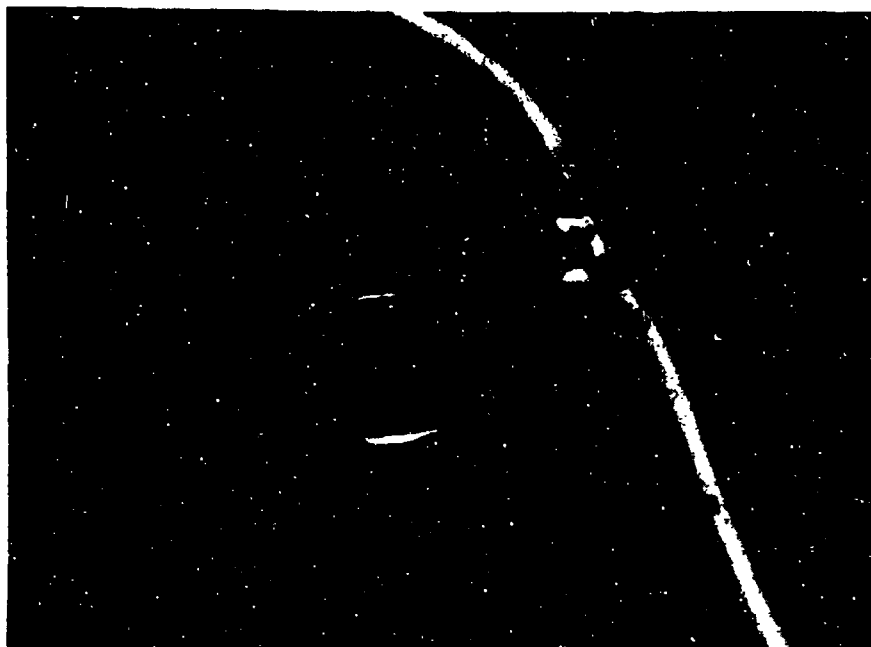


Figure 61: Photograph of the Vertical Magnetic Field Probe.

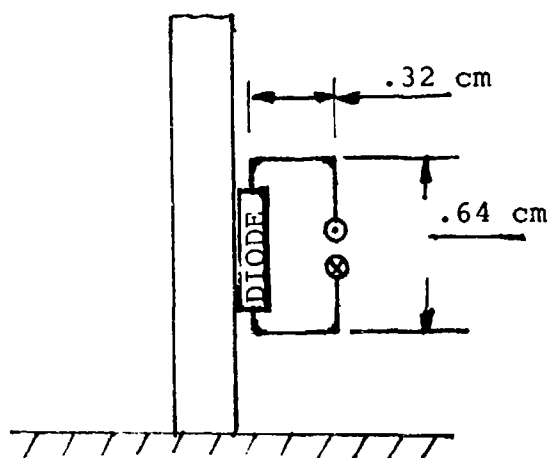


Figure 62: Drawing of the Vertical Magnetic Field Probe.

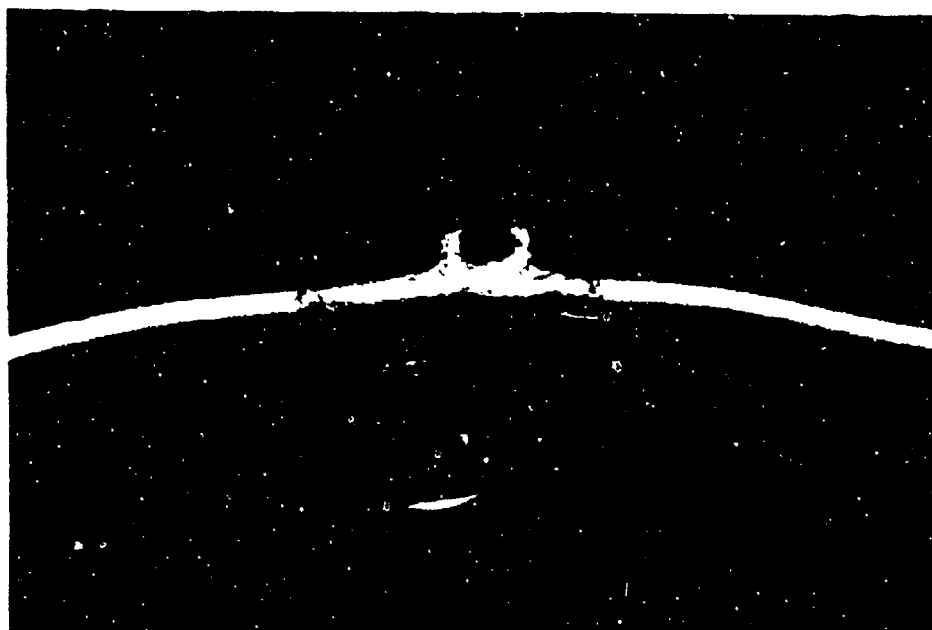


Figure 63: Photograph of the Horizontal Magnetic Field Probe.

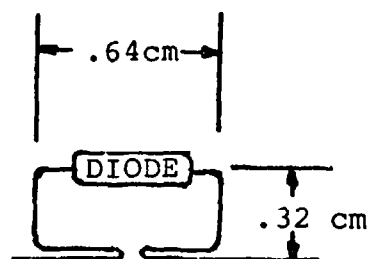


Figure 64: Drawing of the Horizontal Magnetic Field Probe.

Company, which was connected to an RG 58 C/U cable and finally into an HP 8555 A Spectrum Analyzer RF Section with an HP 855 A Spectrum Analyzer - IF Section and 141T Display Section. The D.C. approach (Figures 61 and 63), used a Schottky-barrier diode as a portion of the loop with the signal carried by a braided shield, coaxial cable with a measured capacitance of 87 pF/ft. Horizontal and vertical orientations of the probes corresponded to horizontal and vertical current components. The AC, semirigid coaxial approach involved more difficulty with mechanical scanning, required an operator to read and record from a CRT, and was only used as rough, independent verification of the D.C. results. Fabrication of the loop/diode system evolved to a semi-automatic scanning procedure. The orientation of the probe and coaxial cable in the chamber is seen in Figure 65. Recall that the incident EM field is vertically polarized such that a horizontal cable has little effect on the wave. For structural and grounding considerations the outside shielding on left and right side of the loop, as viewed down the chamber, were soldered together. The loop was designed with the diode positioned at the target surface where the boundary conditions imply a minimum

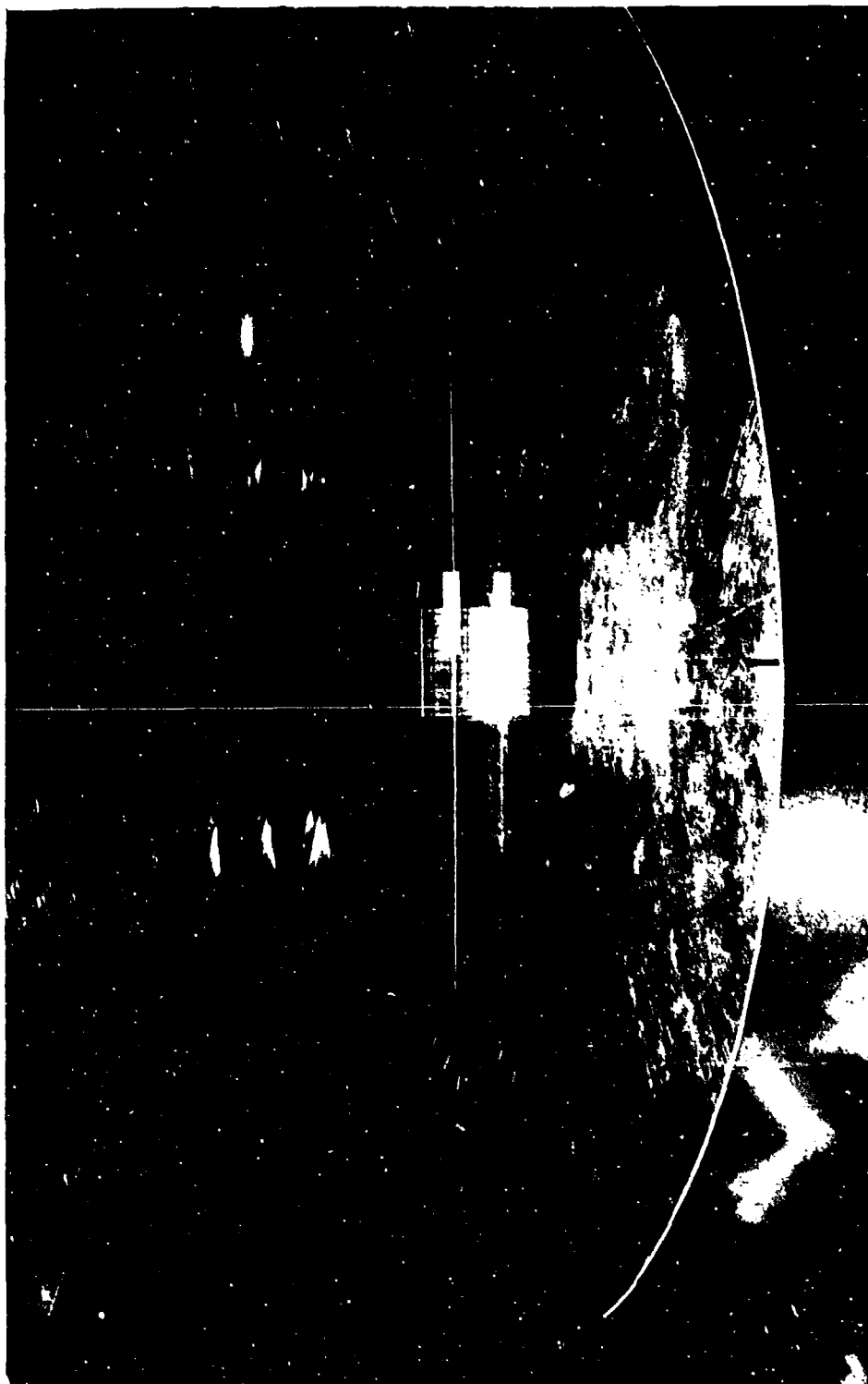


Figure 65: Magnetic field probe - chamber orientation.

horizontal component of the electric field. The loop was formed from the diode wire, covered with insulating shrink-tape up to the diode, and soldered to the center wire of the coaxial cable. Except for the diode casing, the loop wire and center coaxial cable lead were coated with epoxy cement, let dry, then painted with silver conducting paint which also made a good electrical contact with the outer coaxial cable shielding. The signal was rectified by the capacitance of the coaxial cable before being amplified.

The recording equipment for the magnetic field probe signal is seen in Figure 66. On top of the cart is a Hewlett Packard (Model 7004B) X-Y recorder with D.C. preamplifiers (Model 17171A) for both X and Y inputs. Prior to the signal reaching the recorder, it was sent through an amplifying circuit located in the metal box under the recorder which provided shielding. A common ground for the coaxial cable shield, the Proto-Board containing the circuit, the shielding metal box, and the recorder was provided with 10 AWG copper wire attached to a water pipe. The reasons for building the circuit shown in Figure 67, were for the high impedance ($1.5 \text{ T}\Omega$), provided by the operational



Figure 66: Magnetic field probe recording equipment.

amplifier (CA 3140 - FET device), additional filtering for 60 cycle noise, and the gain provided prior to reaching the Y input of the X-Y recorder by way of another shielded cable.

The X-input to the X-Y recorder provided horizontal position information about the probe in the chamber. In Figure 68 is seen a close-up of the



Figure 68: Experimental arrangement for horizontal and vertical probe positioning.

pulley assembly showing the coaxial cable existing through a slit cut in the side wall of the chamber. After passing over the upper pulley, which is matched on the opposite side of the chamber, the cable passes over a rubber covered pulley attached to the shaft of a 1K resistance, 10 turn potentiometer (Helipot). With a 5V power supply connected across the potentiometer, and a vernier feature on the X-input pre-amplifier on the recorder, one-to-one distance information was provided between probe position and X-coordinate.

The mechanical scanning system was simple and effective. The horizontal probe movement was accomplished using the 1/40 HP variable speed, reversible laboratory stirrer (G.K. Heller Corporation, Model GT-18 connected to a GT-21 Motor Controller) shown connected to a lead plate in Figure 66. A casting line was connected to a strap mounted on the coaxial cable and to a threaded shaft on the motor which, when counter balanced from the opposite side of the chamber, provided for positive, variable speed horizontal displacement of the probe. The vertical position was simply adjusted by placing matched, horseshoe shaped, wooden spacers under the vertical stops of the pulley as seen in Figure 68.

Calibration

Several measurements were taken to establish the linearity of the recorded induced voltage to the magnetic field strength at the probe. The first step was to vary a D.C. input voltage to the magnetic field probe pre-amplifier circuit and record the output. The results are shown in Figure 69 (a gain of 5 was eventually sufficient). The next step was to measure the power at the probe and compare it to the recorded voltage. Two calibrated power density meters (Figure 70) were available and tested against each other (a General Microwave Corporation Radiation Hazard Meter, Model 481A with probe Model 82 and a NARDA Microline Electromagnetic Monitor, Model 8100 with probe Models 8122A and 8121A). The situation of needing a power meter in the chamber while taking probe measurements was circumvented by establishing linearity of the microwave source output meter readings with that of a power meter located at the target location with both target and probe removed. The results are shown in Figures 71 through 74. Measurements were now taken of the X-Y recorder response to varying microwave source power inputs. The data best fit with a second degree polynomial (Figures 75 to 78)

MEASURED GAIN RESPONSE OF B-DOT PRE-AMPLIFIER

Input Impedance=1.00E+00 ohms
Gain= 54.0, (18.1db)

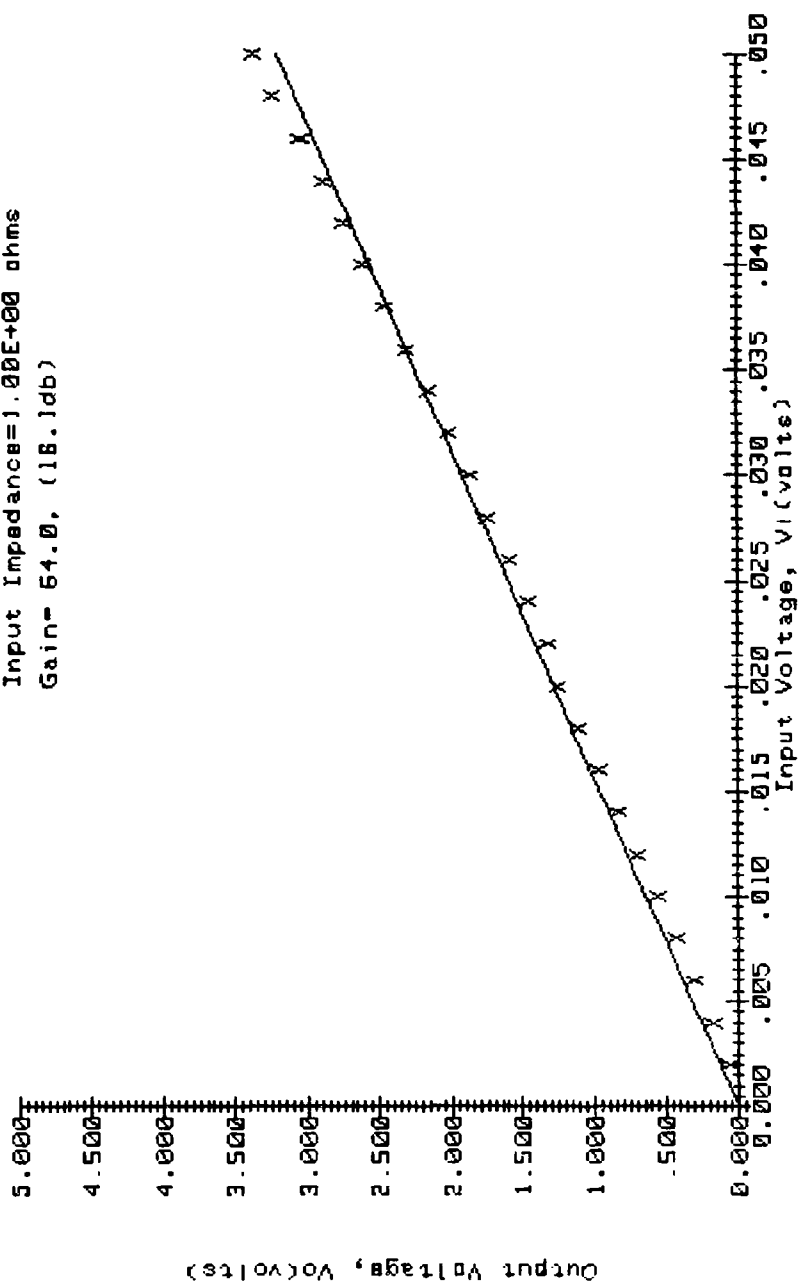


Figure 69: Measured gain response of the magnetic field probe.



Figure 70: Microwave power meters.

as one would expect since power is related to the magnetic field as follows:

$$\vec{S}_{\text{avg}} = \frac{1}{2} \text{Re} (\vec{E} \times \vec{H}^*) = \frac{1}{2} \sqrt{\frac{\mu_0}{\epsilon_0}} H^2 \quad (64)$$

$$\text{since } \frac{E}{H} = \sqrt{\frac{\mu_0}{\epsilon_0}} \text{ in free space}$$

where

$$\vec{S}_{\text{avg}} = \text{time averaged Poynting vector}$$

\vec{E} = electric field intensity

\vec{H} = magnetic field intensity

μ_0 = permeability of free space

ϵ_0 = permittivity of free space

The relationship of the square root of power to induced voltage at the recorder is seen in Figures 79 through 82 to be linear in the region of experimental interest (nonlinear diode characteristics are evident very near zero).

Very similar results were found using the following, more sophisticated equipment from the Precision Measurement Equipment Laboratory:

Power Meters - HP 432A (8478B Thermistor
Mount)

Signal Generator - HP 8640B (937 MHz)
- HP 8620C Sweeper Oscillator
with 86222B-H69 RF plug-in

The signal source was connected at the diode and the output from a microvoltmeter was observed at the X-Y recorder. Results appear in Figures 83 through 90.

Therefore, the voltage seen at the X-Y recorder is linear with the magnetic field at the probe and thus, linear with surface current density on the metal plates.

DATA			NOTE:
Point #	X	Y	
Point #1:	X=0	Y=0	x-coordinate - Source power in watts
Point #2:	X=5	Y=1	
Point #3:	X=10	Y=2	y-coordinate - Free field power in mW/cm ²
Point #4:	X=15	Y=3.5	
Point #5:	X=20	Y=4.5	
Point #6:	X=25	Y=5	
Point #7:	X=30	Y=6.5	
Point #8:	X=35	Y=7	
Point #9:	X=40	Y=8	
Point #10:	X=45	Y=9	
Point #11:	X=50	Y=9.5	
Point #12:	X=55	Y=10	
Point #13:	X=60	Y=11	
Point #14:	X=65	Y=12	
Point #15:	X=70	Y=12.5	

Linear model: $Y=A+B*X$
 $A = .54166666668$
 $B = .177857142857$

Source	Df	SS	MS	F
Regression	1	221.432	221.432	1438.453
Residual	13	2.001	.154	
Total	14	223.433		

Figure 71: Correlation of microwave source power indication to free field power measured at target location (937 MHz).

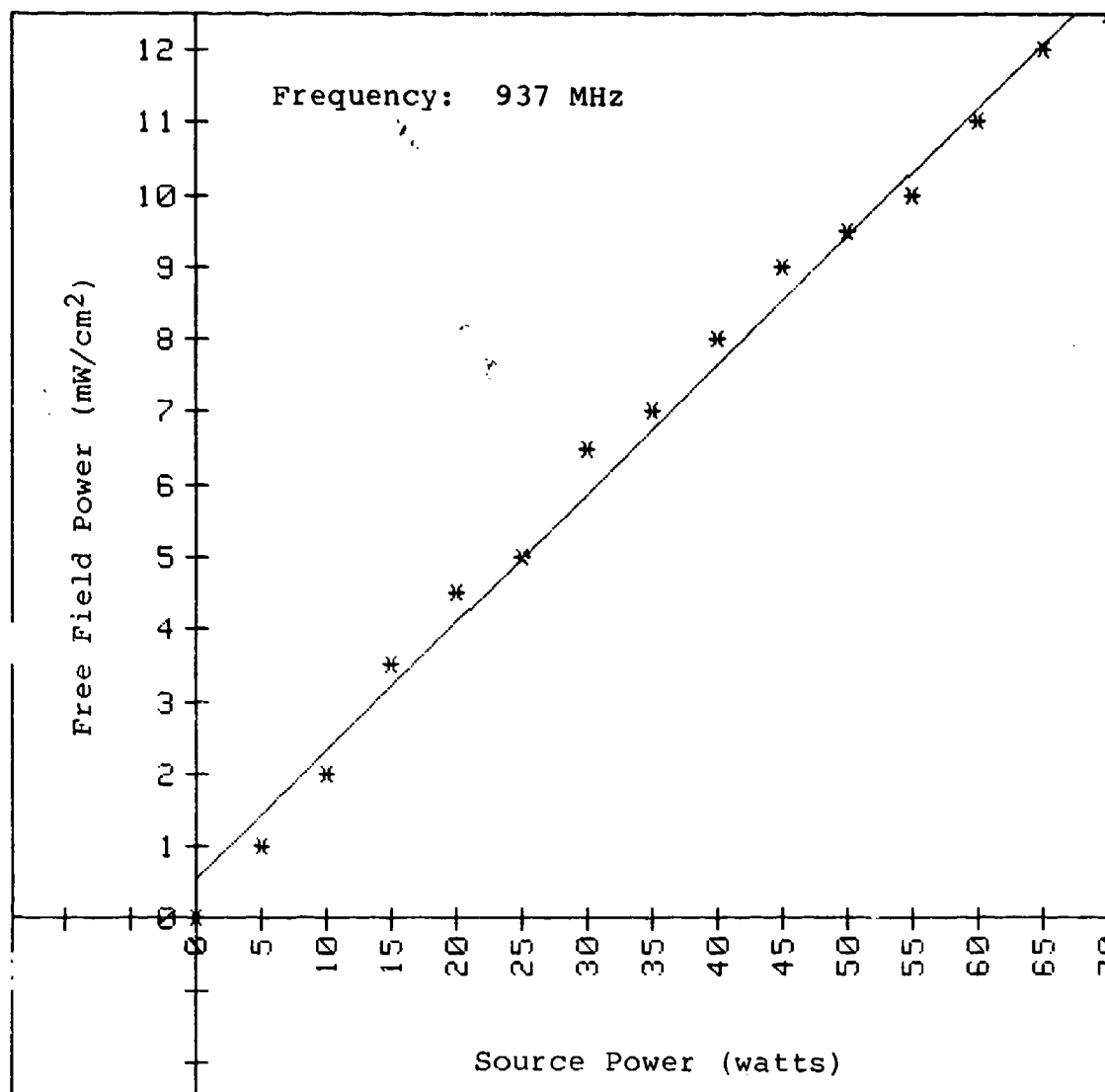


Figure 72: Plot of source power vs free field power (937 MHz).

DATA			
Point #1:	X=0	Y=0	NOTE:
Point #2:	X=10	Y=3.5	x-coordinate - Source
Point #3:	X=20	Y=6	power in watts
Point #4:	X=30	Y=8.5	
Point #5:	X=40	Y=10.5	y-coordinate - Free
Point #6:	X=50	Y=13	field power in
Point #7:	X=60	Y=15	mW/cm ²
Point #8:	X=70	Y=17	
Point #9:	X=80	Y=19	
Point #10:	X=90	Y=21	

Linear model: $Y=A+B*X$
 $A= 1.1363636363$
 $B= .22696969697$

Source	Df	SS	MS	F
Regression	1	425.001	425.001	1346.941
Residual	8	2.524	.316	
Total	9	427.525		

Figure 73: Correlation of microwave source power indication to free field power measured at target location (2.45 GHz).

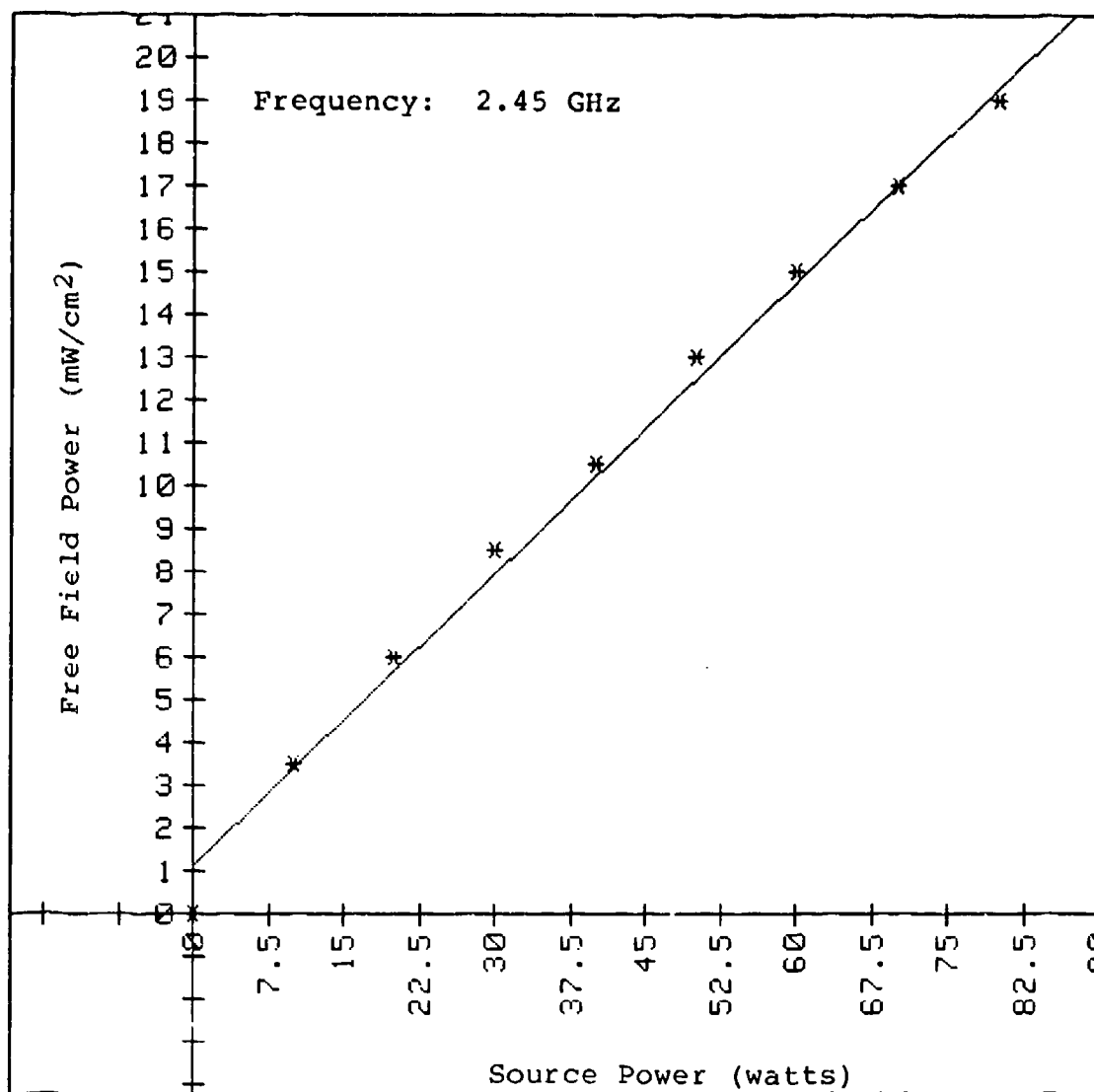


Figure 74: Plot of source power vs free field power (2.45 GHz).

DATA

Point #1:	X=0	Y=0
Point #2:	X=5	Y=.7
Point #3:	X=10	Y=2.3
Point #4:	X=15	Y=2.75
Point #5:	X=20	Y=3.4
Point #6:	X=25	Y=4.03
Point #7:	X=30	Y=4.58
Point #8:	X=35	Y=5.24
Point #9:	X=40	Y=5.9
Point #10:	X=45	Y=6.6
Point #11:	X=50	Y=7.17

POLYNOMIAL MODEL: $Y=A(M)*X^M+A(M-1)*X^{(M-1)}+...+A(1)*X+A(0)$

Coefficients:

$A(0)=.1102797204$

$A(1)=.17834452214$

$A(2)=-.000788344988$

Source	Df	SS	MS	F
Regression	2	53.410	26.705	502.623
Residual	8	.425	.053	
Total	10	53.835		

NOTE: x-coordinate - Source power
in watts

y-coordinate - Probe response
in volts/inch
at the x-y
recorder

Figure 75: Correlation of magnetic field
probe response to source
power (937 MHz).

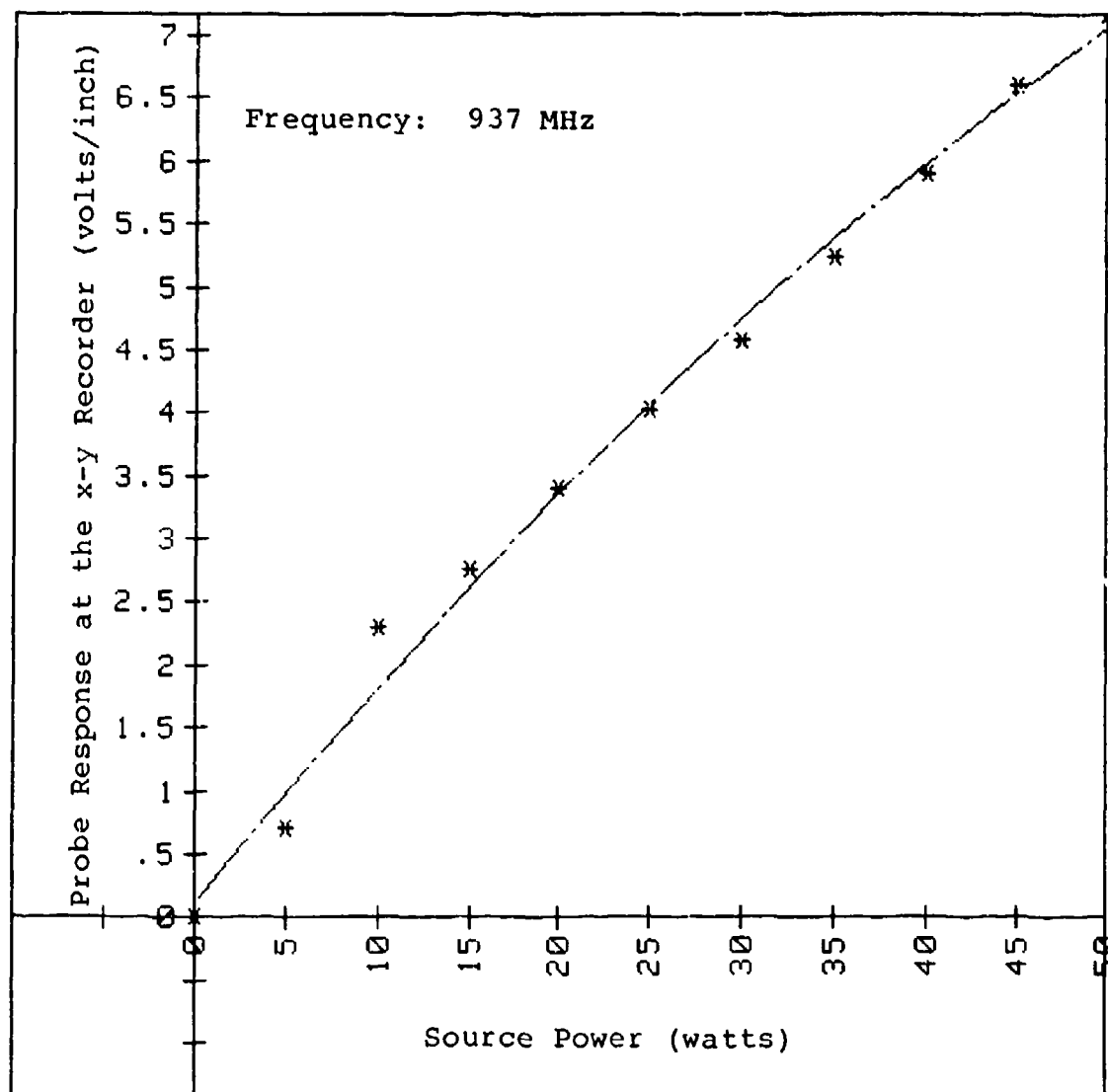


Figure 76: Plot of magnetic field probe response vs source power (937 MHz).

DATA

Point #1:	X=0	Y=.0625
Point #2:	X=10	Y=1.125
Point #3:	X=20	Y=1.625
Point #4:	X=30	Y=2.125
Point #5:	X=40	Y=2.5625
Point #6:	X=50	Y=3
Point #7:	X=60	Y=3.375
Point #8:	X=70	Y=3.5625
Point #9:	X=80	Y=4.375
Point #10:	X=90	Y=4.5
Point #11:	X=100	Y=4.8125
Point #12:	X=110	Y=5.125
Point #13:	X=120	Y=5.5

POLYNOMIAL MODEL: $Y=A(M)*X^M+A(M-1)*X^{(M-1)}+\dots+A(1)*X+A(0)$

Coefficients:

$A(0)=.342032967$

$A(1)=.06075487013$

$A(2)=-1.55157342700E-04$

Source	Df	SS	MS	F
Regression	2	32.795	16.397	621.352
Residual	10	.264	.026	
Total	12	33.059		

NOTE: x-coordinate - Source power
in watts
y-coordinate - Probe response in
volts/inch at the
x-y recorder

Figure 77: Correlation of magnetic field
probe response to source
power (2.45 GHz).

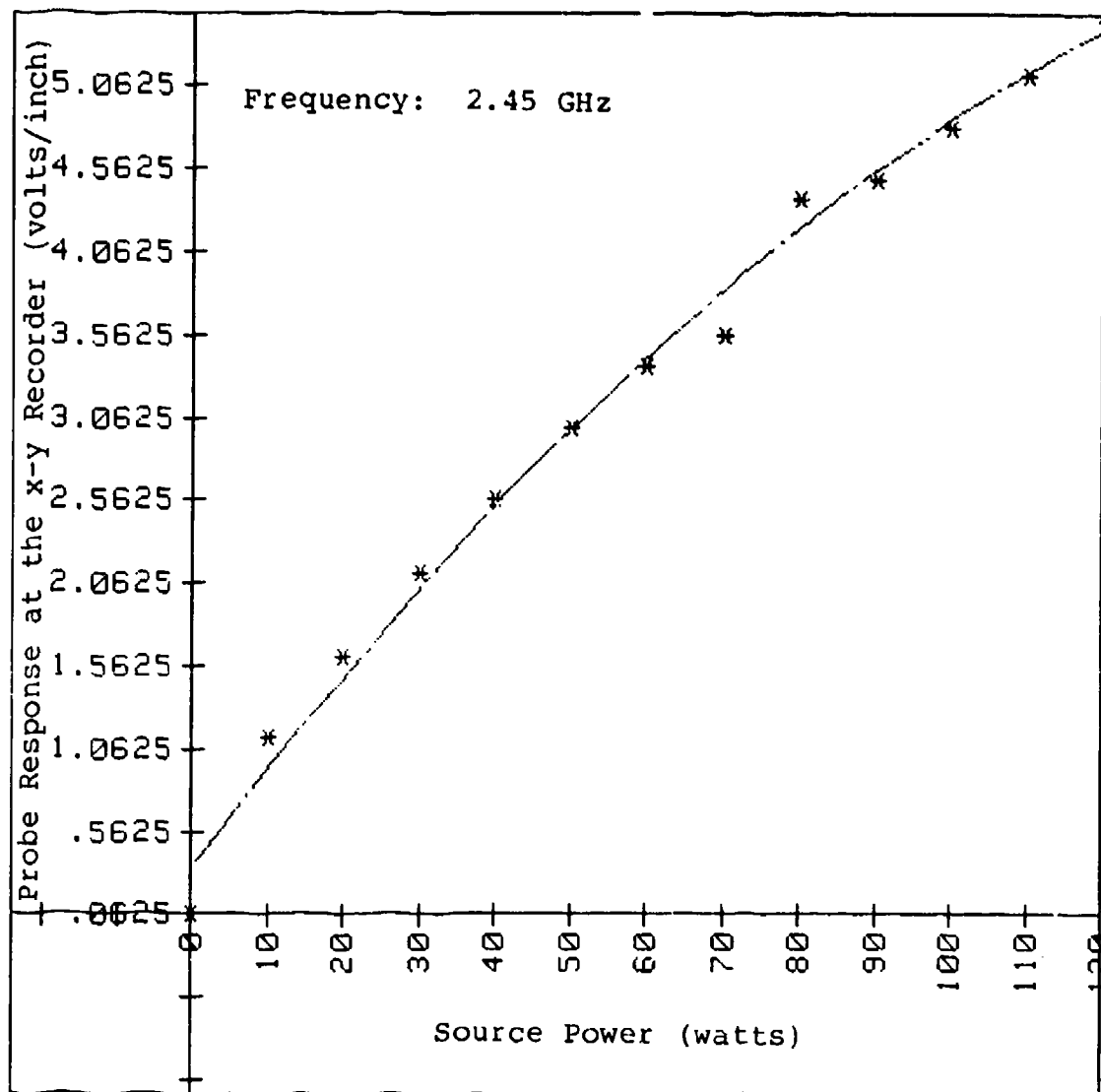


Figure 78: Plot of magnetic field probe response vs source power (2.45 GHz).

DATA

Point #1:	X=3.875	Y=2.75
Point #2:	X=4.472	Y=3.4
Point #3:	X=5	Y=4.03
Point #4:	X=5.477	Y=4.58
Point #5:	X=5.916	Y=5.24
Point #6:	X=6.325	Y=5.9
Point #7:	X=6.708	Y=6.6
Point #8:	X=7.07	Y=7.17

Linear model: $Y=A+B \cdot X$

$A=-2.83736850218$

$B=1.3908290707$

Source	Df	SS	MS	F
Regression	1	16.707	16.707	645.403
Residual	6	.155	.026	
Total	7	16.863		

NOTE: x-coordinate - Square root of
source power

y-coordinate - Probe response
in volts/inch at
the x-y recorder

Figure 79: Correlation of magnetic field
probe response to the square
root of source power (937 MHz).

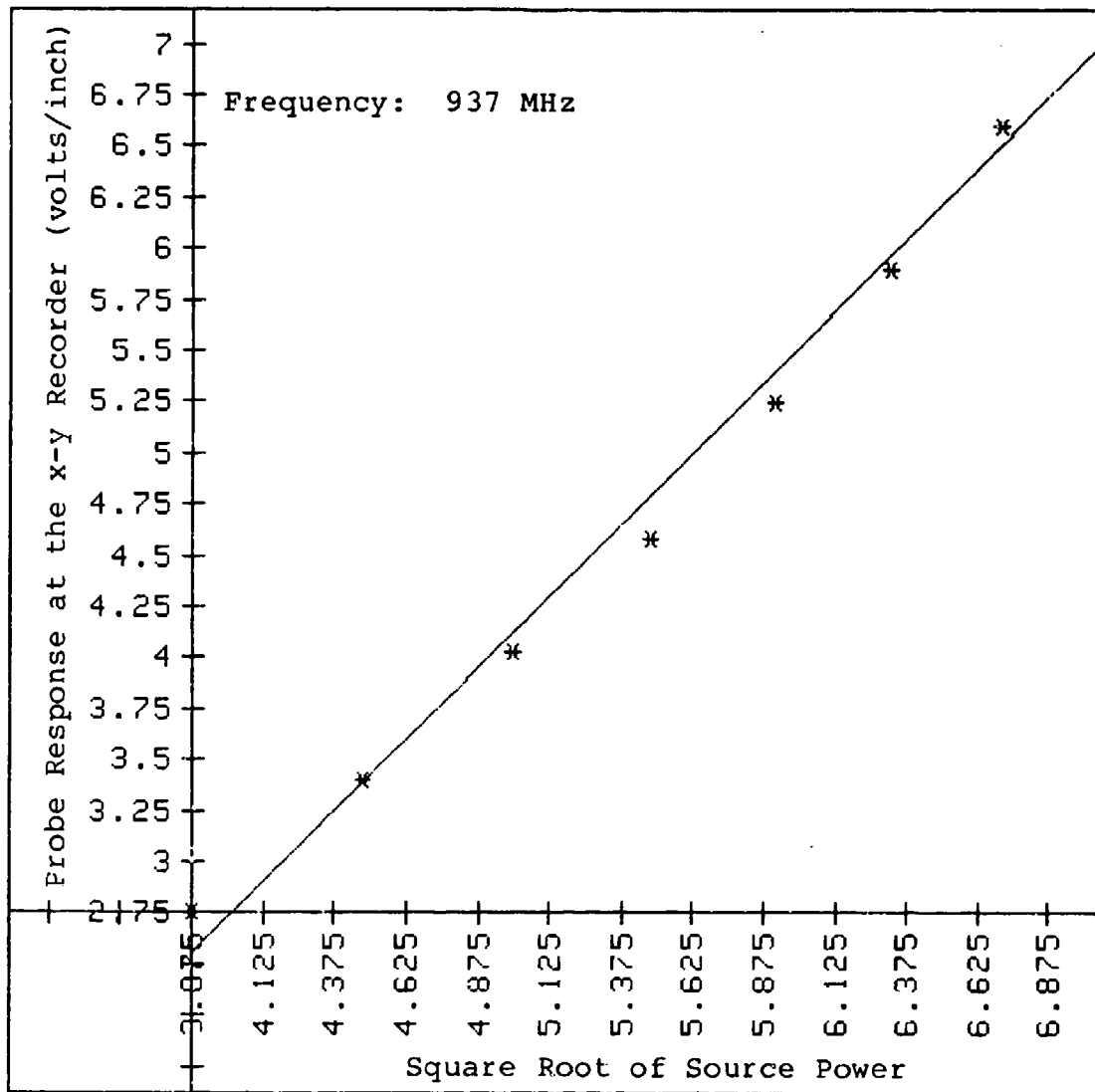


Figure 80: Plot of magnetic field probe response vs square root of source power (937 MHz).

DATA

Point #1:	X=4.472	Y=1.5625
Point #2:	X=5.477	Y=2.0625
Point #3:	X=6.325	Y=2.5
Point #4:	X=7.071	Y=2.9375
Point #5:	X=7.746	Y=3.3125
Point #6:	X=8.367	Y=3.5
Point #7:	X=8.944	Y=4.3125
Point #8:	X=9.487	Y=4.4375
Point #9:	X=10	Y=4.75
Point #10:	X=10.49	Y=5.0625
Point #11:	X=10.95	Y=5.4375

Linear model: $Y=A+B \cdot X$

$A=-1.26463090183$

$B=.602110623875$

Source	Df	SS	MS	F
Regression	1	16.142	16.142	936.785
Residual	9	.155	.017	
Total	10	16.297		

NOTE: x-coordinate - Square root of source power

y-coordinate - Probe response in volts/inch at the x-y recorder

Figure 81: Correlation of magnetic field probe response to the square root of source power (2.45 GHz).

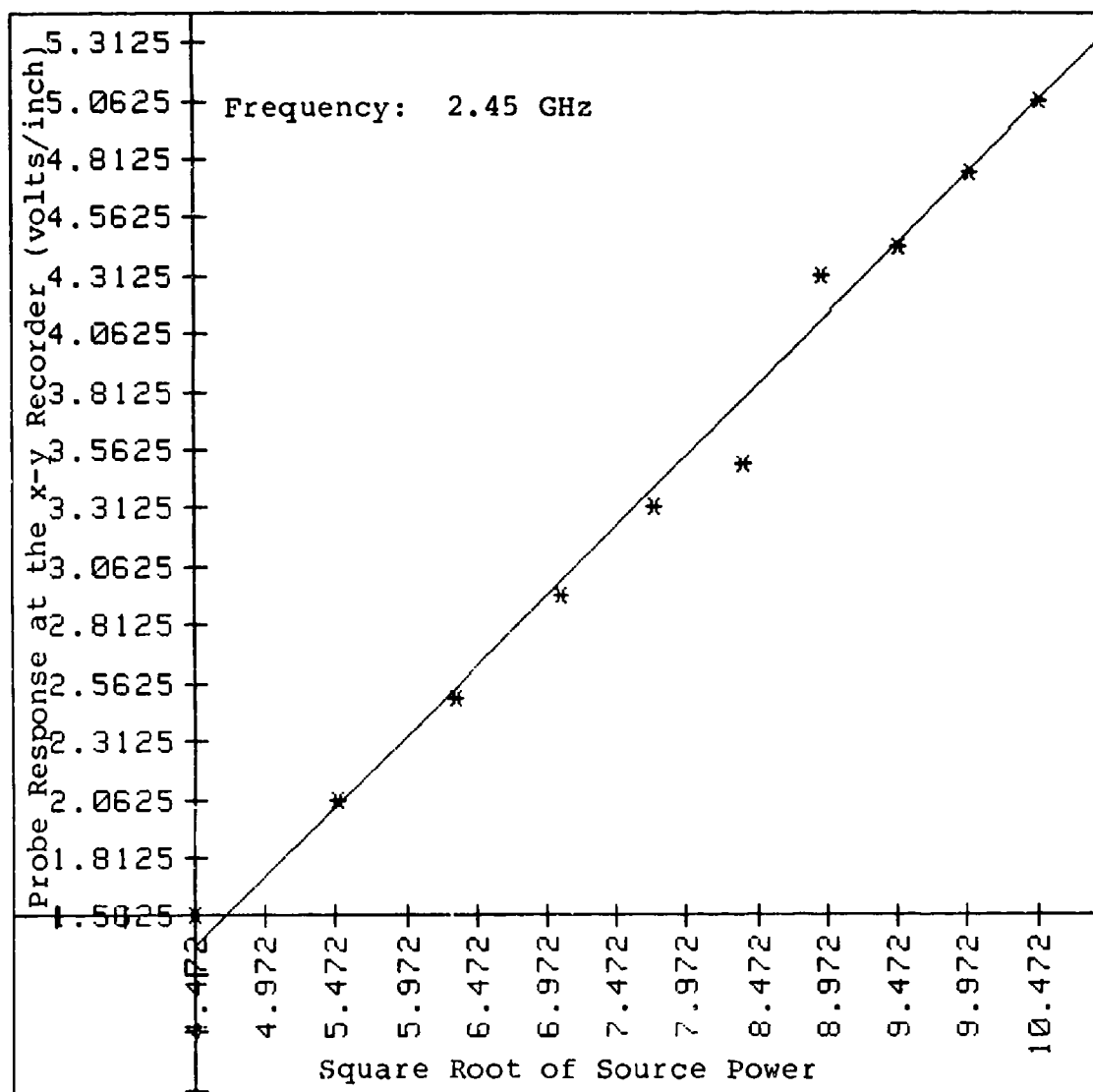


Figure 82: Plot of magnetic field probe response vs square root of source power (2.45 GHz).

DATA

Point #1:	X=0	Y=0
Point #2:	X=.01	Y=.085
Point #3:	X=.03	Y=.227
Point #4:	X=.1	Y=.565
Point #5:	X=.3	Y=.98
Point #6:	X=.5	Y=1.37
Point #7:	X=.7	Y=1.65
Point #8:	X=1	Y=2.04

POLYNOMIAL MODEL: $Y=A(M)*X^M+A(M-1)*X^{(M-1)}+...+A(1)*X+A(0)$

Coefficients:

A(0)=.10211248286
 A(1)=3.2482190112
 A(2)=-1.3444856344

Source	Df	SS	MS	F
Regression	2	4.075	2.038	235.223
Residual	5	.043	.009	
Total	7	4.119		

NOTE: x-coordinate - Input power to
 probe in mW
 y-coordinate - Probe response
 in volts at the
 x-y recorder

Data taken in conjunction with the Precision Measurements Equipment Laboratory (USAF Academy).

Figure 83: Correlation of magnetic field probe response to input power (937 MHz).

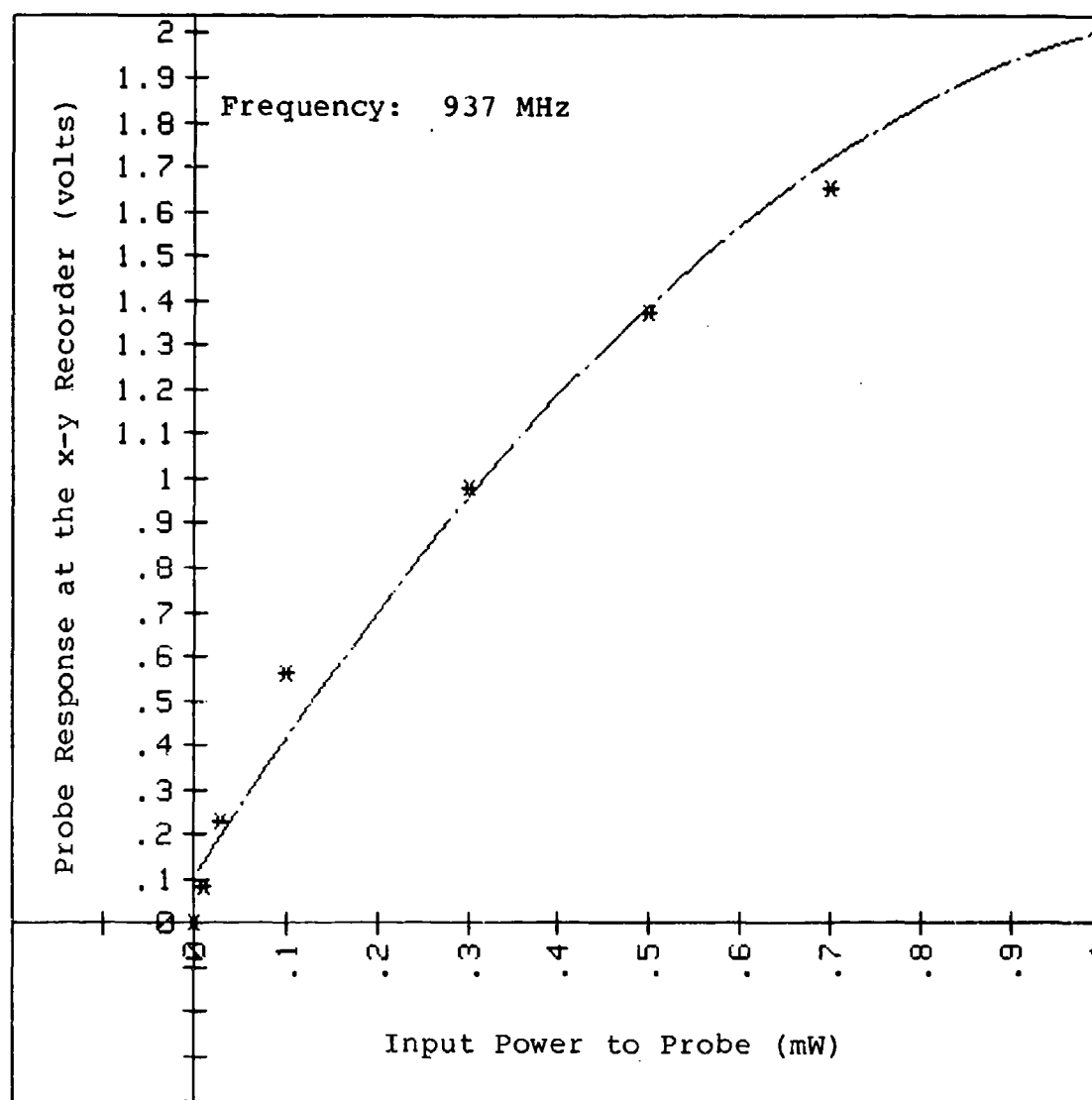


Figure 84: Plot of magnetic field probe response vs input power (937 MHz).

DATA

Point #1:	X=0	Y=0
Point #2:	X=.1	Y=.03
Point #3:	X=.3	Y=.092
Point #4:	X=1	Y=.265
Point #5:	X=3	Y=.653
Point #6:	X=10	Y=1.61
Point #7:	X=15	Y=2.12
Point #8:	X=20	Y=2.65

POLYNOMIAL MODEL: $Y=A(M)*X^M+A(M-1)*X^{(M-1)}+...+A(1)*X+A(0)$

Coefficients:

$A(0)=.04570077953$

$A(1)=.18422614543$

$A(2)=-.002783808761$

Source	Df	SS	MS	F
Regression	2	7.717	3.858	1194.314
Residual	5	.016	.003	
Total	7	7.733		

NOTE: x-coordinate - Input power to
probe in mW
y-coordinate - Probe response
in volts at the
x-y recorder

Data taken in conjunction with the Precision Measurement Equipment Laboratory (USAF Academy).

Figure 85: Correlation of magnetic field
probe response to input power
(2.45 GHz).

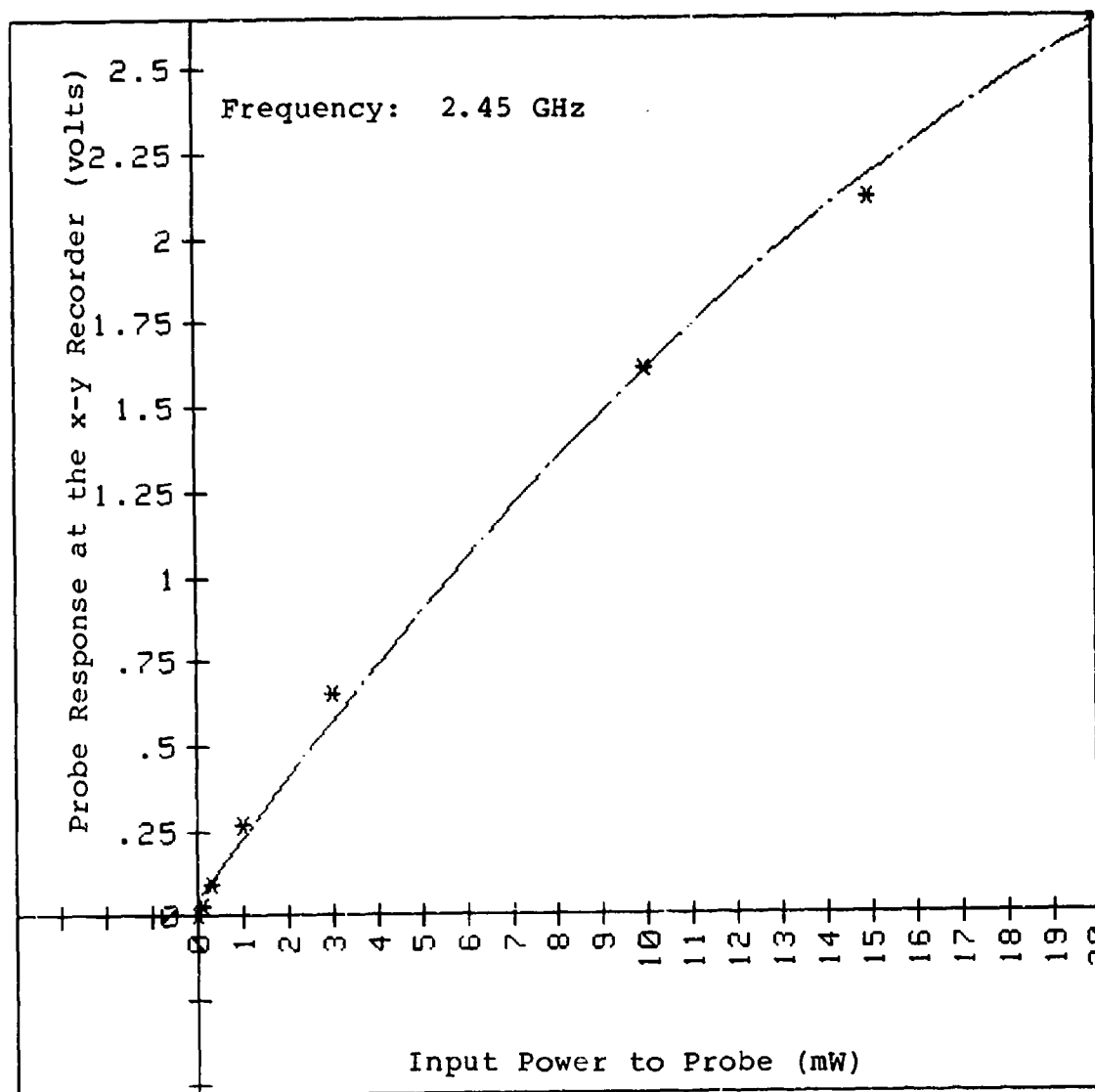


Figure 86: Plot of magnetic field probe response vs input power (2.45 GHz).

DATA

Point #1:	X=.1	Y=.085
Point #2:	X=.173	Y=.227
Point #3:	X=.316	Y=.565
Point #4:	X=.548	Y=.98
Point #5:	X=.707	Y=1.37
Point #6:	X=.837	Y=1.65
Point #7:	X=1	Y=2.04

Linear model: $Y=A+B \cdot X$
 $A=-.1426435313$
 $B= 2.15036803366$

Source	Df	SS	MS	F
Regression	1	3.259	3.259	3123.496
Residual	5	.005	.001	
Total	6	3.264		

NOTE: x-coordinate - Square root
of input power
to probe

y-coordinate - Probe response
in volts at the
x-y recorder

Data taken in conjunction with the Precision Measurement Equipment Laboratory (USAF Academy).

Figure 87: Correlation of magnetic field
probe response to square root
of input power (937 MHz).

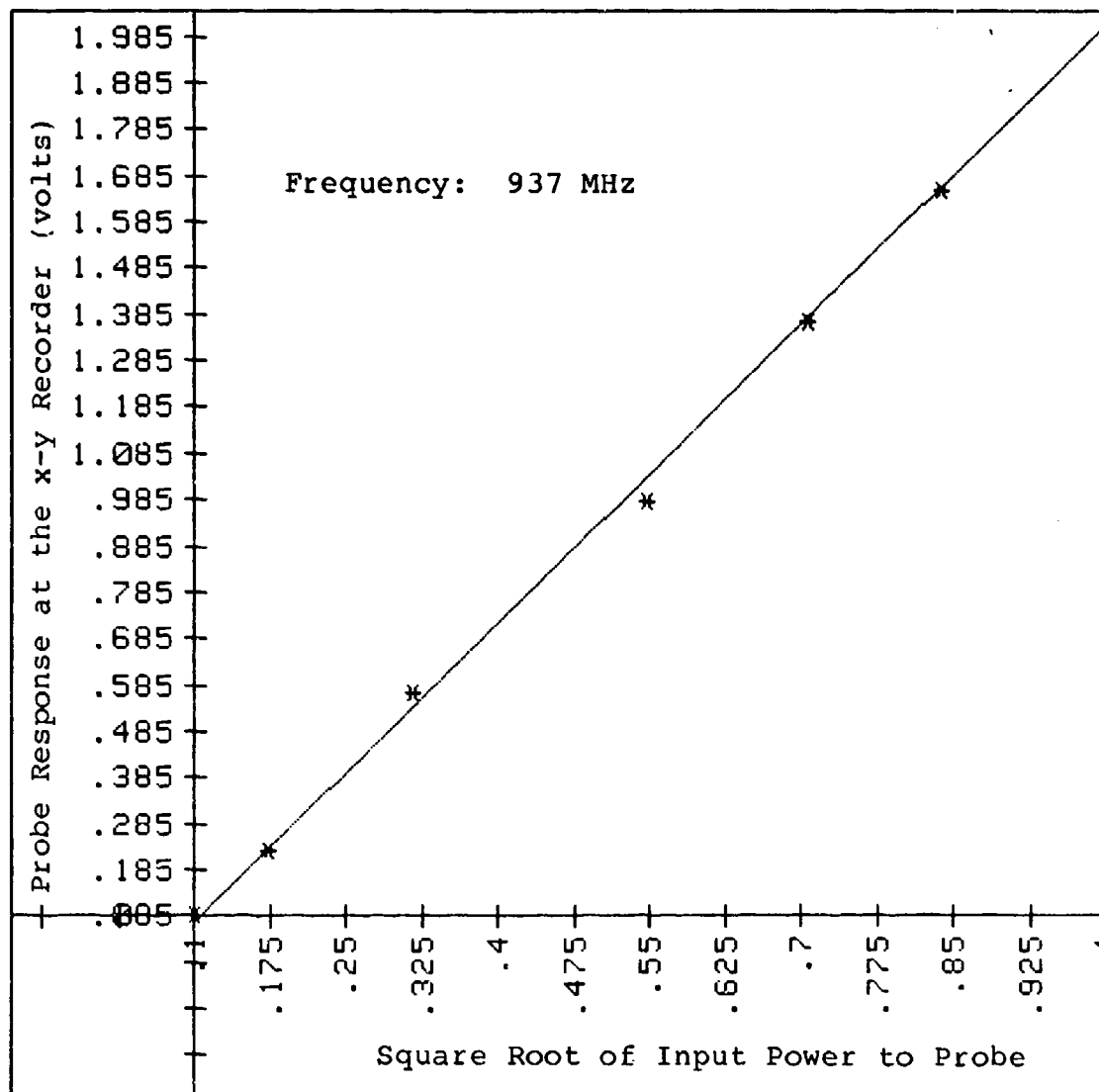


Figure 88: Plot of magnetic field probe response vs square root of input power (937 MHz).

DATA

Point #1:	X=1	Y=.265
Point #2:	X=1.732	Y=.653
Point #3:	X=3.16	Y=1.61
Point #4:	X=3.873	Y=2.12
Point #5:	X=4.47	Y=2.65

Linear model: $Y=A+B \cdot X$

$A=-.48433909502$

$B=.682802632602$

Source	Df	SS	MS	F
Regression	1	3.935	3.935	625.961
Residual	3	.019	.006	
Total	4	3.953		

NOTE: x-coordinate - Square root of
input power to
probe

y-coordinate - Probe response
in volts at the
x-y recorder

Data taken in conjunction with the Precision Measurement Equipment Laboratory (USAF Academy).

Figure 89: Coorelation of magnetic field probe response to square root of input power (2.45 GHz).

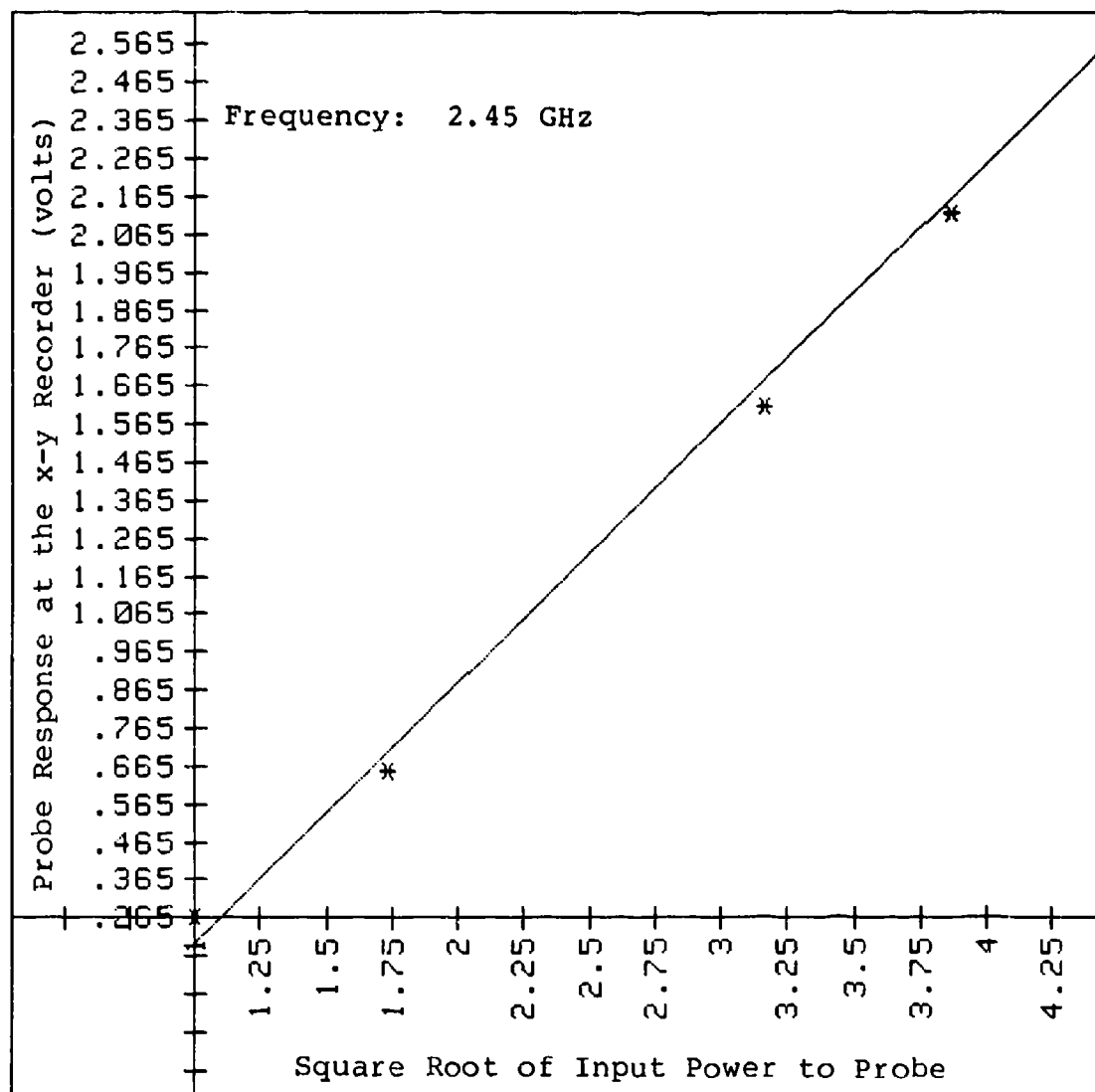


Figure 90: Plot of magnetic field probe response vs square root of input power (2.45 GHz).

CHAPTER V

PROBE MEASUREMENT OF SURFACE CURRENTS

To obtain total current at any point on an object, two orthogonal components are required. For a plane polarized wave at normal incidence on simple symmetric flat plates, it is well known that certain "cuts" or scans across the plate will have a dominant current component in the direction of the incident electric field. The terms "vertical" and "horizontal" will continue to refer to the experimental arrangement whereby incident \vec{E} is vertical and \vec{H} is horizontal. The semirigid coaxial cable probe measurements roughly corresponded to the loop/diode measurements and only the loop/diode type probs are considered here.

Procedure

The probe scans were done at three horizontal positions on each of the plates.

The height above the ground plane were consistently taken as follows:

Plate height (inches)	Scan height (inches)		
	Upper	Middle	Lower
2.41 (6.12 cm)	2	1.25	.5
3.15 (8 cm)	2.5	1.5	.5

These heights were selected so as to sample the surface currents in unique locations with respect to probe integration areas and to remain clear of the needed copper tape used for support and electric contact.

Precautions were taken to assure that the probe remained in a given orientation to the plate with an insulating jacket in contact with the plate. As seen in Figure 91, a styrofoam support was made



Figure 91: Magnetic field probe in front of a metal target.

in which the probe remained fixed. The plates were positioned in an identical centerline location at 100.5 cm from the antenna for probe and IR measurements. This location was slightly ahead of the coaxial cable so that a slight positive pressure was present as the styrofoam/probe structure was guided along the plate surface.

Results

Both horizontal and vertical probe measurements were made. The vertical orientation results are presented in this chapter using scan levels mentioned earlier with the exception of the free field scans which were done at .75 and 1.75 inches from the ground plane.

The results for the horizontal orientation are presented in Appendix E. Free field samplings at .75 and 1.75 were unable to detect a signal as would be expected with the incident \vec{H} field also in the plane of the loop. The induced voltages were down from the dominant, vertical orientation but not quite as symmetric, revealing possible unexpected coupling.

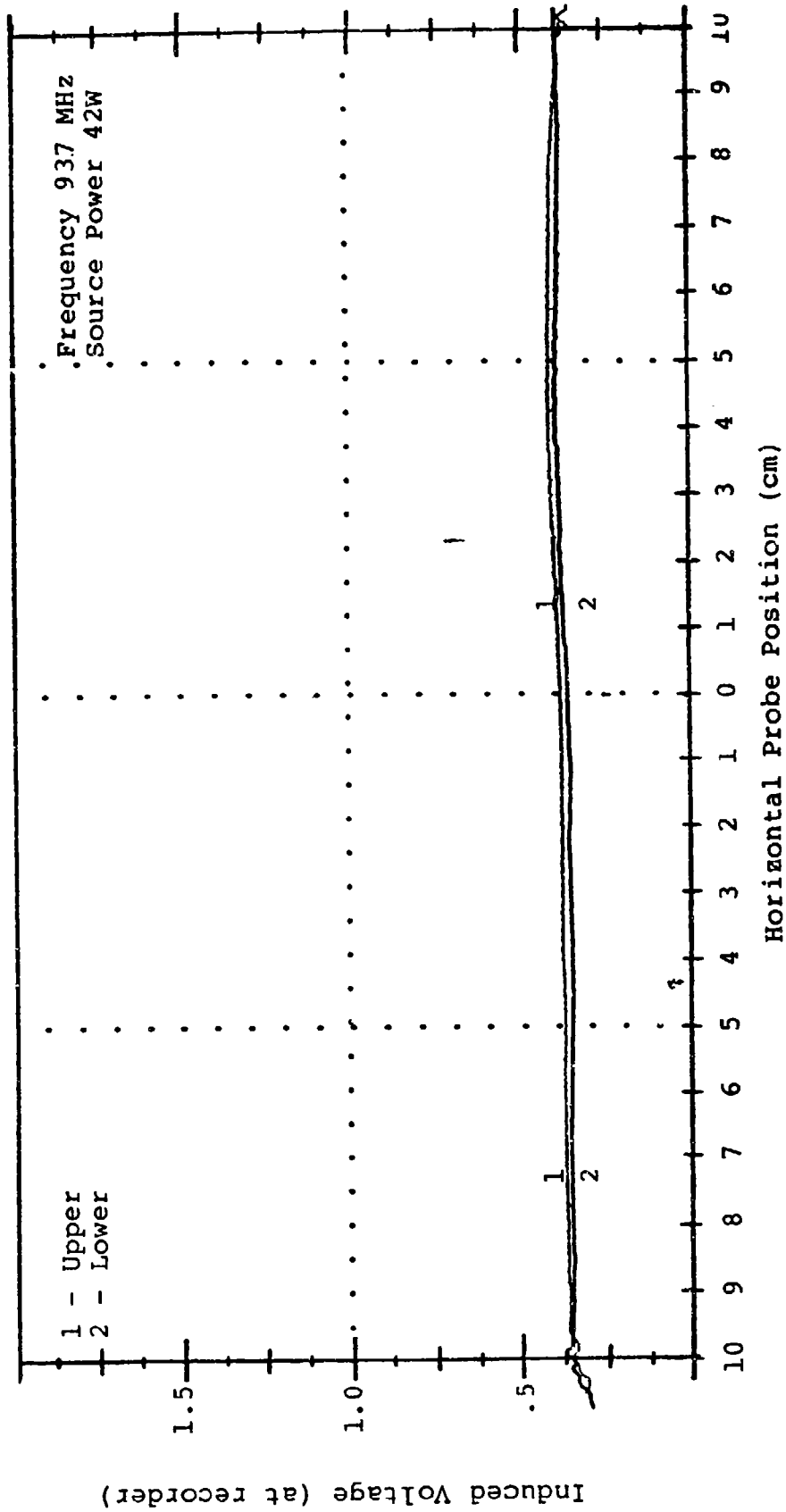


Figure 92: Vertical Magnetic Field Probe Measurements for the free field at 3/4 and 1 3/4 inches above ground plane.

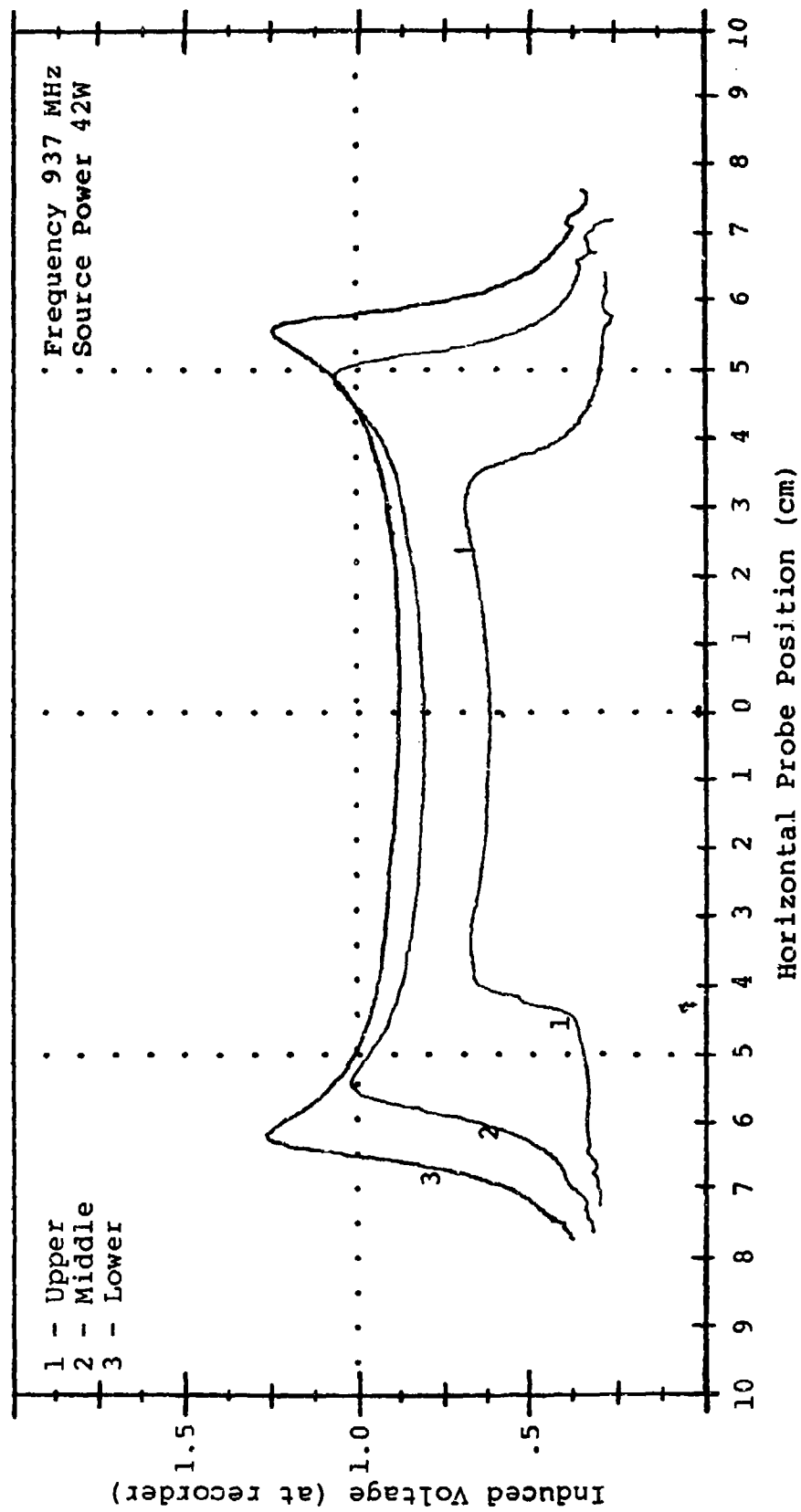


Figure 93: Vertical Magnetic Field Probe Measurements for the .38 wavelength circular disk.

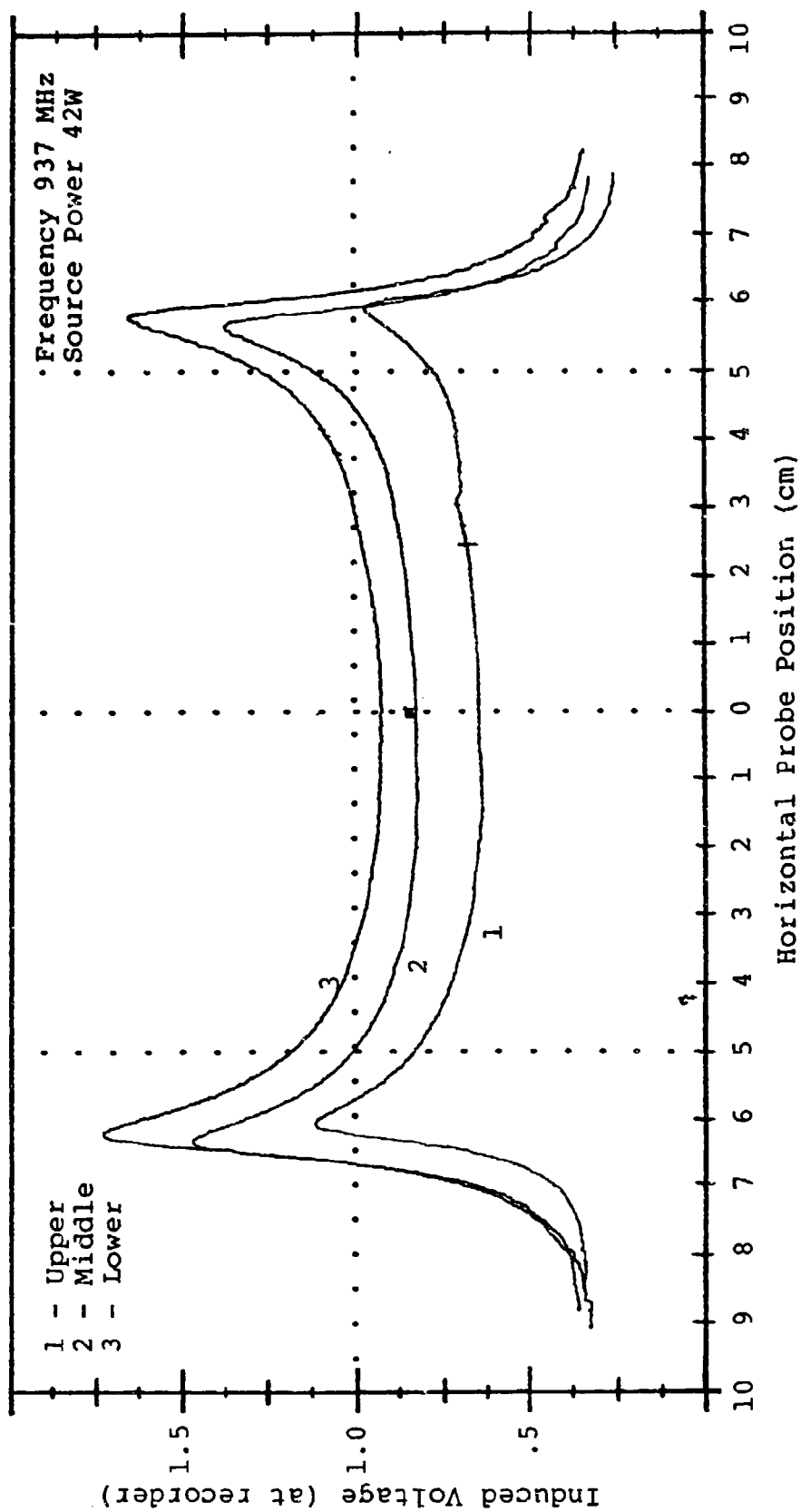


Figure 94: Vertical Magnetic Field Probe Measurements for the .38 wavelength square plate.

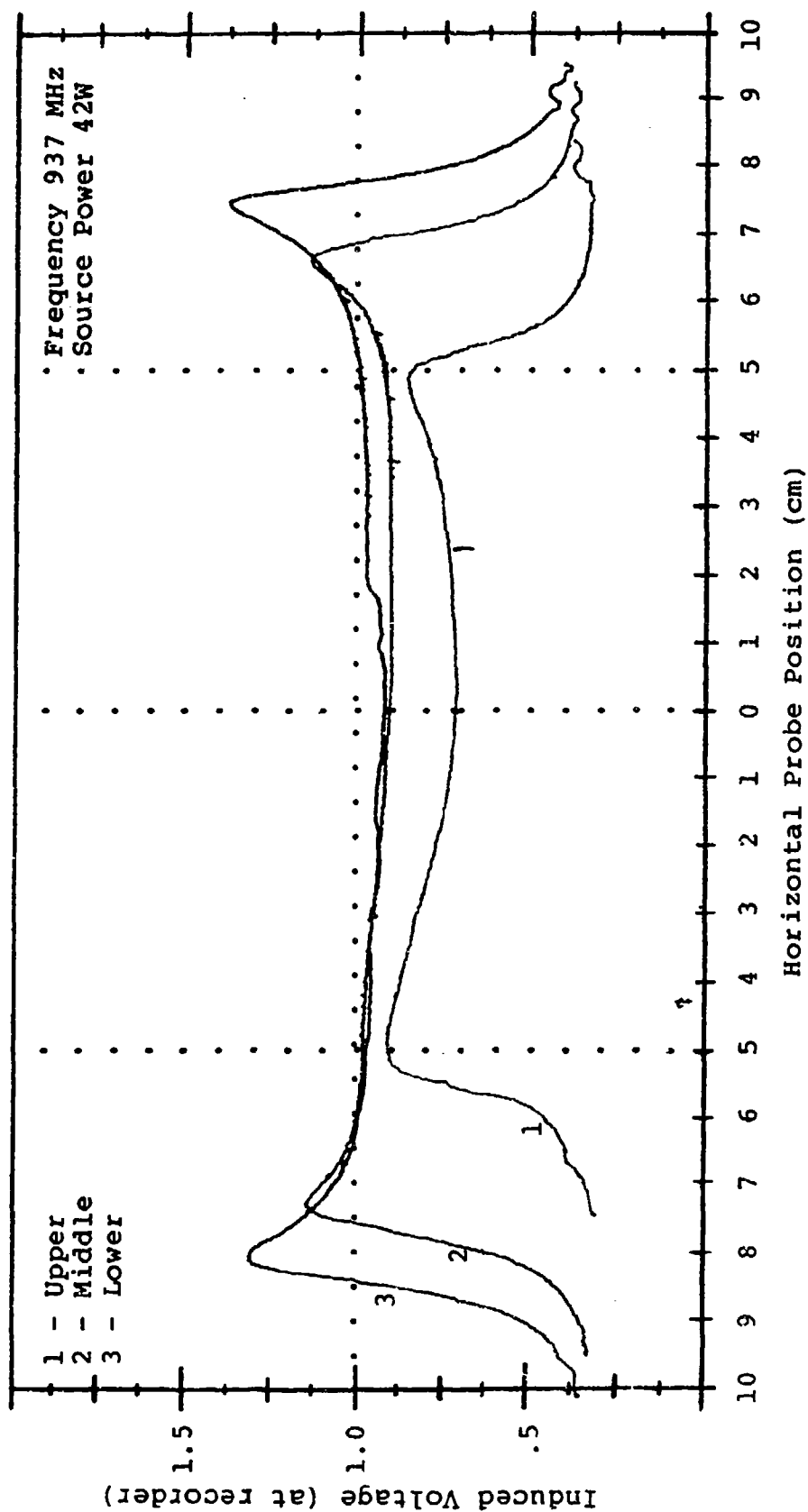


Figure 95: Vertical Magnetic Field Probe Measurements for the .50 wavelength circular disk.

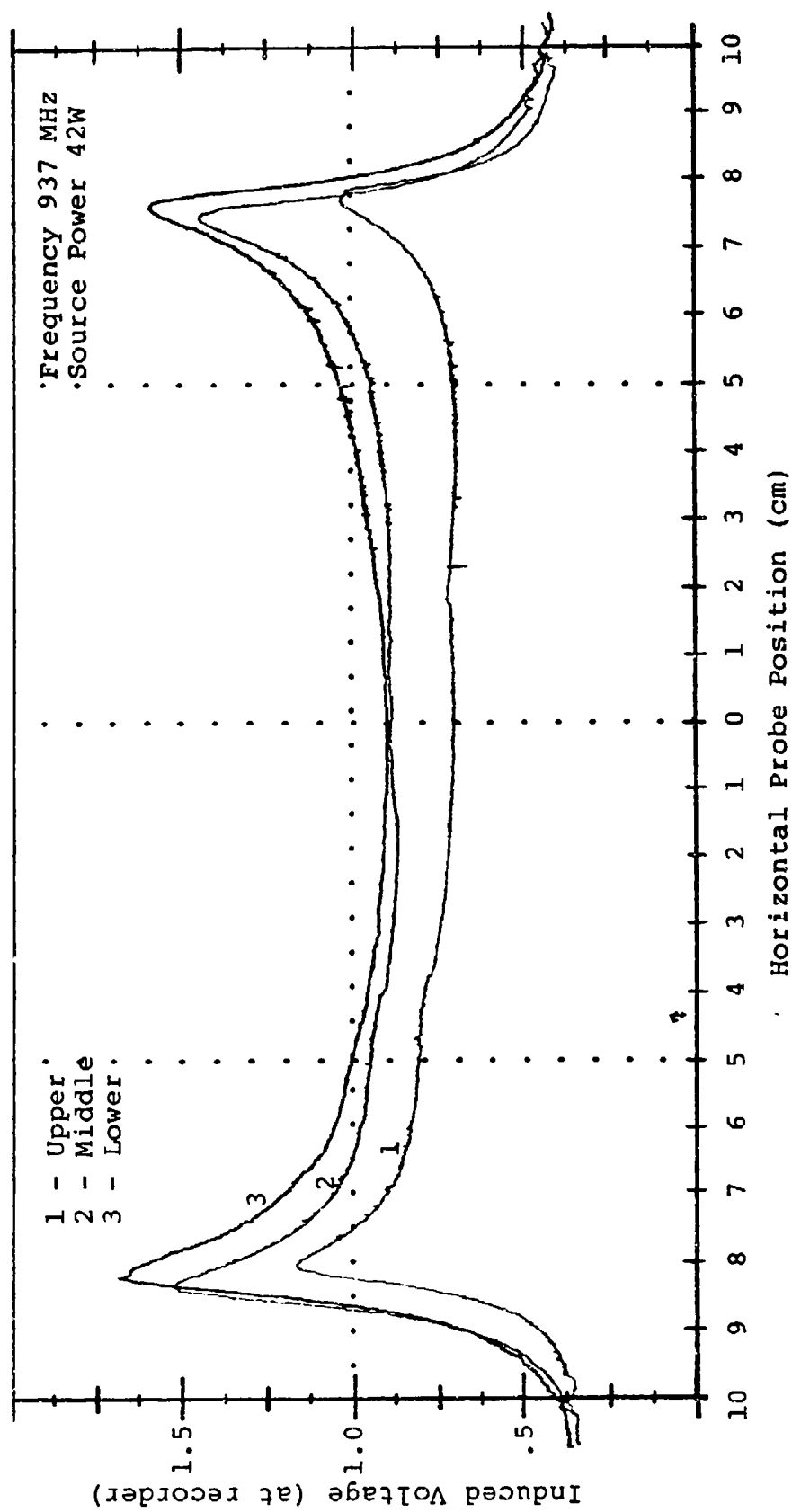


Figure 96: Vertical Magnetic Field Probe Measurements for the .50 wavelength square plate.

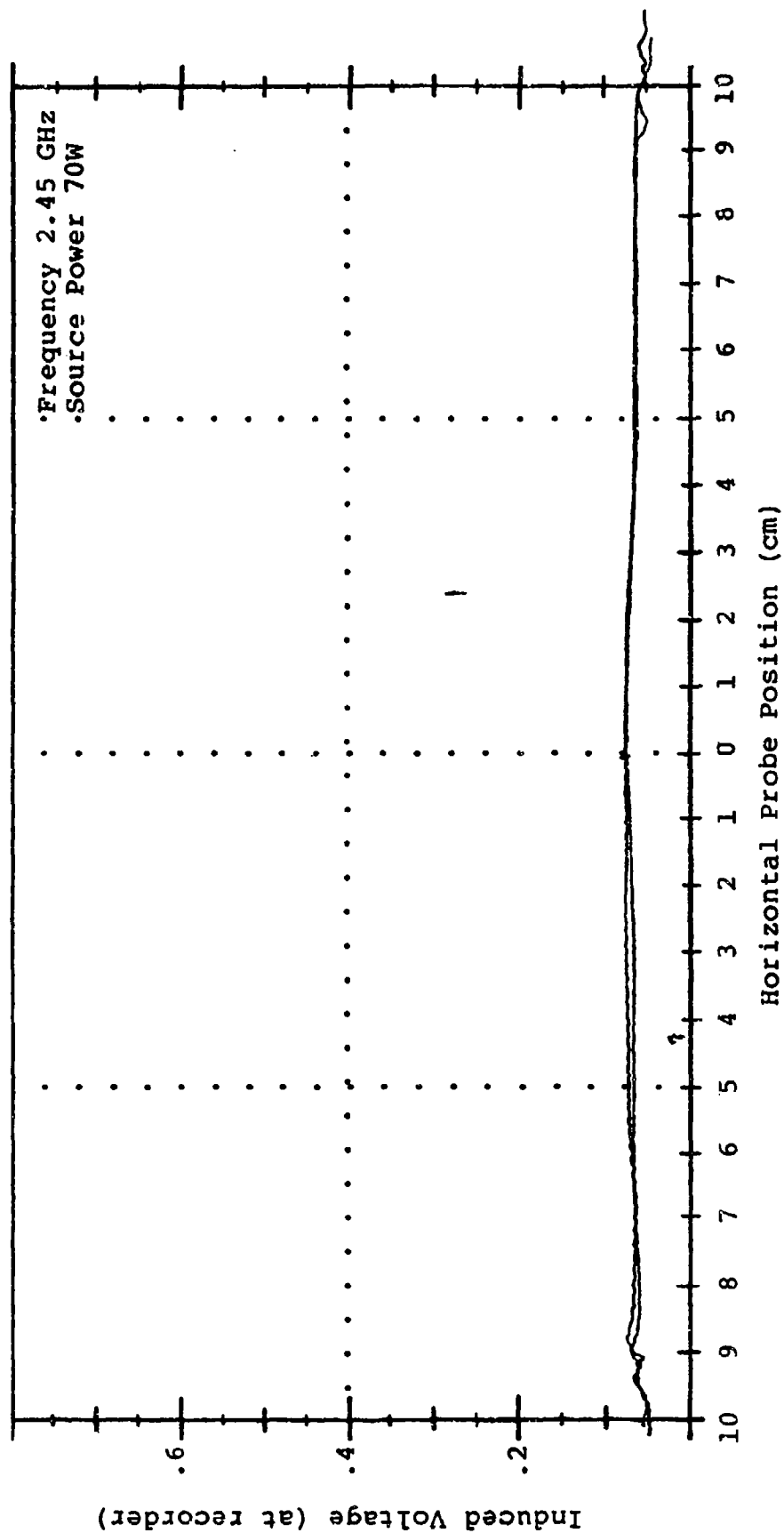


Figure 97: Vertical Magnetic Field Probe Measurements for the free field at 3/4 and 1 3/4 inches above ground plane.

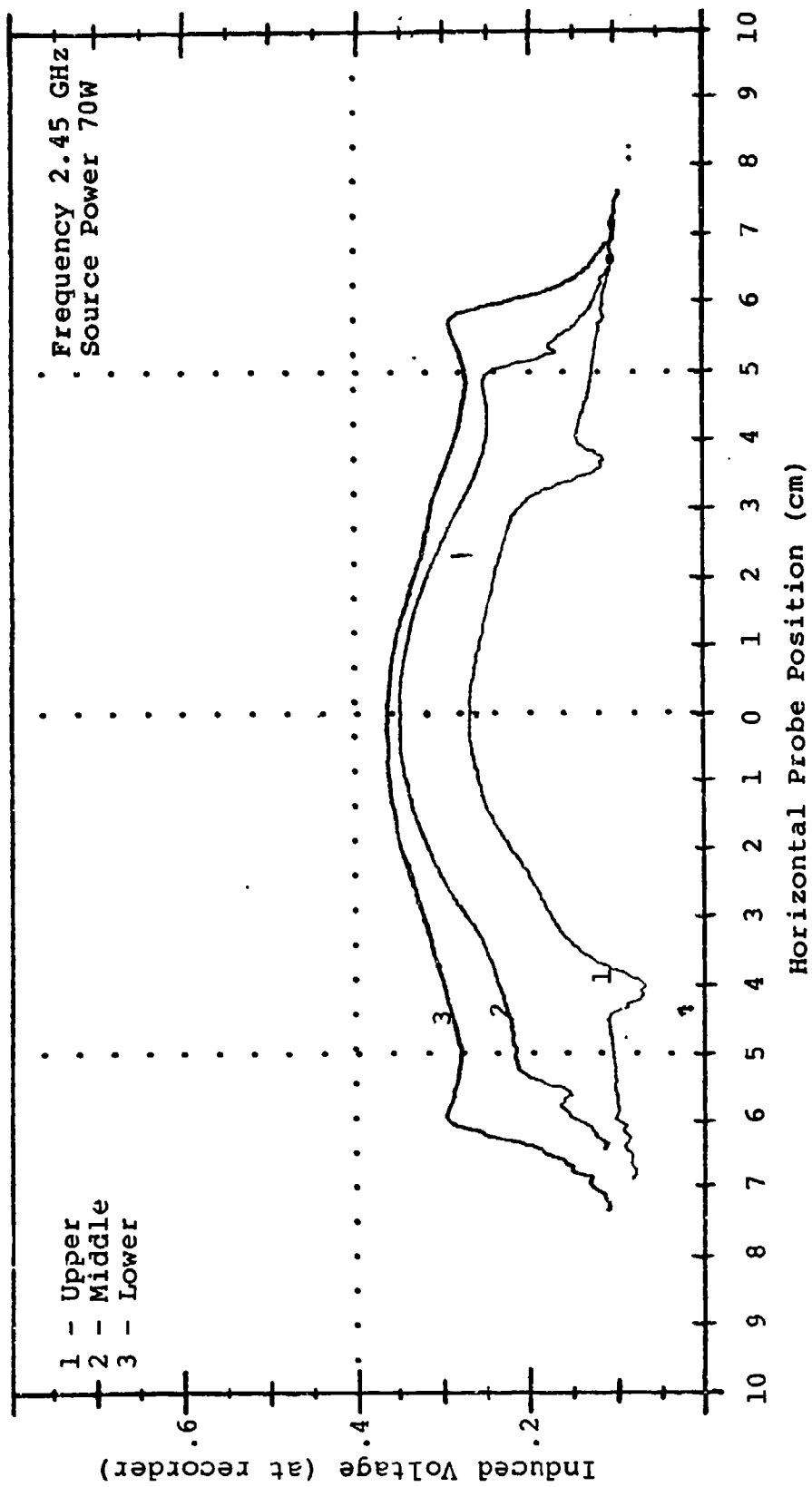


Figure 98: Vertical Magnetic Field Probe Measurements for the 1.0 wavelength circular disk.

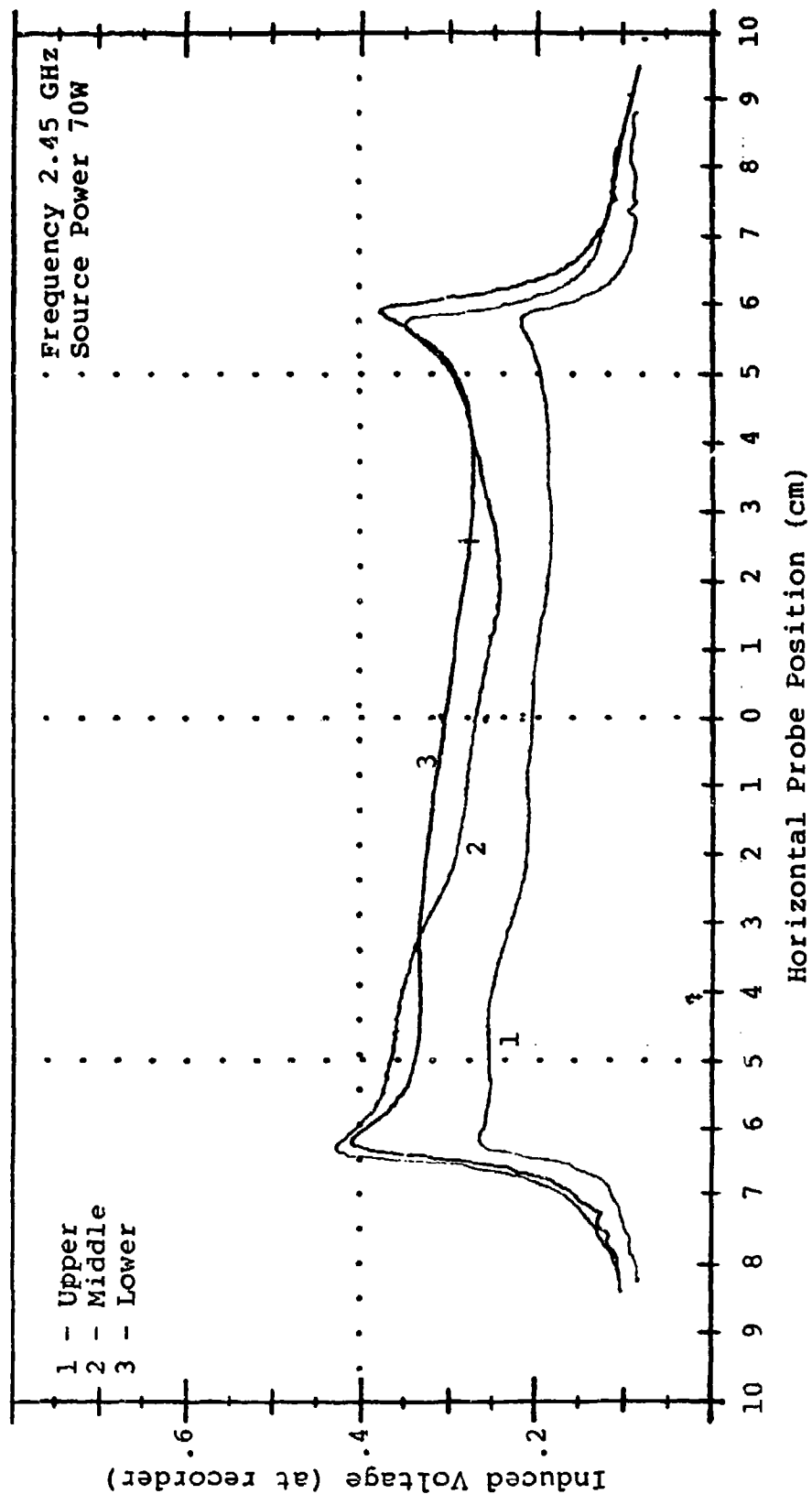


Figure 99: Vertical Magnetic Field Probe Measurements for the 1.0 wavelength square plate.

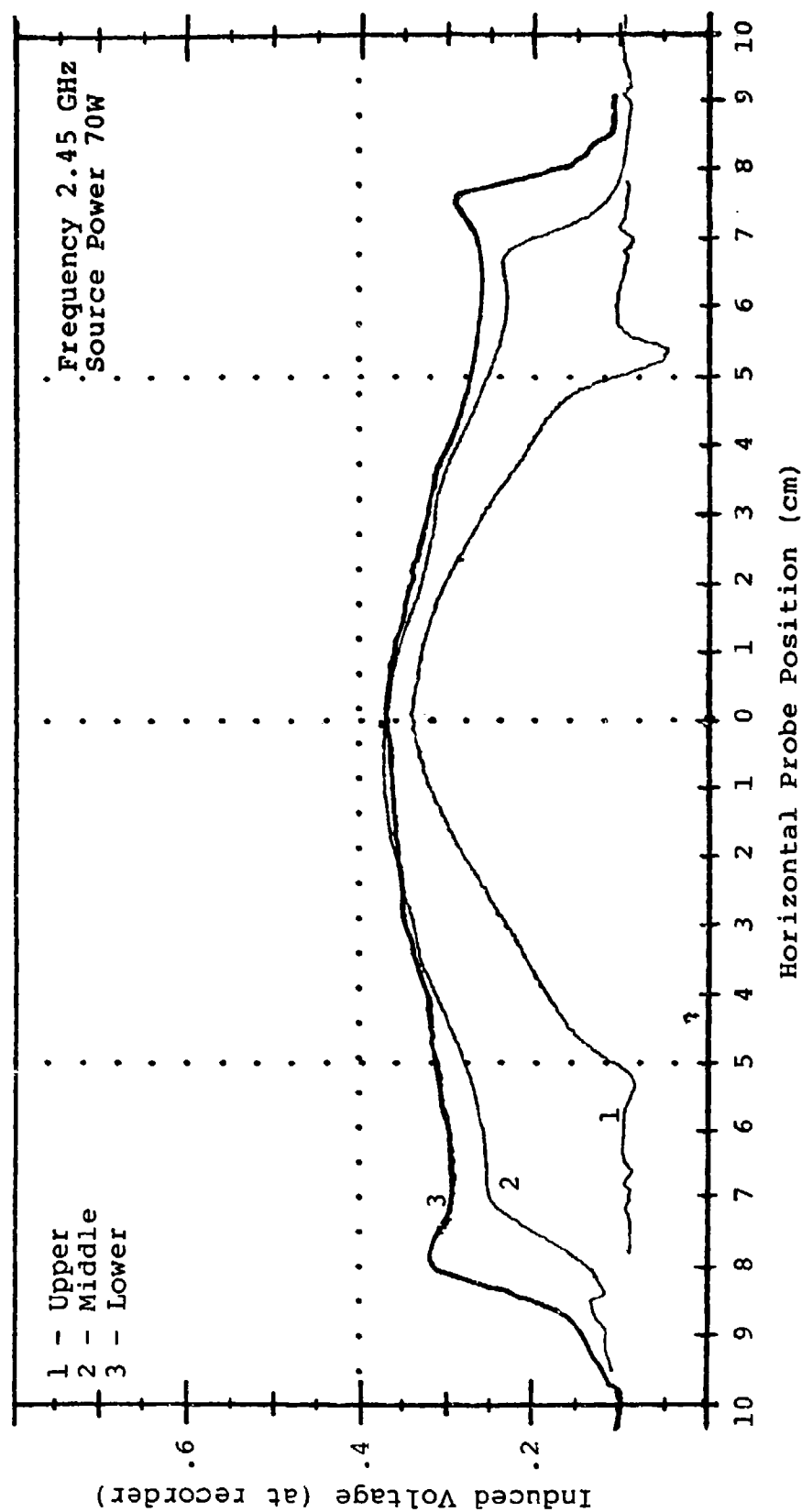


Figure 100: Vertical Magnetic Field Probe Measurements for the 1.3 wavelength circular disk.

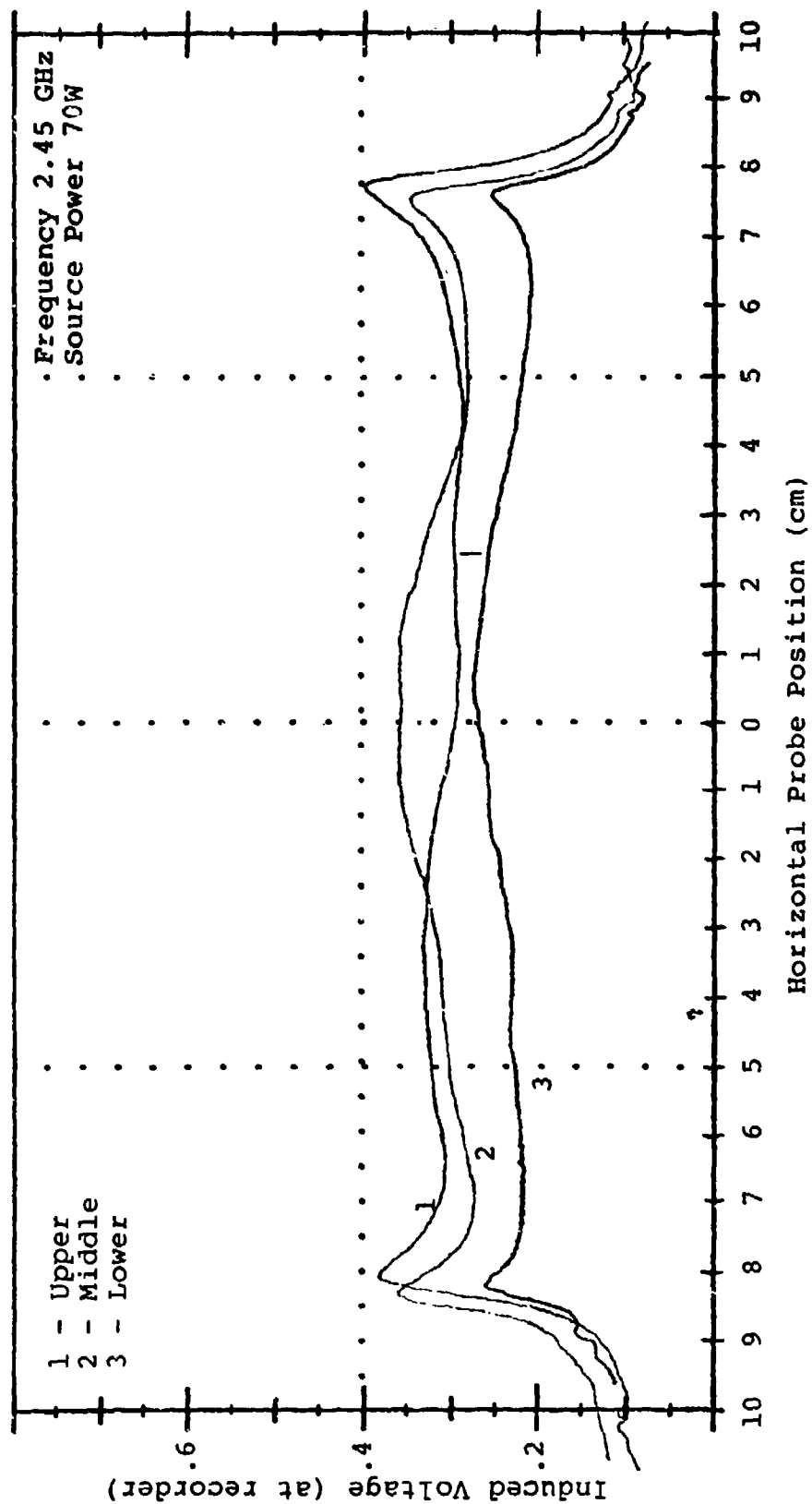


Figure 101: Vertical Magnetic Field Probe Measurements for the 1.3 wavelength square plate.

CHAPTER VI

IR MEASUREMENT OF SURFACE CURRENTS

The capability of detecting a current induced heating pattern and taking the digitized information in isotherms, converting to temperature, then finally to currents will be shown. The target compositions were discussed in Chapter III. It must be emphasized that current densities obtained through the IR technique presented here are the current densities in the given coatings, either aquadac on plexiglass, or carbon/paraffin over metal.

Technique

Having discussed the digitization of thermovision data, and the application of the calibration curve to transform from isotherm to temperature, the relationship between current density and temperature must be made. This is accomplished by fitting empirically obtained data to a functional relation, a second order polynomial.

The experimental arrangement for relating

current density is given in the following figure.

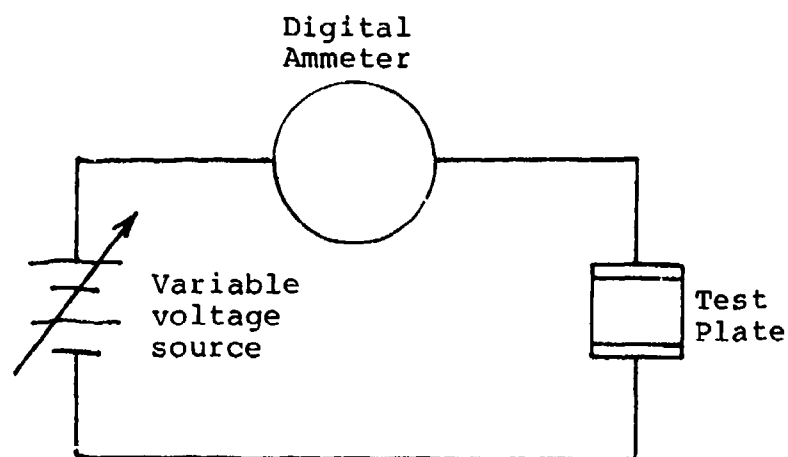


Figure 102: Circuit for relating current and temperature.

The plate shown in Figure 103 is composed of 59 μm

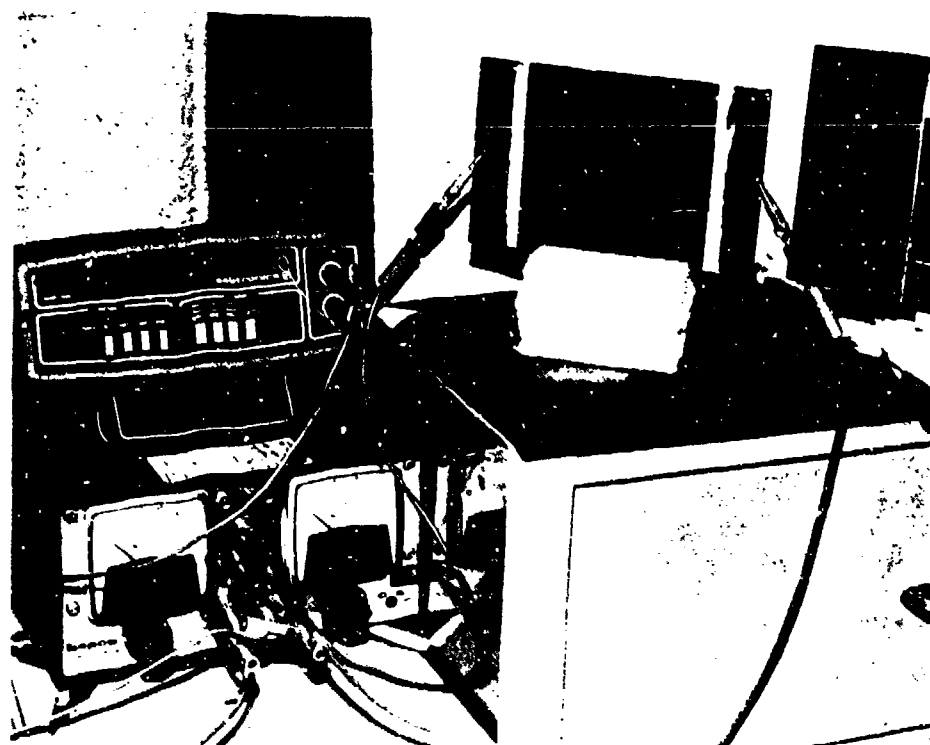


Figure 103: Experimental arrangement for relating current density and temperature.

layer of aquadac on a 1/16 inch thick plexiglass plate. Two parallel copper tape strips were placed on the surface and a thin connecting strip of silver paint was applied on the copper and aquadac surfaces overlapping the junction to assure that good electrical contact was made. The copper strip electrodes were connected to a Kepco Power Supply (Range 0-36V, 0-1.5A) and a digital ammeter (Sabtronics Model 2000). A plate of identical composite was then placed near the test plate (right side in Figure 103) to provide an ambient reference source of identical emissivity. Voltage levels were incrementally increased across the electrodes as the differential temperature levels between test and reference plates were determined using the Thermovision system. At each new total current level the system was allowed to reach steady state (about 15 minutes) before readings were taken. It was assumed that the current densities were uniformly distributed throughout the thin coatings.

The data was then fit to a quadratic function and plotted using a program called 'J vs T' found in Appendix D. A maximum likelihood routine was used to find the coefficients of the squared (V_{avg}) and linear (V_{2avg}) terms. The results for the two target

compositions are found in Figures 104 and 105. Now, on a point by point basis, knowing the differential temperature between an illuminated elemental area and the ambient condition the functional relation was easily solved for current density. Having the needed relationship to obtain current density, the problem of random errors associated with the interface remained.

A statistical procedure was developed to reduce the influence of random errors on the final matrix from which calculations were made. The IR data was accomplished with known sources of IR, such as overhead lights, extinguished, and a steady state heating pattern established. Approximately 10 minutes of illumination at approximately 10 mW/cm^2 at 937 MHz and approximately 15 mW/cm^2 at 2.45 GHz were used. Seven frames of data were collected for the statistical analysis in all cases. Sensitivity settings of one and two were used such that nearly full scale variation of \bar{E} isotherm units (0 to 9) existed on the surface but without being outside of the selected sensitivity window. Any spurious readings outside of the 0 to 9 range were not included in the averaging procedure. The remaining data was considered on an element by element basis. The values

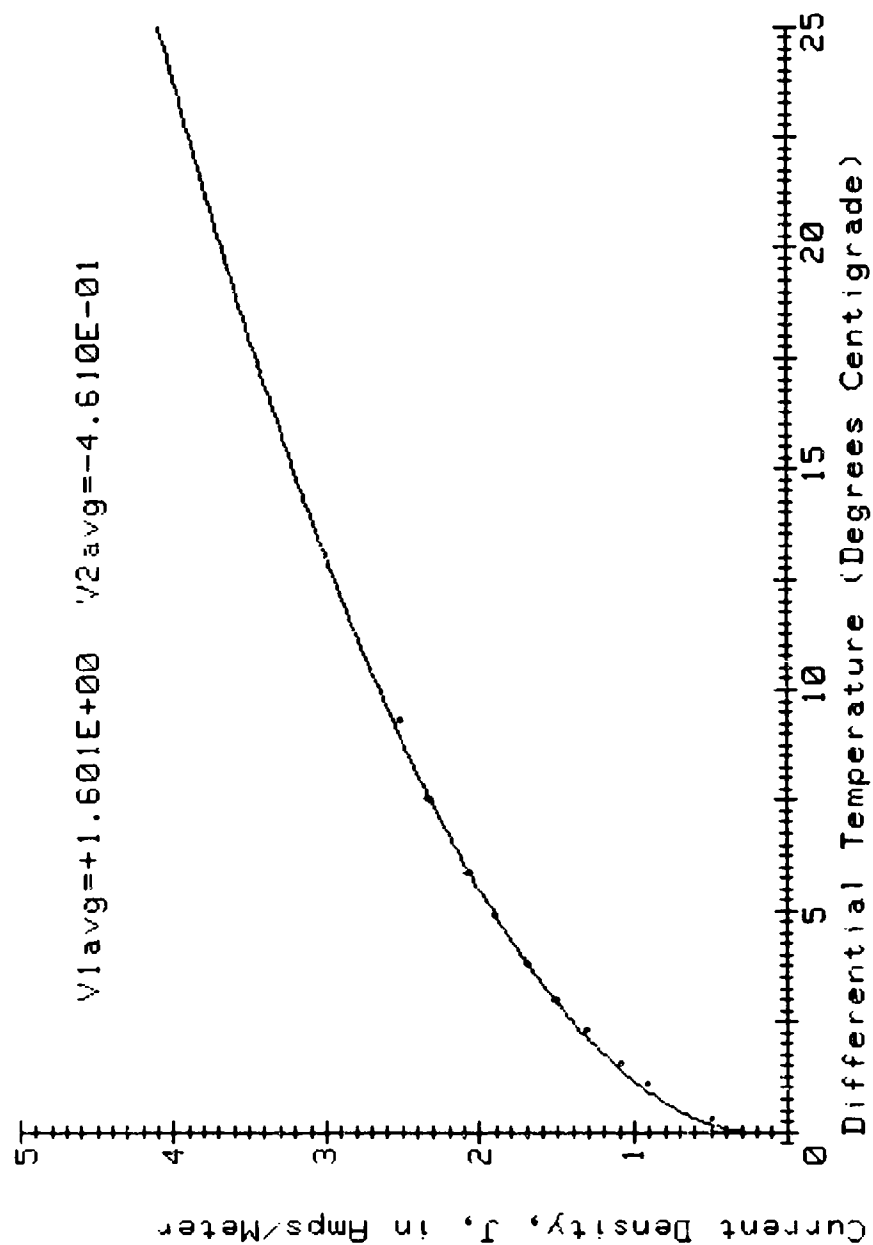


Figure 104: Quadratic curve fit for empirical J vs T
(carbon/paraffin over metal).

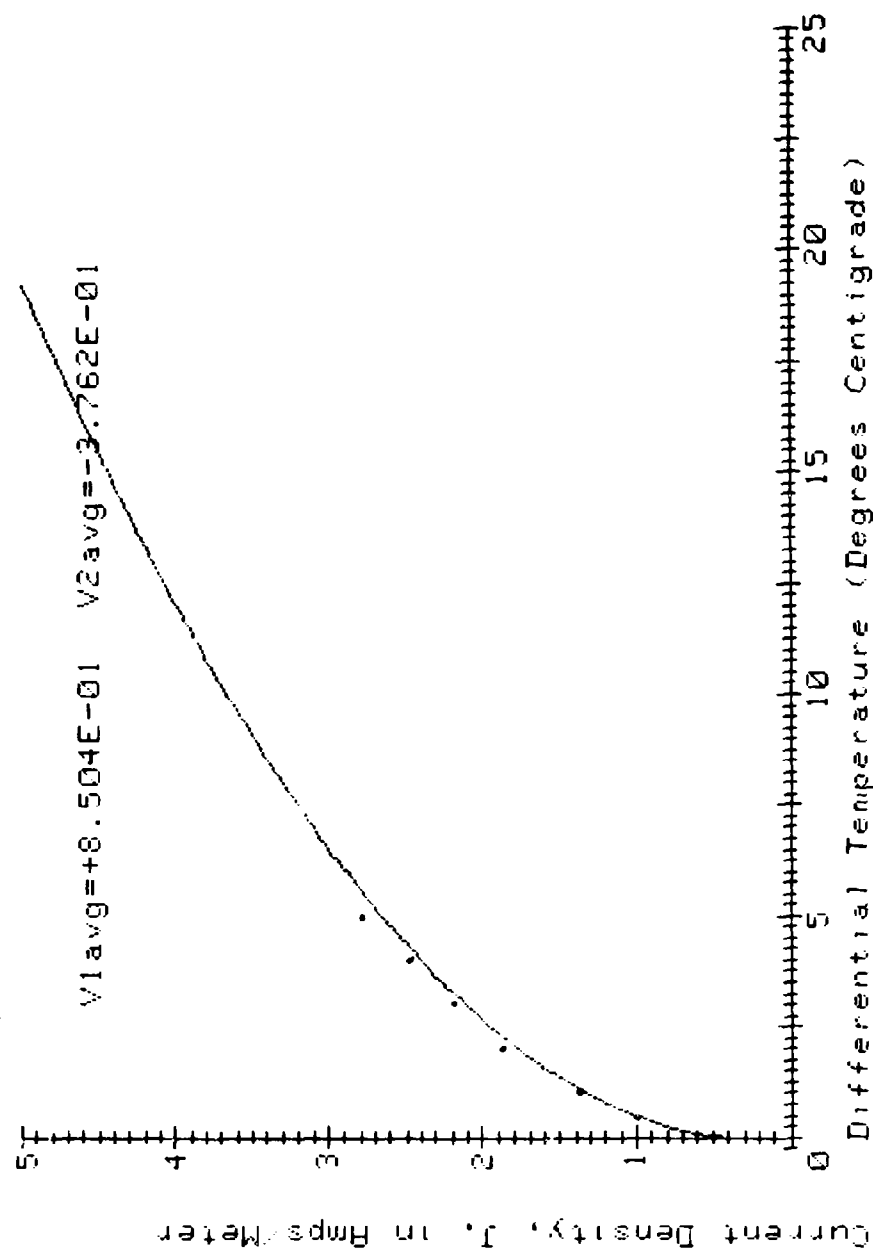


Figure 105: Quadratic curve fit for empirical J vs T (aquadac on plexiglass).

at an element position were averaged, a standard deviation was taken and points outside of one standard deviation were discarded. Thus, a new mean was computed from the remaining values and the element was now assigned this new mean for the "FINAL" matrix. This procedure is the basis of the program called 'IRSTAT' found in Appendix D.

Results

From the statistical procedure the remaining matrix or "FINAL" matrix could be transformed to a temperature matrix or a current matrix using the previously discussed development which, along with some graphics routines, comprise the basis of a program called "MEGAIR" found in Appendix D.

All electric sizes are presented for the composition of carbon/paraffin over metal. Only the .50 and 1.0 wavelength disks and square plates are examined for the aquadac on plexiglass case. The digital presentation in numbers for the temperature and current matrices and complete profile matrices for the illuminated, temperature, and current matrices are given for the 1.0 wavelength square plate for carbon/paraffin over metal.

The depicted profiles are IR obtained matrix rows that correspond to the horizontal scans of the magnetic field probe given in Chapter V. The key is as follows:

Upper - dotted line (·····)

Middle - broken line (—·—·—·—)

Lower - solid line (———)

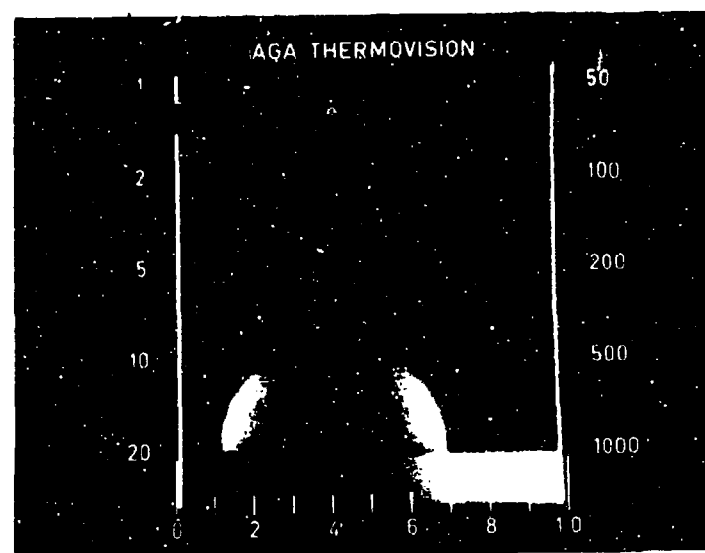


Figure 106: Thermogram for an illuminated .38 wavelength circular disk - carbon/paraffin over metal.

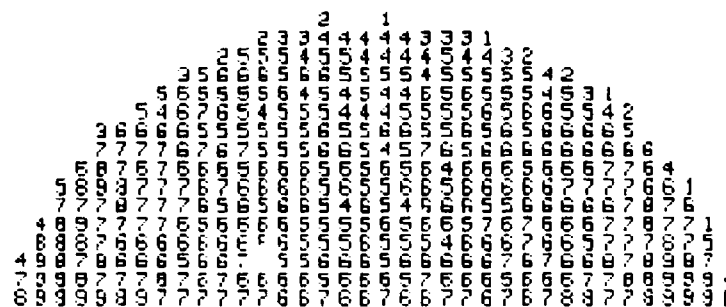


Figure 107: Digitized thermovision data for .38 wavelength circular disk - carbon/paraffin over metal.

FINAL .38 LAMBDA DISK

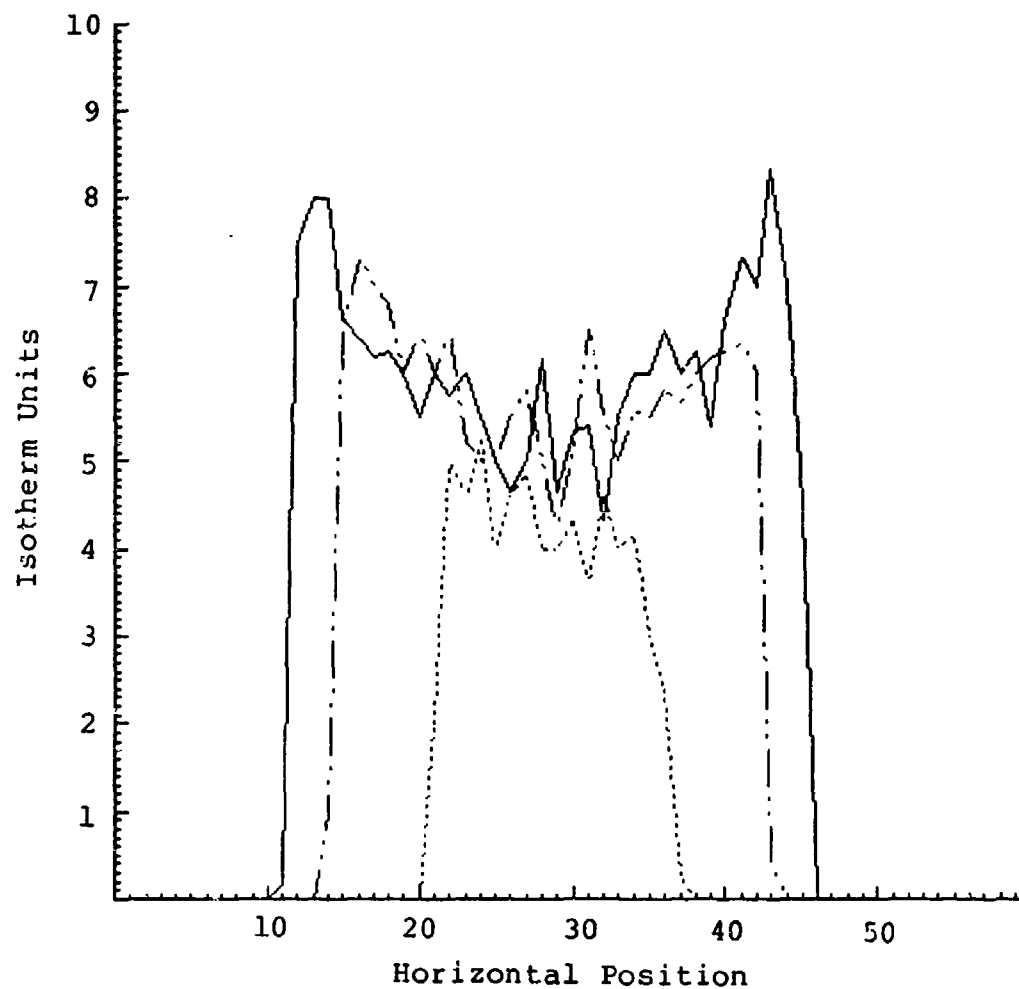


Figure 108: Thermovision data profiles for
.38 wavelength circular disk -
carbon/paraffin over metal.

TEMP .38 LAMBDA DISK

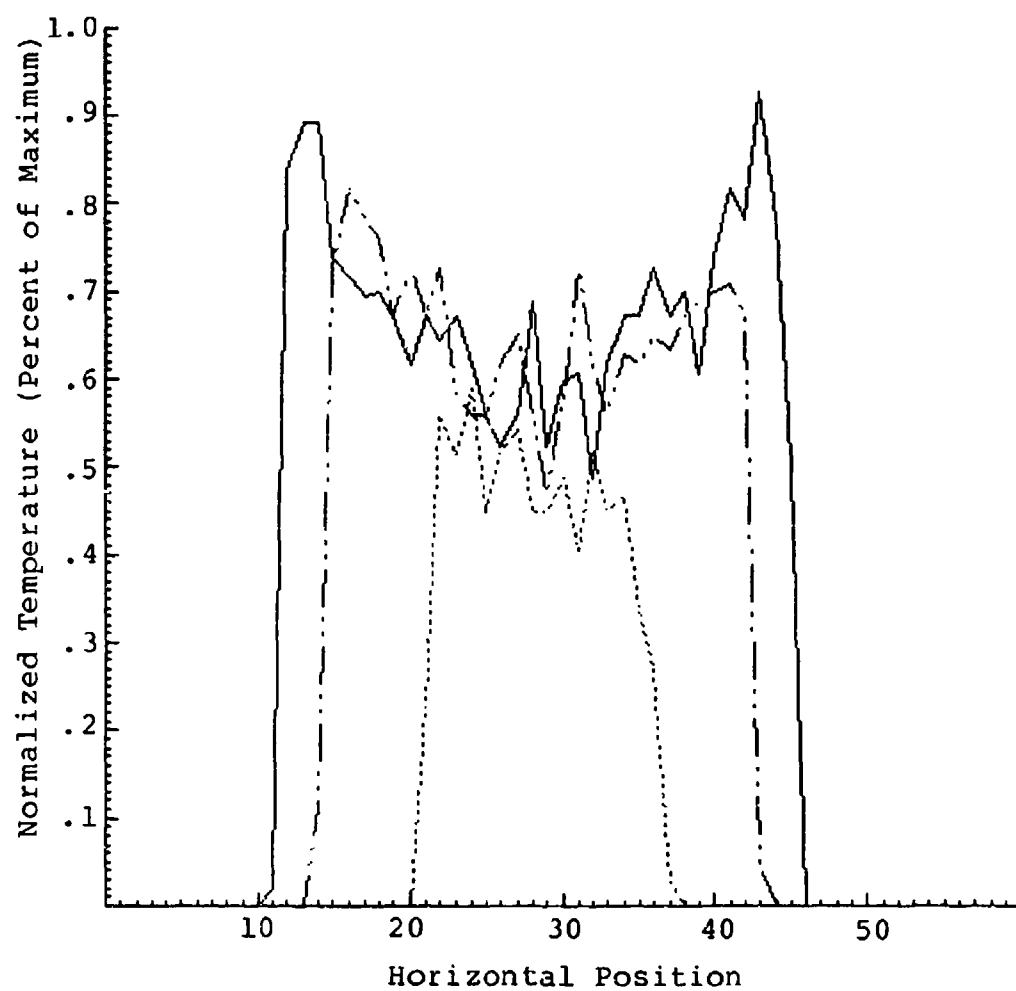


Figure 109: Temperature profiles for .38 wavelength circular disk - carbon/paraffin over metal.

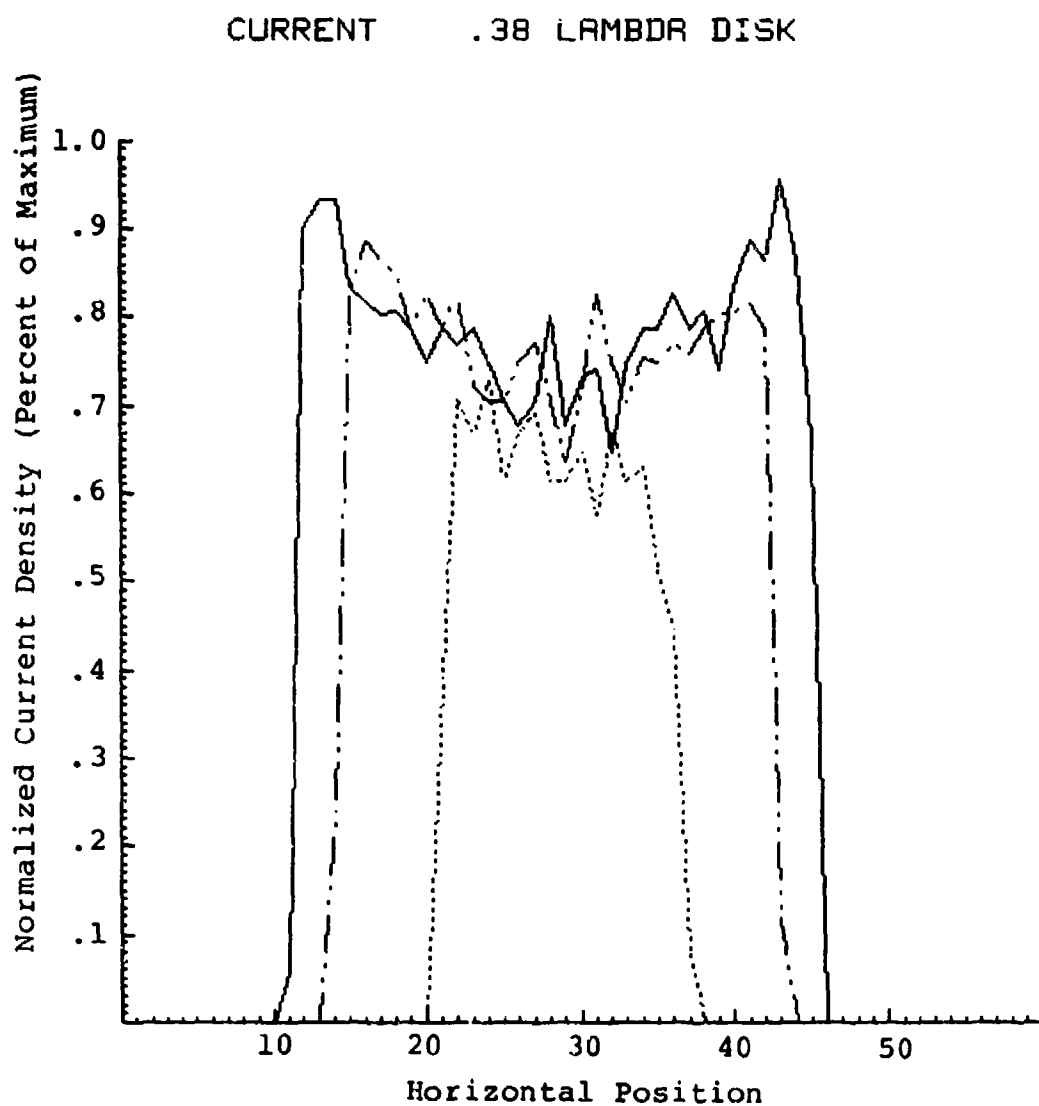


Figure 110: Infrared obtained current profiles for .38 wavelength circular disk - carbon/paraffin over metal.

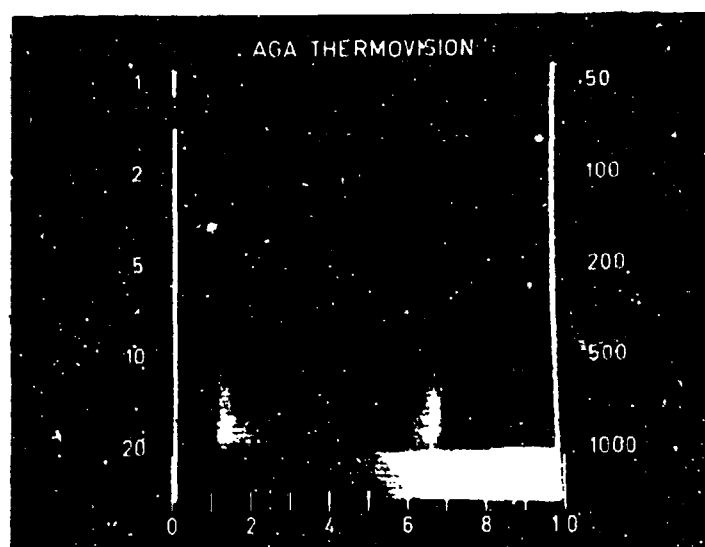


Figure 111: Thermogram for an illuminated .38 wavelength square plate - carbon/paraffin over metal.

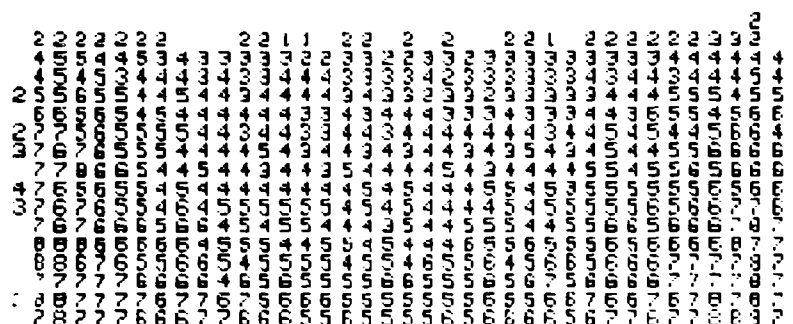


Figure 112: Digitized thermovision data for .38 wavelength square plate - carbon/paraffin over metal.

FINAL .38 LAMBDA SQUARE PLATE

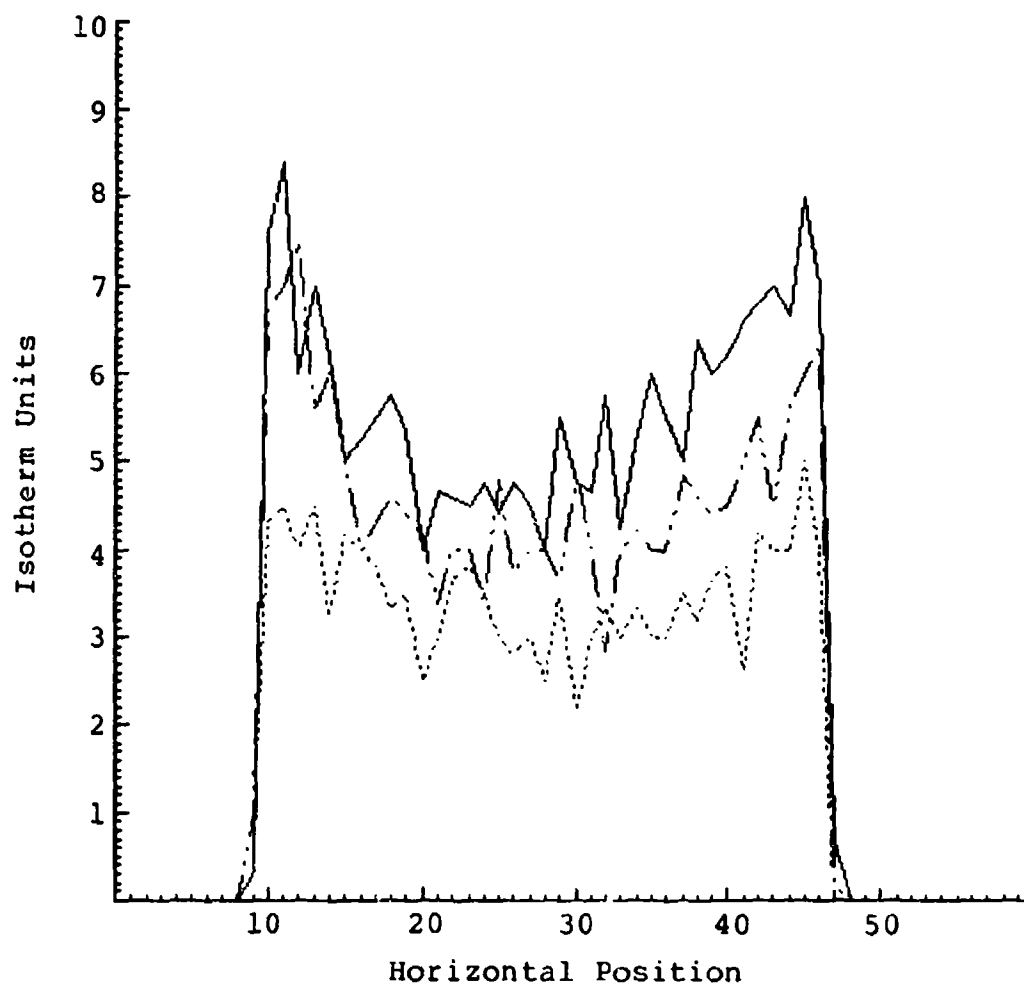


Figure 113: Thermovision data profiles for .38 wavelength square plate - carbon/paraffin over metal.

TEMP .38 LAMBDA SQUARE PLATE

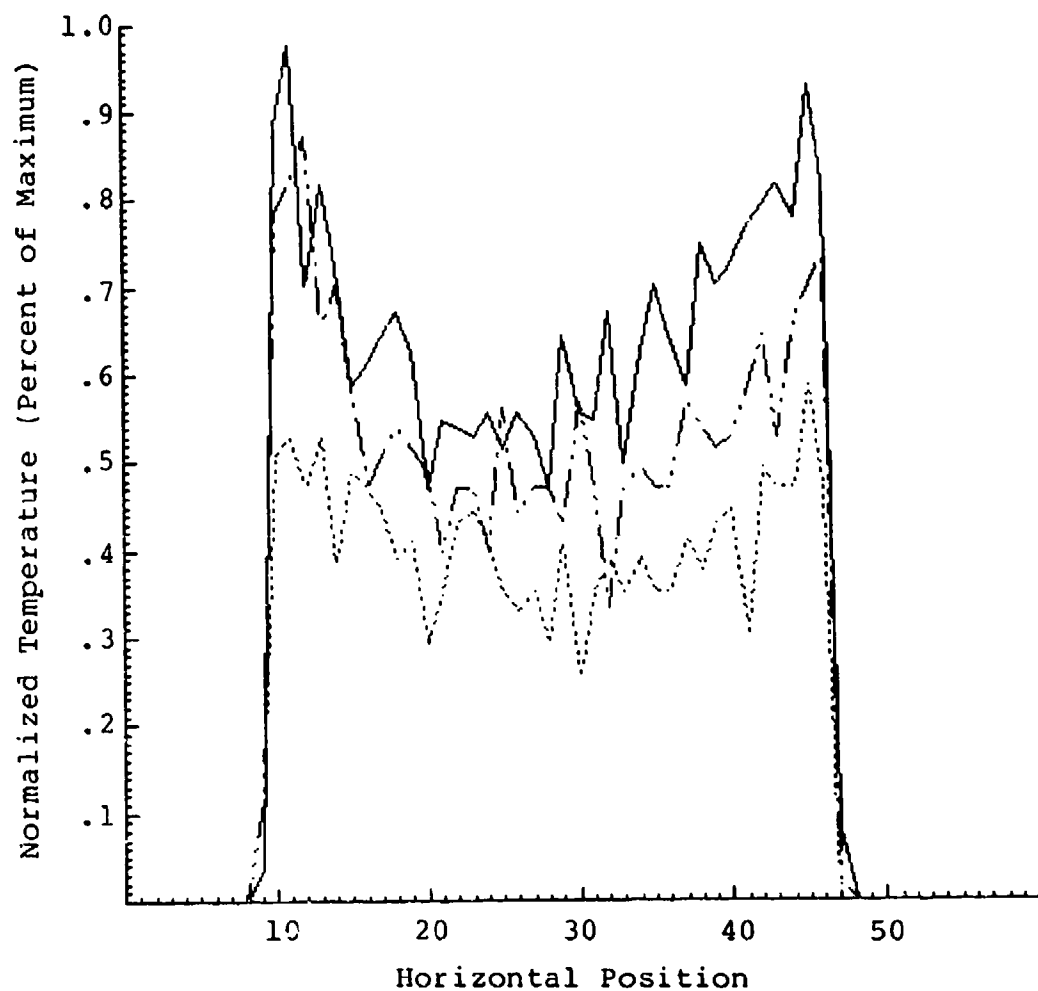


Figure 114: Temperature profiles for .38 wavelength square plate - carbon/paraffin on metal.

CURRENT .38 LAMBDA SQUARE PLATE

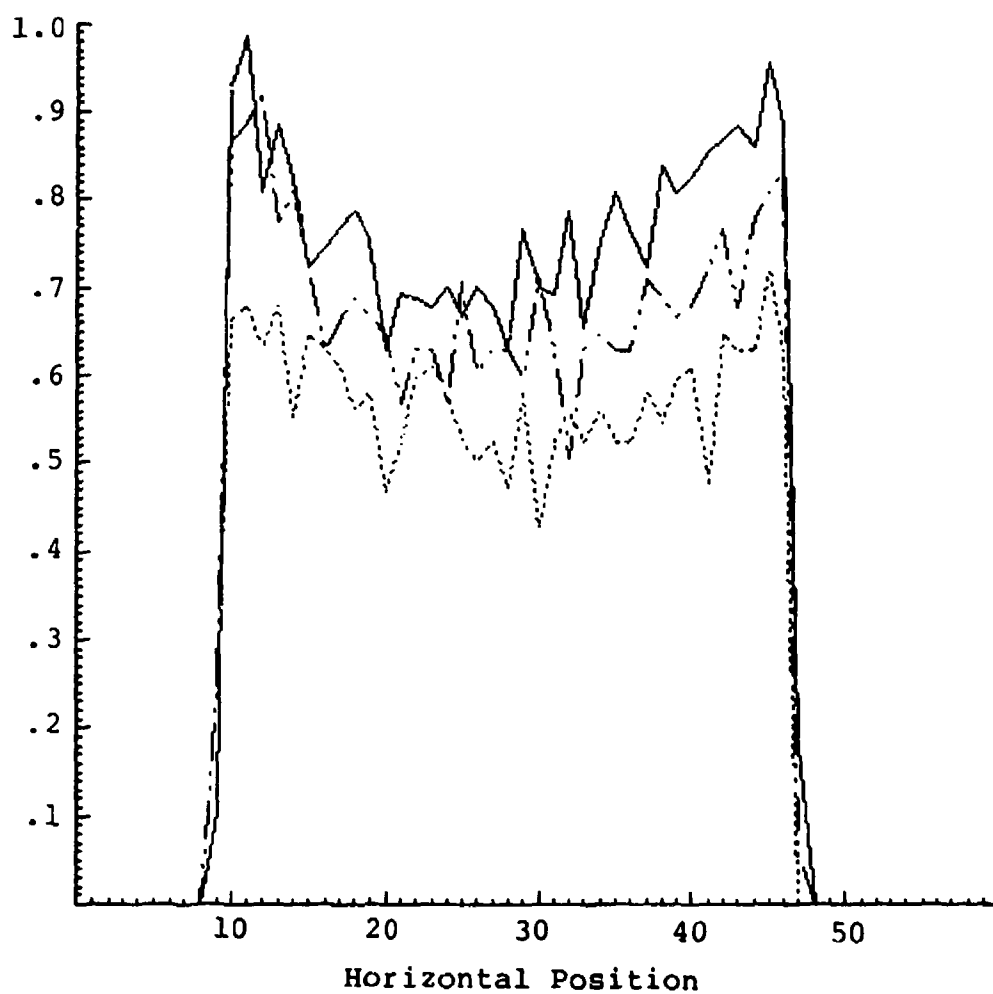


Figure 115: Infrared obtained current profiles for .38 wavelength square plate - carbon/paraffin on metal.

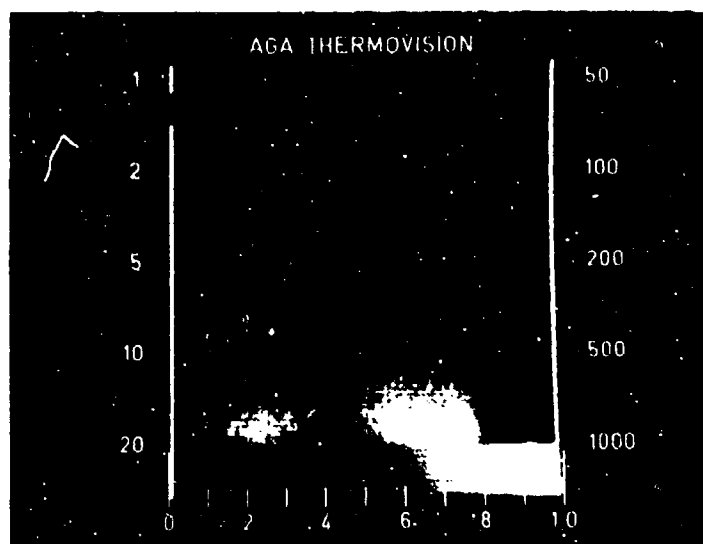


Figure 116: Thermogram for an illuminated .50 wavelength circular disk - carbon/paraffin over metal.

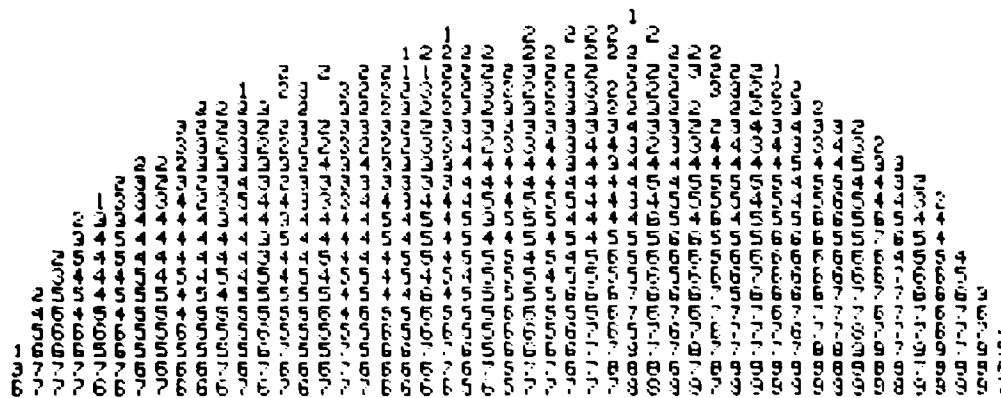


Figure 117: Digitized thermovision data for .50 wavelength circular disk - carbon/paraffin over metal.

FINAL .50 LAMBDA DISK

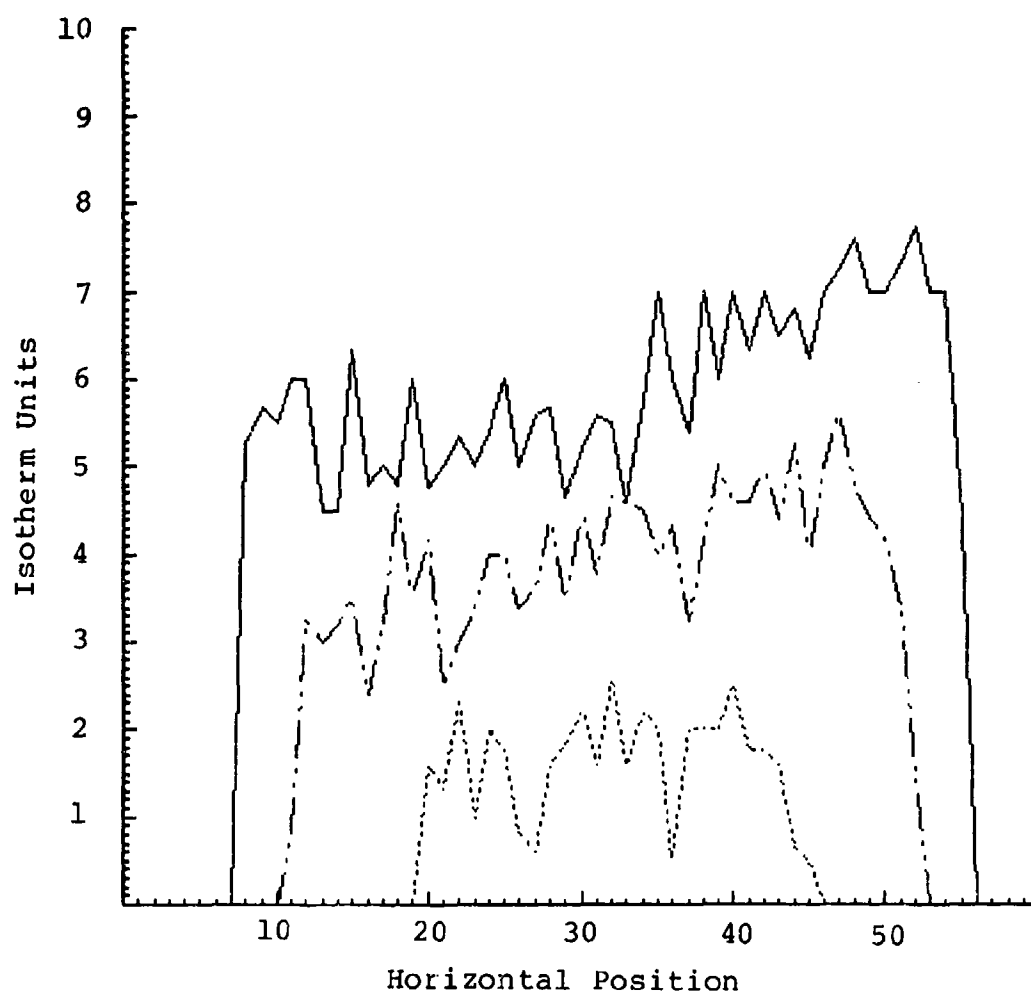


Figure 118: Thermovision data profiles for .50 wavelength circular disk - carbon/paraffin over metal.

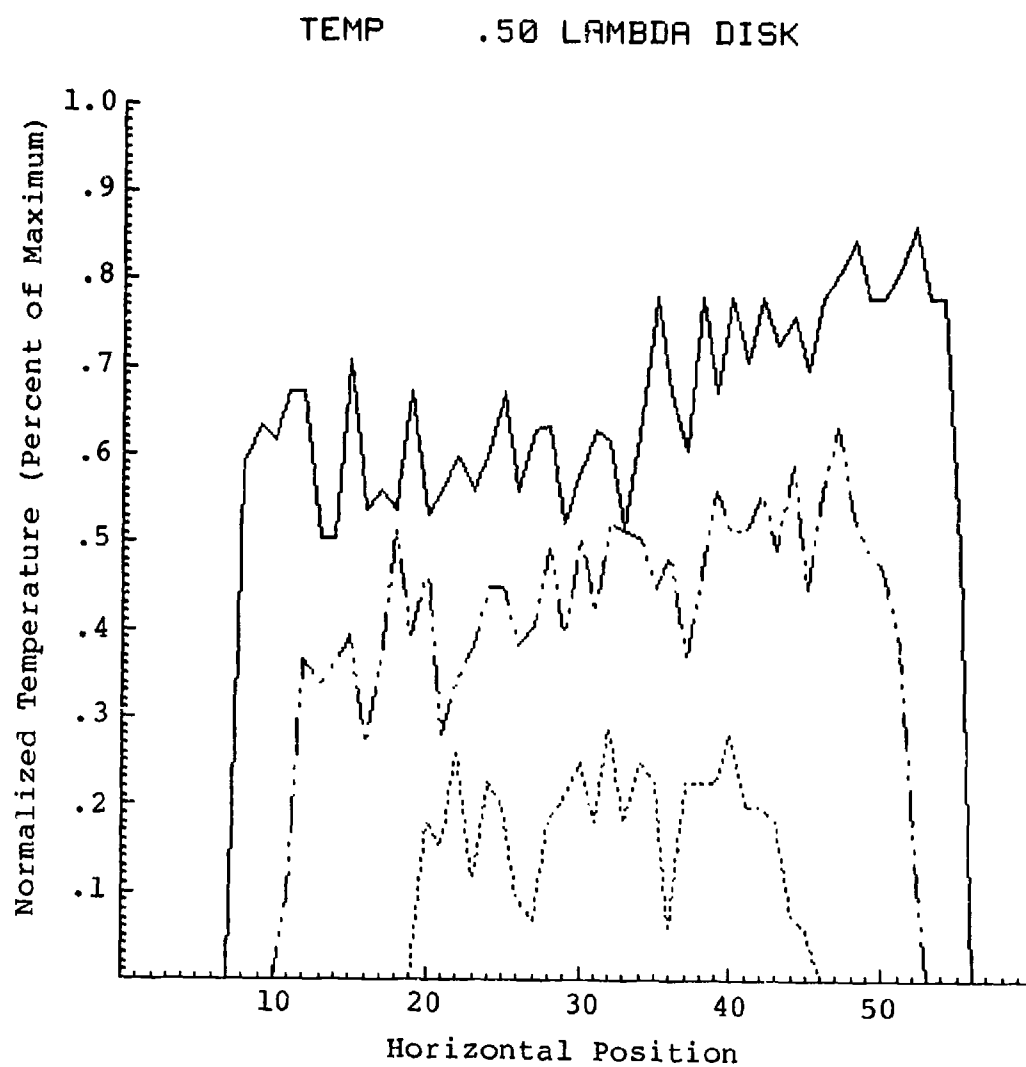


Figure 119: Temperature profiles for .50 wavelength circular disk - carbon/paraffin over metal.

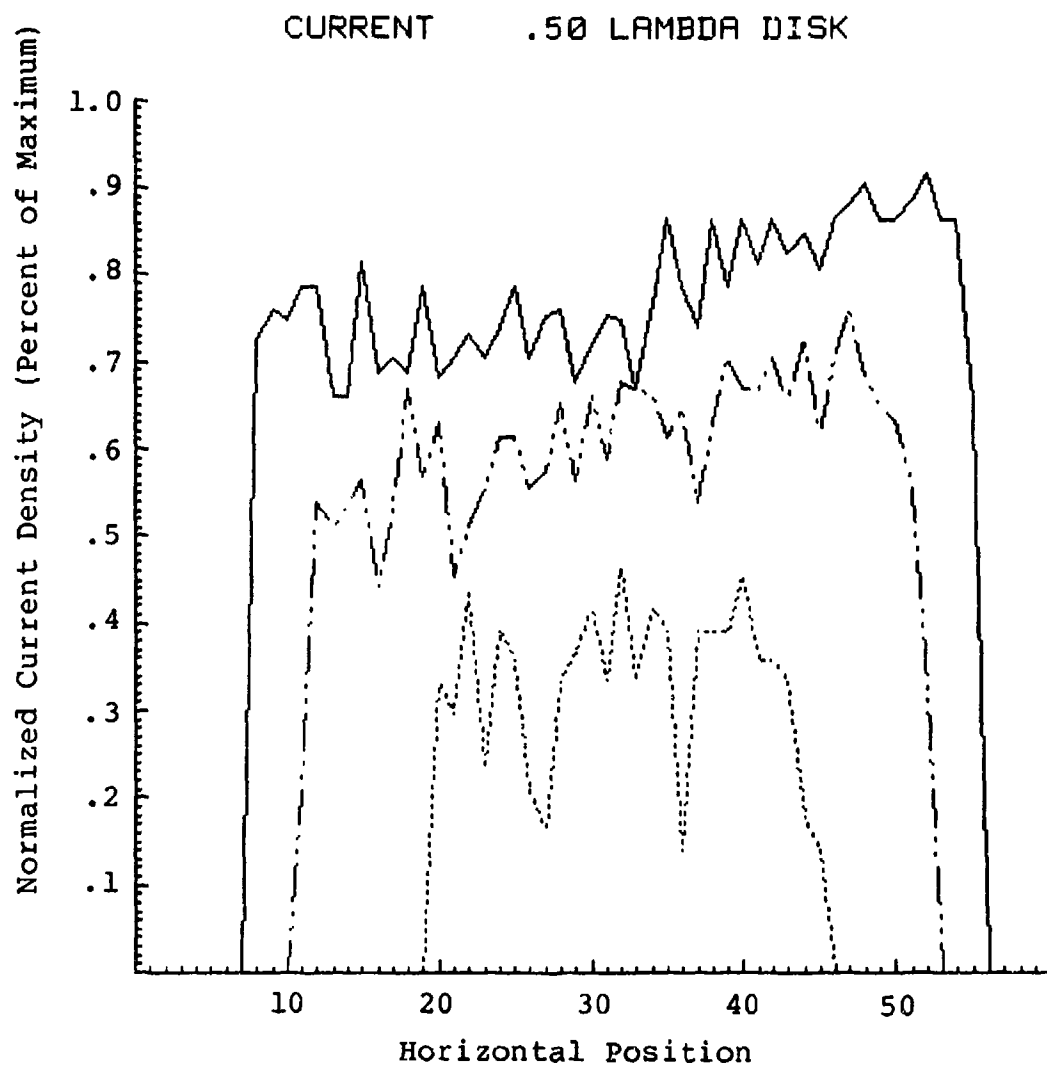


Figure 120: Infrared obtained current profiles for .50 wavelength circular disk - carbon/paraffin over metal.

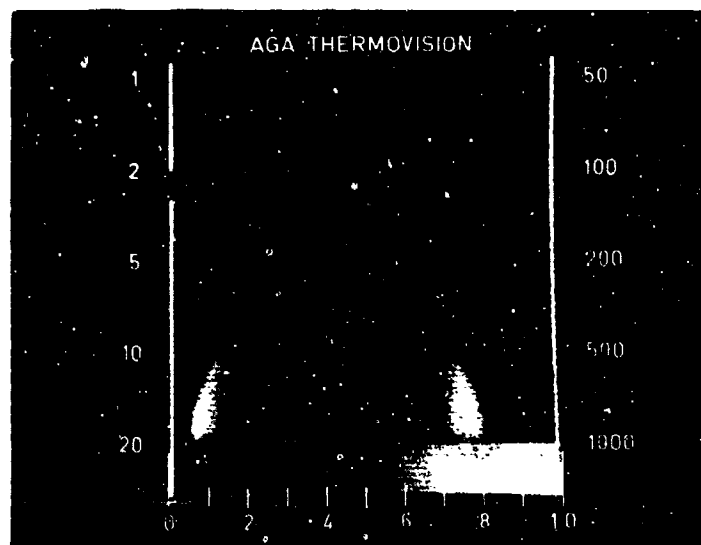


Figure 121: Thermogram for an illuminated .50 wavelength circular disk - aquadac on plexiglass.



Figure 122: Digitized thermovision data for .50 wavelength circular disk - aquadac on plexiglass.

FINAL .50 LAMBDA DISK *

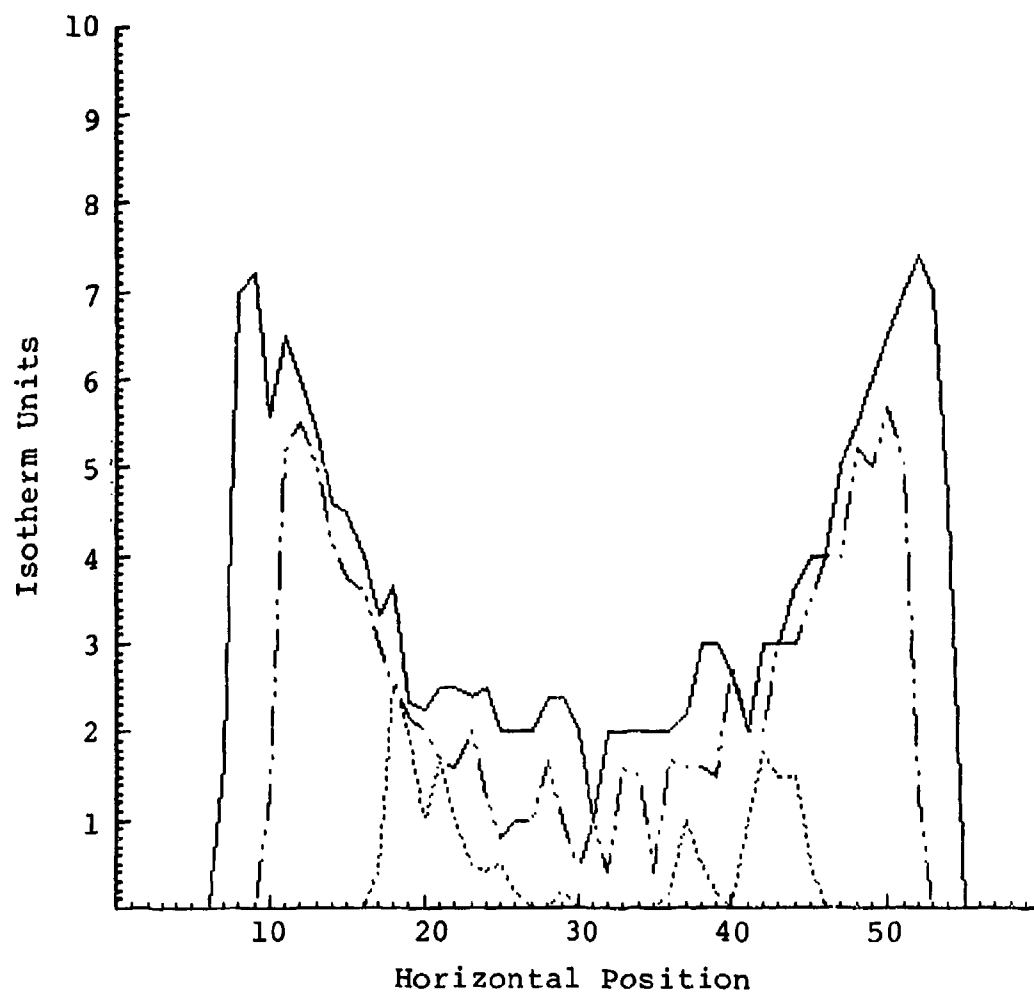


Figure 123: Thermovision data profiles for .50 wavelength circular disk - aquadac on plexiglass.

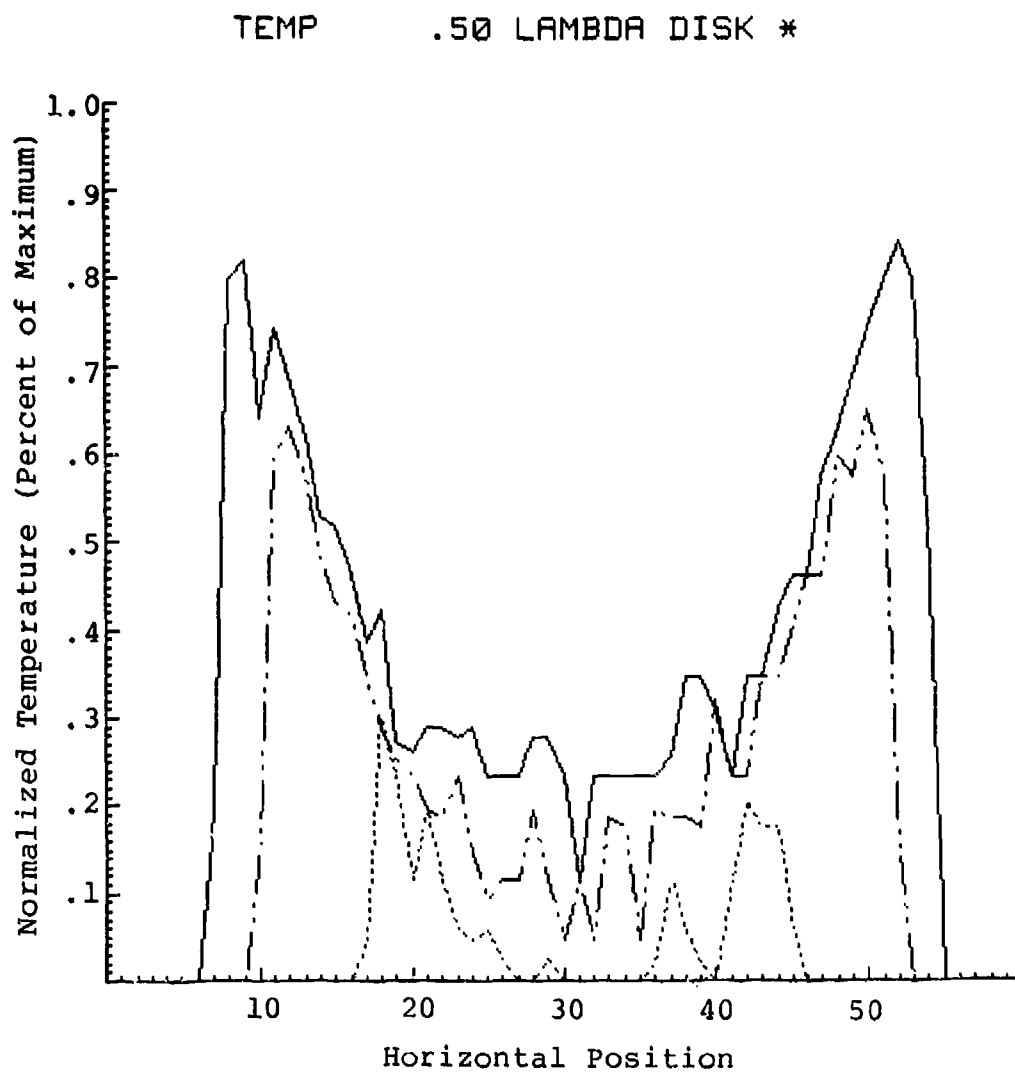


Figure 124: Temperature profiles for
.50 wavelength circular
disk - aquadac on
plexiglass.

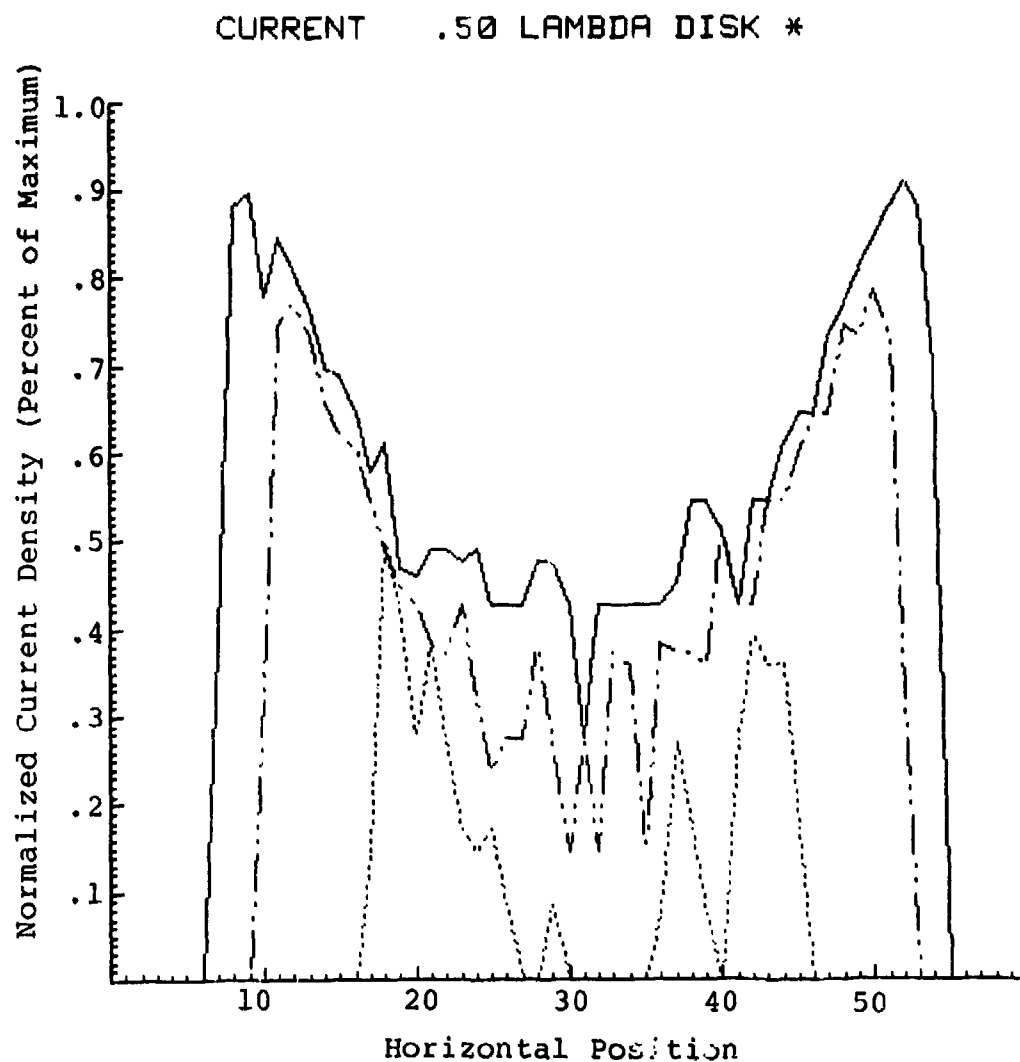


Figure 125 Infrared obtained current profiles for .50 circular disk - aquadac on plexiglass.

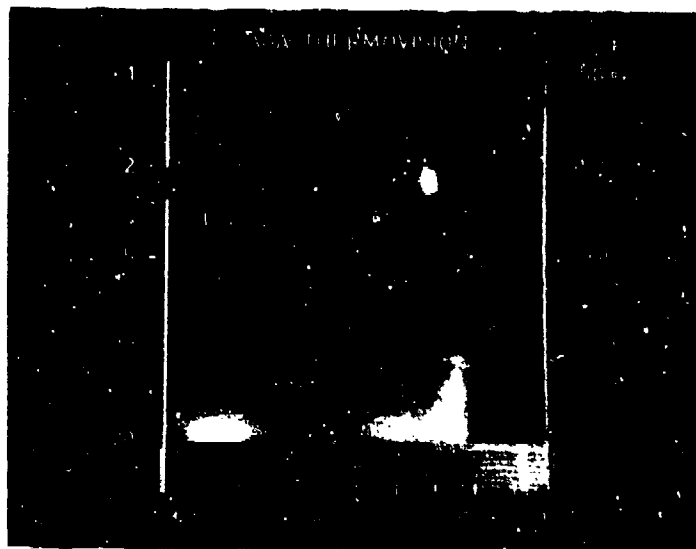


Figure 126: Thermogram for an illuminated .50 wavelength square plate - carbon/paraffin over metal.

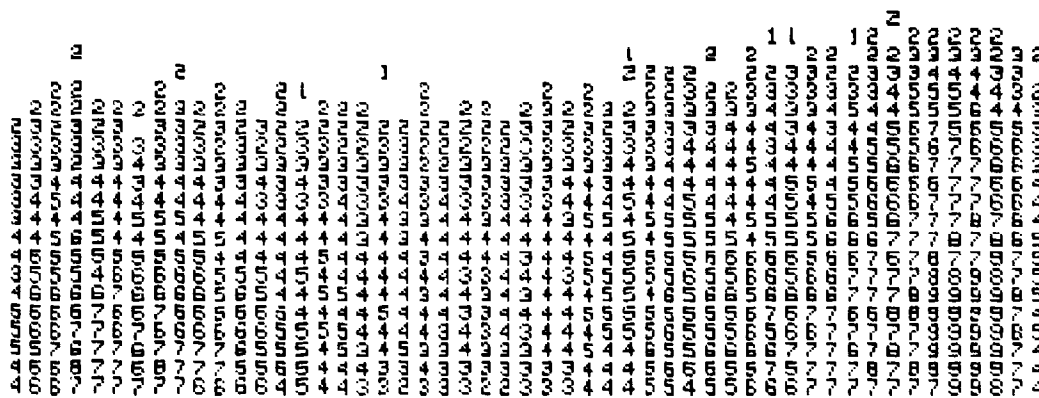


Figure 127: Digitized thermovision data for .50 wavelength square plate - carbon/paraffin over metal.

FINAL .50 LAMBDA SQUARE PLATE

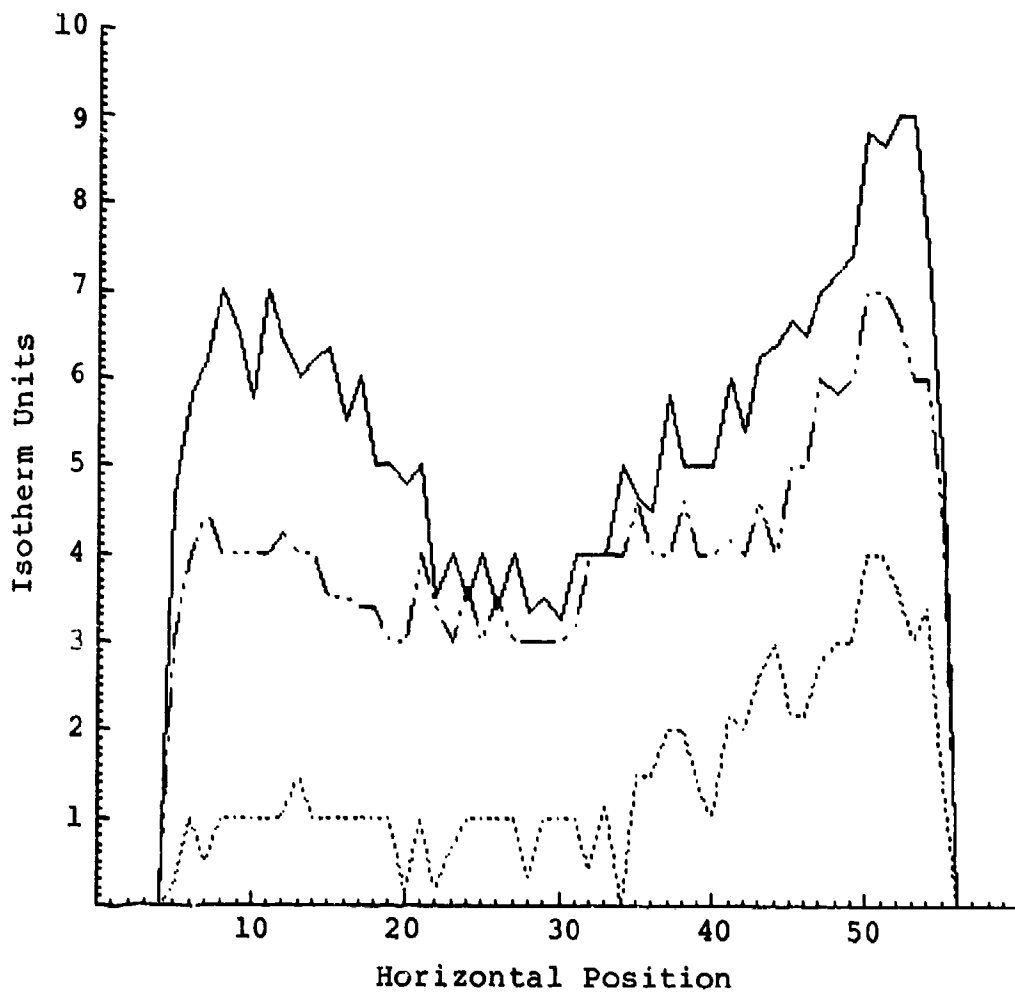


Figure 128: Thermovision data profiles for .50 wavelength square plate - carbon/paraffin over metal.

TEMP .50 LAMBDA SQUARE PLATE

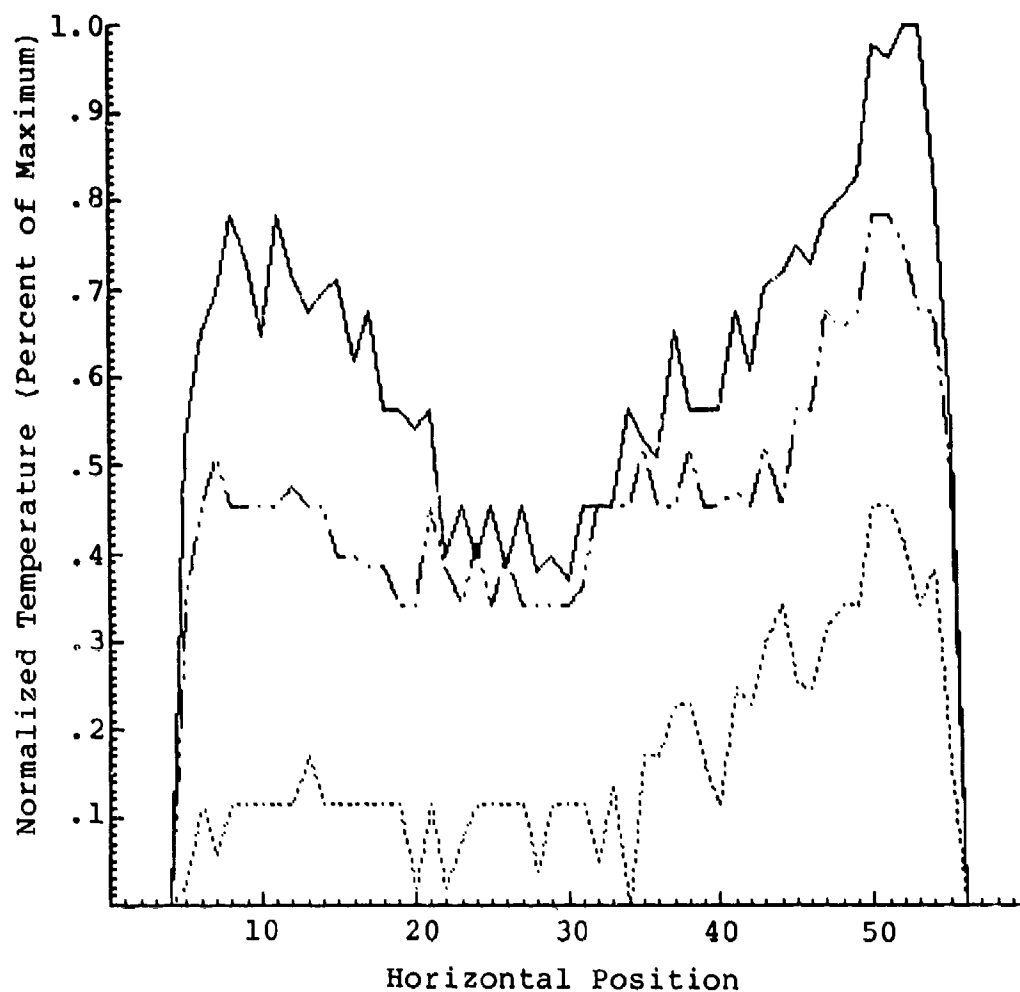


Figure 129: Temperature profiles for
.50 wavelength square
plate - carbon/paraffin
over metal.

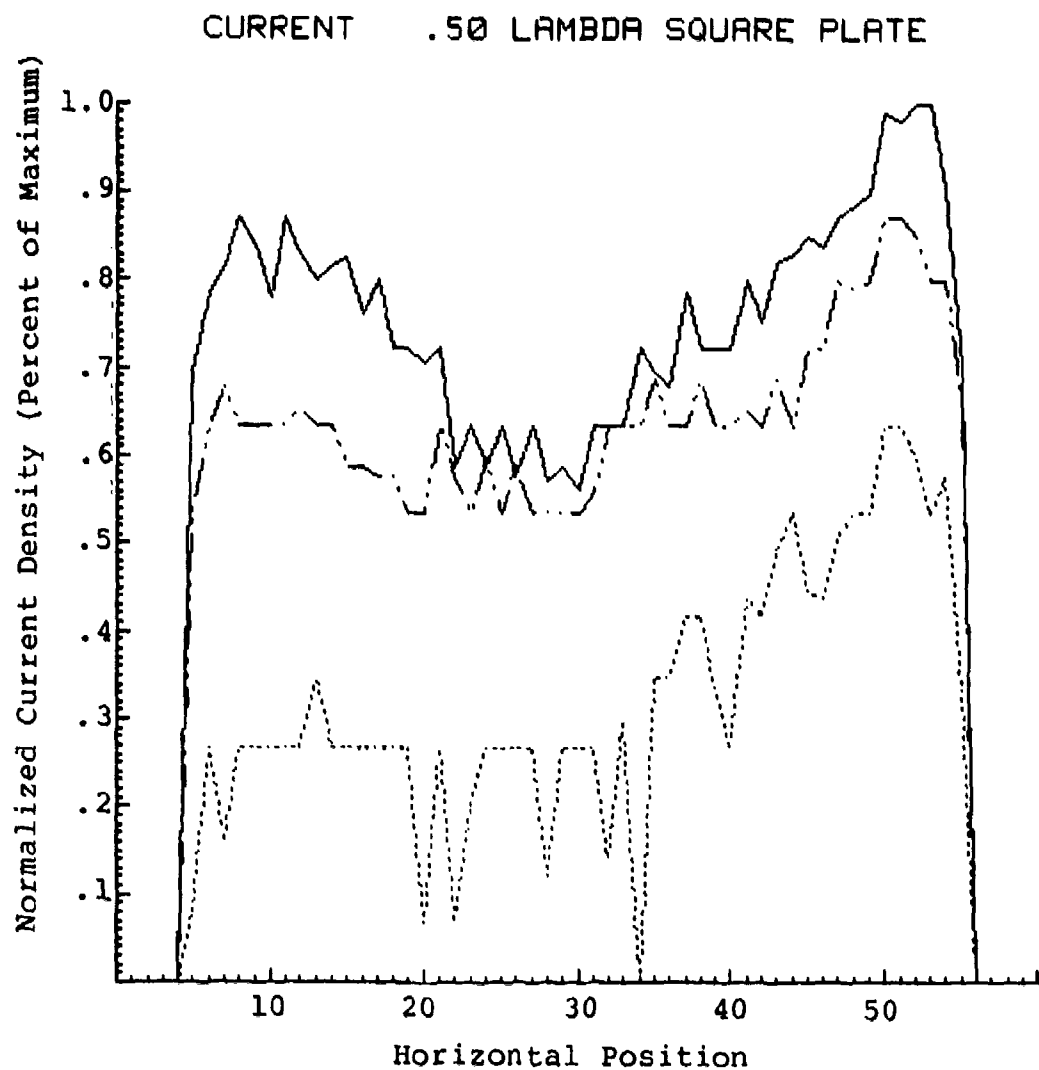


Figure 130: Infrared obtained current profiles for .50 wavelength square plate - carbon/paraffin over metal.

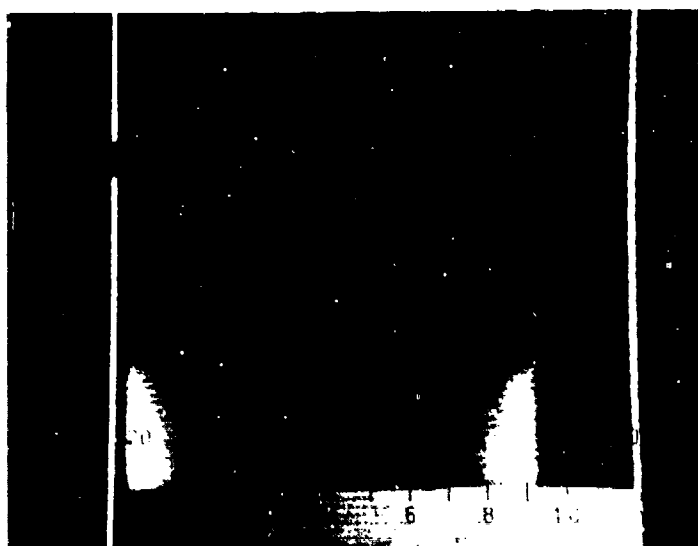


Figure 131: Thermogram for an illuminated .50 wavelength square plate - aquadac on plexiglass.

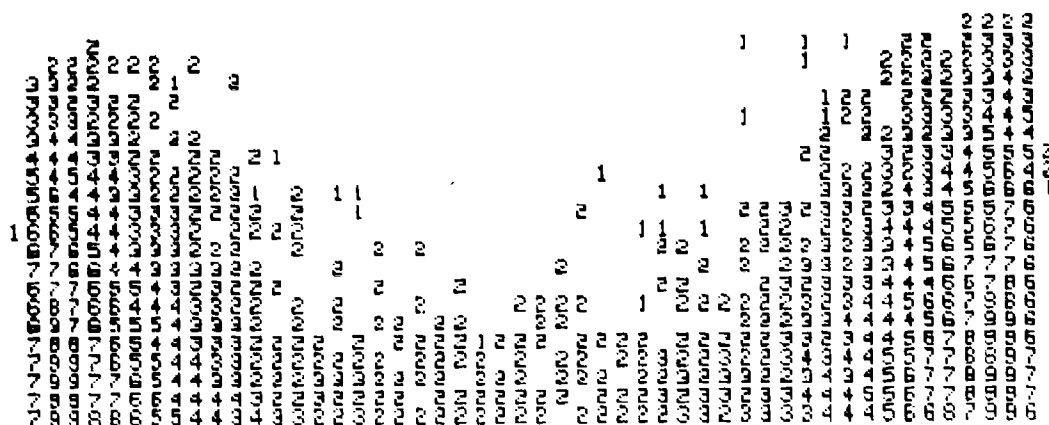


Figure 132: Digitized thermovision data for .50 wavelength square plate - aquadac on plexiglass.

FINAL .50 LAMBDA SQUARE PLATE *

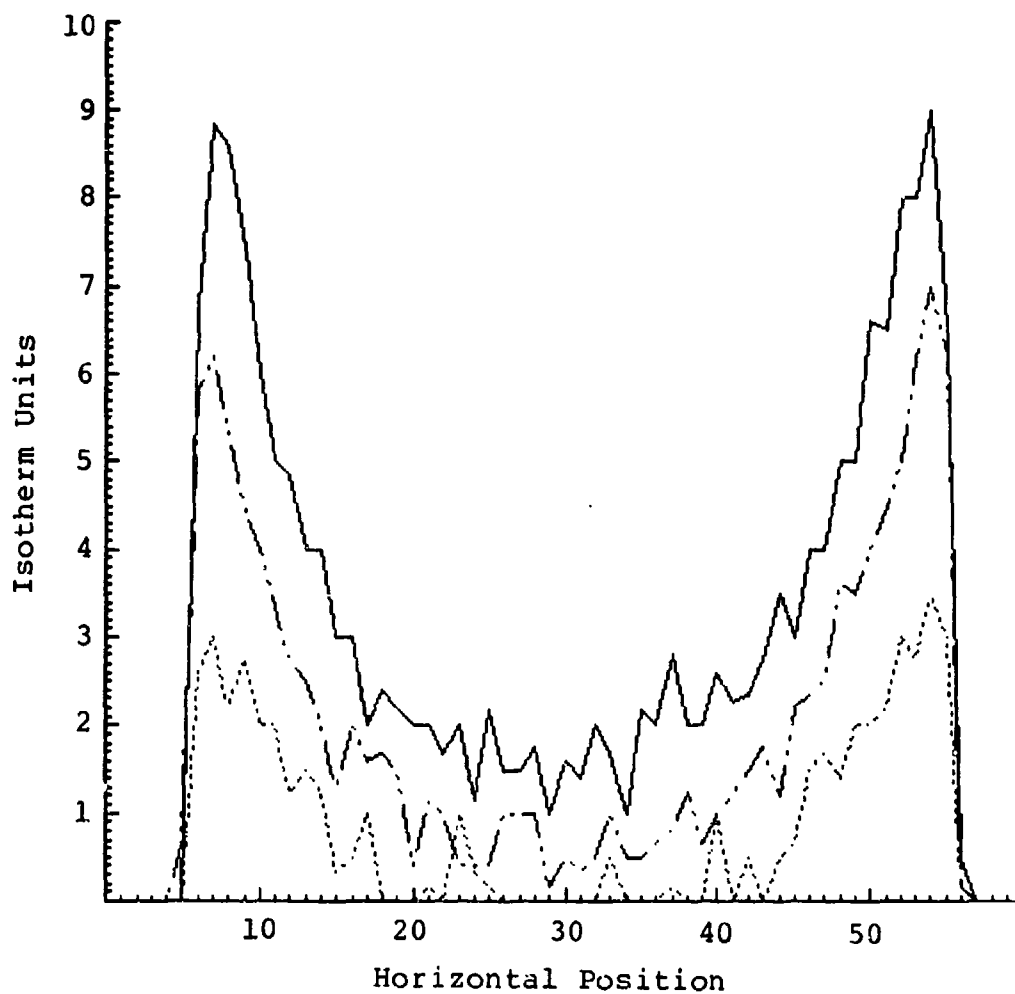


Figure 133: Thermovision data profiles for .50 wavelength square plate - aquadac on plexiglass.

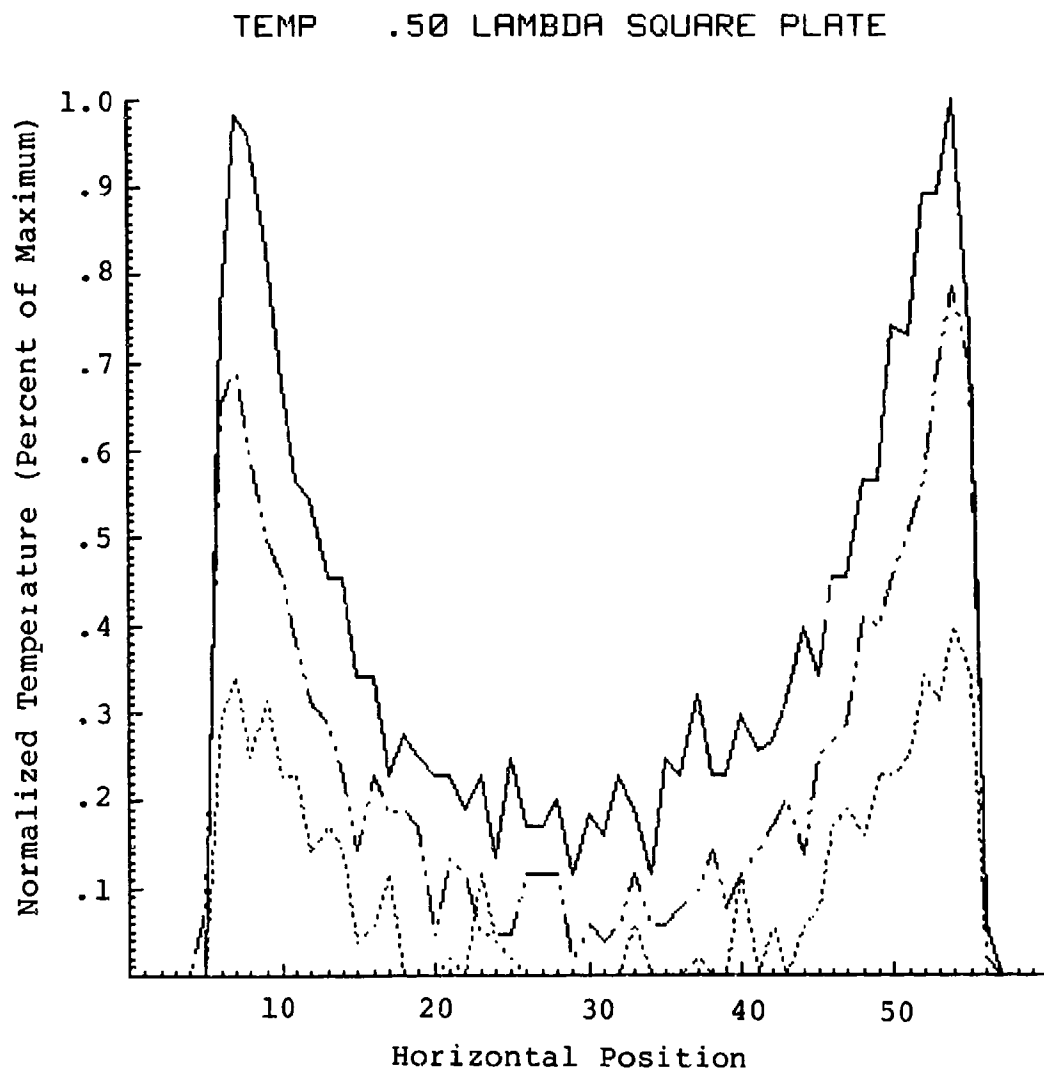


Figure 134: Temperature profiles for
.50 wavelength square
plate - aquadac on
plexiglass.

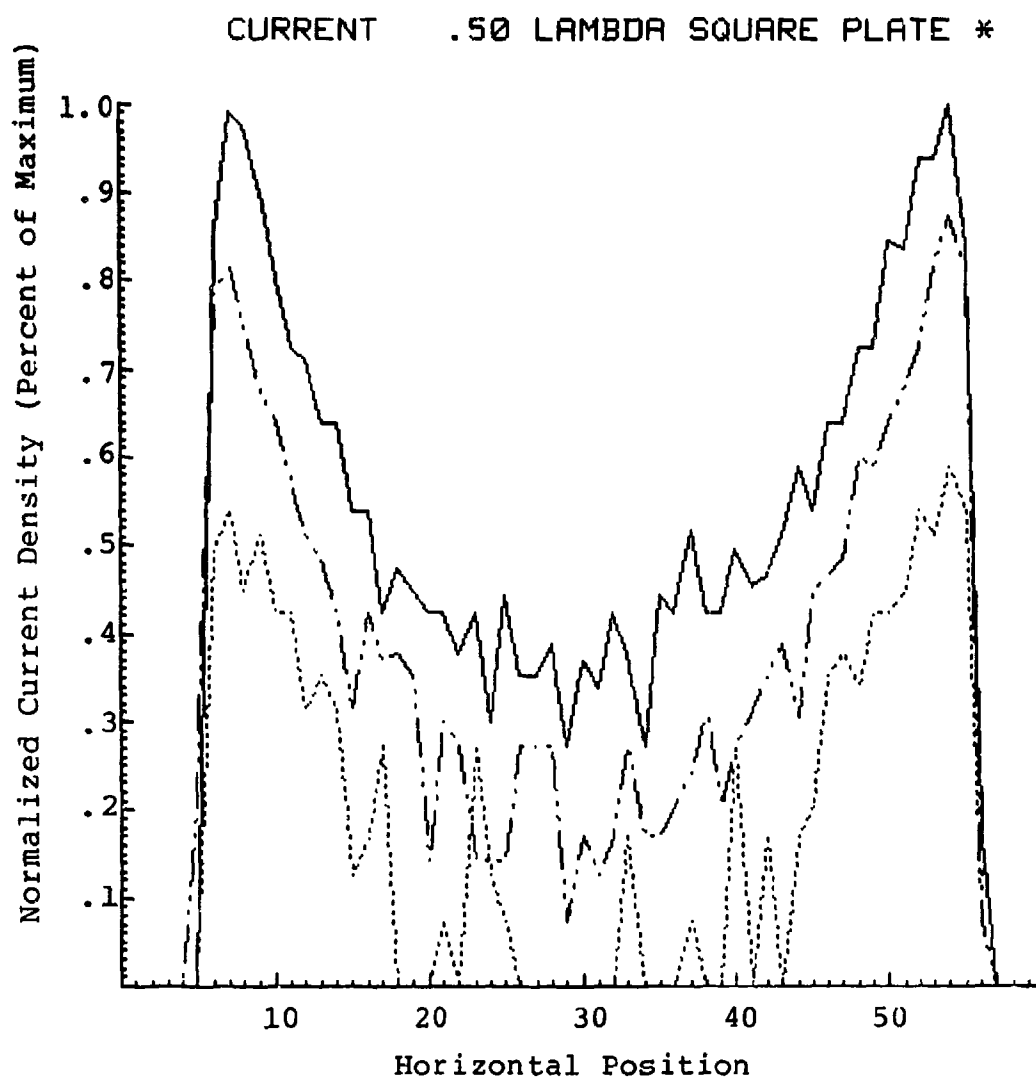


Figure 135: Infrared obtained current profiles for .50 wavelength square plate - aquadac on plexiglass.

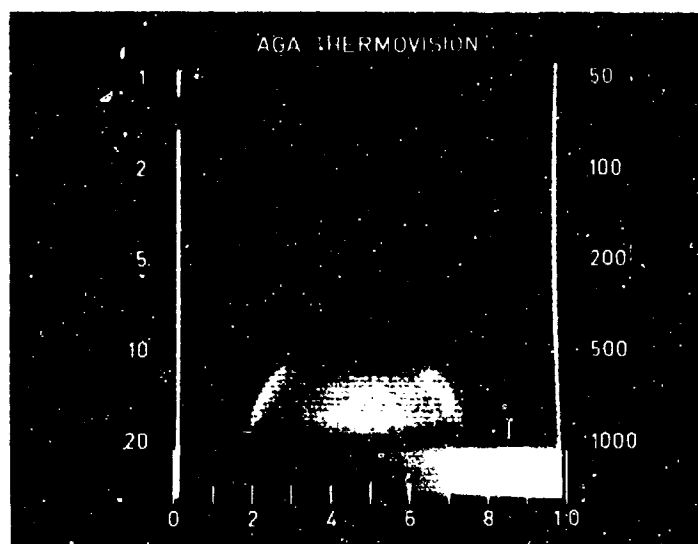


Figure 136: Thermogram for an illuminated 1.0 wavelength circular disk - carbon/paraffin over metal.

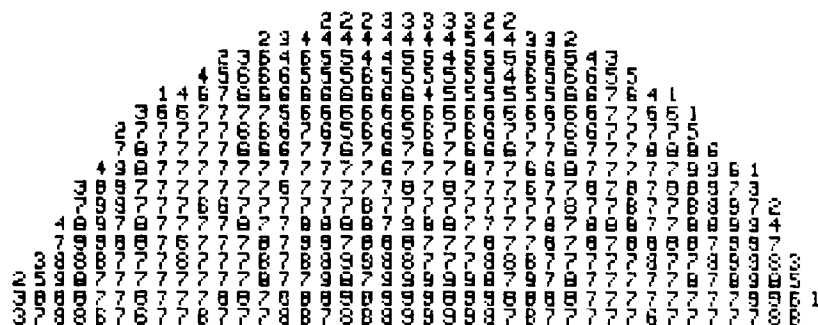


Figure 137: Digitized thermovision data for 1.0 wavelength circular disk - carbon/paraffin over metal.

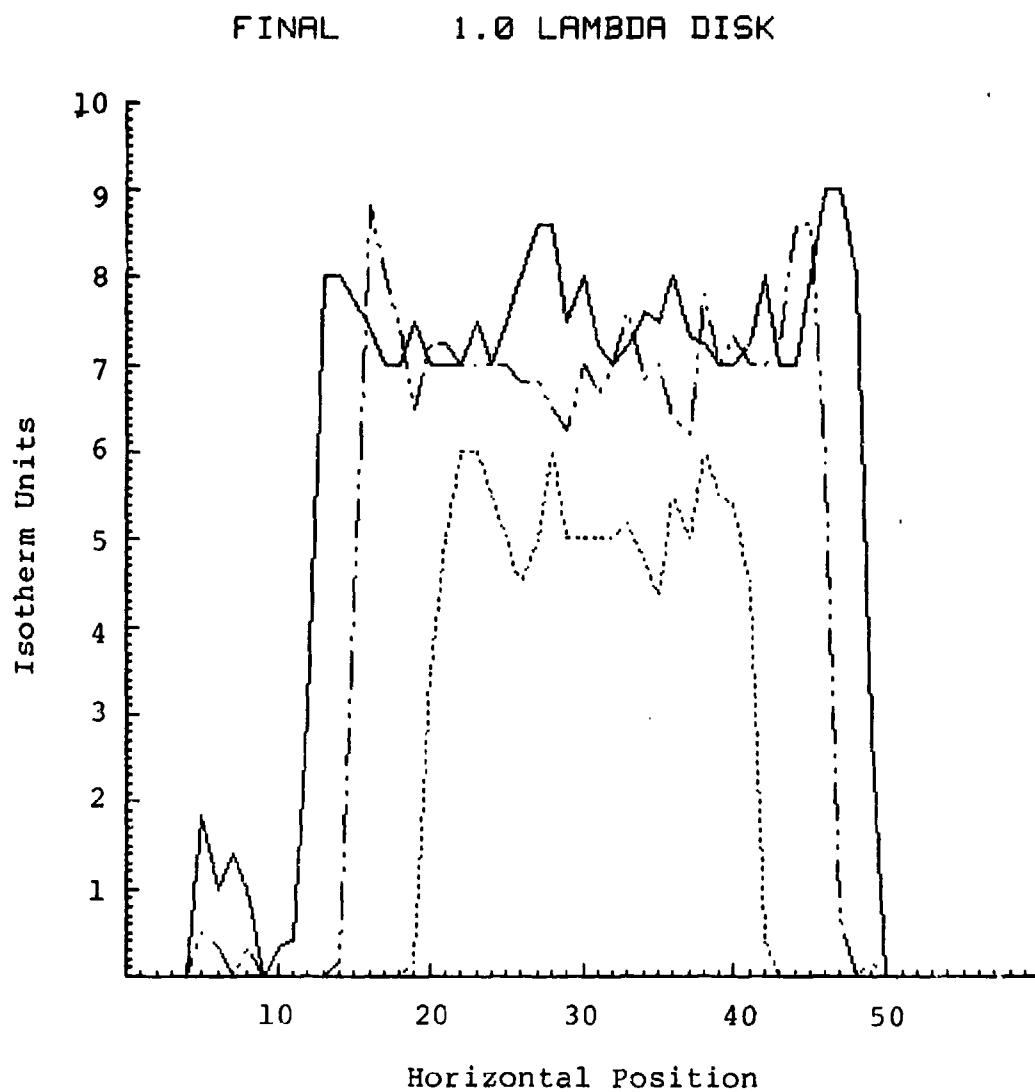


Figure 138: Thermovision data profiles for 1.0 wavelength circular disk - carbon/paraffin on metal.

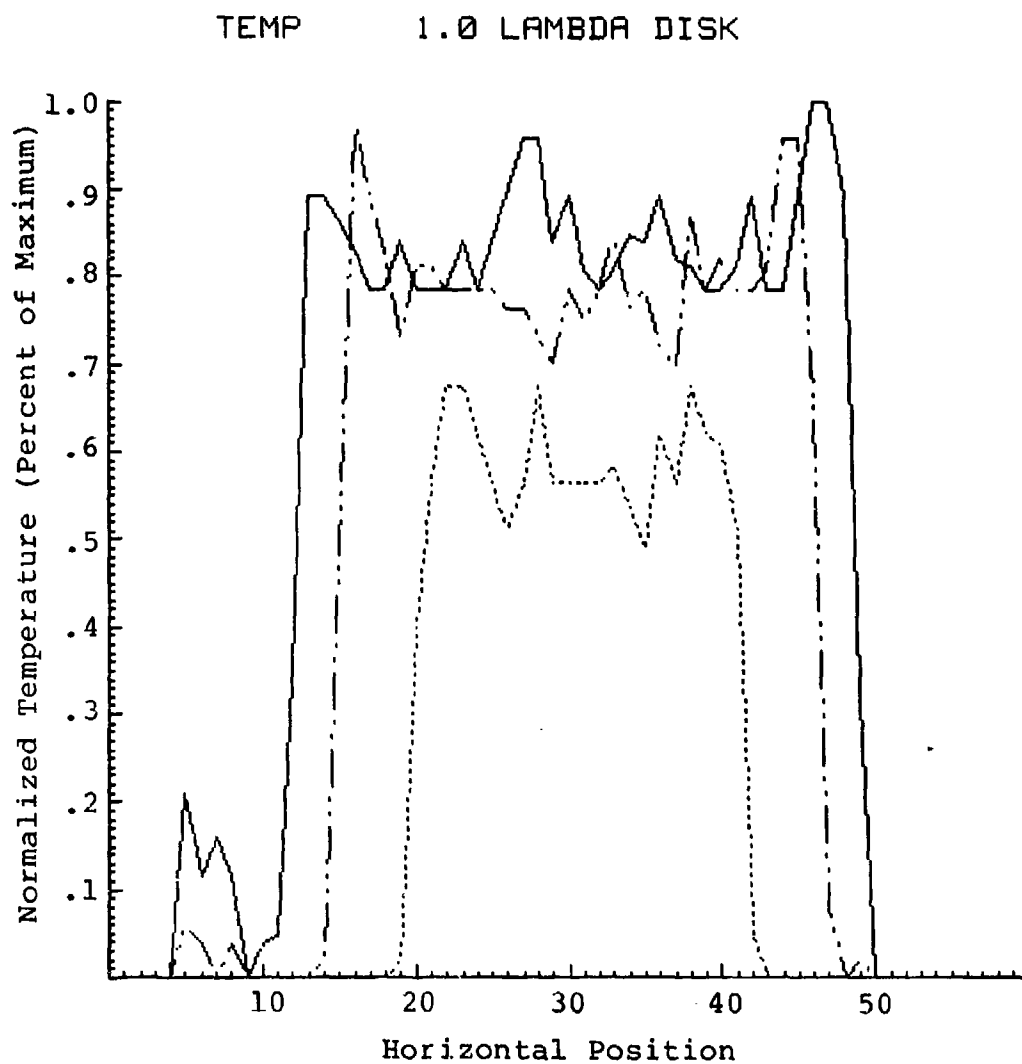


Figure 139: Temperature profiles for 1.0 wavelength circular disk - carbon/paraffin on metal.

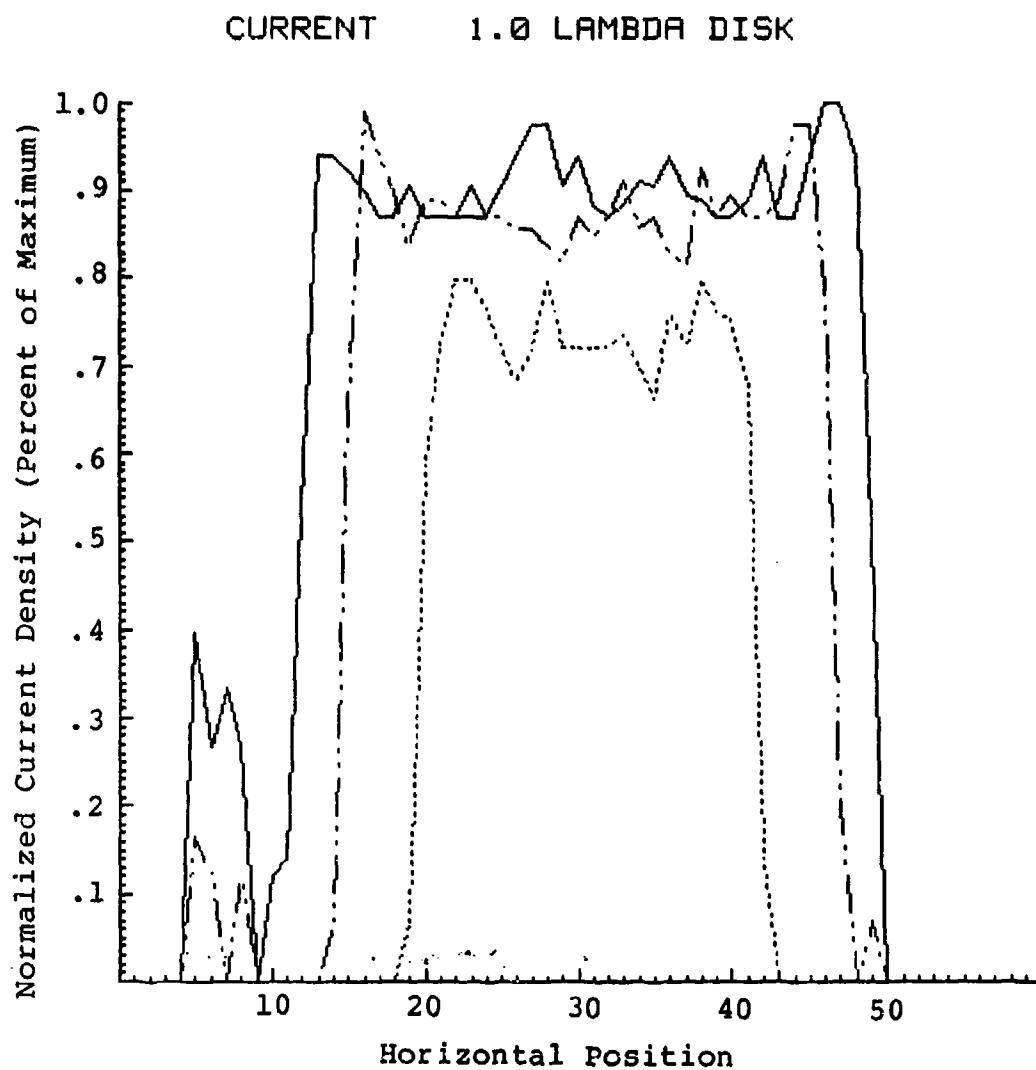


Figure 140: Infrared obtained current profiles for 1.0 wavelength circular disk - carbon/paraffin on metal.

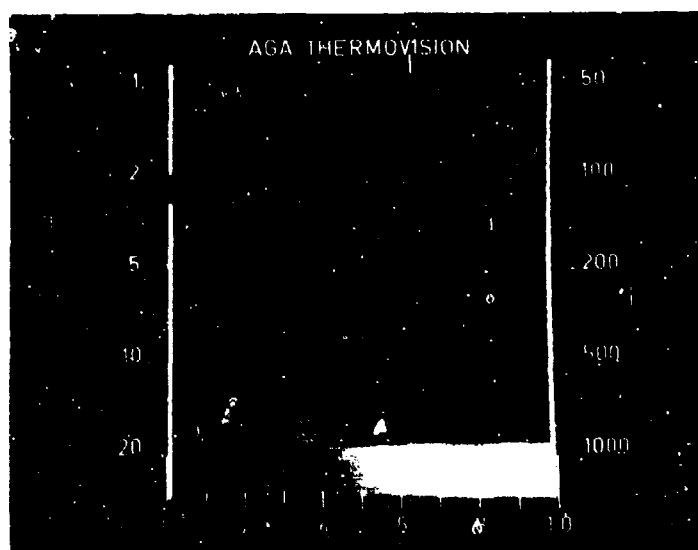


Figure 141: Thermogram for an illuminated 1.0 wavelength circular disk - aquadac on plexiglass.

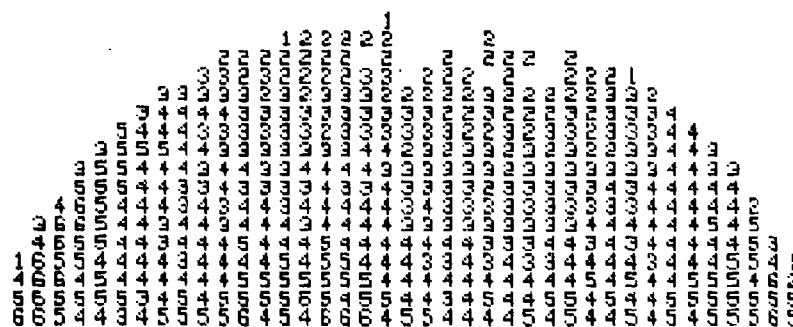


Figure 142: Digitized thermovision data for 1.0 wavelength circular disk - aquadac on plexiglass.

FINAL 1.0 LAMBDA DISK*

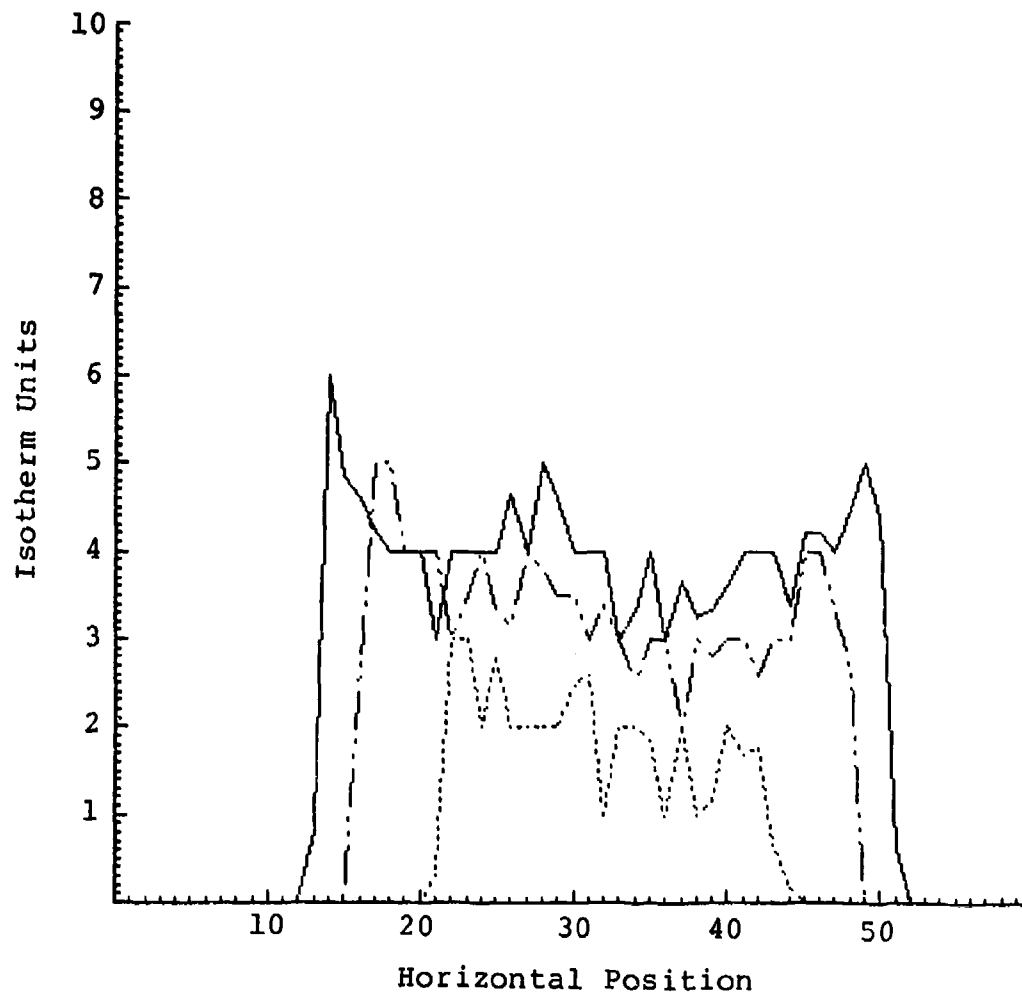


Figure 143: Thermovision data profiles
for 1.0 wavelength circular
disk - aquadac on plexiglass.

TEMP 1.0 LAMBDA DISK *

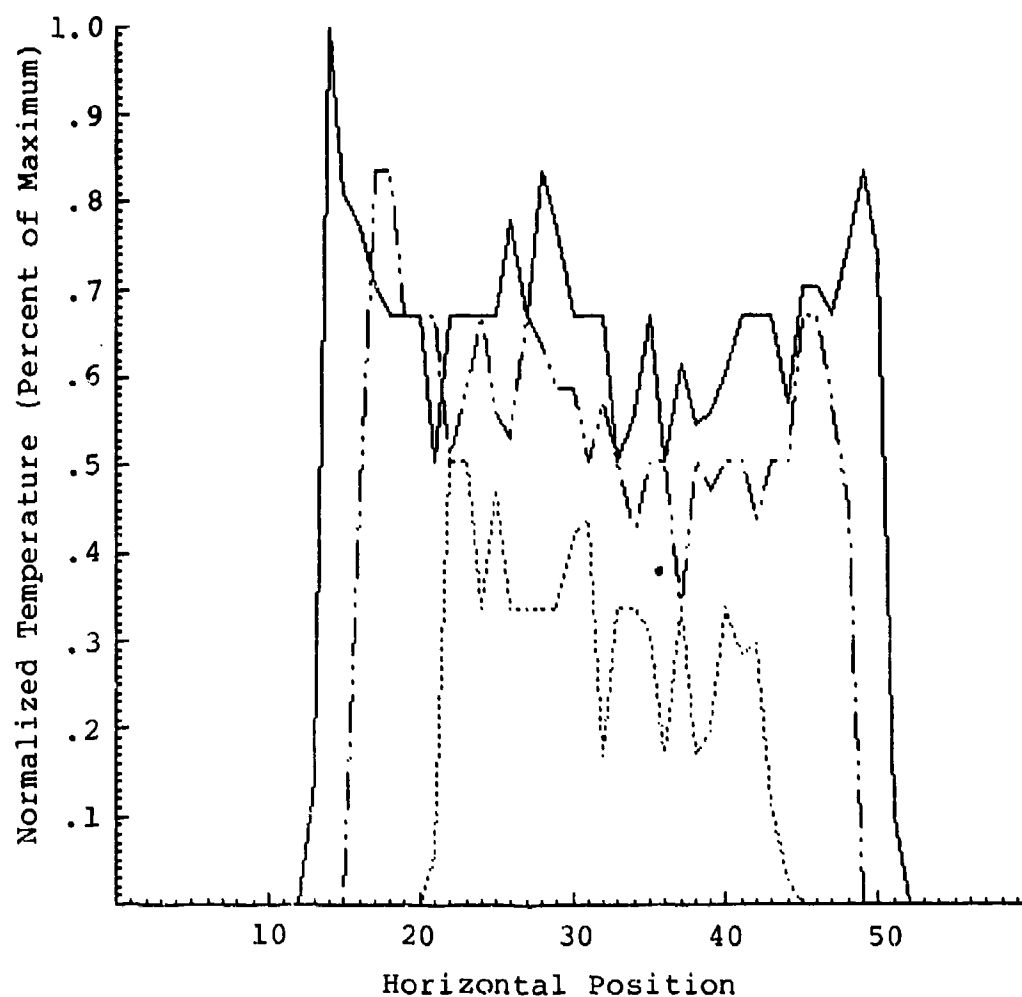


Figure 144: Temperature profiles for
1.0 wavelength circular
disk - aquadac on plexiglass.

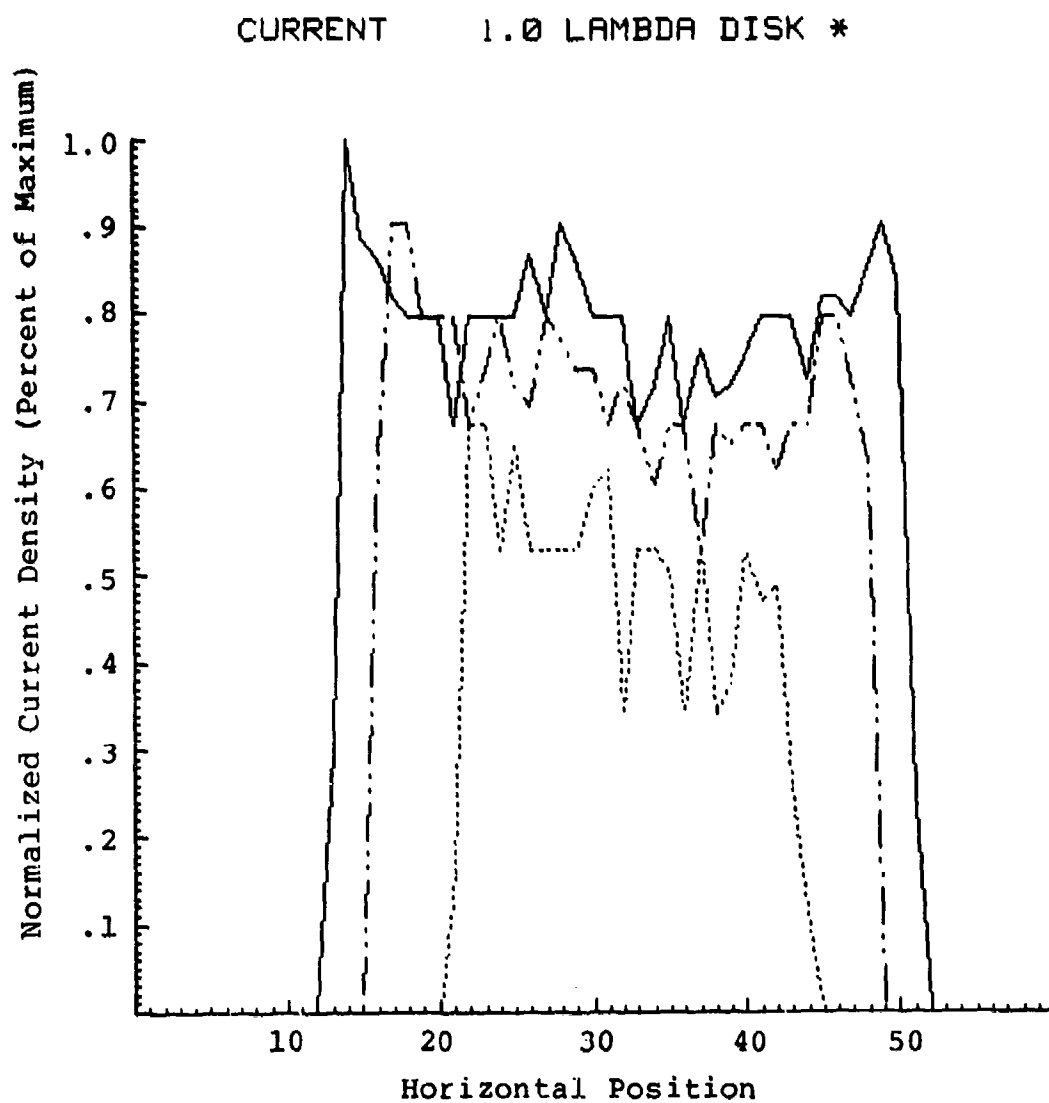


Figure 145: Infrared obtained current profiles for 1.0 wavelength circular disk - aquadac on plexiglass.

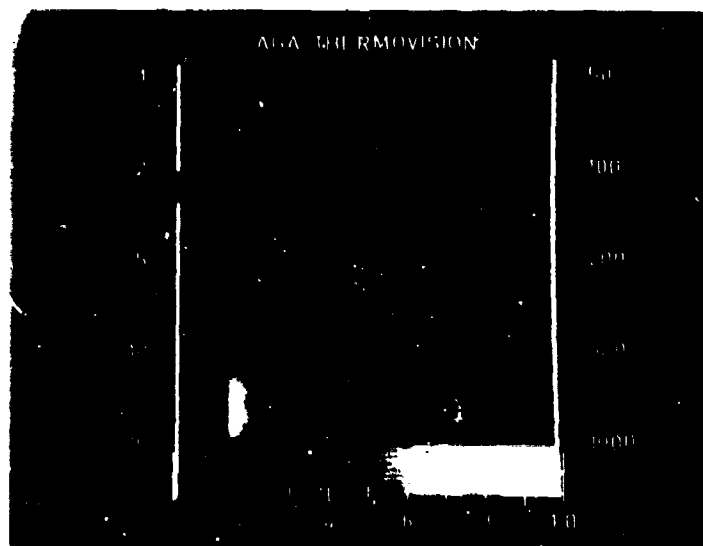


Figure 146: Thermogram for an illuminated 1.0 wavelength square plate - carbon/paraffin over metal.

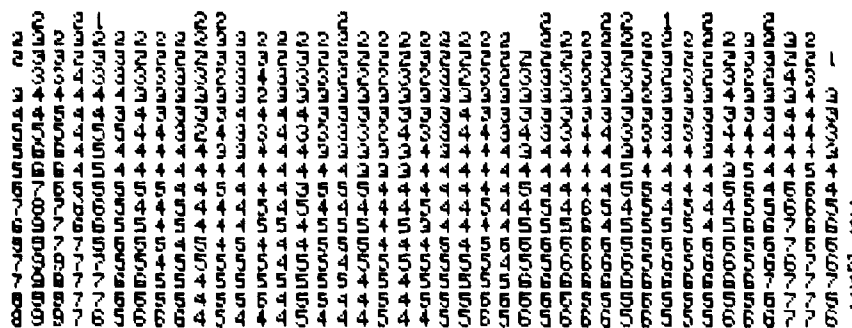


Figure 147: Digitized thermovision data for 1.0 wavelength square plate - carbon/paraffin over metal.

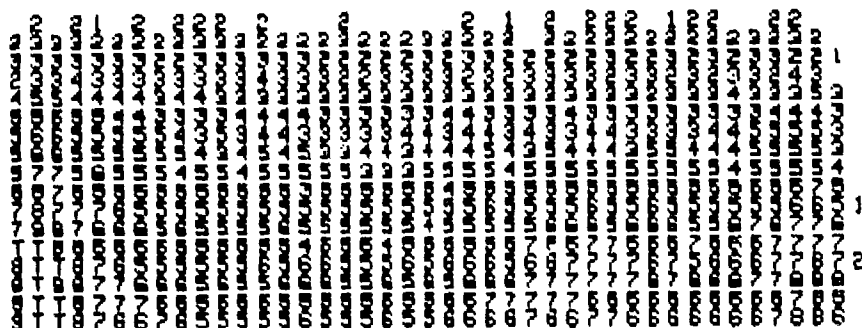


Figure 148: Temperature matrix for 1.0 wavelength square plate - carbon/paraffin over metal.

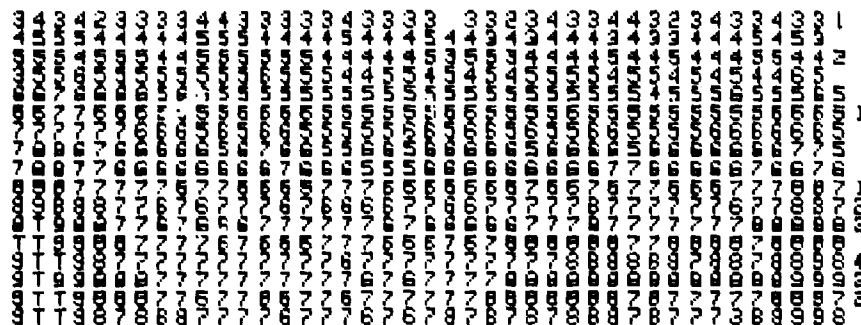
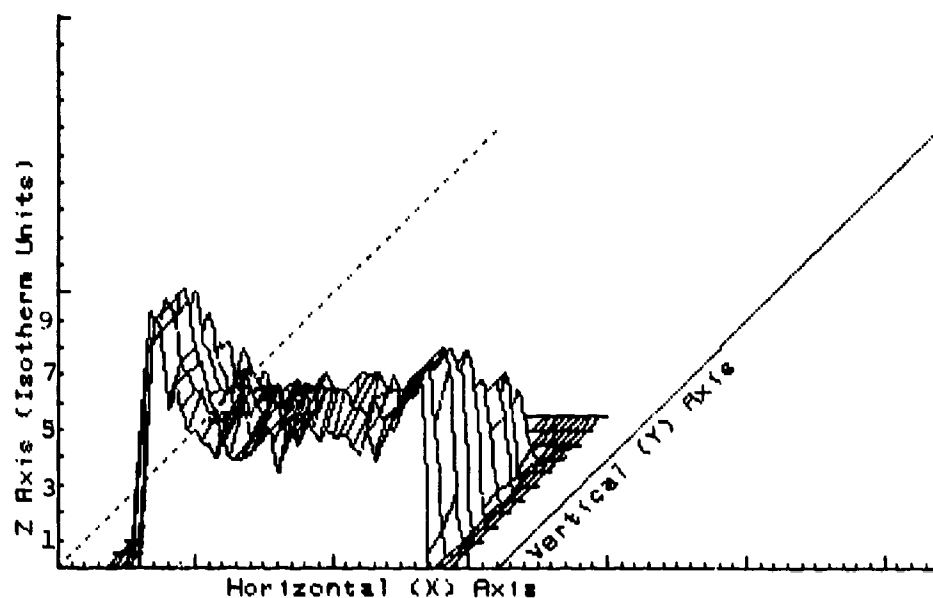
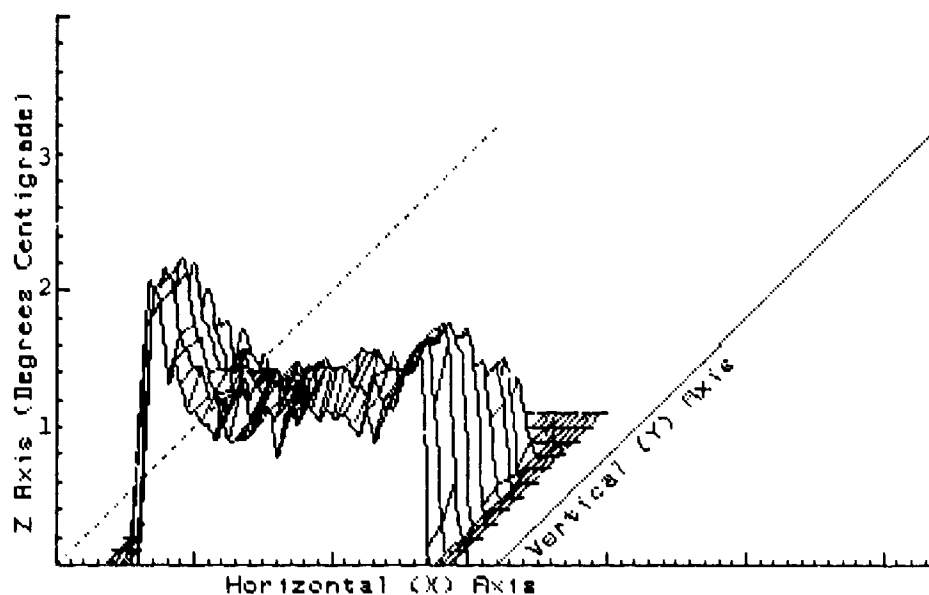


Figure 149: Current matrix for 1.0 wavelength square plate - carbon/paraffin over metal.



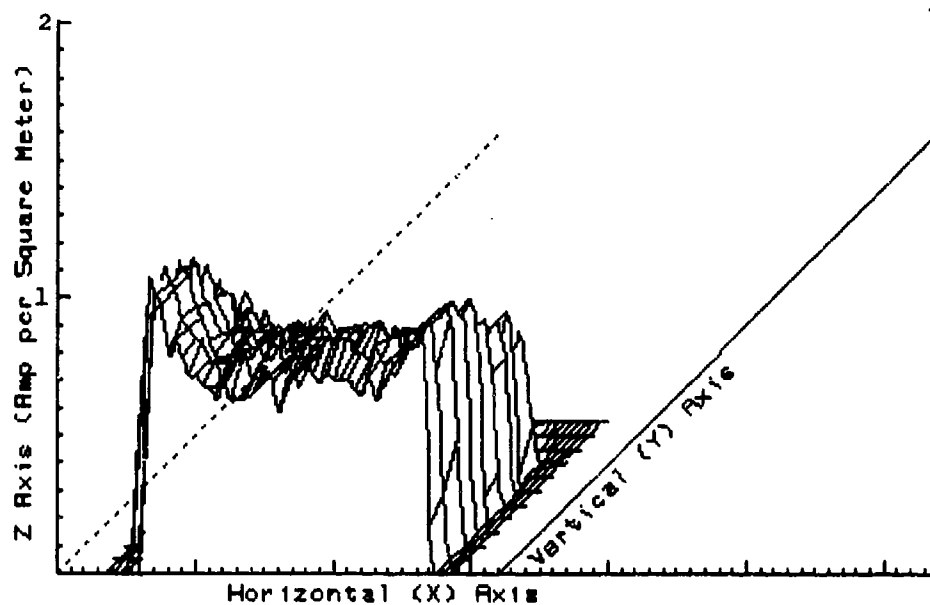
FINAL MATRIX AFTER RADIATION

Figure 150: Thermovision data matrix profile for 1.0 wavelength square plate - carbon/paraffin over metal.



DELTA TEMPERATURE MATRIX (C)

Figure 151: Temperature matrix profile for 1.0 wavelength square plate - carbon paraffin over metal.



CURRENT DENSITY MATRIX (J)

Figure 152: Infrared obtained current matrix profile for 1.0 wavelength square plate - carbon paraffin over metal.

FINAL 1.0 LAMBDA SQUARE PLATE

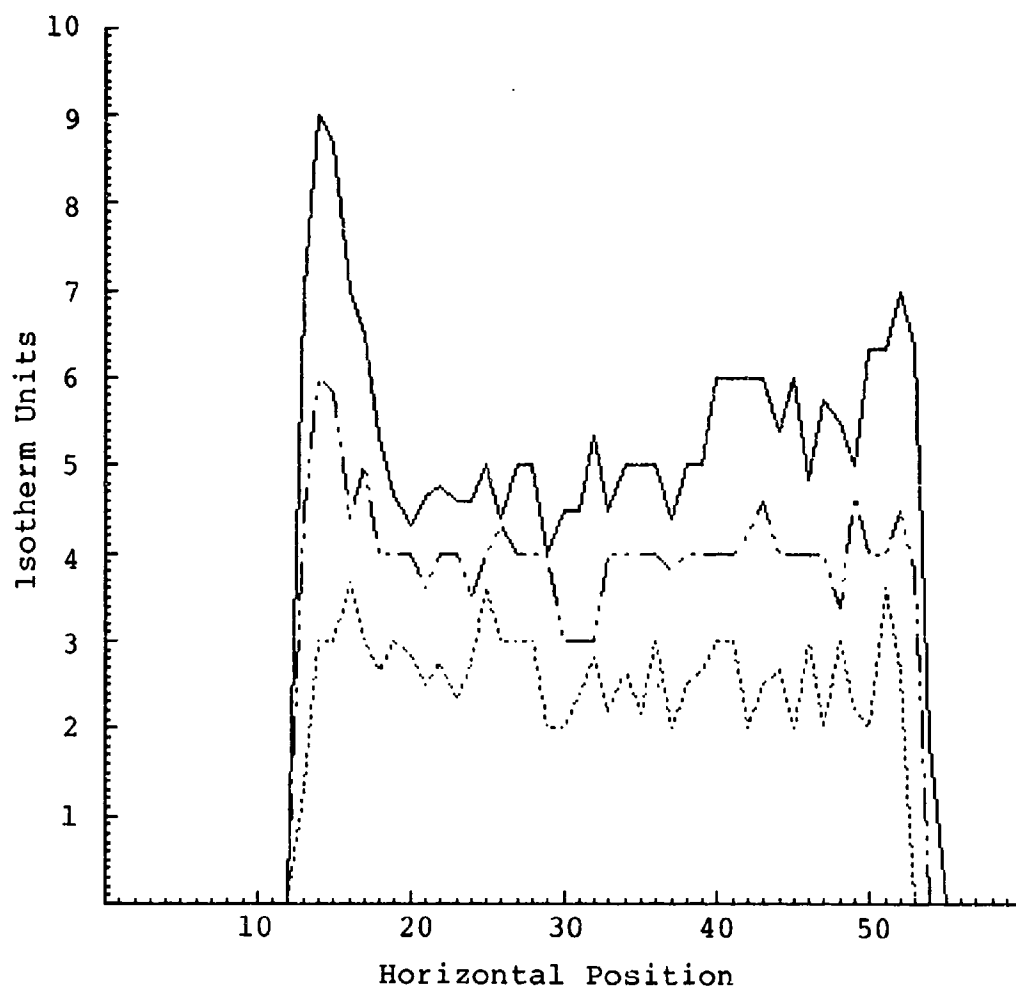


Figure 153: Thermovision data profiles for 1.0 wavelength square plate - carbon/paraffin over metal.

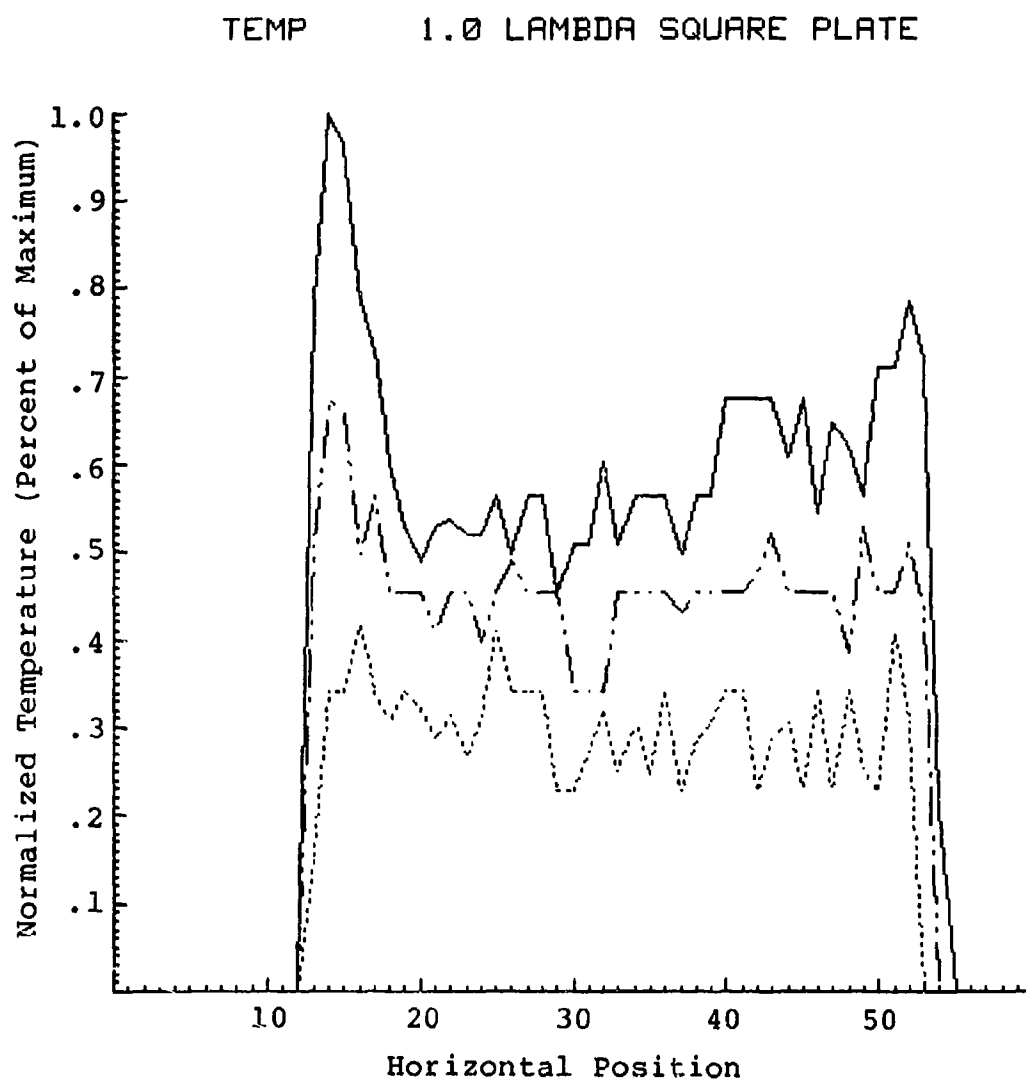


Figure 154: Temperature profiles for 1.0 wavelength square plate - carbon/paraffin over metal.

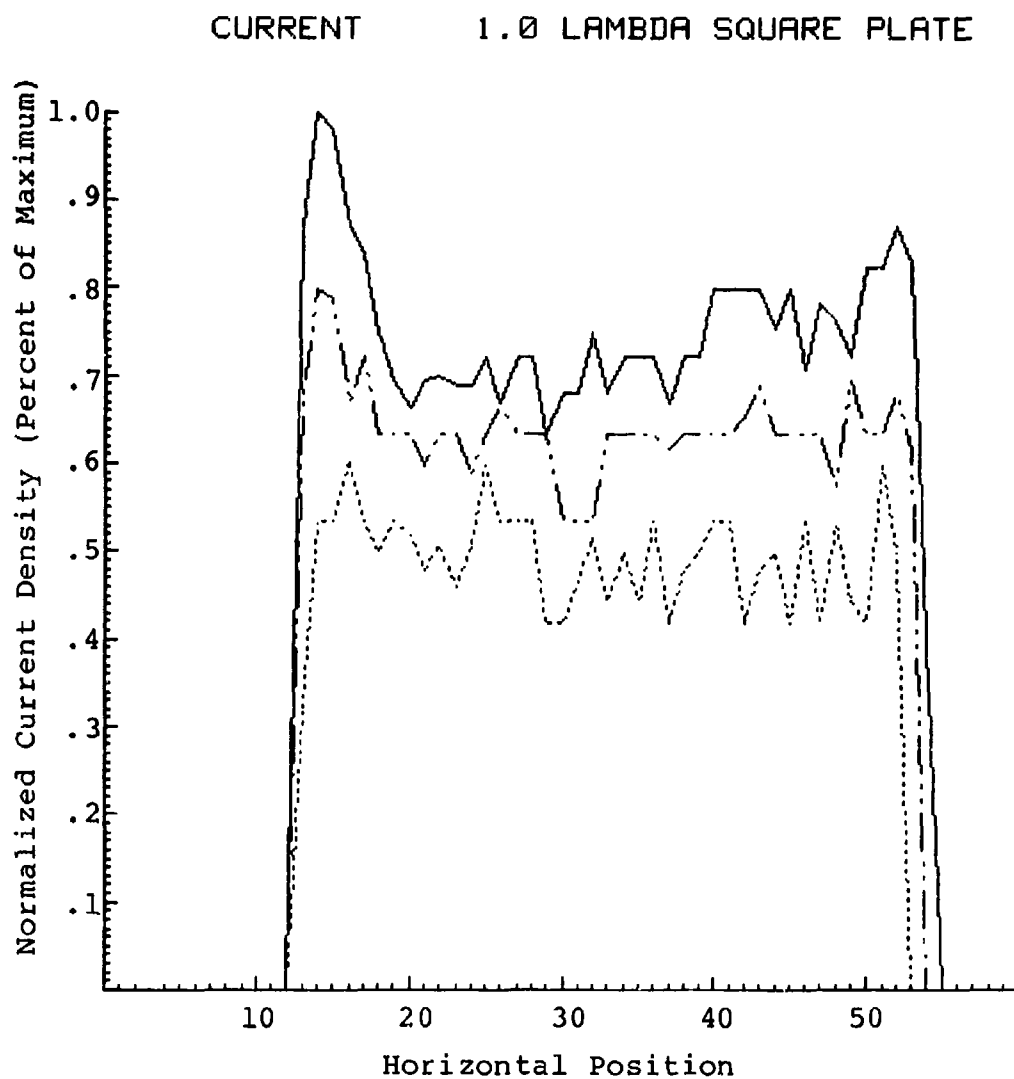


Figure 155: Infrared obtained current profiles for 1.0 wavelength square plate - carbon/paraffin over metal.

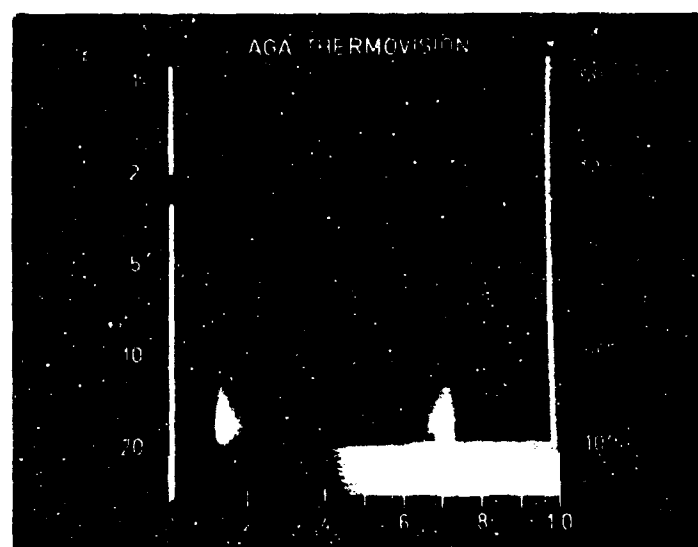


Figure 156: Thermogram for an illuminated 1.0 wavelength square plate - aquadac on plexiglass.

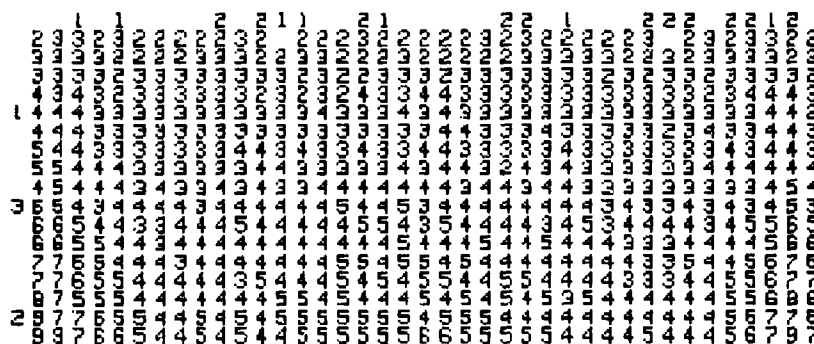


Figure 157: Digitized thermovision data
for 1.0 wavelength square
plate - aquadac on plexiglass.

FINAL 1.0 LAMBDA SQUARE PLATE *

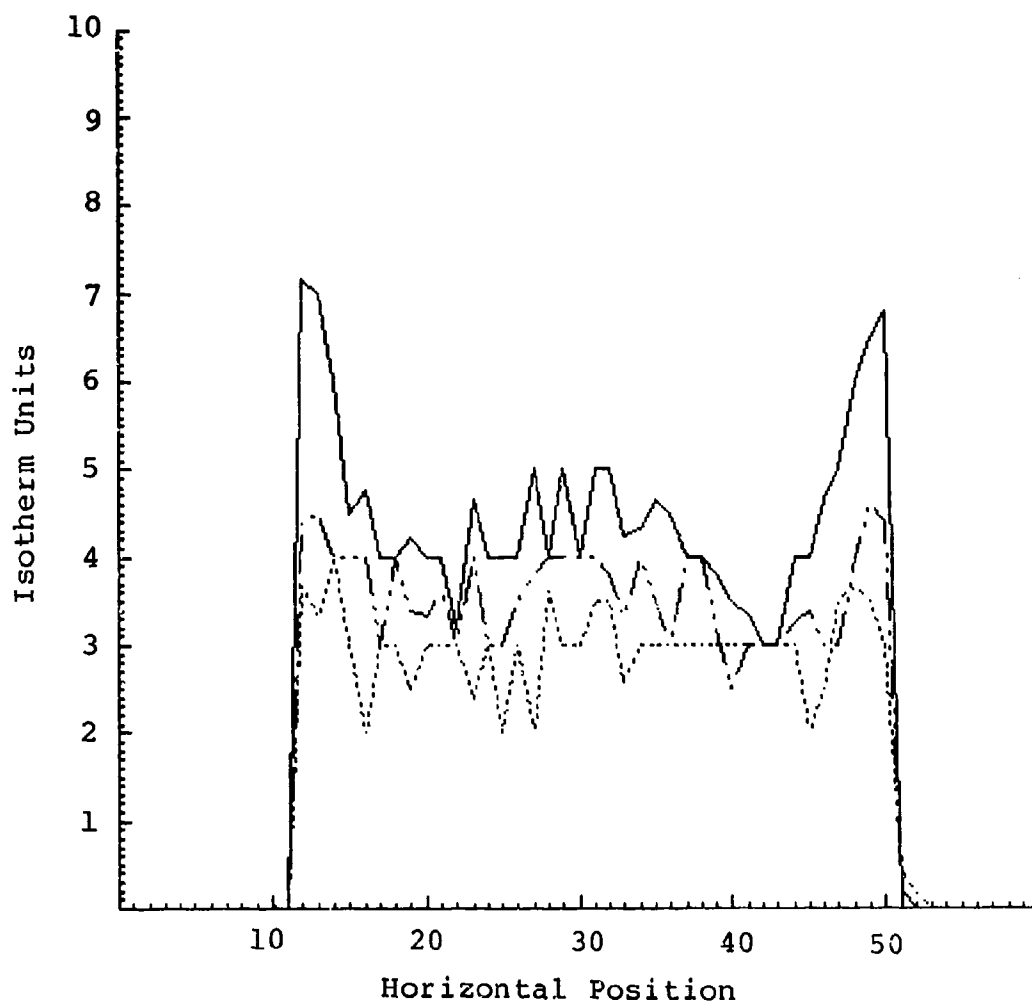


Figure 158: Thermovision data profiles for 1.0 wavelength square plate - aquadac on plexiglass.

TEMP 1.0 LAMBDA SQUARE PLATE *

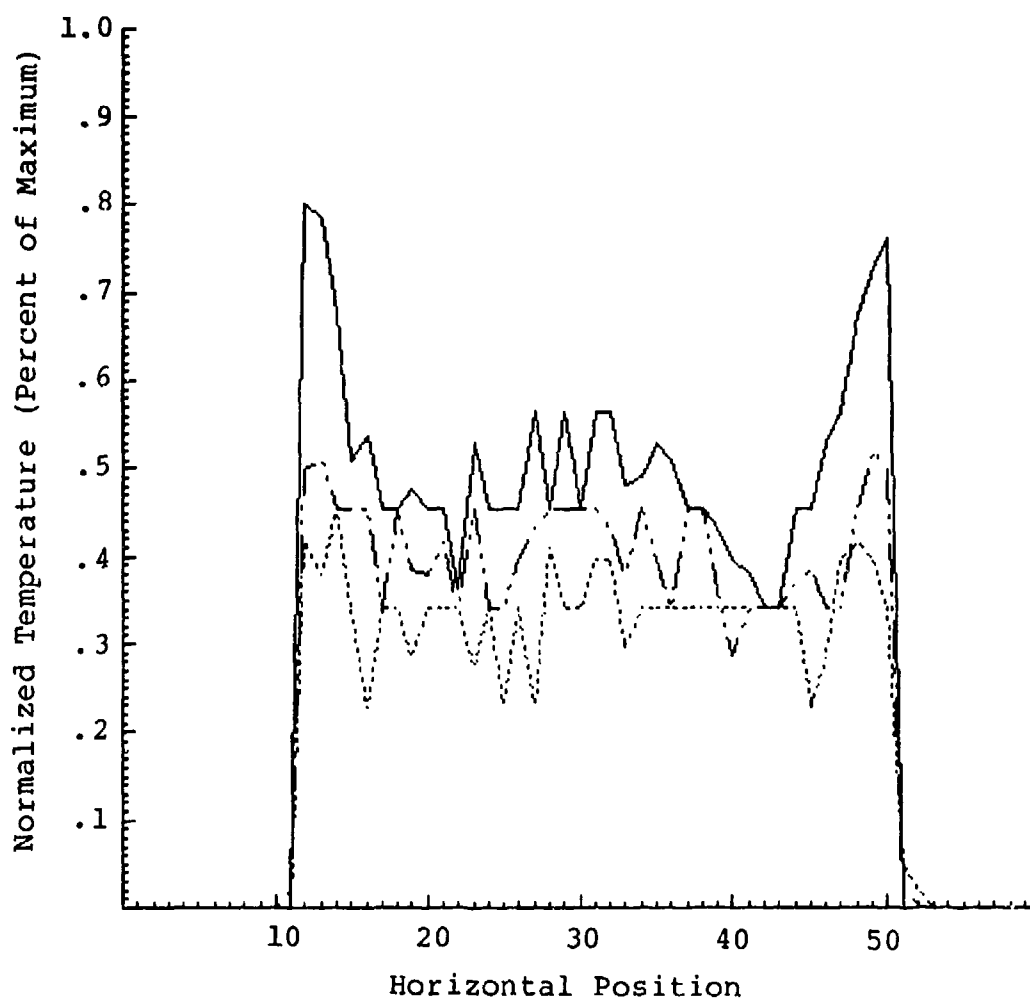


Figure 159: Temperature profiles for 1.0 wavelength square plate - aquadac on plexiglass.

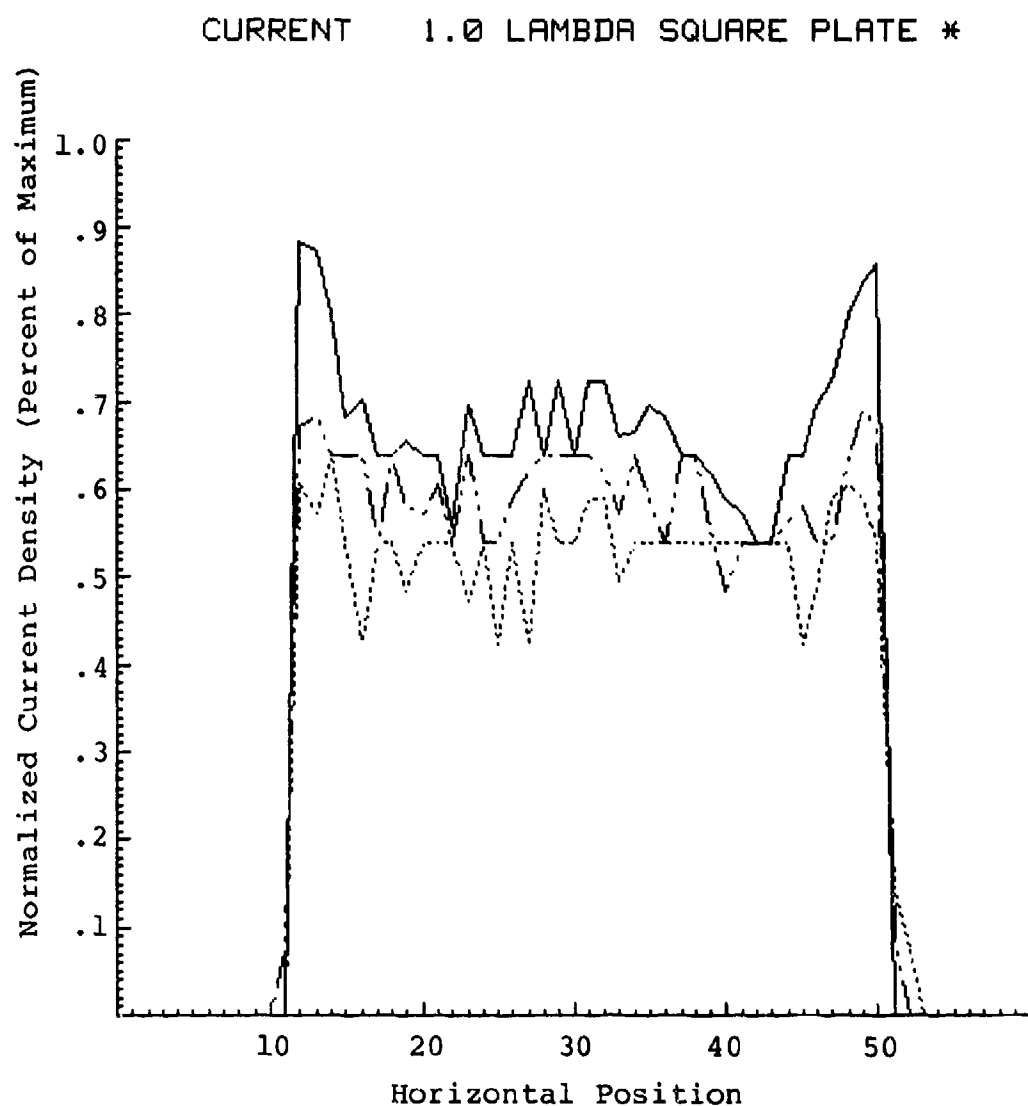


Figure 160: Infrared obtained current profiles for 1.0 wavelength square plate - aquadac on plexiglass.

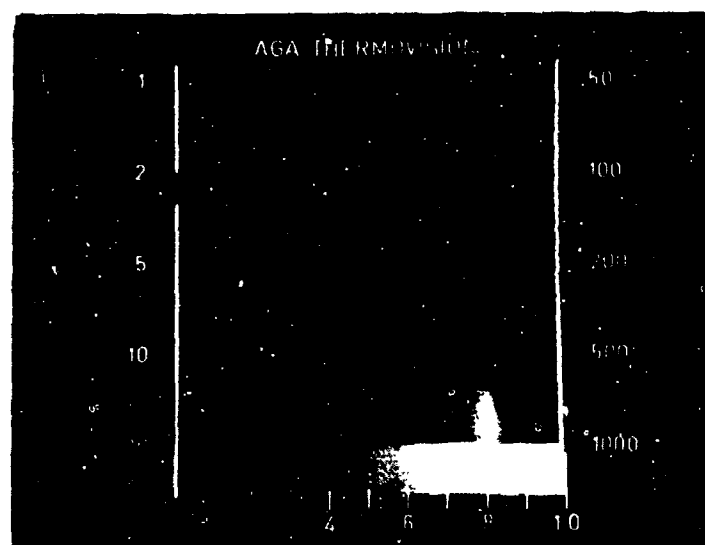


Figure 161: Thermogram for an illuminated 1.3 wavelength circular disk - carbon/paraffin over metal.

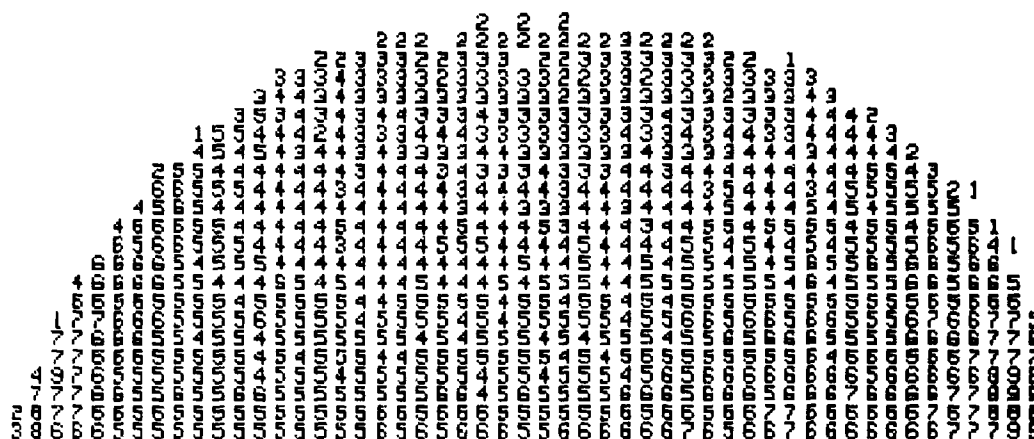


Figure 162: Digitized thermovision data for 1.3 wavelength circular disk - carbon/paraffin over metal.

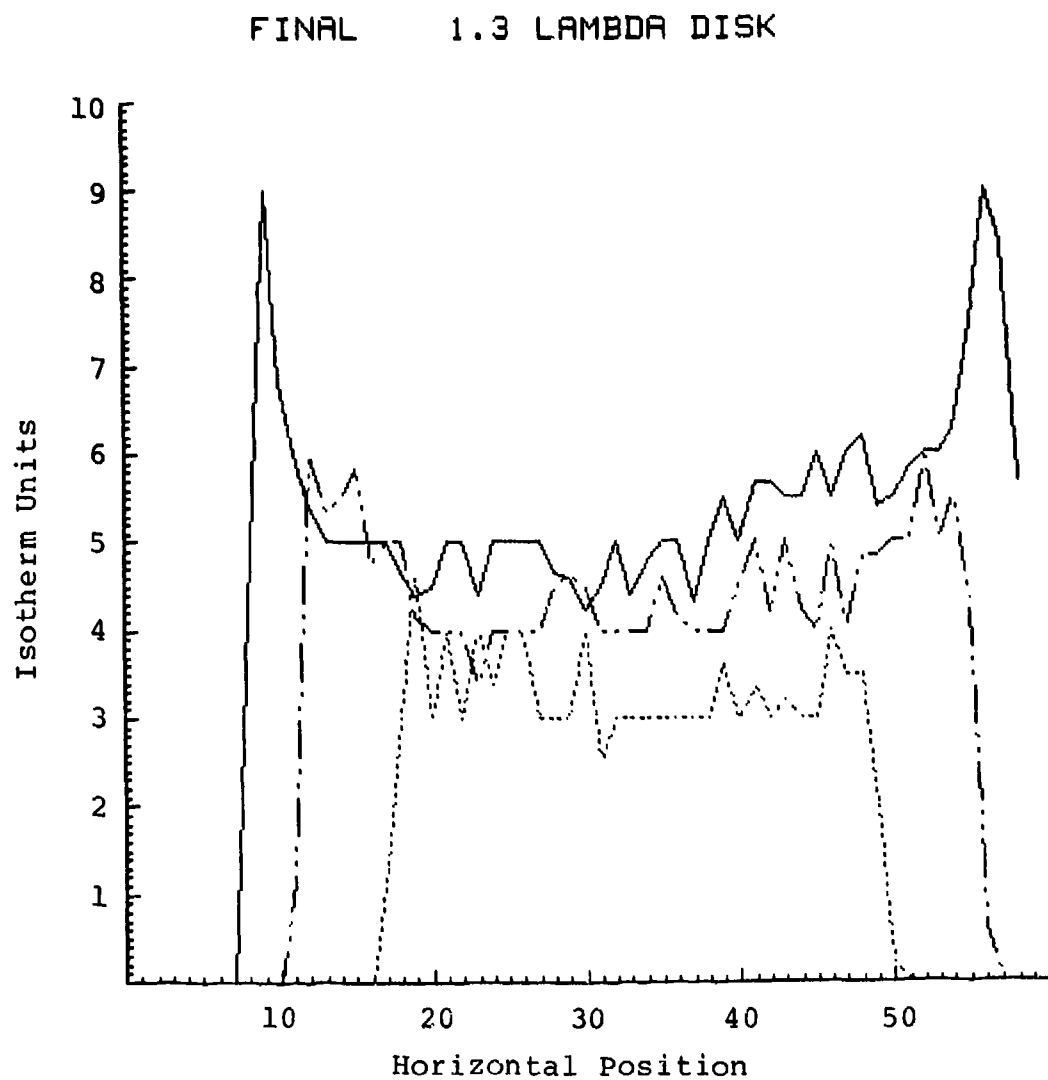


Figure 163: Thermovision data profiles for 1.3 wavelength circular disk - carbon/paraffin over metal.

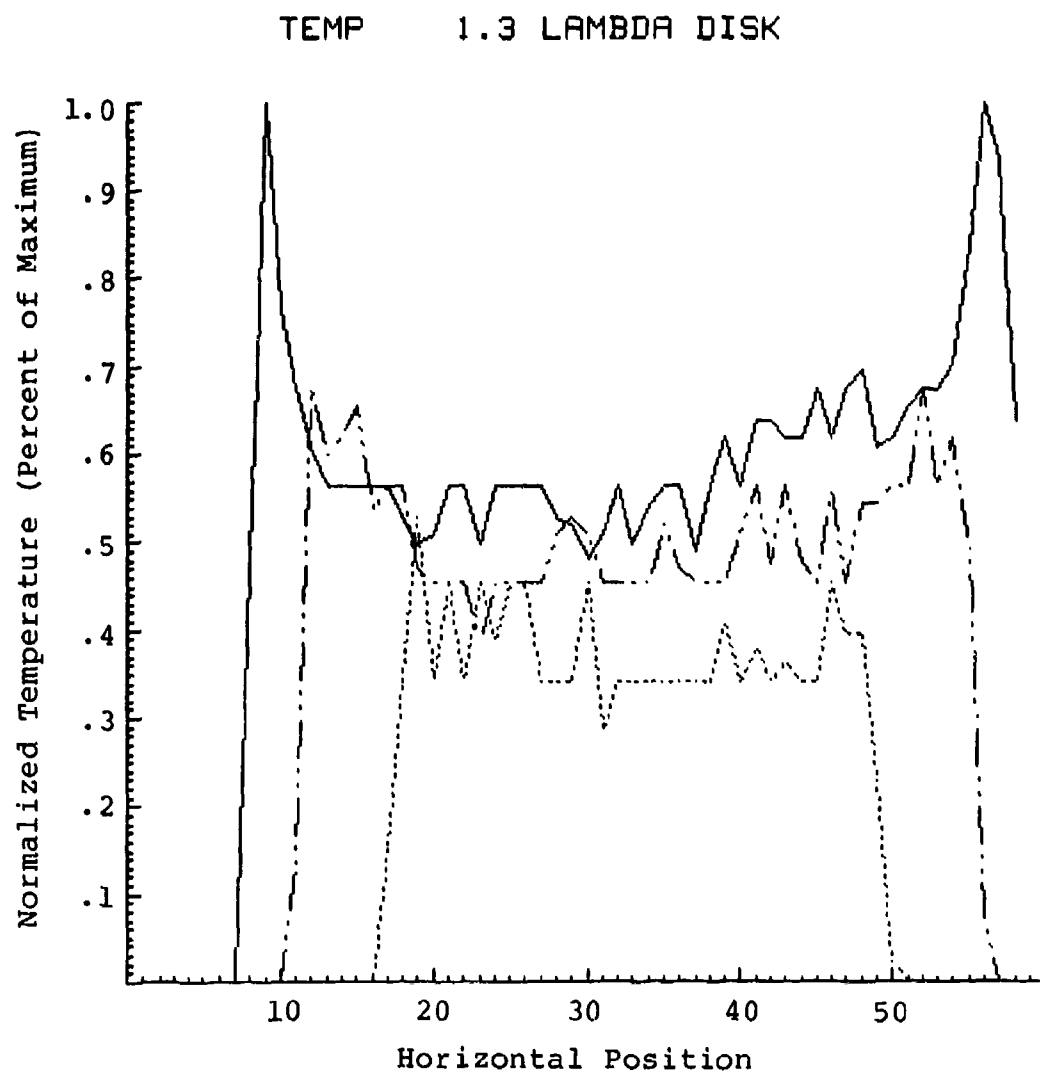


Figure 164: Temperature profiles for
1.3 wavelength circular disk -
carbon/paraffin over metal.

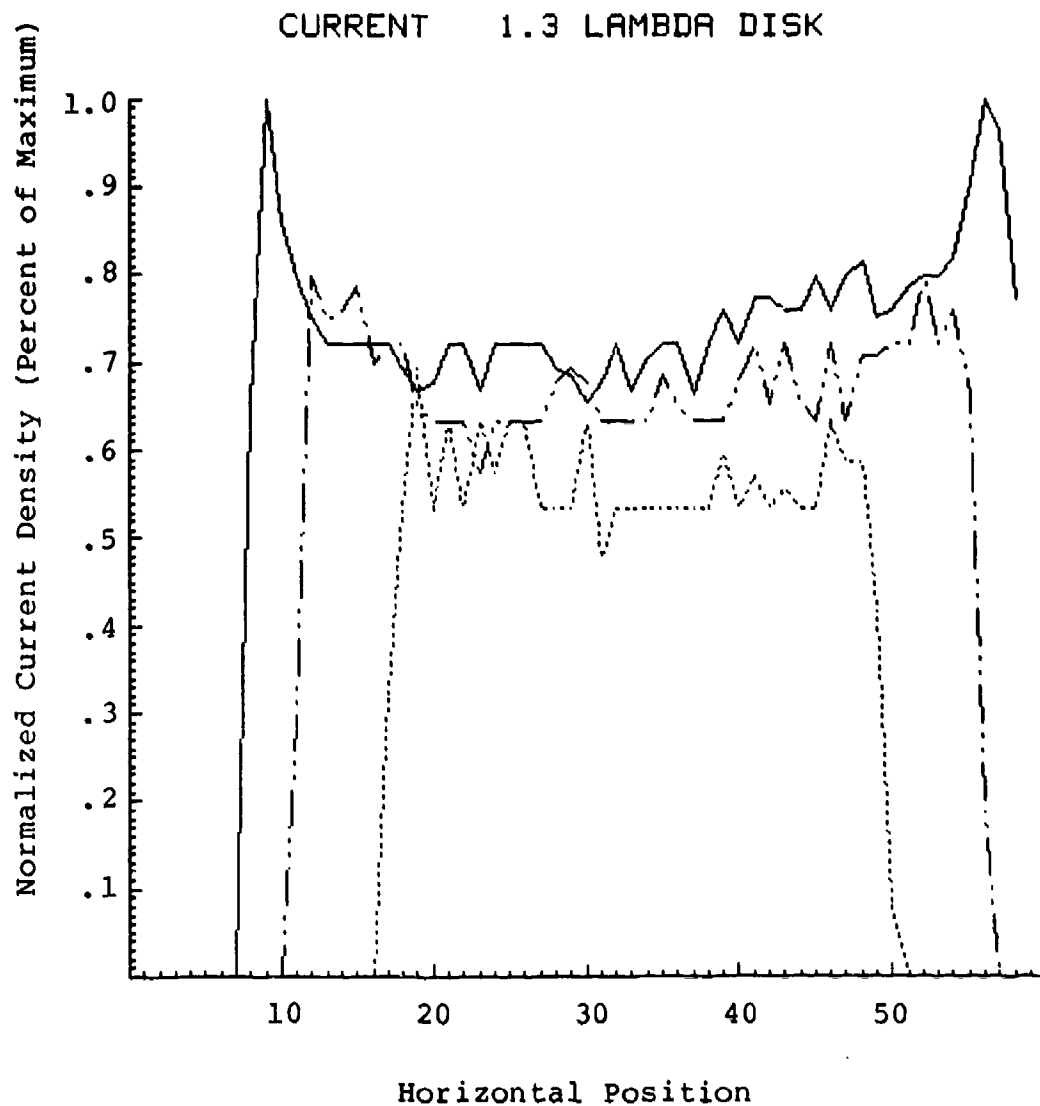


Figure 165: Infrared obtained current profiles for 1.3 wavelength circular disk - carbon/paraffin over metal.

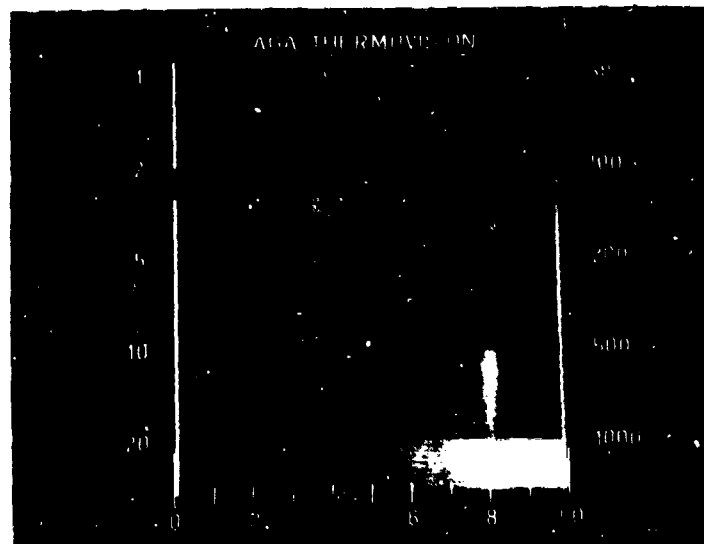


Figure 166: Thermogram for an illuminated 1.3 wavelength square plate - carbon/paraffin over metal.

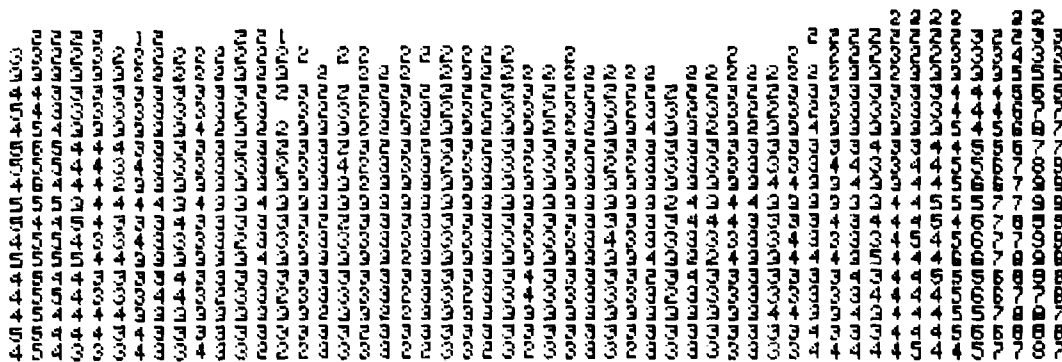


Figure 167: Digitized thermovision data for 1.3 wavelength square plate - carbon/paraffin over metal.

FINAL 1.3 LAMBDA SQUARE PLATE

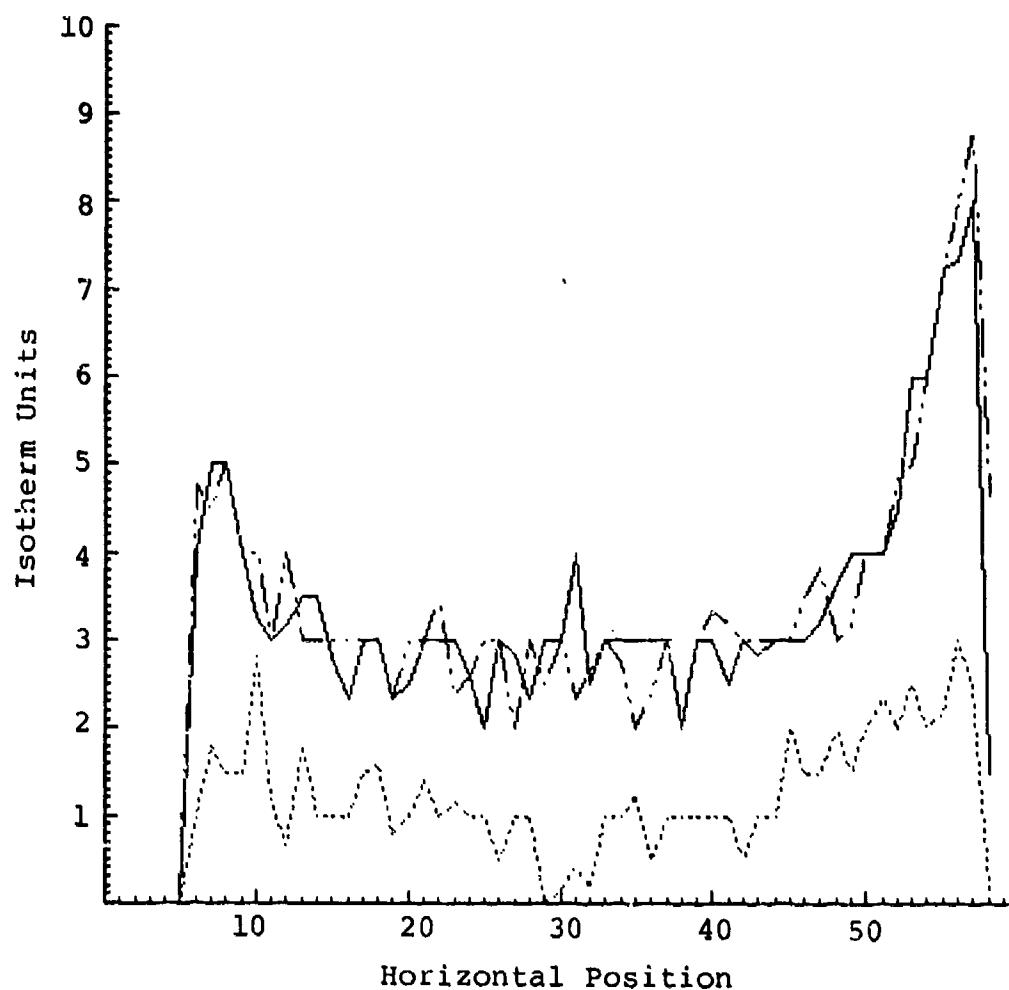


Figure 168: Thermovision data profiles for 1.3 wavelength square plate - carbon/paraffin over metal.

TEMP 1.3 LAMBDA SQUARE PLATE

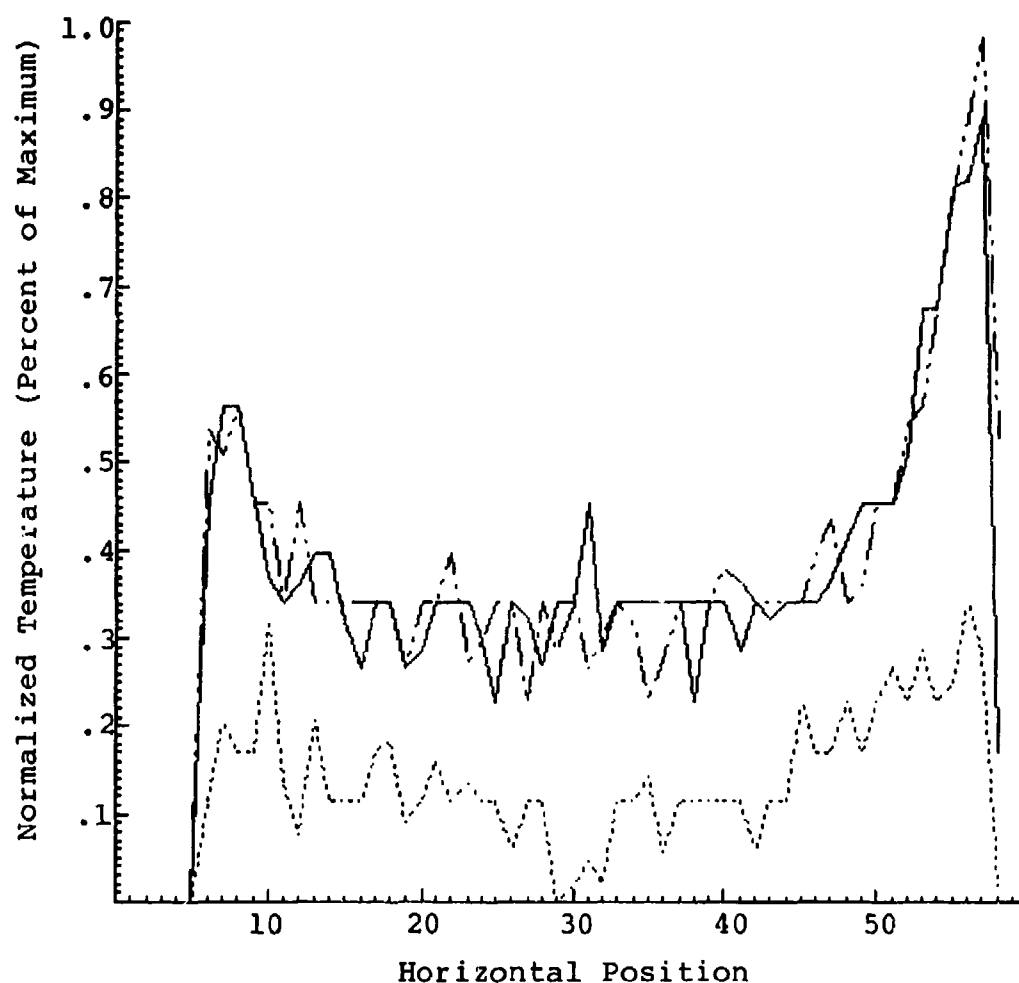


Figure 169: Temperature profiles for 1.3 wavelength square plate - carbon/paraffin over metal.

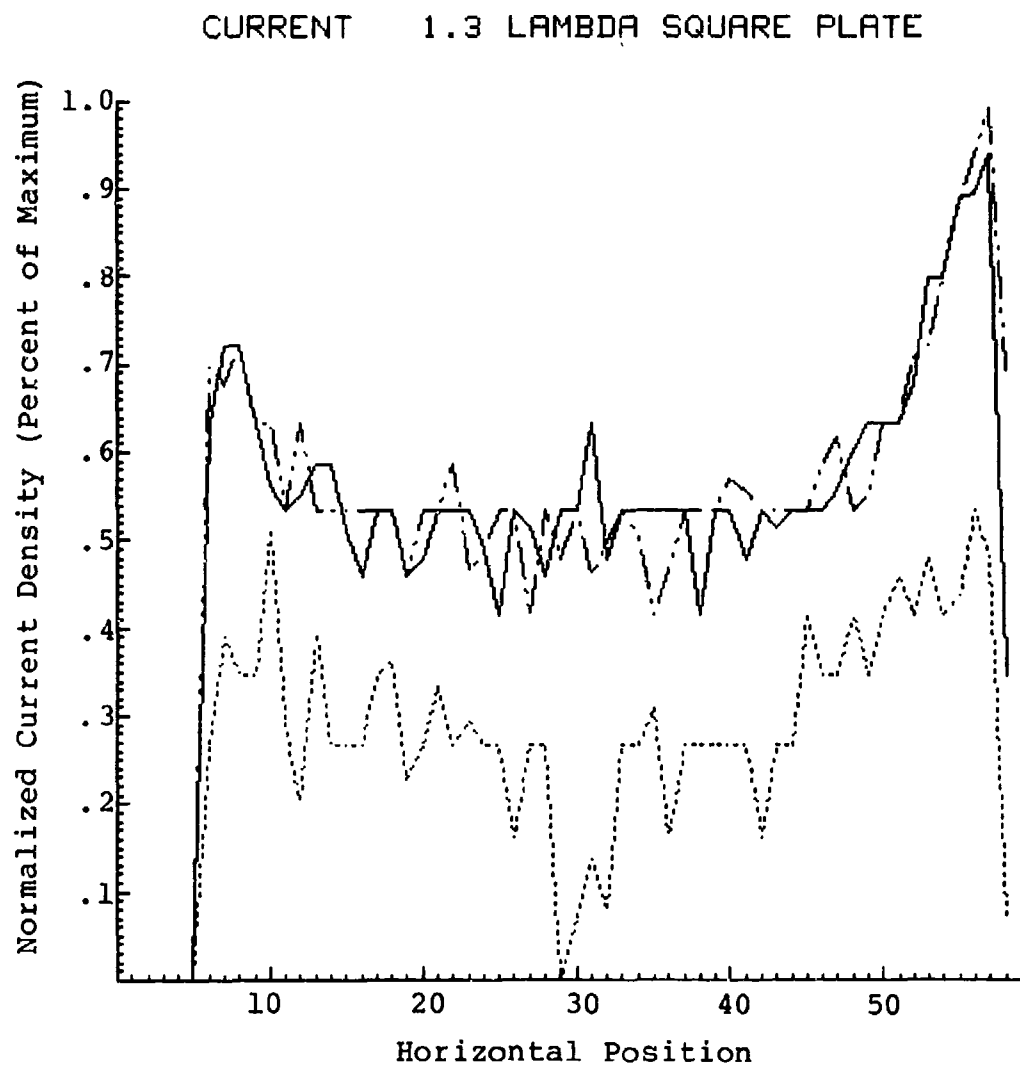


Figure 170: Infrared obtained current profiles for 1.3 wavelength square plate - carbon/paraffin over metal.

CHAPTER VII

CORRELATION

Selected situations for relating current density distributions from theory, magnetic field probe measurements, and IR obtained results will be presented. The computer solution for the perfectly conducting disk was favorably compared in Chapter II to disks of smaller and larger electrical size than those observed in the experimental portion of this work. The theoretical solutions to the square plates differ and the only directly applicable scan to this study would be the 1.0 wavelength square plate and the observation that the small plate (.15 wavelength) solved by Wilton compares well in form with the smallest plate (.38 wavelength) used in this work. The .38 wavelength disk and square plate provide situations where the dominant current component is vertical and thus probe measurement for the vertical component can be considered as that of total current, thus compared with the IR result for total current.

Disk Components

The disk problem has been solved theoretically in Chapter II in the logical coordinate system, cylindrical. To compare the theoretical disk results with the magnetic field probe scans, the polynomial fits for the maximum J_ρ and J_ϕ current components can be used to solve for the horizontal and vertical components of points along horizontal lines. The restriction of remaining somewhat away from the center and rim for the computed results will still apply. The three vertical distances from the ground plane used with the probe are now used when solving for theoretical J_{horiz} , J_{vert} , and J_{total} . The expression for total current would still be

$$J_{\text{total}} = (J_\rho^2 + J_\phi^2)^{1/2} \quad (65)$$

where

$$J_\rho = J_{\rho \text{ max}} \sin\phi$$

$$J_\phi = J_{\phi \text{ max}} \cos\phi$$

Now, the horizontal and vertical components are simply

$$J_{\text{horiz}} = J_\rho \sin\phi + J_\phi \cos\phi \quad (66)$$

$$J_{\text{vert}} = J_\rho \cos\phi + J_\phi \sin\phi \quad (67)$$

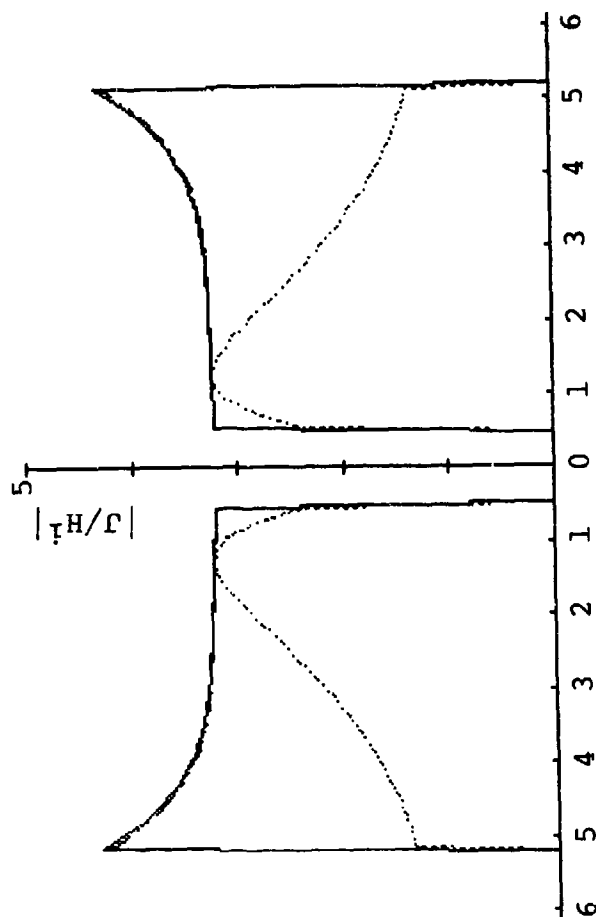
In the program called "DISK" found in Appendix D, it was convenient to transform to rectangular coordinates and iterate along the horizontal limits of the disk at a particular height. The key to the following figures is:

J_{total} - solid line (——)

J_{horiz} - broken line (—..—..—..)

J_{vert} - dotted line (.....)

.38 LAMBDA DISK LOWER SCAN



Horizontal Position From Vertical Bisector (cm)

Figure 171: Plot of current components for the .38 wavelength circular disk (lower scan).

.38 LAMBDA DISK MIDDLE SCAN

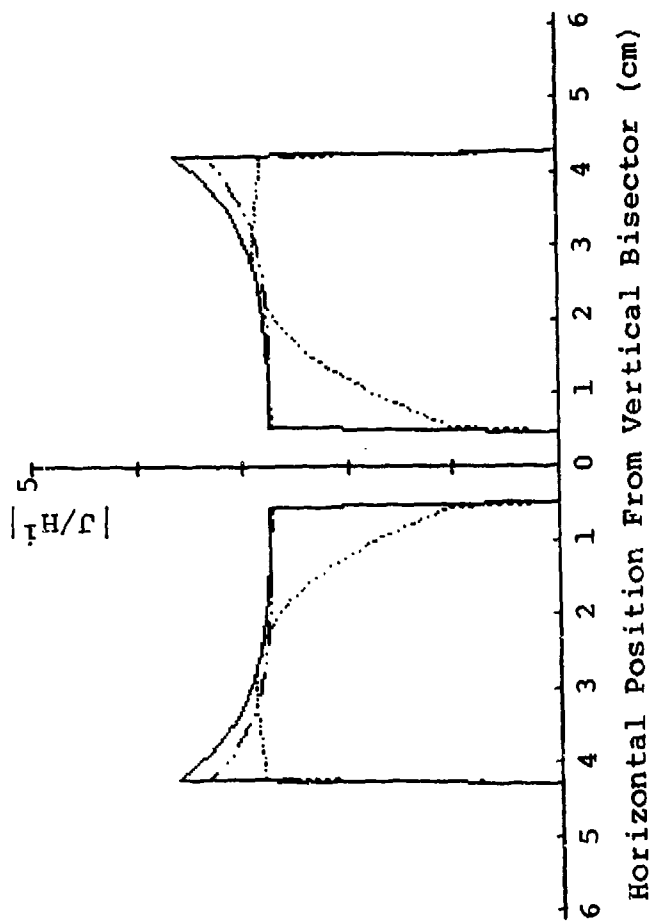


Figure 172: Plot of current components for the .38 wavelength circular disk (middle scan).

.38 LAMBDA DISK UPPER SCAN

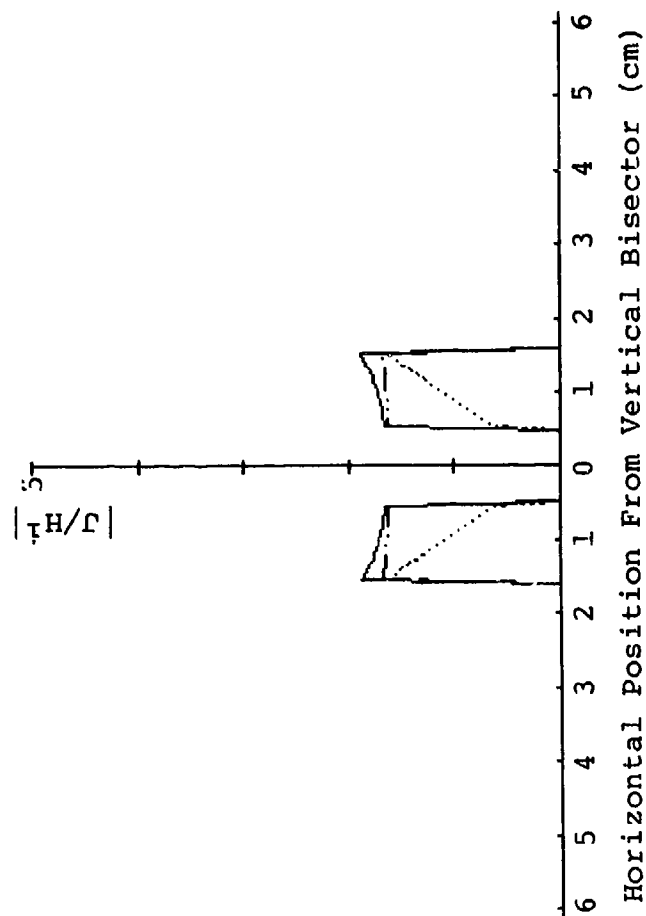


Figure 173: Plot of current components for the .38 wavelength circular disk (upper scan).

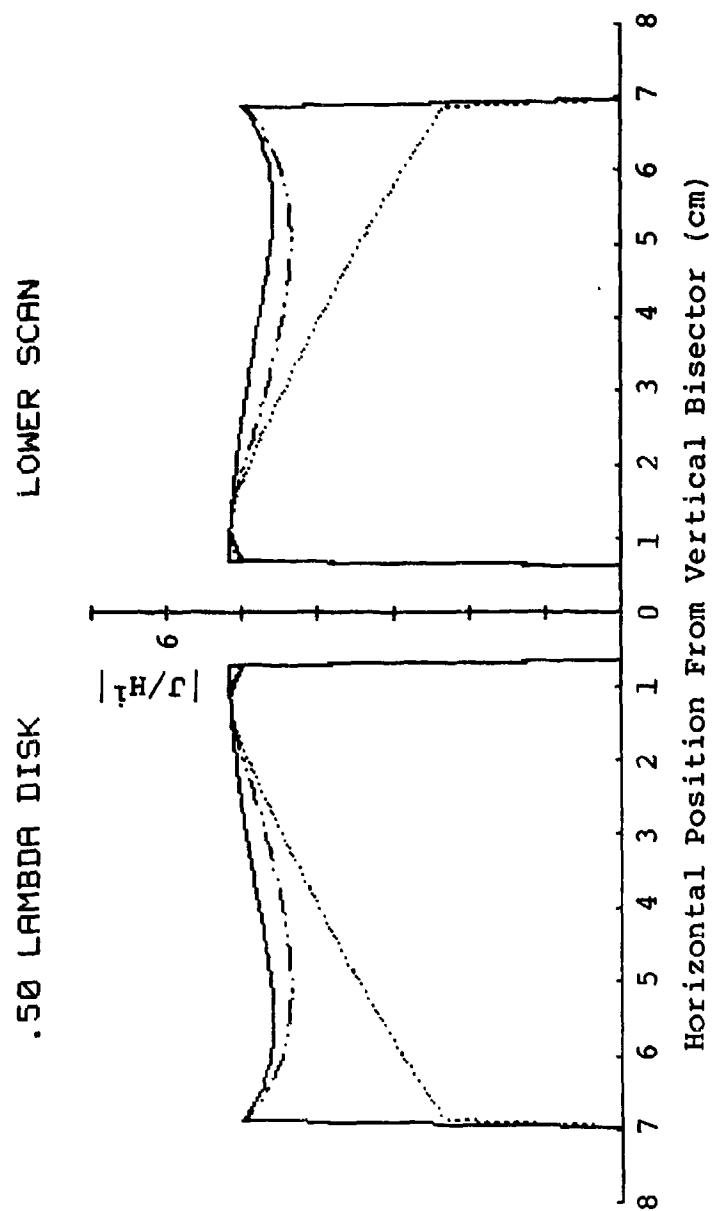


Figure 174: Plot of current components for the .50 wavelength circular disk (lower scan).

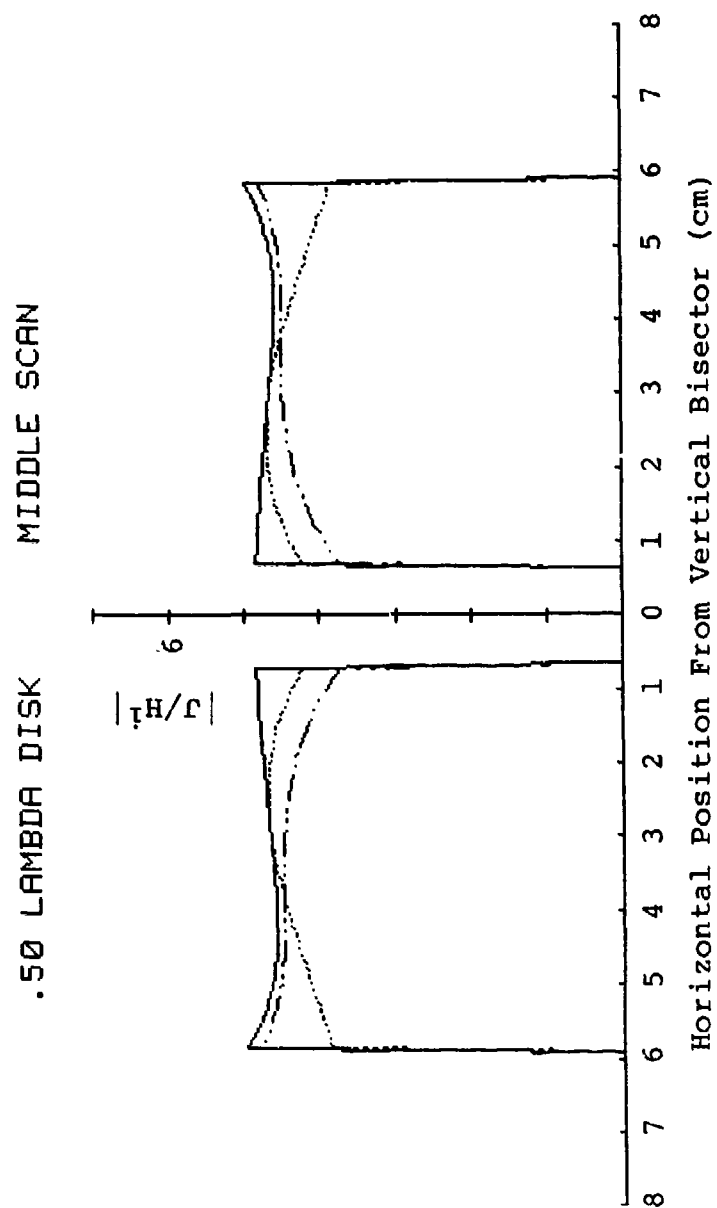


Figure 175: Plot of current components for the .50 wavelength circular disk (middle scan).

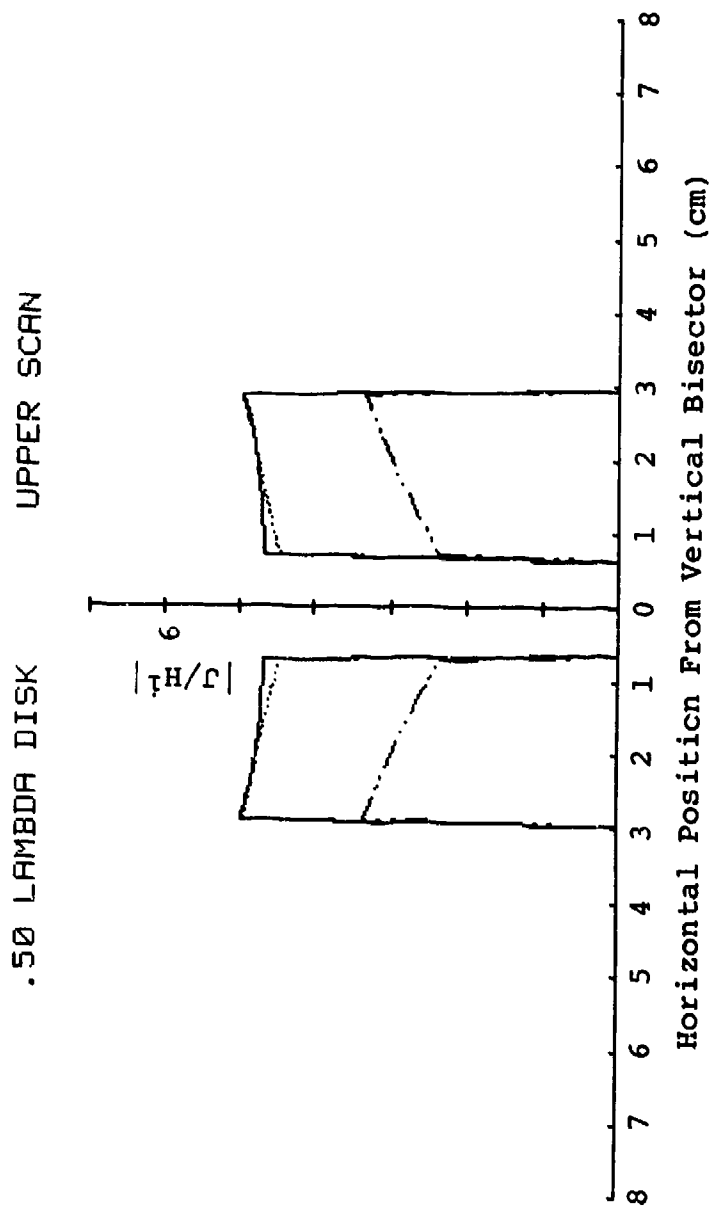


Figure 176: Plot of current components from the .50 wavelength circular disk (upper scan).

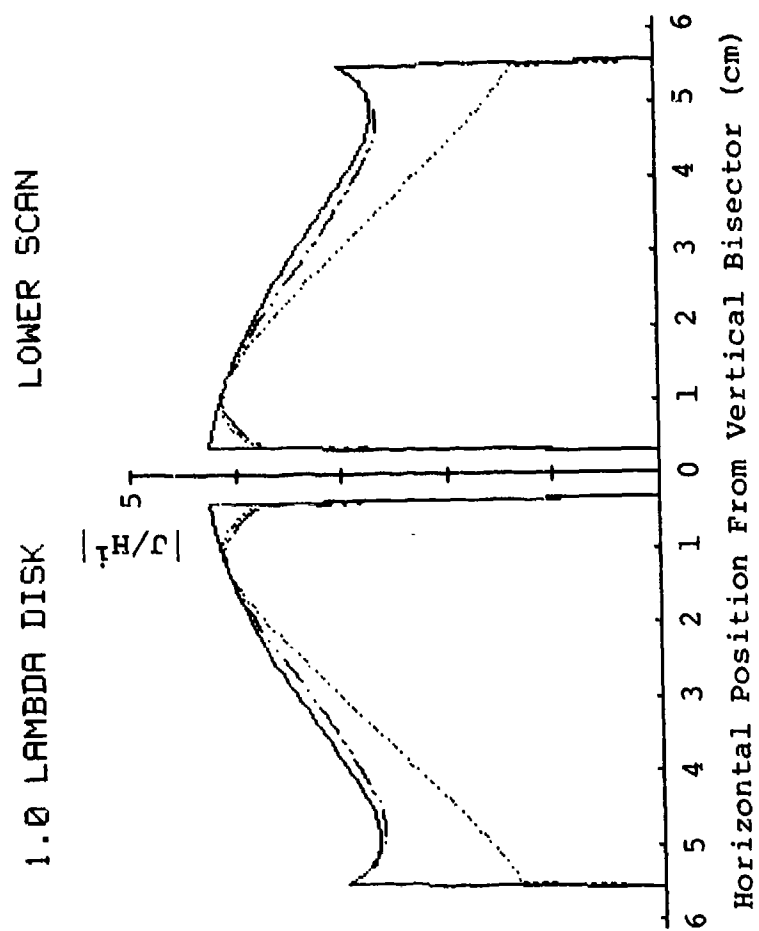


Figure 177: Plot of current components for the
1.0 wavelength circular disk
(lower scan).

1.0 LAMBDA DISK MIDDLE SCAN

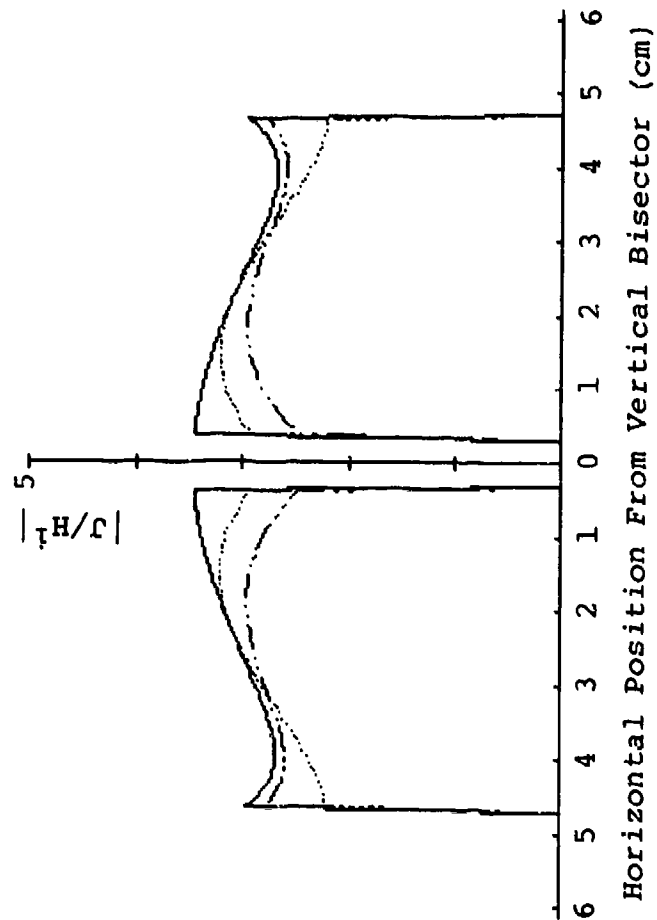


Figure 178: Plot of current components for the 1.0 wavelength circular disk (middle scan).

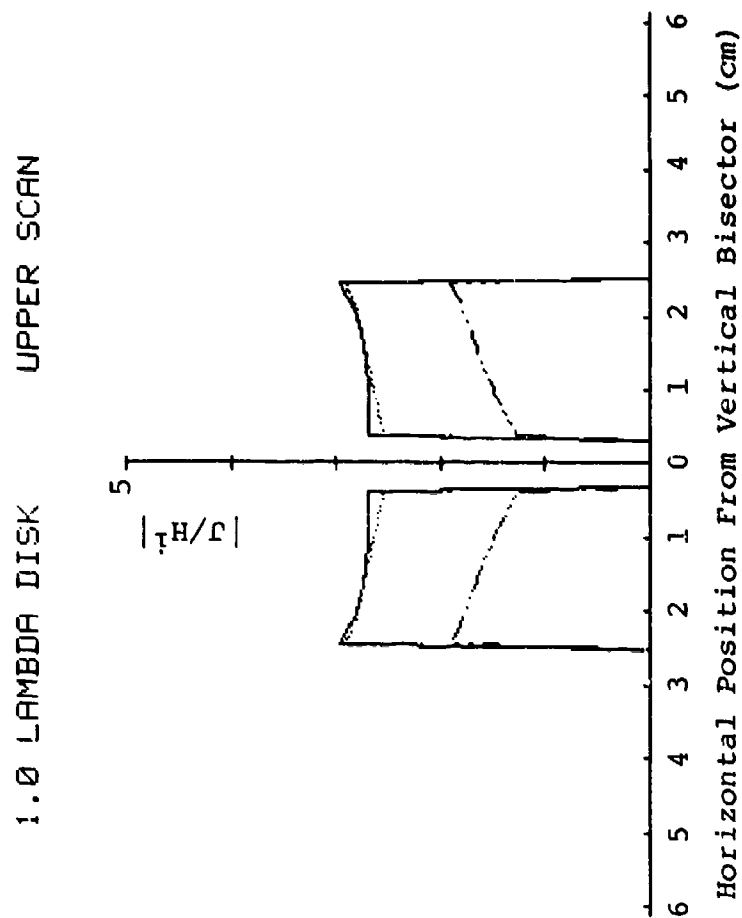


Figure 179: Plot of current components for the 1.0 wavelength circular disk (upper scan).

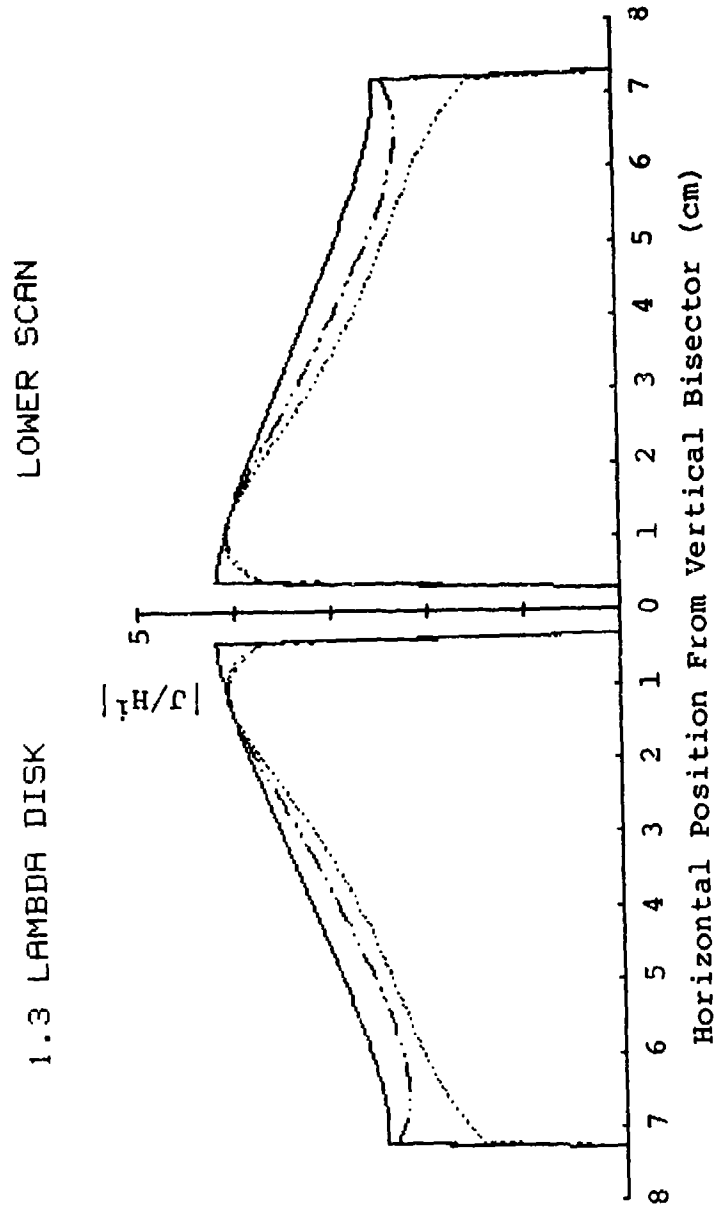


Figure 180: Plot of current components for the 1.3 wavelength circular disk (lower scan).

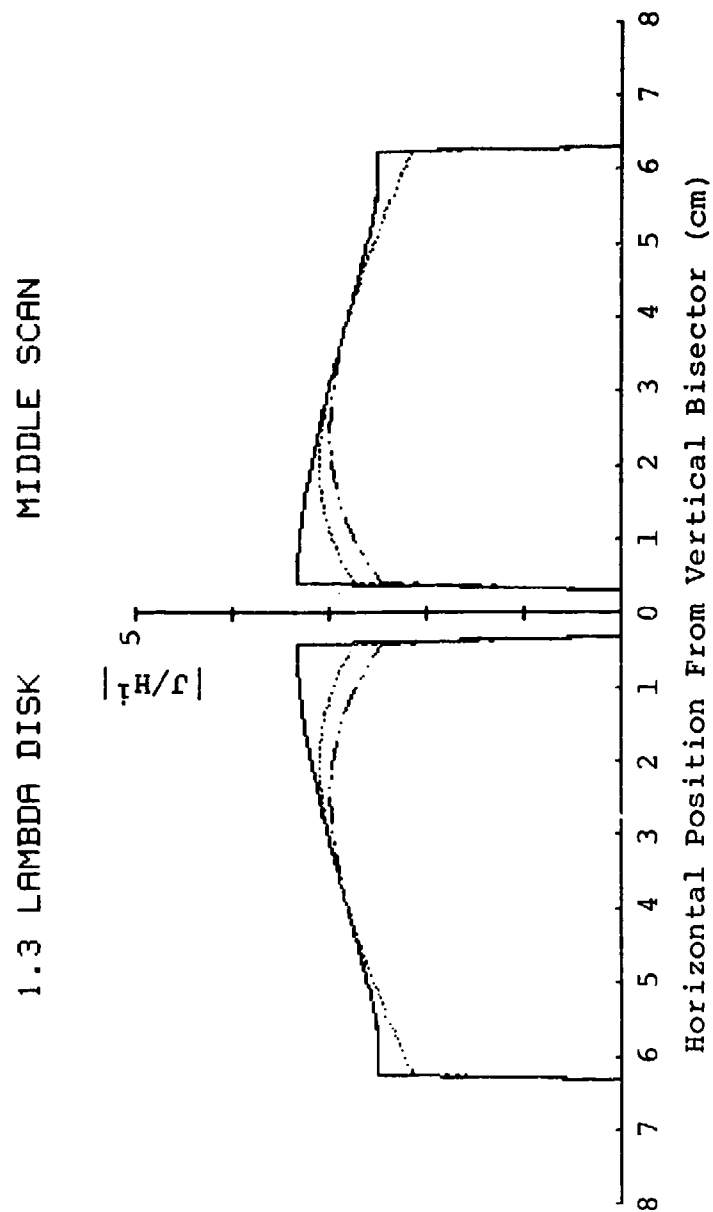


Figure 181: Plot of current components for the 1.3 wavelength circular disk (middle scan).

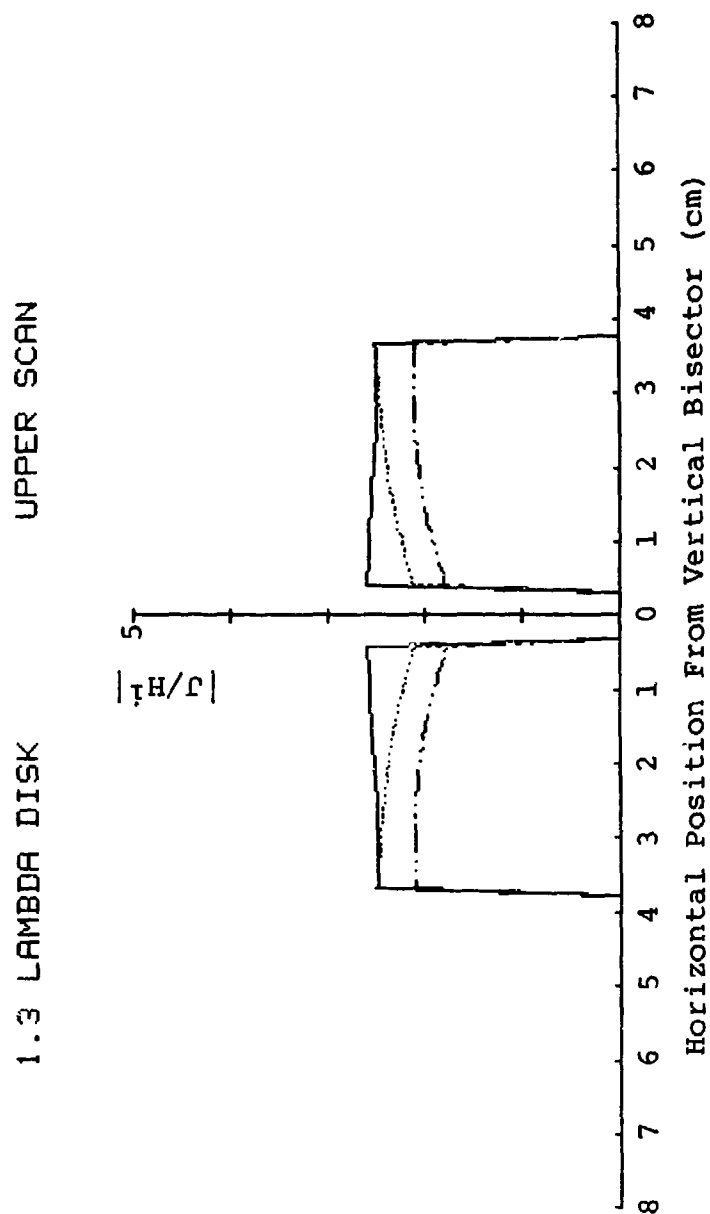


Figure 182: Plot of current components of the 1.3 wavelength circular disk (upper scan).

Relative Current

To compare the validity of IR detection at this stage in the overall project, one is interested in the form of the obtained current solution rather than a closed form relationship of coating current density to the unperturbed metal plate current density. Thus, for the .38 wavelength square plate and disk, a comparison follows for the vertical magnetic field probe results which correspond essentially to total current in this case, the IR results, and the theoretical solution for the disk. The technique is that of scaling the plots from this work to a common horizontal distance for a given horizontal scan and scaling the vertical distance from the zero current base line to a common vertical distance for the current at the mid point of the scan. The equipment used included an HP 9875A Digitizer, an HP 9835A Minicomputer and an HP 9872A Plotter. Thus, form is perserved though a numerical comparison does not apply.

The key to the following plots is as follows:

Magnetic Field Probe - smooth line

IR Detection Results - jagged line

Theoretical Solution - xxxxx

.38 WAVELENGTH CIRCULAR DISK (LOWER SCAN)

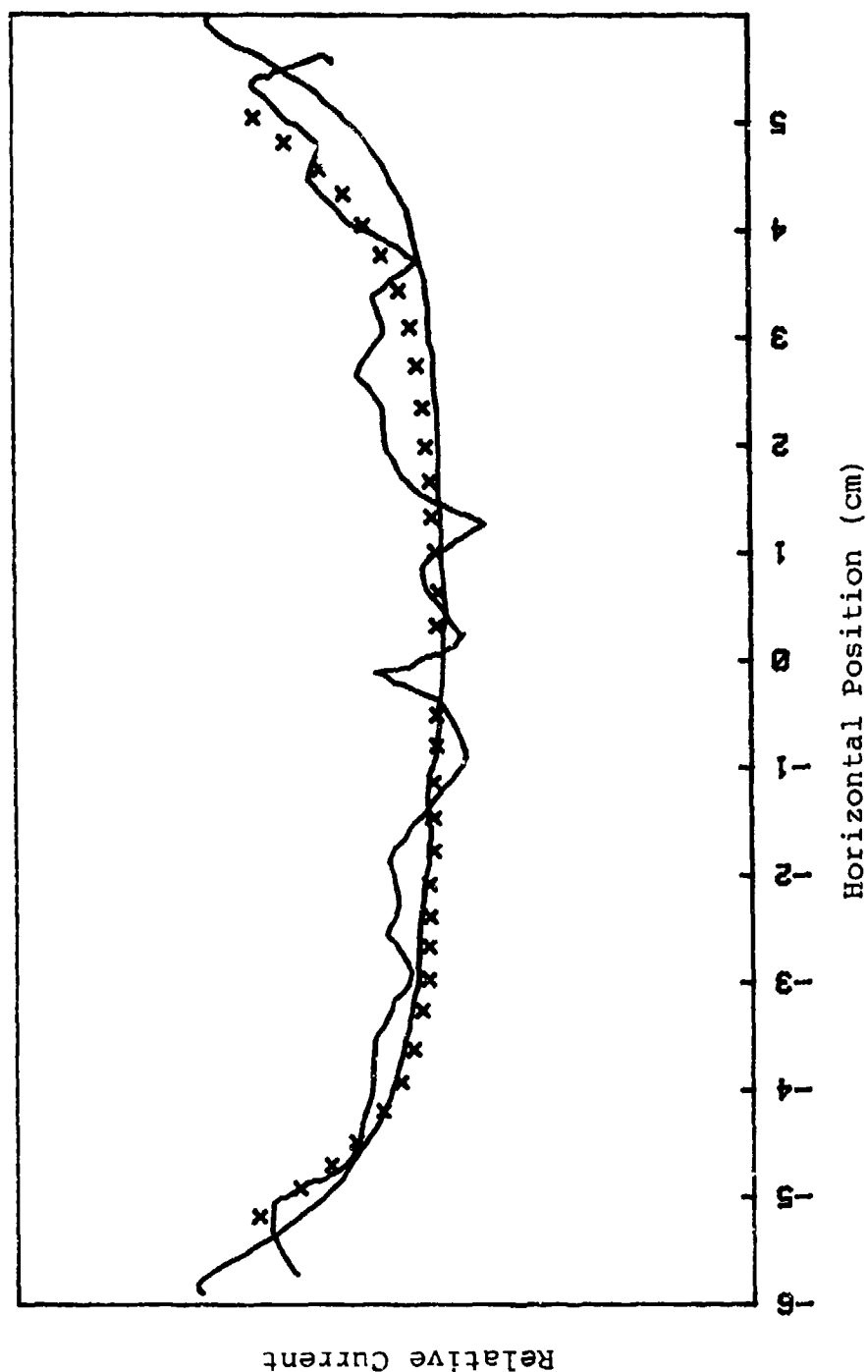


Figure 183: Correlation of theoretical, probe, and IR results for the .38 wavelength circular disk (lower scan).

.38 WAVELENGTH CIRCULAR DISK (MIDDLE SCAN)

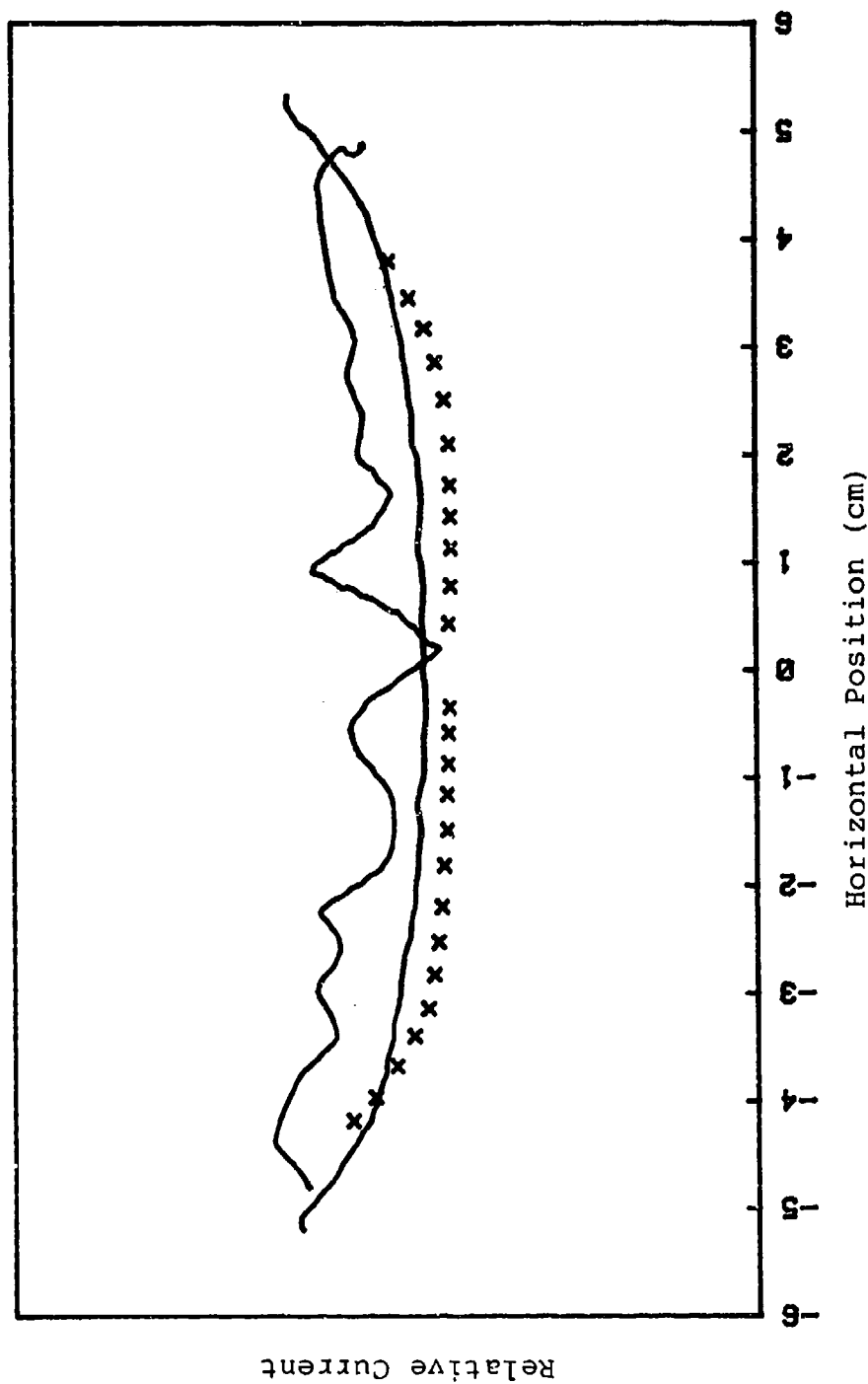


Figure 184: Correlation of theoretical, probe, and IR results for the .38 wavelength circular disk (middle scan).

.38 WAVELENGTH CIRCULAR DISK (UPPER SCAN)

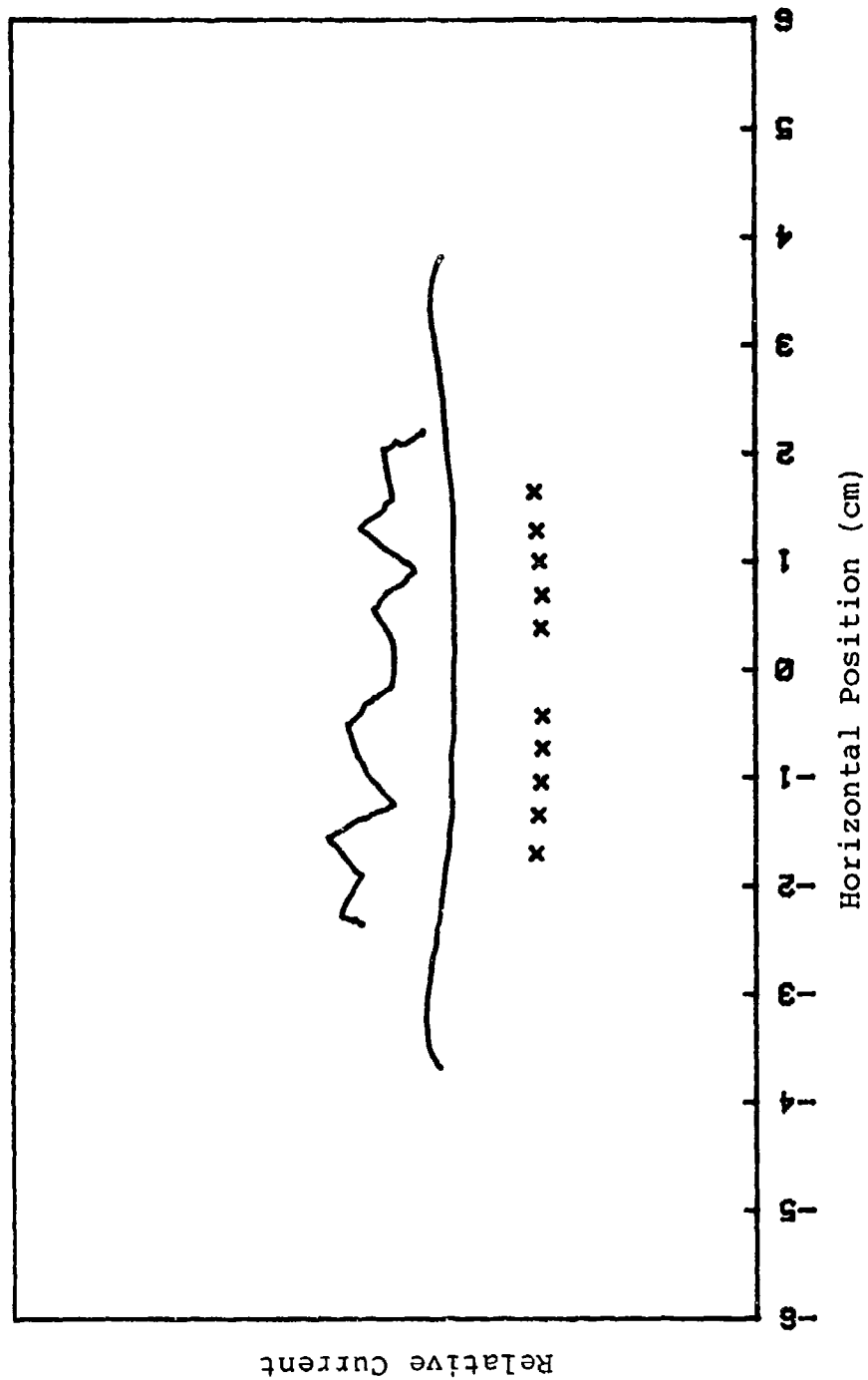


Figure 185: Correlation of theoretical, probe, and IR results for the .38 wavelength circular disk (upper scan).

.38 WAVELENGTH SQUARE PLATE (LOWER SCAN)

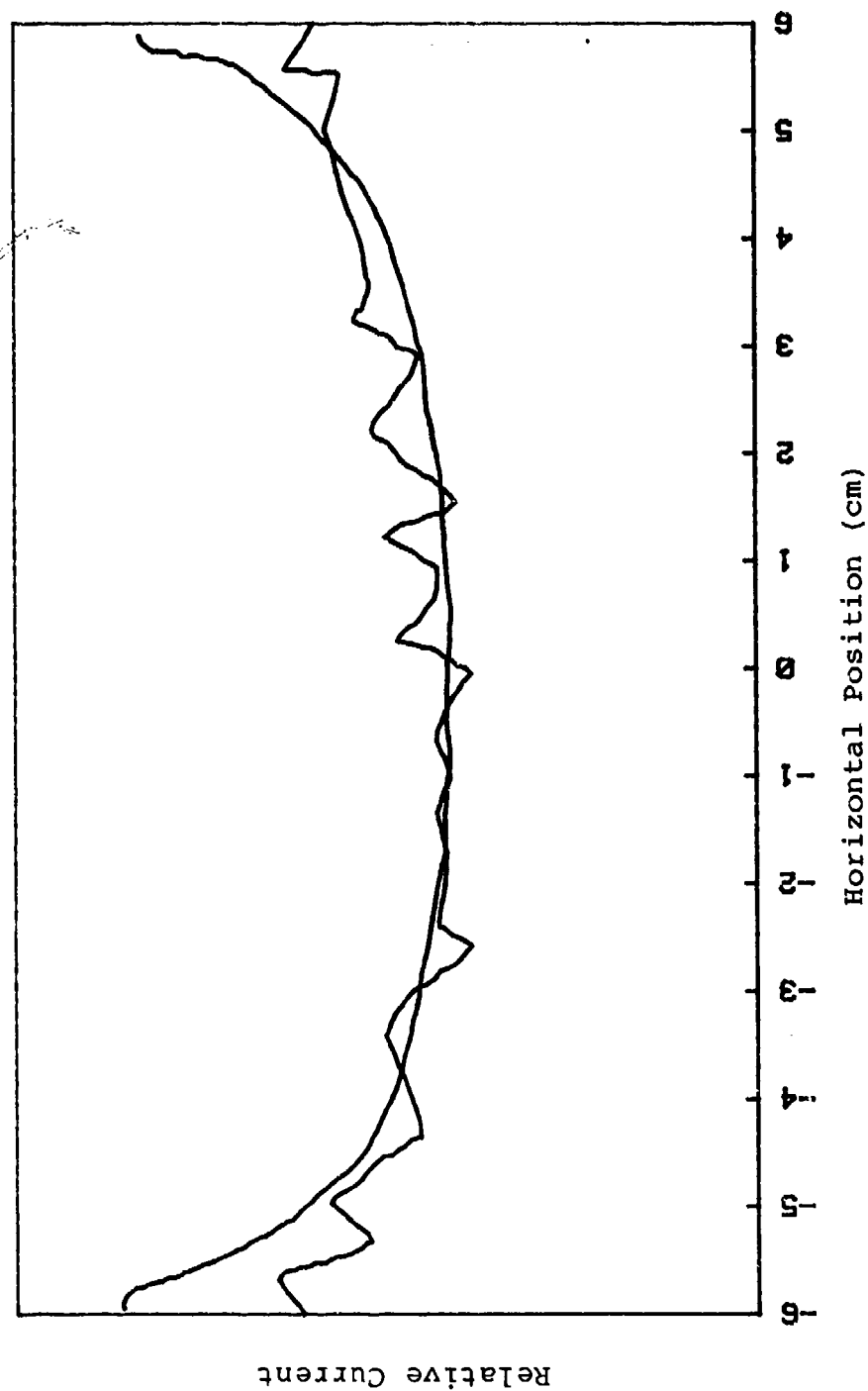


Figure 186: Correlation of the magnetic field probe and IR results for the .38 wavelength square plate (lower scan).

.38 WAVELENGTH SQUARE PLATE (MIDDLE SCAN)

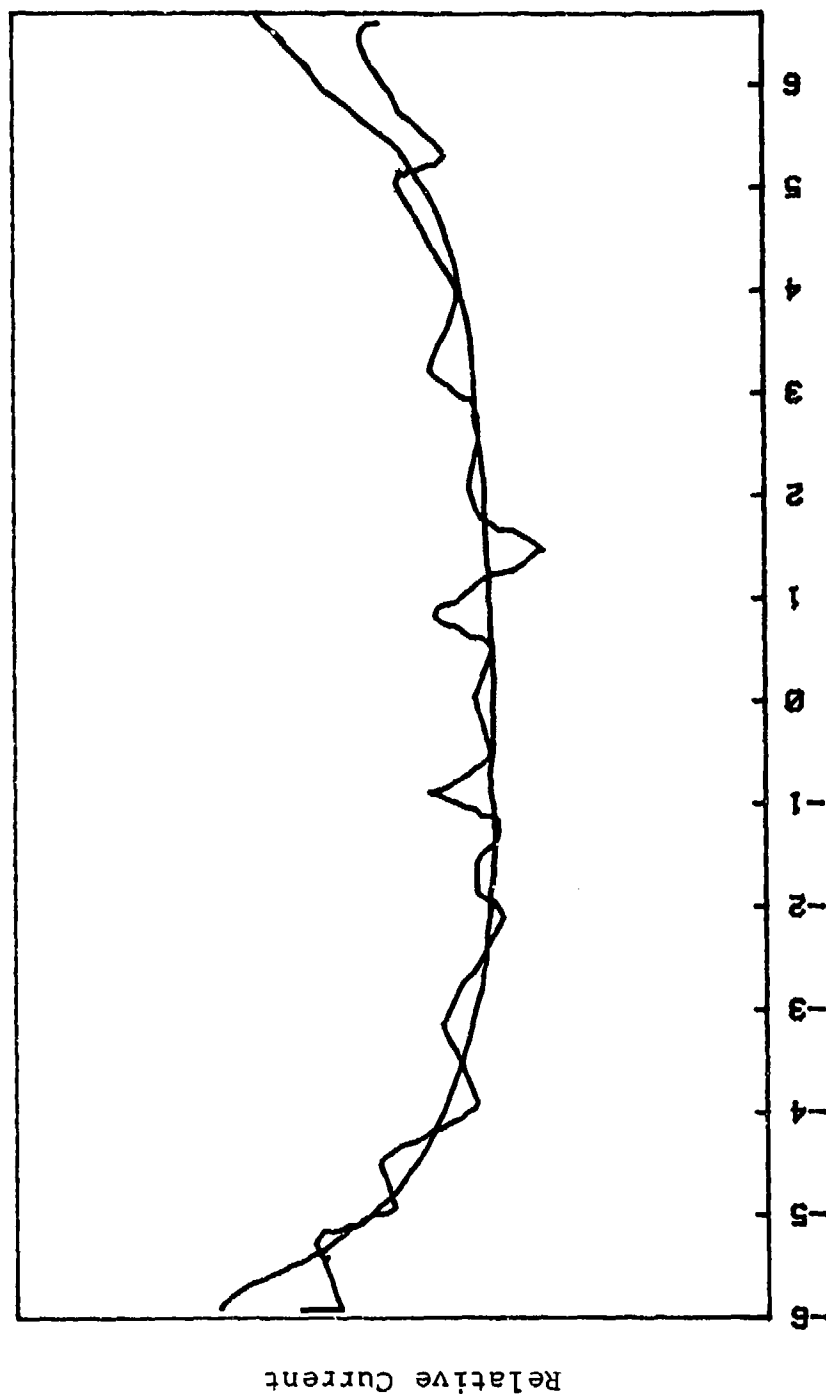


Figure 187: Correlation of the magnetic field probe and IR results for the .38 wavelength square plate (middle scan).

.38 WAVELENGTH SQUARE PLATE (UPPER SCAN)

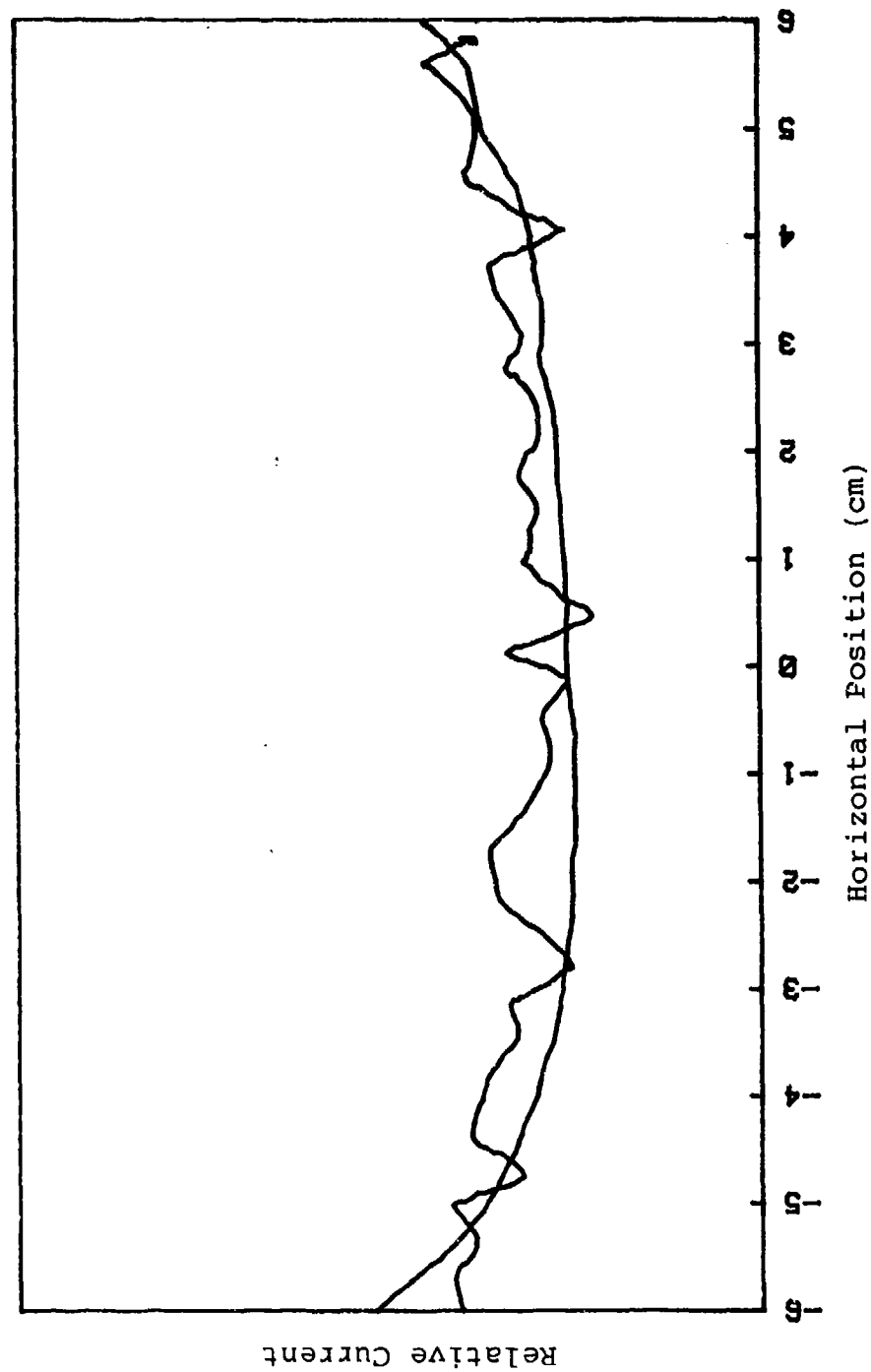


Figure 188: Correlation of the magnetic field probe and IR results for the .38 wavelength square plate (upper scan).

Now, to compare the square plate theoretical results one looks at the bisecting lines of the 1.0 wavelength square plate solved by Wilton and notes once again that the dominant current is vertical so that the vertical magnetic probe measurement applies though, unfortunately, is the least symmetric probe result obtained. The 1.0 wavelength and .50 wavelength square plates are included for the lower scan for plots on carbon/paraffin over metal and for aquadac on plexiglass. Note that the shapes are essentially the same but the variations from maximum to minimum current density levels are higher for aquadac on plexiglass. The key for these four plots remains as in the previous ones. The last plot is a comparison of the theoretical solutions. Wilton's is the solid line and the Body of Translational results from Appendix C are "X"s. Note the decrease at the midpoint of the "X" plot.

1.0 WAVELENGTH SQUARE PLATE (LOWER SCAN)

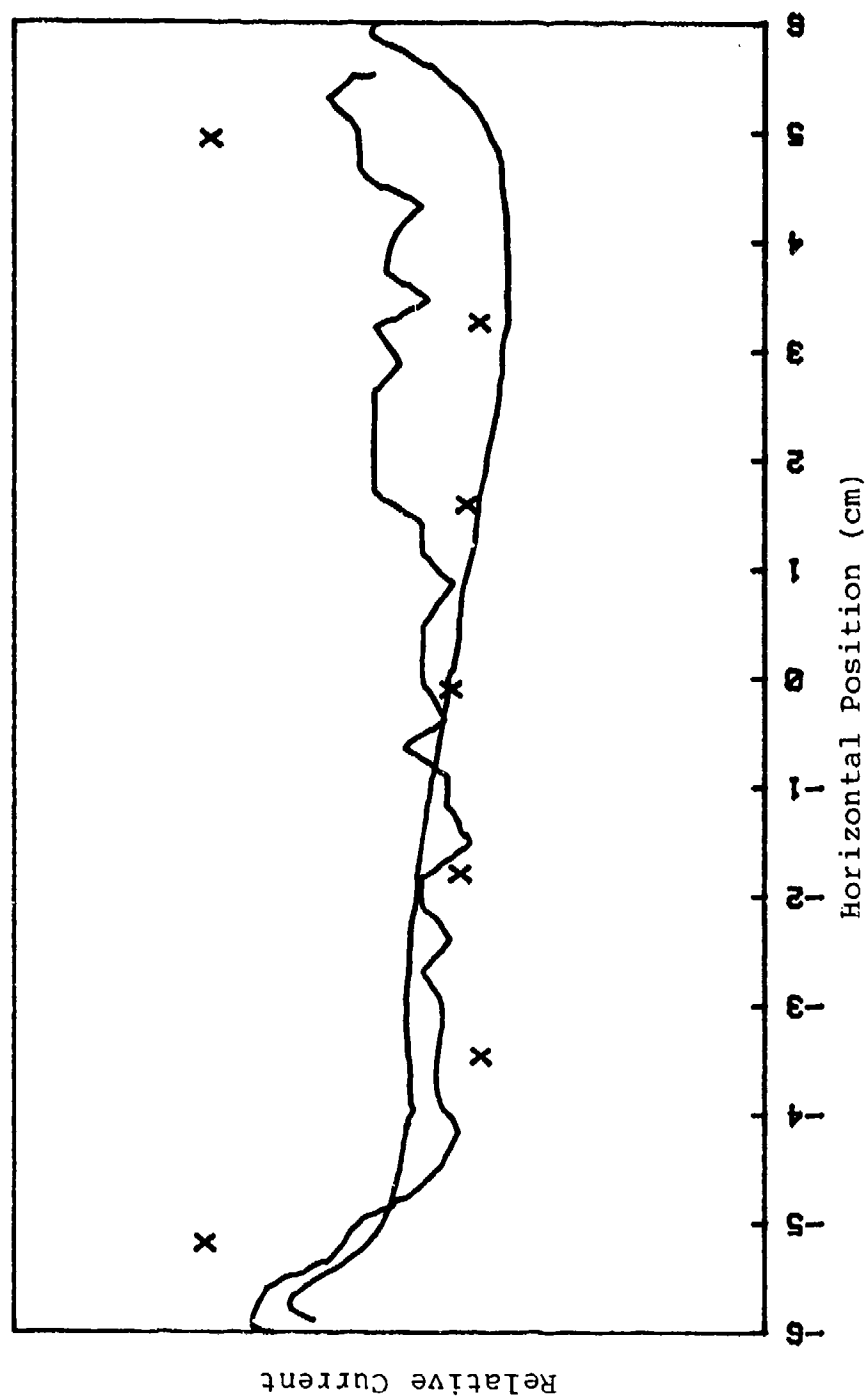


Figure 189: Correlation of theoretical, probe, and IR results for the 1.0 wavelength square plate (carbon/paraffin on metal).

1.0 WAVELENGTH SQUARE PLATE (LOWER SCAN) *

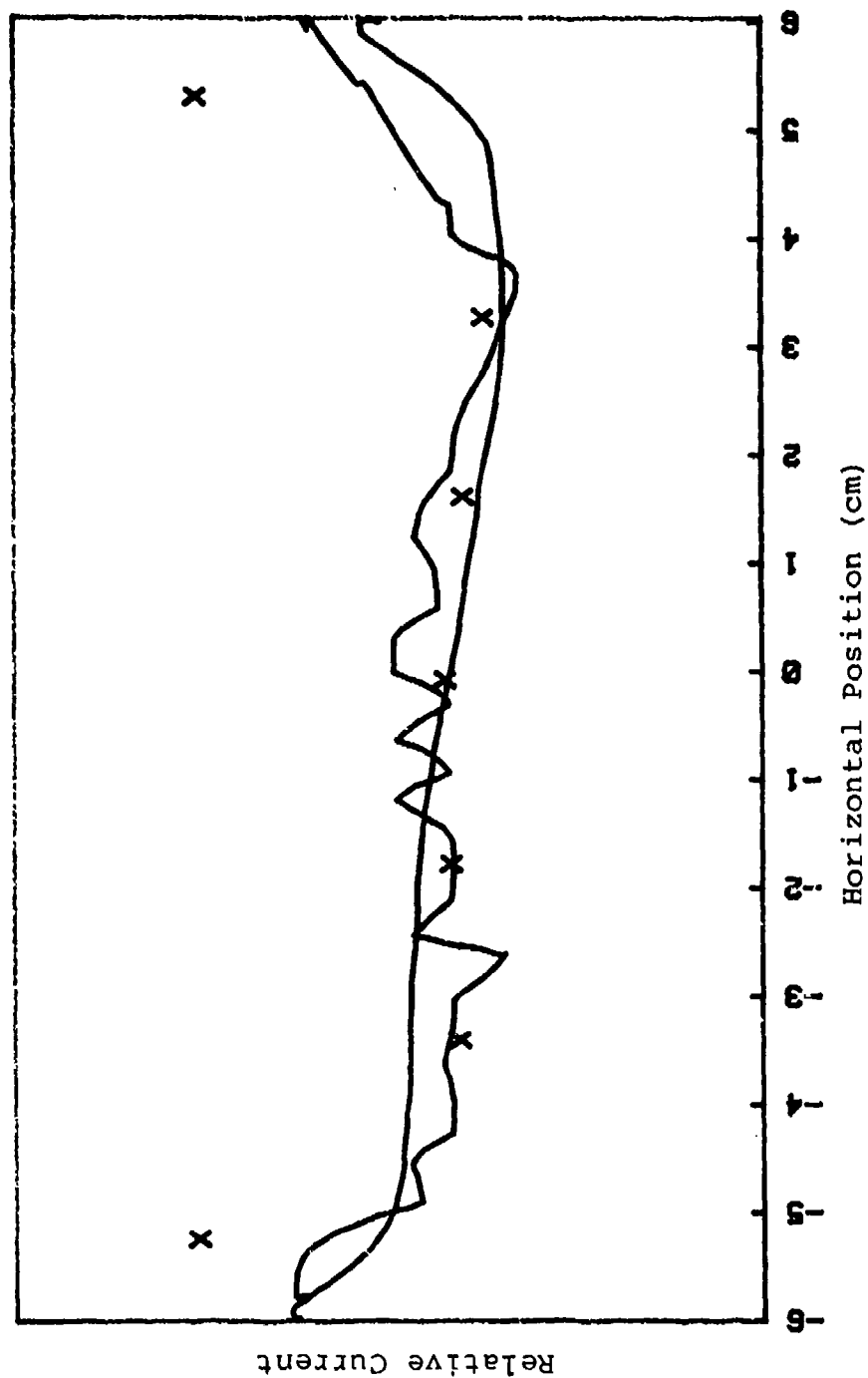


Figure 190: Correlation of theoretical, probe, and IR results for the 1.0 wavelength square plate (aquadac on plexiglass).

.50 WAVELENGTH SQUARE PLATE (LOWER SCAN)

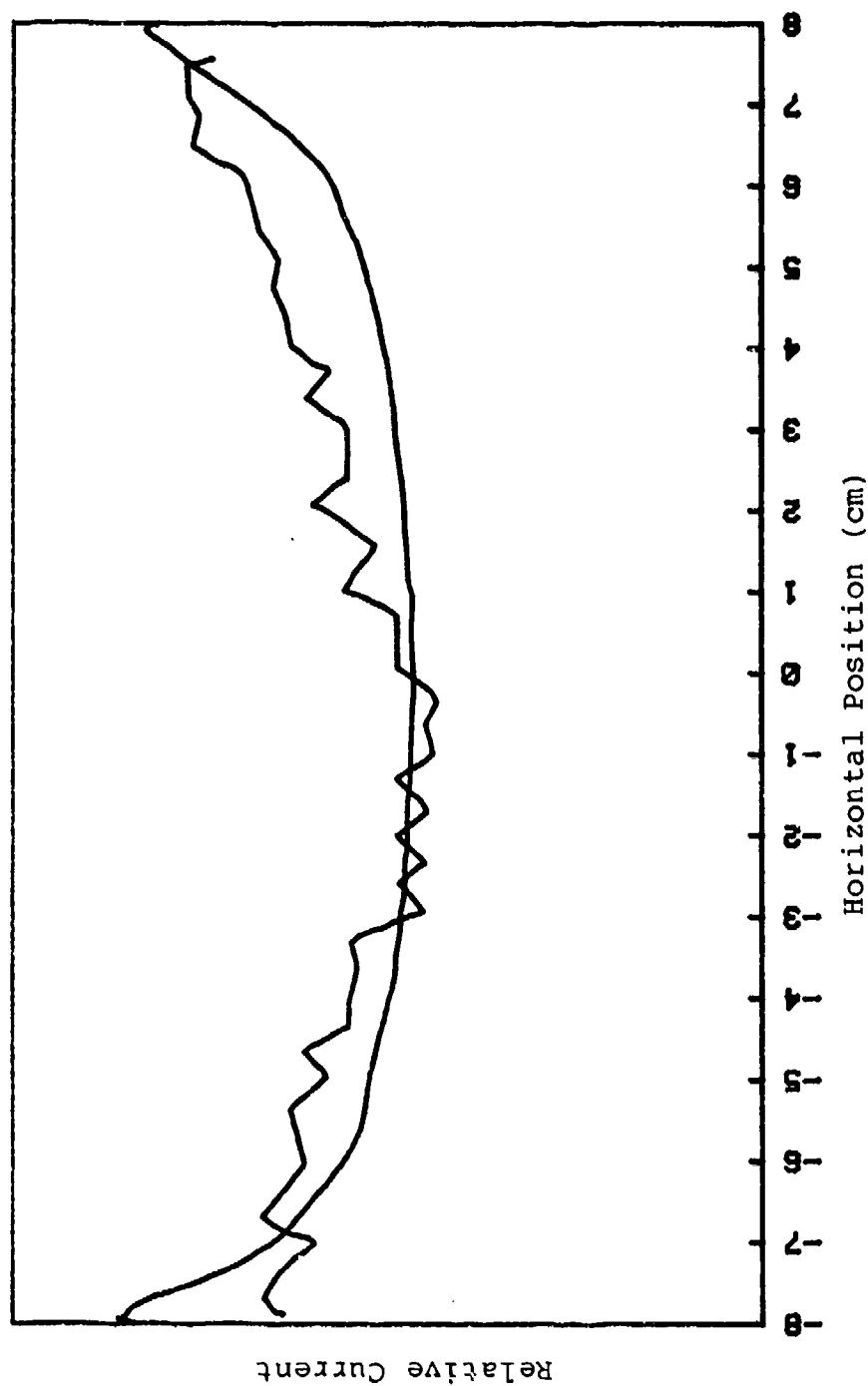


Figure 191: Correlation of theoretical, probe, and IR results for the .50 wavelength square plate (carbon/paraffin over metal).

.50 WAVELENGTH SQUARE PLATE (LOWER SCAN) *

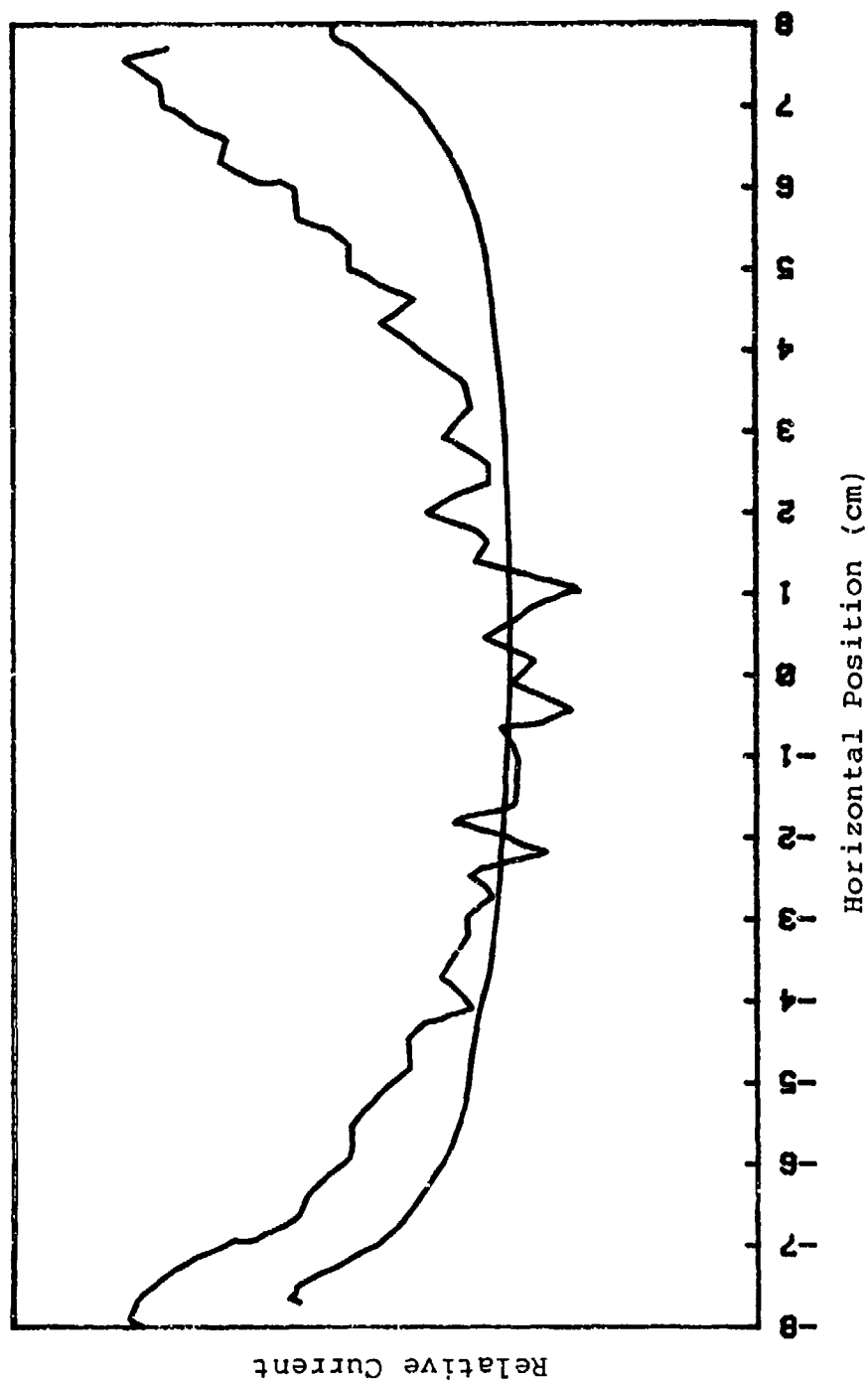


Figure 192: Correlation of theoretical, probe, and IR results for the .50 wavelength square plate (aquadac on plexiglass).

ELECTROMAGNETIC COMPUTER CODE COMPARISON

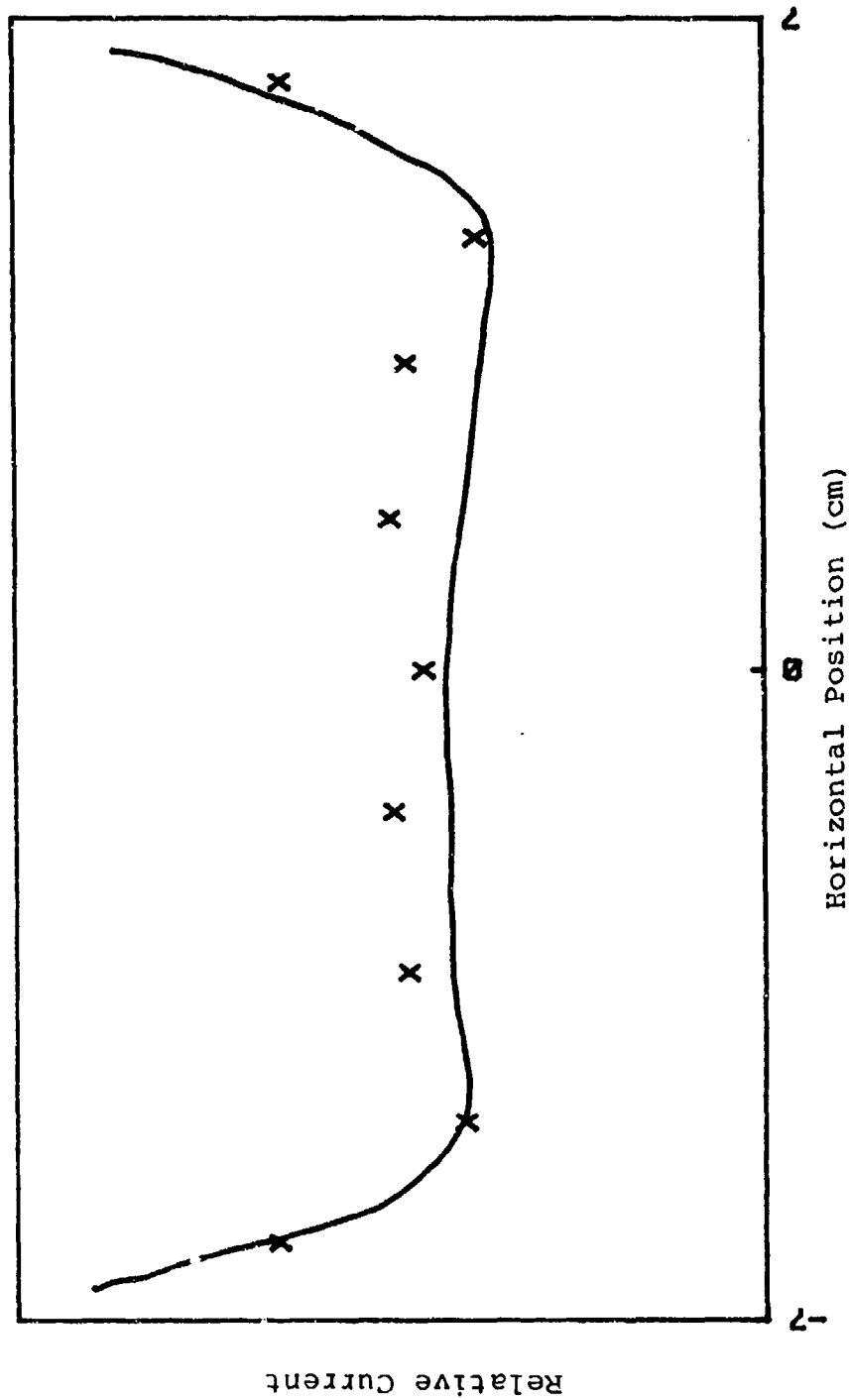


Figure 193: Theoretical comparison of Body of Translation
Computer Code for the 1.0 wavelength square plate.

CHAPTER VIII

CONCLUSIONS

The qualitative studies on the infrared detection of microwave induced surface currents has been extended to a quantitative investigation for flat plates. Though high resolution, infrared-obtained current density distributions were not achievable with the present state of coating development and available equipment, a methodology for verifying the IR results against classic approaches was demonstrated.

A laboratory facility was designed and constructed to test the merits of the IR approach using simple shapes. A plane wave was established at the target and verified with a magnetic field probe. The vertical current component was correlated through magnetic field probe measurements with the theoretical prediction for the perfectly conducting case. The vertical probe measurements for dominant vertical component cases detected total current and compared favorably with similar patterns seen by the IR on both

carbon/paraffin over metal and aquadac on plexi-glass.

The case of the .38 wavelength square plate and circular disk exhibited a high degree of correlation with theoretical and magnetic field probe results. The asymmetries and lack of high resolution of some of the other targets could be attributed in part to coating inhomogeneities and separation distance from the metallic plate as well as a digitization and storing process that eliminates one half of the available data. The thermal reservoir effect of a large aluminum ground plane is also detrimental for optimum current detection based on a heating pattern.

Supplementary investigations such as the angular dependence of emissivity and subsequent utilization of a correction matrix point to applicability for complex structure where probe measurements become increasingly more difficult and time consuming.

Having developed an experimental procedure to relate isotherm unit determinations to temperature, and finally current density, one can proceed with further study of the coating problem. Verification should continue along this established path of correlation with magnetic field probes and theoretical

results until coatings are improved and simple shapes have been studied. As target complexity increases, the rapid method of information collection over the entire object using infrared techniques should prove to be increasingly significant when contrasted with classic point by point measurements and mathematical modeling techniques.

BIBLIOGRAPHY

1. AGA Thermovision 680 Operating Manual, AGA Infrared Systems AB, 5-81 Lidingsö, Sweden, 1975.
2. Andrejewski, W., "Die Beugung elektromagnetischer Wellen an der leitenden Kreisscheibe und an der kreisförmigen Öffnung im leitenden ebenen Schirm," Zeitschrift für angewandte Physik, Vol. 5, 1953, pp 173-186.
3. Andrews, C. L., "Diffraction Pattern in a Circular Aperture Measured in the Microwave Region," Journal of Applied Physics, Vol. 21, August 1950, pp 761-767.
4. Baum, C. E., "Parameters for Some Electrically Small Electromagnetic Sensors, AFWL EMP 1-2, Sensor and Simulation Note 38, 1968.
5. Bevan, E. J. and Effinger, W. C., "An AGA-680 Thermovision Calibration," NWC Technical Memorandum 4107, Naval Weapons Center, China Lake, CA, February 1980.
6. Bevington, P. R., Data Reduction and Error Analysis for the Physical Sciences, McGraw-Hill Book Company, NY, 1969.
7. Bouwkamp, C. J., "On the Diffraction of Electromagnetic Waves by Small Circular Disks and Holes," Philips Research Reports, Vol. 5, No. 6, December 1950, pp 401-422.
8. Bouwkamp, C. J., "A Note on Singularities Occurring at Sharp Edges in Electromagnetic Diffraction Theory," Physica XII, No. 7, October 1946, pp 467-474.
9. Bowman, J. J., Senior, T. B. A., and Uslenghi, P. L. E., Electromagnetic and Acoustic Scattering by Simple Shapes, North-Holland Publishing Company, Amsterdam, 1969.

10. Burton, R. W., Sega, R. M., and Martin, V. M., "Experimental Determination of Electromagnetic Pulse (EMP) Absorption on Complex Shapes," Proceedings of the Nuclear Electromagnetic Pulse Meeting (NEM) 1980, Anaheim, CA, August 1980.
11. Burton, R. W., "Real Time Infrared Detection of Surface Current Distributions," Proceedings of the Eighth European Microwave Conference, Paris, France, September 1978.
12. Butler, C. M., "Aperture Fundamentals," Applications of the Method of Moments to Electromagnetic Fields, Strait, B. J., Editor, The SCEEE Press, 1980, pp 171-211.
13. Carpenter, C. R. and Andrews, C. L., "Measurement of Surface-Current Densities," Journal of the Optical Society of America, Vol. 65, No. 3, March 1975, pp 246-247.
14. Cottony, H. V. and Wilson, A. C., "Gains of Finite-Size Cover-Reflector Antennas," IRE Transactions on Antennas and Propagation, October 1958, pp 366-369.
15. Dancak, C., "Temperature Calibration of Fast Infrared Scanners," Photogrammetric Engineering and Remote Sensing, Vol. 45, No. 6, June 1979, pp 799-751.
16. Dell, R. O., Carpenter, C. R., and Andrews, C. L., "Optical Design of Anechoic Chambers," Journal of the Optical Society of America, Vol. 62, No. 7, July 1972, pp 902-906.
17. Eggiman, W. H., "Higher-Order Evaluation of Electromagnetic Diffraction by Circular Disks," IRE Transactions on Microwave Theory and Techniques, September 1961, pp 408-418.
18. Electromagnetic Pulse Sensor Handbook, Vol. 1, Air Force Weapons Laboratory, June 1971.
19. Ginzton, E. L., Microwave Measurements, McGraw-Hill Book Company, Inc., NY, 1957.
20. Greene, F. M., "NBS Field Strength Standards and Measurements (30 Hz to 1000 MHz)," Proceedings of The IEEE, Vol. 55, No. 6, June 1967, pp 970-981.

21. Harrington, R. F., Field Computations by Moment Methods, The Macmillan Company, NY, 1968.
22. Harrington, R. F., Time-Harmonic Electromagnetic Fields, McGraw-Hill Book Company, NY, 1961.
23. Harrington, R. F. and Mautz, J. R., "Theory and Computation of Characteristic Modes for Conducting Bodies," AFCRL-70-0657, Scientific Report No. 9, December 1970.
24. Hewlett Packard 9845B Software Manual, Hewlett Packard Corporation, 1980.
25. Hsieh, C. K. and Ellingson, W. A., "A Quantitative Determination of Surface Temperatures Using an Infrared Camera," Modern Utilization of Infrared Technology III, SPIE, Vol. 124, 1977, pp 228-235.
26. Jackson, J. D., Classical Electrodynamics, John Wiley & Sons, Inc., NY, 1962.
27. Jasik, H., Editor, Antenna Engineering Handbook, McGraw-Hill Book Company, Inc., NY, 1961.
28. King, R. W. P., Mimno, H. R., and Wing, A. H., Transmission Lines, Antennas, and Wave Guides, Dover Publications, Inc., NY, 1965.
29. Kraus, J. D., Antennas, McGraw-Hill Book Company, NY, 1950.
30. Kraus, J. D., "The Corner-Reflector Antenna," Proceedings of the I.R.E., November 1940, pp 513-519.
31. Mallon, C., Denson, R., Leadon, R. E., and Flanagan, T. M., "Coaxial Geometry Experiments," EMP Theoretical Notes, Note 317, 12 January 1981.
32. Martin, V. M., Sega, R. M., Stewart, C. V., and Burton, R. W., "Application of Infrared Thermography in the Analysis of Induced Surface Currents due to Incident Electromagnetic (EM) Radiation on Complex Shapes," Infrared Systems, Vol. 256, Society of Photo-Optical Instrumentation Engineers (SPIE), September 1980.

33. Mautz, J. R. and Harrington, R. F., "An Improved E-Field Solution for a Conducting Body of Revolution," RADC-TR-80-194, Phase Report, June 1980.
34. Meixner, J., "The Behavior of Electromagnetic Fields at Edges," IEEE Transaction on Antennas and Propagation, Vol. AP-20, No. 4, July 1972, pp 442-446.
35. Naor, M., and Senior, T. B. A., "Scattering by Resistive Plates," RADC TR-82-47, March 1982.
36. Perala, R. A., "Integral Equation Solution for Induced Surface Currents on Bodies of Revolution," IEEE Transactions on Electromagnetic Compatibility, Vol. EMC-16, No. 3, August 1974, pp 172-177.
37. Schelkunoff, S. A., Antennas, Theory, and Practice, John Wiley & Sons, Inc., NY, 1957.
38. Sega, R. M. and Burton, R. W., "Correlation of Known Surface Current Values With Measurements Utilizing Infrared Techniques," Proceedings of the National Radio Science Meeting, Boulder, CO, January 1982.
39. Sega, R. M. and Burton, R. W., "Experimental Determination of Electromagnetic Energy Absorption on Complex Shapes," Proceedings of the National Radio Science Meeting (URSI), Boulder, CO, January 1981.
40. Sega, R. M., Martin, V. M., and Burton, R. W., "Experimental Determination of Electromagnetic Energy Absorption on Complex Shapes; A Progress Report," Proceedings 1981 International Union of Radio Science (URSI), Low Angeles, CA, June 1981.
41. Sega, R. M., Stewart, C. V., and Burton, R. W., "Induced Surface Currents Obtained Through Infrared Techniques Correlated with Known Values for Simple Shapes," Proceedings of the IEEE Region 5 Conference, Colorado Springs, CO, May 1982.

42. Sega, R. M., Martin, V. M., Warmuth, D. B., and Burton, R. W., "An Infrared Application to the Detection of Induced Surface Currents," Modern Utilization of Infrared Technology VII, Vol. 304, SPIE-The International Society for Optical Engineering, August 1981.
43. Sega, R. M., Martin, V. M., and Burton, R. W., "Microwave Induced Surface Current Measurement via Infrared Detection," 1982 International Symposium Digest-Antennas and Propagation (IEEE), Albuquerque, NM, May 1982.
44. Selim, J. D. and Burton, R. W., "Infrared Detection of Surface Charge and Current Distributions," Thesis Report, Naval Postgraduate School, Monterey, CA, December 1977.
45. Senior, T. B. A., "Low Frequency Scattering by Metallic Plates; A Critique," Proceedings of the National Radio Science Meeting, Albuquerque, NM, May 1982, pp 65.
46. Sparrow, E. M. and Cess, R. D., Radiation Heat Transfer, Augmented Edition, McGraw-Hill Book Company, NY, 1978.
47. Stark, Introduction to Numerical Methods, MacMillan Company, New York, NY, 1970.
48. Tyras, G., Radiation and Propagation of Electromagnetic Waves, Academic Press, NY, 1969.
49. Uslenghi, P. L. E., "Computation of Surface Currents on Bodies of Revolution," Alta Frequenza, N. 8, Vol. XXXIX, 1970.
50. Whiteside, H. and King, R. W. P., "The Loop Antenna as a Probe," IEEE Transactions on Antennas and Propagation, May 1964, pp 291-297.
51. Wilton, D. R., Rao, S. S. M., and Glisson, A. W., "Electromagnetic Scattering by Surfaces of Arbitrary Shape," Applications of the Method of Movements to Electromagnetic Fields, Strait, B. J., Editor, The SCEEE Press, 1980, pp 139-170.
52. Wolff, E. A., Antenna Analysis, John Wiley & Sons, Inc., NY, 1966.

APPENDIX A

WAVE DEMONSTRATOR

A ripple tank was designed and constructed for two-dimensional modeling and visualization of wave phenomena. The water wave interactions should roughly correspond to electromagnetic wave interactions in an anechoic chamber. This appendix develops the basic theory of water wave propagation and includes data from experiments conducted to characterize water wave propagation in the tank.

Tank

The wave demonstrator tank was constructed of a 5' x 8' sheet of 3/16 inch plexiglas, with 2" x 6" wood sides waterproofed with epoxy paint and fastened with 1/4 inch bolts at the corners. The plexiglass sheet was fitted into a 3/4 inch slot around the wood sides and sealed with silicon adhesive. Figure A1 shows the construction drawings. The assembled wave generator apparatus is seen in Figure A2. The center support was usually necessary to prevent sagging of the plexiglass sheet as the tank could be filled with up to 3 cm depth of water.

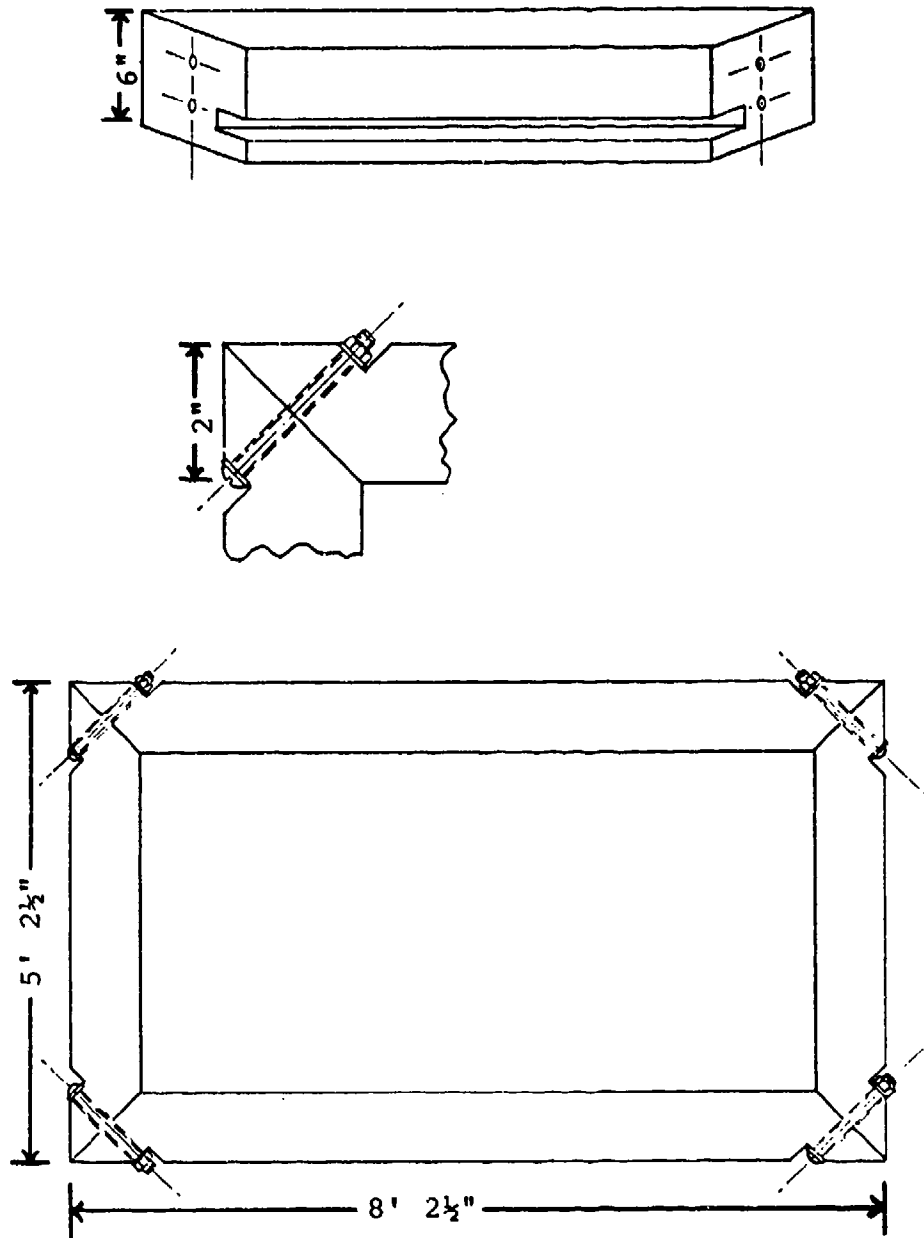


Figure A1: Construction drawings.



Figure A2. The wave generator apparatus.

A 28 volt D.C. motor turned the wave generator drive shaft, which rotated two eccentric circular cams. Ten inch aluminum rods set on the cams, which drove the probes which extended into the water and produced the water wave. The circular cams were drilled $3/16$ inch off center, which produced a near-sinusoidal motion at the cam of $3/32$ inch amplitude. The pivot ends of the aluminum rods and the probe attachments were moved toward or away from the cams to make the probe oscillation amplitude variable between $3/32$ inch and $1/2$ inch.

Several different probes were attached to the wave generator. With the cams rotated in phase, a cylindrical rod was attached to produce plane waves. A single round bead was attached to one rod to produce spherical waves. Two element antenna array simulation was accomplished with a two bead/two rod arrangement. The point sources could also be driven out of phase by rotation of the cams on the drive shaft.

The wave generator was designed to be clamped to the side of the wave demonstrator tank, or it may be suspended above the tank for experiments away from the tank sides.

When a variable voltage power supply was used, the frequency of the wave generator was variable up to six cycles per second. The maximum voltage which

could be applied to the D.C. motor was 28 volts. The graph (Figure A6) shows the frequency for the wave generator as a function of applied voltage, and was used to obtain desired frequencies in the wave demonstrator tank.

Miscellaneous Equipment

A point light source suspended from the ceiling was necessary to project the images of the water waves onto the floor beneath the tank. Also, a strobe light was used to stop or slow the apparent motion of the waves for detailed study or wavelength measurement. A white screen ruled in 20 cm x 20 cm squares was used on the floor beneath the tank to facilitate viewing and analysis of the waves. Black and white photographs of the wave images on the floor were also taken by mounting the flash above the tank and focusing the camera on the floor from the side of the tank. The proper camera f-stop for tank photographs with 400 ASA film was f/8.5. Absorbing material, including cloth strips, foam rubber, and sloping barrier inserts could be added to the tank wherever reflections were not desired.

Theory of Water Wave Propagation

The following analysis is from Water Waves by N. F. Barber (1). A more detailed derivation including water viscosity and surface tension may be

found in Ripple Tank Studies of Wave Motion by W. Llowarch (2), and a circulation approach by complex analysis is developed in Water Waves by J. J. Stoker (3). The approach taken in this appendix is sufficient to understand wave propagation for ripple tank modeling, and gives results which correspond closely to those observed in the tank.

The motion of water molecules in water waves is both transverse and longitudinal--the actual motion is approximately elliptical. The molecules at the tops of the wave crests move forward, in the troughs they move opposite the direction of the wave, and in the leading and trailing slopes the molecules move up and down, respectively.

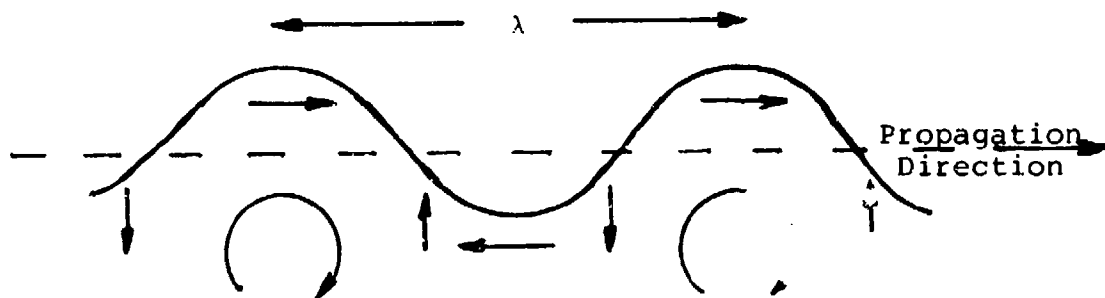


Figure A3. Wave Motion.

The motion of any single molecule may be broken down into two components: Transverse and longitudinal. These amplitudes, A and B, respectively, are shown in Figure A4.

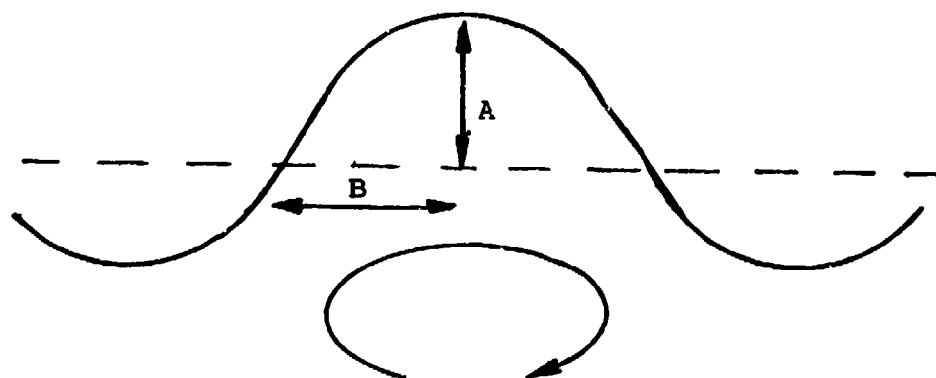


Figure A4. Wave Amplitudes.

Note that A is not necessarily equal to B , and in a shallow wave tank, A will generally be much smaller than B . Also, the amplitudes of the motion A and B will be much smaller than the wave length λ . If the shape of the wave is assumed to be sinusoidal, then the angle between the vertical and the normal to the water surface where the water slope is the greatest is $\frac{2\pi A}{\lambda}$, shown in Figure A5, below.

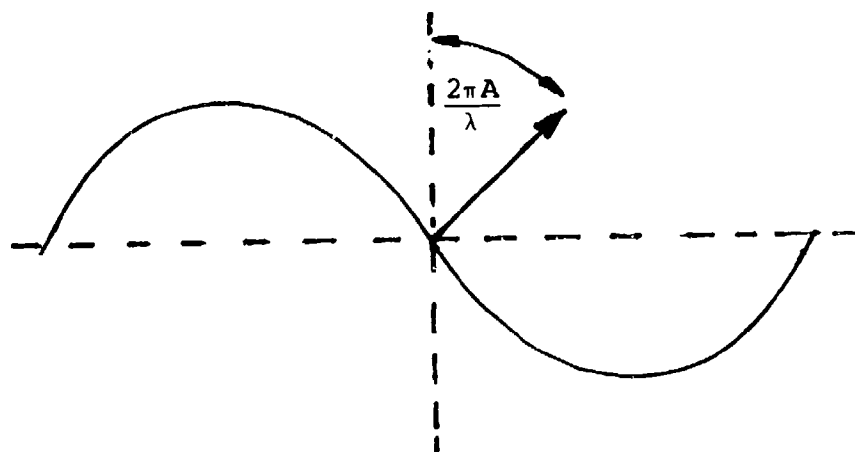


Figure A5. Wave Slope.

The ratio of the horizontal acceleration of the water at that point to the acceleration of gravity is simply the tangent of $\frac{2\pi A}{\lambda}$, and since $A \ll \lambda$, can be considered equal to $\frac{2\pi A}{\lambda}$. Thus,

$$\frac{\text{Horizontal Acceleration (Max)}}{\text{Gravitational Acceleration}} = \frac{2\pi A}{\lambda}$$

and thus

$$\text{Horizontal Acceleration (Max)} = \frac{2\pi A g}{\lambda}$$

Knowing the longitudinal amplitude of the sinusoid B and the horizontal acceleration, the angular frequency ω may be deduced:

$$\text{Horizontal acceleration (Max)} = \omega^2 B,$$

$$\text{thus } \frac{2\pi A g}{\lambda} = \omega^2 B$$

$$\text{so } \omega = \sqrt{\frac{2\pi A g}{B \lambda}}$$

The period T equals $\frac{2\pi}{\omega}$, so

$$\lambda = \frac{g T^2}{2\pi} \frac{A}{B}$$

Since the wave velocity V equals $\frac{\lambda}{T}$,

$$V = \sqrt{\frac{A}{B} \frac{g \lambda}{2\pi}} \quad (\text{A1})$$

Equation A1 shows how the wave velocity depends on the wavelength, and thus the frequency. As the frequency increases, the wavelength decreases, and thus the wave velocity decreases.

Also as the water gets shallower, the ratio

$\frac{A}{B}$ in equation A1 gets correspondingly lower. Therefore, as the depth of the water increases or decreases, the velocity of the waves in turn increases or decreases.

For very shallow water (for example 5 mm in the wave demonstrator tank) the depth of the water D is much less than the wavelength λ . If the vertical velocity component of the water is assumed to also follow a sinusoidal function, then the ration $\frac{A}{B}$ equals $\frac{2\pi D}{\lambda}$.

Substituting into equation A1:

$$V = \sqrt{gD} \quad (A2)$$

Therefore, for very shallow water (where $D \ll \lambda$), the wave velocity is only dependent on the depth of the water, and little dispersion of the different frequency components of a wave should occur.

Comparing the predicted results from equation A1 to actual results in the wave demonstrator tank:

For $\frac{A}{B}$ assumed equal to 1, $\lambda = 0.1\text{m}$, $g = 9.81 \frac{\text{m}}{\text{s}^2}$

$$\begin{aligned} V &= \sqrt{\frac{A}{B} \frac{g\lambda}{2\pi}} \\ &= 0.4 \frac{\text{m}}{\text{s}} \end{aligned}$$

The experimental value tank measurements was

$V = 0.5 \frac{\text{m}}{\text{s}}$. For a water depth of 5 mm, using equation

A2:

$$\begin{aligned}
 V &= \sqrt{gD} \\
 &= 0.7 \frac{\text{m}}{\text{s}}
 \end{aligned}$$

The experimental value from tank measurements was $V = 0.4 \frac{\text{m}}{\text{s}}$. Therefore, the theoretical results corresponded favorably to the actual results obtained from the wave demonstrator tank.

Theory of Wave Demonstrator Operation

The wave demonstrator tank provided a visualization in two dimensions of wave phenomena by comparison with water waves. The water waves exhibit many of the characteristics of electromagnetic waves: They reflect at their incident angle with a 180° phase change; they interfere constructively and destructively to produce standing waves and interference patterns; they travel slower through shallower water to simulate higher indices of refraction, etc.

Although the waves themselves were very difficult to see in the tank, they were easily observed by projecting their images onto the floor beneath the tank. When a "point" light source was suspended above the tank in a dark room and a sheet of white paper was placed beneath the tank, the convex and concave curvature of the waves acted like converging and diverging lenses, projecting bright and dark lines on the paper. The arrangement is shown in Figure A2, which also shows the distances from the tank to the

light and the paper used for the experiments described in this appendix. These distances were not optimum for all wavelengths and water depths, but were convenient and suitable for a general range of use.

Experimental Wave Characterization

Plane Waves

The wave generator was clamped to the tank side and the plane wave generator attachment (a 4' wooden dowel) was connected to the wave generator arms. Using a meterstick and a stopwatch, measurements of wave velocity and wavelength were made at various water depths from 5 mm to 30 mm and frequencies ranging between 1.5 and 5.5 cycles per second. The experimental data and calculations of wave velocity, frequency, wavelength, and voltage applied to the motor are available in a laboratory notebook at the Air Force Academy. The data is shown in Figures A6 through A8 as graphs of frequency as a function of voltage applied to the motor, and wave velocity and wavelength of functions of frequency for various water depths. These graphs were used to choose the required water depth and motor voltage to produce a desired frequency, wavelength, and/or wave velocity.

Circular Waves

Because the circular wave probe (a wooden bead) displaces much less water than the plane wave

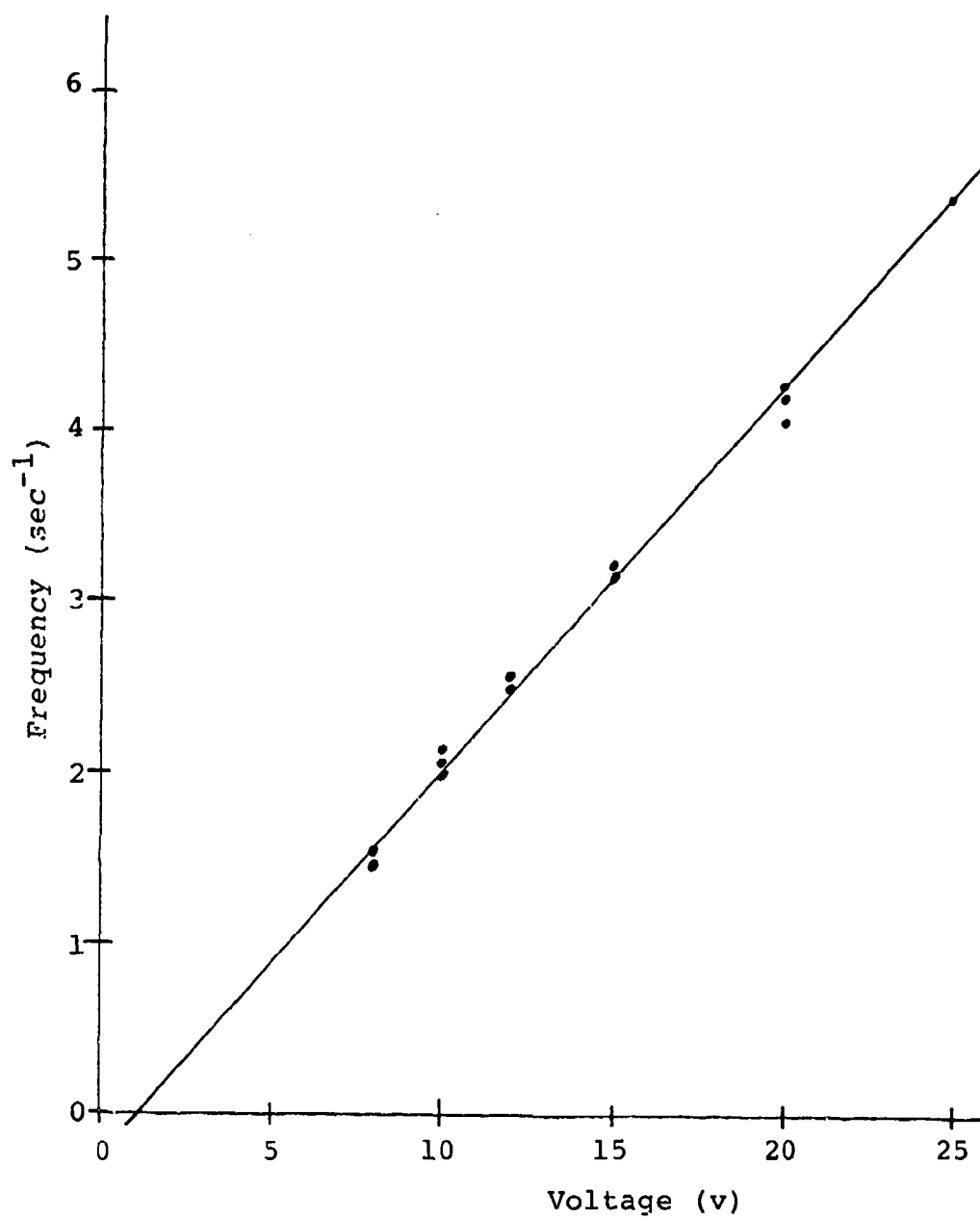


Figure A6: Plot of Frequency vs Voltage.

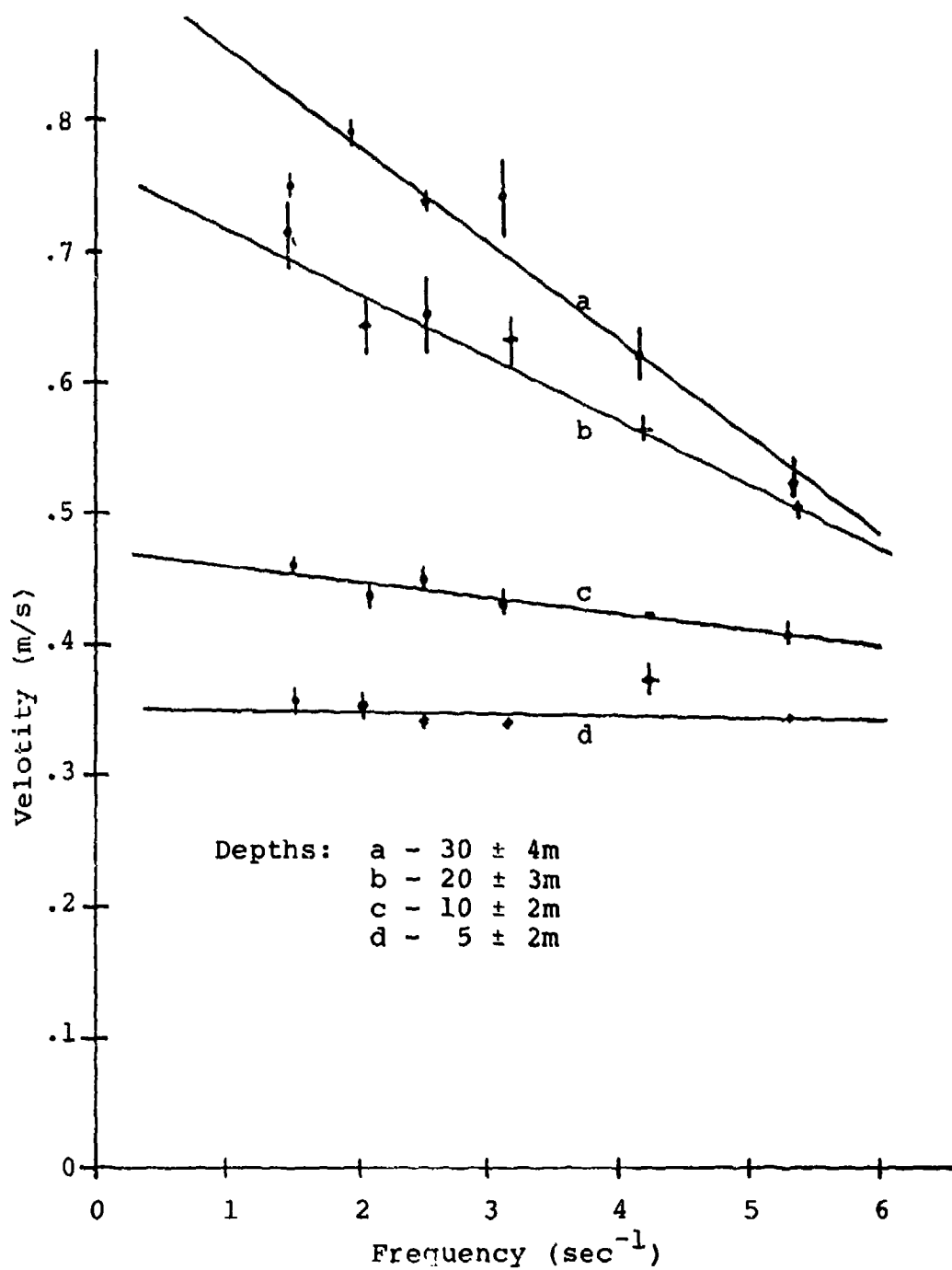


Figure A7: Velocity vs Frequency

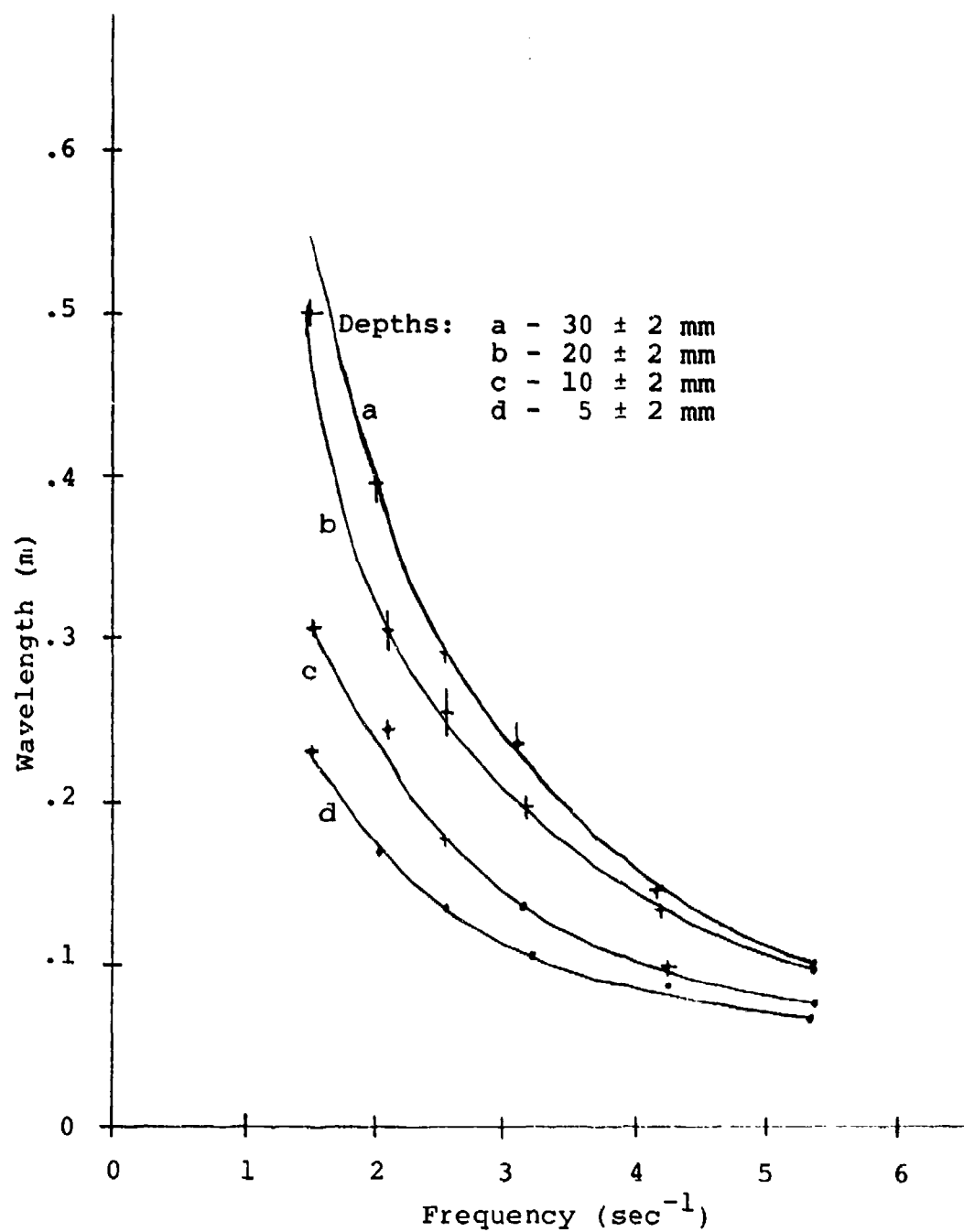


Figure A8: Plot of Wavelength vs Frequency

probe, and due to the $\frac{1}{\lambda}$ dependence of the amplitude of a two dimensional wave and the great attenuation over distance of a water wave, the images formed of a circular wave were considerable dimmer, especially at low frequency and shallow water depth.

Consequently, it was recommended that a minimum water depth of 10 mm or minimum wave generator frequency of 3 cycles per second be used to obtain easily visible circular wave images. The included calibration charts were used to set approximate motor voltages and water depths for desired frequencies, wavelengths, and wave velocities.

Visual Characteristics

The waves in the tank projected sharper images on the floor as the water depth was increased. However, dispersion of the higher frequency components becomes more of a problem with increased water depth, as shown in the wave velocity vs. frequency chart in Figure A7. The best balance between image clarity and reduced dispersion was determined experimentally to occur at approximately 15 mm water depth, for wavelengths associated with antenna modeling and acoustic characterization experiments. This is especially important for circular waves produced by a spherical probe, since the amplitude of the plane waves produced by a cylindrical probe is greater. For reflection,

refraction, and interference experiments where higher frequencies (5 to 6 cycles per second) were used, slower waves with less dispersion were obtained and seen easily using shallower water depths (less than 10 mm. .

Operation of the Wave Demonstrator

Water depth and wave generator frequency most suitable for proper wavelength and velocity and sharpest viewing were selected. For short wavelengths with maximum clarity, a shallow water depth (10 mm or less) is most desirable, providing the least dispersion and low wave velocity at the shortest wavelengths. For demonstrations of varying wave velocity with varying frequency (dispersion), a deeper water depth (30 mm) were most effective. Where waves were scaled to the dimensions of an anechoic chamber containing a reflector and scattering object a compromise between wave image brightness and frequency dispersion was achieved with a water depth of about 15 mm. Once the proper water depth had been selected, the desired wavelength or wave velocity was found from the included graphs. After selecting the required wavelength or wave velocity from the family of water depth curves, the required frequency was read from Figure A8. The applied voltage for the motor was determined from the frequency vs. voltage graph.

The wavelengths in the graphs were measured from the images projected on the paper by the setup in Figure A2. To convert these lengths to actual wavelengths of the water waves in the tank, the dimensions were multiplied by $\frac{170}{270}$ --the ratio of distances of the light from the tank and floor.

With the tank filled to the required depth, the light was suspended approximately 1.7 meters above the water, and a white screen positioned approximately one meter below the tank. For the best wave images, the height of the probe was adjusted so that the probe comes as close as possible to the plexiglass bottom of the tank, without touching the bottom at the lowest point in its motion, or breaking contact with the water surface at the top. The best images usually occurred with minimum wave generator amplitude, except when using the circular wave generator at low frequency, where a larger amplitude will be needed. The images of the waves in the tank were clearly visible on the screen beneath the tank when illuminated by a "point" light source above the tank.

The antenna patterns from corner reflector antennas were modeled to scale in the tank using the circular wave generator probe and placing straight rigid barriers at an angle behind the probe. Recommended dimensions for corner reflectors were

found in "Gains of Finite-Size Corner Reflector Antennas" by H. V. Cottony and A. C. Wilson (4).

Parabolic transmitting antennas were modeled in the tank by generating circular waves at the focus of the parabolic reflector. A waveguide and microwave horn antenna were also modeled in the tank by propagating plane waves down a $\frac{1}{2}\lambda$ wide constriction in the tank and into a diverging set of rigid barriers. Recommended dimensions for horn antennas may be found in Antennas by John D. Kraus (5).

The photographs that follow were taken using only a flash mounted above the tank in an otherwise dark room. An open shutter at f/8.5 was used with 400 ASA film. Note the relatively plane wavefronts after approximately three divisions on the screen. The dark vertical lines are meter stick barriers modeling the sides of "perfectly" reflecting anechoic chamber walls. Corner reflector aperature angles and antenna to apex distances were varied to investigate gain and plane wavefront parameters.



Figure A9: Parabolic Reflector.

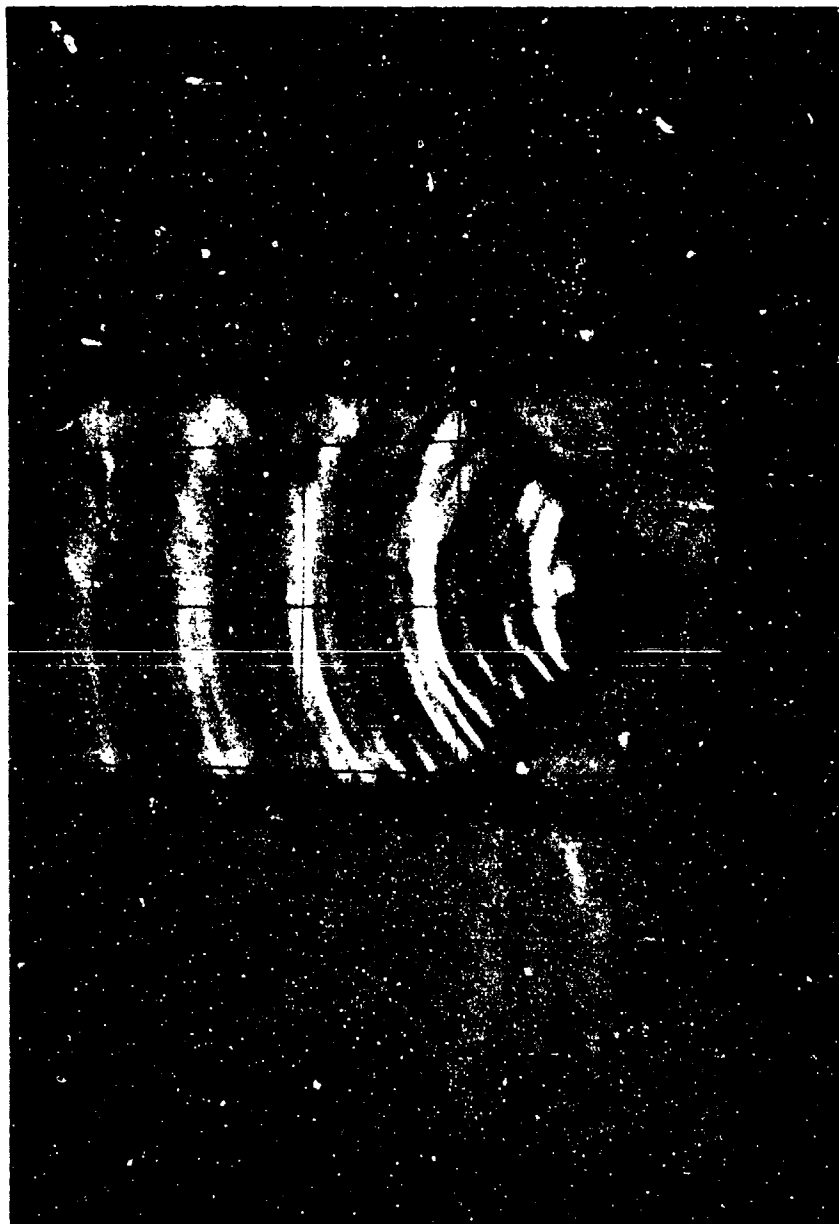


Figure A10: 90° Corner Reflector.

References

1. Barber, N. F., Water Waves. London: Wykeham Publications Ltd., 1969.
2. Llowarch, W., Ripple Tank Studies of Wave Motion, London: Oxford University Press, 1961.
3. Stoker, J. J., Water Waves, New York: Interscience Publishers, Inc., 1957.
4. Cottony, H. V., and Wilson, A. C., "Gains of Finite-Size Corner Reflector Antennas," in IRE Transactions on Antennas and Propagation, October 1958, pp. 366-368.
5. Kraus, John D., Antennas, New York: McGraw-Hill Book Co., 1950.

APPENDIX B

BODY OF REVOLUTION INPUT DATA

Disk sizes (wavelengths)

.15

.38

.50

1.0

1.3

3.0

[illegible]

[illegible]

IIIIIIIIIIIIIIIIIIII
P0000000000000000
E+0000000000000000
W+0000000000000000
U+0000000000000000
A5000000000000000
H0000000000000000
M0000000000000000
.....

00000000000000000000
P000000000000000000
E+0000000000000000
W+0000000000000000
U+0000000000000000
A5000000000000000
H0000000000000000
M0000000000000000
.....

IIIIIIIIIIIIIIIIIIII
P0000000000000000
E+0000000000000000
W+0000000000000000
U+0000000000000000
A5000000000000000
H0000000000000000
M0000000000000000
.....

[illegible]

APPENDIX C

BODY OF TRANSLATION SQUARE PLATE RESULTS

The square plate problems were run with a Bodies of Translation Code (BOT) called A-STAR. This code, developed by McDonnell Douglas Research Labs, models bodies which have a constant cross sectional geometry such as flat plates and cylinders. The code predicts two orthogonal components of surface current distribution and radiated near and far electric and magnetic fields. The code also has the capability of modeling enclosing encaps on the geometry as well as attached thin wires.

The concept of this model assumes model current distributions of the form $\exp(jntA/L)$ along the length of the body. This model is presently limited to bodies of about 10 square wavelengths.

.38 LAMBDA SQUARE PLATE

.108E-08	.623E-09	.200E-08	.715E-09	.785E-09	.229E-08	.730E-09	.217E-09	.317E-08
.360E-03	.563E-03	.413E-03	.323E-03	.150E-03	.323E-03	.413E-03	.563E-03	.360E-03
.115E-02	.118E-02	.983E-03	.883E-03	.299E-03	.883E-03	.938E-03	.118E-02	.115E-02
.203E-02	.173E-02	.126E-02	.124E-02	.748E-03	.124E-02	.126E-02	.173E-02	.203E-02
.292E-02	.226E-02	.189E-02	.210E-02	.120E-02	.210E-02	.189E-02	.226E-02	.292E-02
.378E-02	.287E-02	.229E-02	.269E-02	.165E-02	.269E-02	.229E-02	.287E-02	.378E-02
.505E-02	.325E-02	.272E-02	.329E-02	.209E-02	.329E-02	.272E-02	.325E-02	.505E-02
.591E-02	.364E-02	.292E-02	.393E-02	.239E-02	.393E-02	.292E-02	.364E-02	.591E-02
.677E-02	.380E-02	.344E-02	.459E-02	.269E-02	.459E-02	.344E-02	.380E-02	.677E-02
.719E-02	.400E-02	.346E-02	.492E-02	.284E-02	.492E-02	.346E-02	.400E-02	.719E-02
.762E-02	.397E-02	.375E-02	.526E-02	.299E-02	.526E-02	.375E-02	.397E-02	.762E-02
.761E-02	.396E-02	.374E-02	.557E-02	.299E-02	.557E-02	.374E-02	.396E-02	.761E-02
.806E-02	.397E-02	.372E-02	.556E-02	.299E-02	.556E-02	.372E-02	.397E-02	.806E-02
.807E-02	.397E-02	.371E-02	.557E-02	.284E-02	.557E-02	.371E-02	.397E-02	.807E-02
.807E-02	.397E-02	.398E-02	.593E-02	.284E-02	.593E-02	.398E-02	.397E-02	.807E-02
.807E-02	.424E-02	.400E-02	.597E-02	.269E-02	.597E-02	.400E-02	.424E-02	.807E-02
.852E-02	.450E-02	.455E-02	.631E-02	.269E-02	.631E-02	.455E-02	.450E-02	.852E-02
.852E-02	.477E-02	.482E-02	.630E-02	.269E-02	.630E-02	.482E-02	.477E-02	.852E-02
.895E-02	.502E-02	.506E-02	.660E-02	.284E-02	.660E-02	.506E-02	.502E-02	.895E-02
.895E-02	.528E-02	.531E-02	.656E-02	.284E-02	.656E-02	.531E-02	.528E-02	.895E-02
.895E-02	.528E-02	.530E-02	.655E-02	.299E-02	.655E-02	.530E-02	.528E-02	.895E-02

Figure C1: Body of translation solution for total current on the upper half of a .38 wavelength square plate.

.50 LAMBDA SQUARE PLATE

.829E-09	.206E-09	.159E-08	.898E-09	.123E-08	.104E-08	.215E-08	.816E-09	.209E-08
.665E-03	.682E-03	.390E-03	.902E-04	.150E-08	.902E-04	.390E-03	.682E-03	.665E-03
.141E-02	.125E-02	.806E-03	.369E-03	.699E-03	.369E-03	.806E-03	.125E-02	.141E-02
.200E-02	.179E-02	.146E-02	.705E-03	.140E-02	.705E-03	.146E-02	.179E-02	.200E-02
.262E-02	.207E-02	.209E-02	.121E-02	.210E-02	.121E-02	.209E-02	.207E-02	.262E-02
.360E-02	.232E-02	.271E-02	.154E-02	.280E-02	.154E-02	.271E-02	.232E-02	.360E-02
.424E-02	.243E-02	.332E-02	.205E-02	.385E-02	.205E-02	.332E-02	.243E-02	.424E-02
.493E-02	.262E-02	.395E-02	.238E-02	.420E-02	.238E-02	.395E-02	.262E-02	.493E-02
.528E-02	.290E-02	.427E-02	.255E-02	.490E-02	.255E-02	.427E-02	.290E-02	.528E-02
.567E-02	.308E-02	.495E-02	.270E-02	.524E-02	.270E-02	.495E-02	.308E-02	.567E-02
.609E-02	.330E-02	.529E-02	.287E-02	.524E-02	.287E-02	.529E-02	.330E-02	.609E-02
.649E-02	.332E-02	.529E-02	.286E-02	.559E-02	.286E-02	.529E-02	.332E-02	.649E-02
.649E-02	.331E-02	.565E-02	.285E-02	.559E-02	.285E-02	.565E-02	.331E-02	.649E-02
.648E-02	.328E-02	.600E-02	.284E-02	.559E-02	.284E-02	.600E-02	.328E-02	.648E-02
.689E-02	.327E-02	.600E-02	.284E-02	.594E-02	.284E-02	.600E-02	.327E-02	.689E-02
.690E-02	.348E-02	.635E-02	.284E-02	.594E-02	.284E-02	.635E-02	.348E-02	.690E-02
.731E-02	.351E-02	.671E-02	.301E-02	.629E-02	.301E-02	.671E-02	.351E-02	.731E-02
.773E-02	.371E-02	.671E-02	.318E-02	.664E-02	.318E-02	.671E-02	.371E-02	.773E-02
.772E-02	.370E-02	.706E-02	.318E-02	.664E-02	.318E-02	.706E-02	.370E-02	.772E-02
.811E-02	.386E-02	.706E-02	.334E-02	.699E-02	.334E-02	.706E-02	.386E-02	.811E-02
.810E-02	.385E-02	.706E-02	.334E-02	.899E-02	.334E-02	.706E-02	.385E-02	.810E-02

Figure C2: Body of translation solution for total current on the upper half of a .50 wavelength square plate.

1.0 LAMBDA SQUARE PLATE

.768E-09	.234E-09	.870E-09	.360E-09	.115E-08	.505E-09	.136E-08	.910E-10	.662E-09
.215E-03	.268E-03	.278E-03	.165E-03	.115E-08	.165E-03	.278E-03	.268E-03	.215E-03
.464E-03	.636E-03	.551E-03	.513E-03	.187E-03	.513E-03	.551E-03	.636E-03	.464E-03
.728E-03	.859E-03	.921E-03	.726E-03	.561E-03	.726E-03	.921E-03	.859E-03	.728E-03
.939E-03	.115E-02	.125E-02	.109E-02	.936E-03	.109E-02	.125E-02	.115E-02	.939E-03
.113E-02	.154E-02	.157E-02	.146E-02	.131E-02	.146E-02	.157E-02	.154E-02	.113E-02
.129E-02	.182E-02	.187E-02	.181E-02	.187E-02	.181E-02	.187E-02	.182E-02	.129E-02
.171E-02	.210E-02	.201E-02	.218E-02	.206E-02	.218E-02	.201E-02	.210E-02	.171E-02
.191E-02	.223E-02	.235E-02	.237E-02	.243E-02	.237E-02	.235E-02	.223E-02	.191E-02
.214E-02	.238E-02	.233E-02	.256E-02	.262E-02	.256E-02	.233E-02	.238E-02	.214E-02
.260E-02	.255E-02	.251E-02	.275E-02	.281E-02	.275E-02	.251E-02	.255E-02	.260E-02
.283E-02	.272E-02	.270E-02	.275E-02	.299E-02	.275E-02	.270E-02	.272E-02	.283E-02
.307E-02	.272E-02	.270E-02	.295E-02	.318E-02	.295E-02	.270E-02	.272E-02	.307E-02
.354E-02	.290E-02	.290E-02	.295E-02	.318E-02	.295E-02	.290E-02	.290E-02	.354E-02
.378E-02	.307E-02	.309E-02	.315E-02	.337E-02	.315E-02	.309E-02	.307E-02	.378E-02
.403E-02	.307E-02	.328E-02	.334E-02	.337E-02	.334E-02	.328E-02	.307E-02	.403E-02
.426E-02	.325E-02	.349E-02	.354E-02	.356E-02	.354E-02	.349E-02	.325E-02	.426E-02
.450E-02	.325E-02	.368E-02	.374E-02	.356E-02	.374E-02	.368E-02	.325E-02	.450E-02
.472E-02	.341E-02	.368E-02	.374E-02	.374E-02	.374E-02	.368E-02	.341E-02	.472E-02
.472E-02	.341E-02	.386E-02	.393E-02	.374E-02	.393E-02	.386E-02	.341E-02	.472E-02
.472E-02	.341E-02	.386E-02	.393E-02	.374E-02	.393E-02	.386E-02	.341E-02	.472E-02

Figure C3: Body of translation solution for total current on the upper half of a 1.0 wavelength square plate.

1.3 LAMBDA SQUARE PLATE

.106E-07	.353E-08	.790E-08	.126E-07	.995E-09	.956E-08	.895E-08	.143E-08	.825E-08
.568E-04	.174E-03	.178E-03	.187E-03	.190E-03	.185E-03	.185E-03	.190E-03	.187E-03
.451E-03	.488E-03	.518E-03	.527E-03	.558E-03	.370E-03	.370E-03	.558E-03	.527E-03
.887E-03	.953E-03	.102E-02	.130E-02	.926E-03	.924E-03	.924E-03	.926E-03	.103E-02
.133E-02	.157E-02	.153E-02	.154E-02	.166E-02	.148E-02	.148E-02	.166E-02	.154E-02
.197E-02	.218E-02	.203E-02	.203E-02	.221E-02	.203E-02	.203E-02	.221E-02	.203E-02
.219E-02	.265E-02	.254E-02	.254E-02	.275E-02	.258E-02	.258E-02	.275E-02	.254E-02
.241E-02	.295E-02	.286E-02	.288E-02	.311E-02	.295E-02	.295E-02	.311E-02	.288E-02
.263E-02	.310E-02	.303E-02	.303E-02	.311E-02	.314E-02	.314E-02	.311E-02	.303E-02
.241E-02	.310E-02	.303E-02	.303E-02	.311E-02	.314E-02	.314E-02	.311E-02	.303E-02
.241E-02	.279E-02	.286E-02	.303E-02	.311E-02	.314E-02	.314E-02	.311E-02	.303E-02
.241E-02	.264E-02	.270E-02	.287E-02	.293E-02	.314E-02	.314E-02	.293E-02	.287E-02
.241E-02	.248E-02	.270E-02	.287E-02	.293E-02	.295E-02	.295E-02	.293E-02	.287E-02
.285E-02	.233E-02	.270E-02	.270E-02	.293E-02	.295E-02	.295E-02	.293E-02	.270E-02
.307E-02	.233E-02	.270E-02	.287E-02	.311E-02	.314E-02	.314E-02	.311E-02	.287E-02
.351E-02	.248E-02	.286E-02	.287E-02	.311E-02	.332E-02	.332E-02	.311E-02	.287E-02
.395E-02	.264E-02	.303E-02	.303E-02	.330E-02	.332E-02	.332E-02	.330E-02	.303E-02
.416E-02	.264E-02	.320E-02	.320E-02	.348E-02	.351E-02	.351E-02	.348E-02	.320E-02
.416E-02	.279E-02	.337E-02	.337E-02	.366E-02	.369E-02	.369E-02	.366E-02	.337E-02
.438E-02	.279E-02	.337E-02	.337E-02	.366E-02	.369E-02	.369E-02	.366E-02	.337E-02
.438E-02	.279E-02	.337E-02	.337E-02	.366E-02	.369E-02	.369E-02	.366E-02	.337E-02

Figure C4: Body of translation solution for total current on the upper half of a 1.3 wavelength square plate.

1.3 LAMBDA SQUARE PLATE

.802E-08	.333E-08	.630E-08
.178E-03	.174E-03	.567E-04
.518E-03	.488E-03	.451E-03
.102E-02	.953E-03	.887E-03
.153E-02	.157E-02	.133E-02
.203E-02	.218E-02	.197E-02
.254E-02	.265E-02	.219E-02
.286E-02	.295E-02	.241E-02
.303E-02	.310E-02	.263E-02
.303E-02	.310E-02	.241E-02
.266E-02	.279E-02	.241E-02
.270E-02	.264E-02	.241E-02
.270E-02	.248E-02	.241E-02
.270E-02	.233E-02	.285E-02
.270E-02	.233E-02	.307E-02
.286E-02	.248E-02	.351E-02
.303E-02	.264E-02	.395E-02
.320E-02	.264E-02	.416E-02
.337E-02	.279E-02	.416E-02
.337E-02	.279E-02	.438E-02
.337E-02	.279E-02	.438E-02

Figure C5: Body of translation solution for total current on the upper half of a 1.3 wavelength square plate (continued).

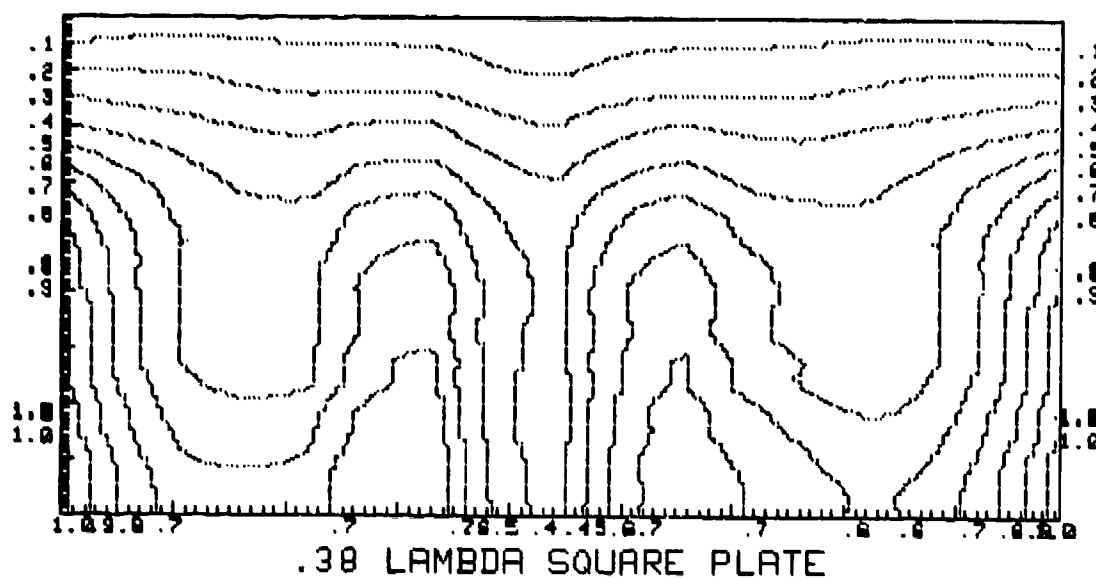


Figure C6: Normalized current contour plot for the $.38$ wavelength square plate (BOT).

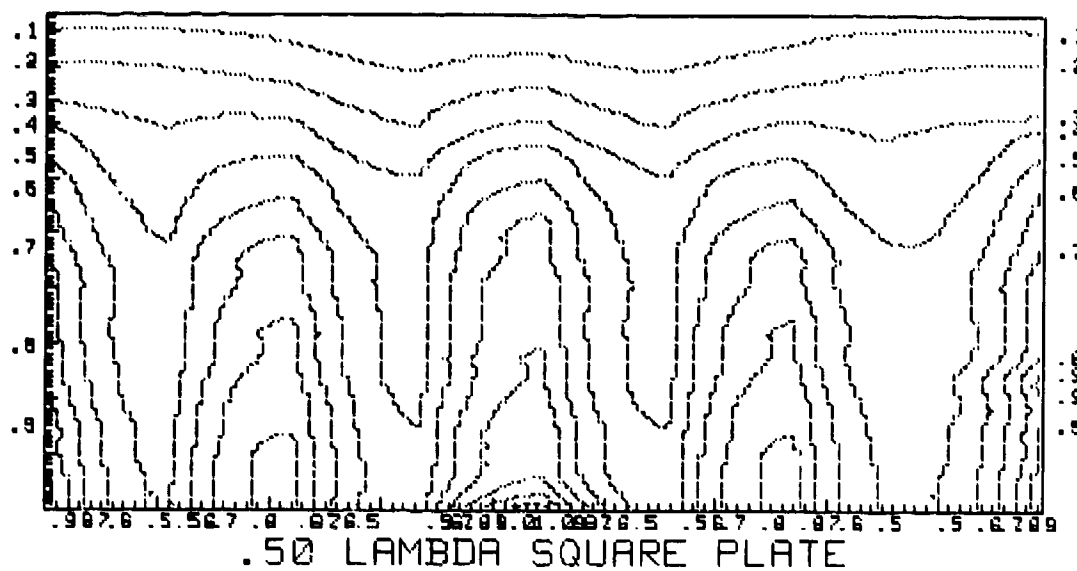


Figure C7: Normalized current contour plot for the $.50$ wavelength square plate (BOT).

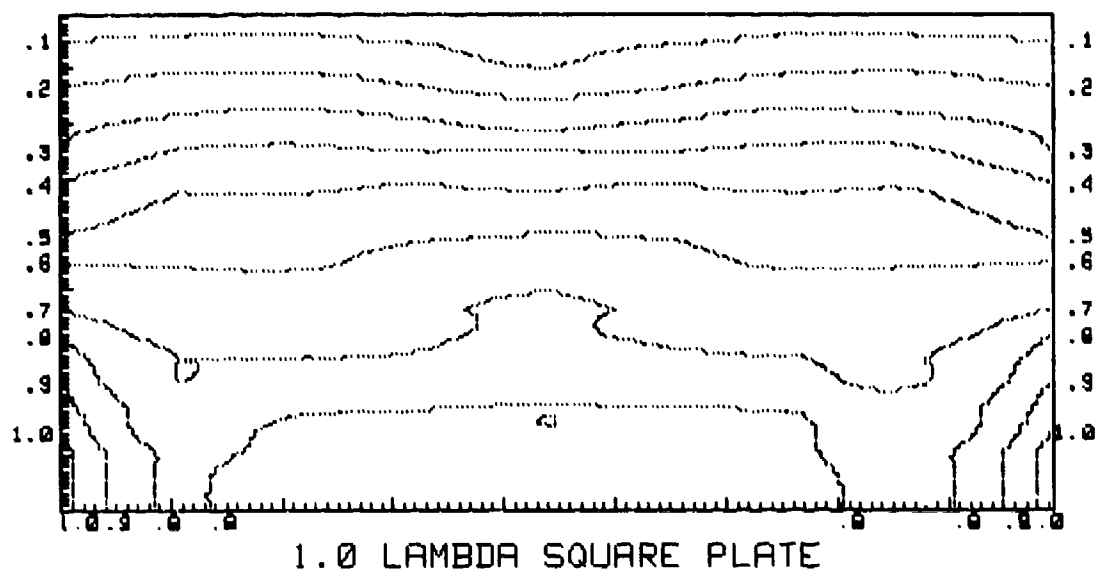


Figure C8: Normalized current contour plot for the 1.0 wavelength square plate (BOT).

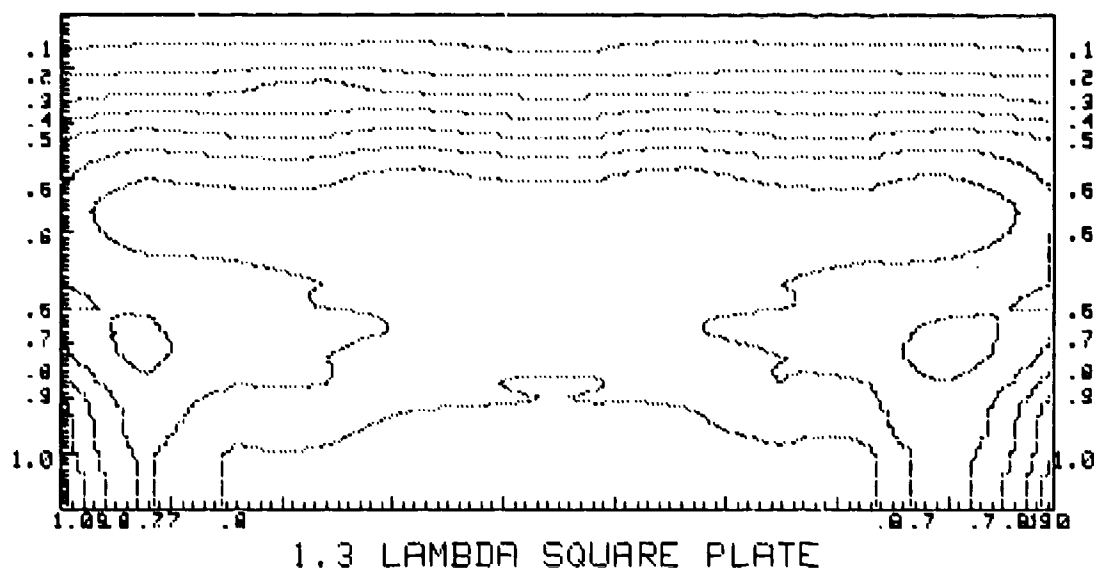


Figure C9: Normalized current contour plot for the 1.3 wavelength square plate (BOT).

Table C1

Current Components from the Body
of Translation Code for a 1.0
wavelength square plate

$J_{\text{horizontal}}$ (A/m)	J_{vertical} (A/m)
.763E-09	.472E-02
.226E-09	.341E-02
.864E-09	.386E-02
.355E-09	.393E-02
.115E-08	.374E-02
.502E-09	.393E-02
.135E-08	.386E-02
.455E-11	.341E-02
.661E-09	.472E-02

APPENDIX D

COMPUTER PROGRAMS

CAMCAL - Calibration for Thermovision

J vs T - Quadratic fit from empirical data

IRSTAT - Statistical Analysis on the
Initial and Final IR data then
stores it

MEGAIR - Calculates temperature and
current from data - also graphs

PDISC - Bouwkamp disk solution

DISK - Cartesian and Total current
calculation


```

10  ! THE NAME OF THIS PROGRAM IS 'CAMCAL'
20  DIM T(201), I(201)
30  GCLEAR
40  EXIT GRAPHICS
50  INPUT "Enter I1 (absolute isothermal units).", I1
60  INPUT "Enter T1 (degrees Centigrade).", T1
70  INPUT "Enter I2 (absolute isothermal units).", I2
80  INPUT "Enter T2 (degrees Centigrade).", T2
90  INPUT "Enter Maximum Temperature in Degrees C.", Tmax
100 INPUT "Enter Maximum Isothermal Units.", Imax
110 INPUT "Enter the Convergence Criteria Desired.", Con
120 Tinc=Tmax/199
130 Qn=T1*T2/(T1-T2)*LOG(I1/I2)
140 Exp=EXP(Qn/T1)
150 Fq=T2*LOG(I1/I2*(Exp-1))-Qn
160 Fpq=T2/T1*Exp/(Exp-1)-1
170 Qn1=Qn-Fq/Fpq
180 Diff=ABS(Qn1-Qn)
190 IF Diff<Con THEN 220
200 Qn=Qn1
210 GOTO 140
220 P=I1*(EXP(Qn/T1)-1)
230 T=273
240 FOR J=1 TO 200
250 T(J)=T-273
260 I(J)=P/(EXP(Qn/T))-1
270 T=T+Tinc
280 NEXT J
290 GCLEAR
300 GRAPHICS
310 LINE TYPE 1
320 LOCATE 20,115,15,80
330 SCALE 0,Tmax,0,Imax
340 LOCATE 19,115,14,80
350 AXES 1,2,0,0,10,5

```

```

360 MOVE T(1),I(1)
370 FOR J=1 TO 200
380 DRAW T(J),I(J)
390 NEXT J
400 Devx=Imax/10
410 Devy=Imax/10
420 MOVE 1.5*Devx,-.8*Devy
430 LABEL "Temperature in Degrees Centigrade"
440 MOVE -Devx,2.5*Devy
450 LDIR PI/2
460 LABEL "Isothermal Units"
470 LDIR 0
480 MOVE -.5*Devx,-.4*Devy
490 LABEL 0
500 MOVE -.7*Devx,9.8*Devy
510 LABEL USING 520;Imax
520 IMAGE DDD
530 MOVE -.7*Devx,4.8*Devy
540 LABEL USING 550;Imax/2
550 IMAGE DDD
560 MOVE 9.6*Devx,-.4*Devy
570 LABEL USING 580;Tmax
580 IMAGE DDD
590 MOVE 4.6*Devx,-.4*Devy
600 LABEL USING 610;Tmax/2
610 IMAGE DDD
620 MOVE Devx,-1.6*Devy
630 CSIZE 4.2,9/15,0
640 LABEL "THERMOVISION CALIBRATION CURVE"
650 CSIZE 2.5,9/15,15*PI/180
660 MOVE 4.1*Devx,-1.9*Devy
670 LABEL "c AGA"
680 CSIZE 3.3,9/15,0
690 MOVE Devx,11*Devy
700 LABEL USING 710;P

```

```
710 IMAGE "P=", DDDDDD.D
720 MOVE 5*Devx, 11*Devy
730 LABEL USING 740; Qn
740 IMAGE "Q=", DDDD.D
750 LINE TYPE 3
760 MOVE Devx, 0
770 DRAW Devx, Imax
780 MOVE 2*Devx, 0
790 DRAW 2*Devx, Imax
800 MOVE 3*Devx, 0
810 DRAW 3*Devx, Imax
820 MOVE 4*Devx, 0
830 DRAW 4*Devx, Imax
840 MOVE 5*Devx, 0
850 DRAW 5*Devx, Imax
860 MOVE 6*Devx, 0
870 DRAW 6*Devx, Imax
880 MOVE 7*Devx, 0
890 DRAW 7*Devx, Imax
900 MOVE 8*Devx, 0
910 DRAW 8*Devx, Imax
920 MOVE 9*Devx, 0
930 DRAW 9*Devx, Imax
940 MOVE 10*Devx, 0
950 DRAW 10*Devx, Imax
960 MOVE 0, Devy
970 DRAW Tmax, Devy
980 MOVE 0, 2*Devy
990 DRAW Tmax, 2*Devy
1000 MOVE 0, 3*Devy
1010 DRAW Tmax, 3*Devy
1020 MOVE 0, 4*Devy
1030 DRAW Tmax, 4*Devy
1040 MOVE 0, 5*Devy
1050 DRAW Tmax, 5*Devy
```

```
1060 MOVE 0,6*DevY
1070 DRAW Tmax,6*DevY
1080 MOVE 0,7*DevY
1090 DRAW Tmax,7*DevY
1100 MOVE 0,8*DevY
1110 DRAW Tmax,8*DevY
1120 MOVE 0,9*DevY
1130 DRAW Tmax,9*DevY
1140 MOVE 0,10*DevY
1150 DRAW Tmax,10*DevY
1160 LINE TYPE 1
1170 STOP
```

```

10 ! THE NAME OF THIS PROGRAM IS 'JUST'!
20 INTEGER I,J,N
30 DIM J(30),T(30),Jcal(250),Tcal(250),V1(15),V2(15),I(30)
40 GCLEAR
50 EXIT GRAPHICS
60 INPUT "Enter an even number of data points.",N
70 INPUT "Enter the sample width (M).",M
80 FOR I=1 TO N
90   DISP "T(";I;")=";
100  INPUT T(I)
110  DISP "V(";I;")(<VOLTS>=";
120  INPUT V(I)
130  DISP "I(";I;")(<A>=";
140  INPUT I(I)
150  J(I)=I(I)/M
160  NEXT I
170  FOR I=1 TO N STEP 2
180    Denom=J(I+1)*J(I)^2-J(I)*J(I+1)^2
190    V1((I+1)/2)=(T(I)*J(I+1)-T(I+1)*J(I))/Denom
200    V2((I+1)/2)=(T(I+1)*J(I)^2-T(I)*J(I+1)^2)/Denom
210    V1avg=V1avg+V1((I+1)/2)/(N/2)
220    V2avg=V2avg+V2((I+1)/2)/(N/2)
230  NEXT I
240  Cinc=5/250
250  FOR I=0 TO 249
260    Tcal(I)=V1avg*Cur^2+/2avg*Cur
270    Jcal(I)=Cur
280    Cur=Cur+Cinc
290  NEXT I
300  GRAPHICS
310  LOCATE 10,110,10,80
320  SCALE 0,25,0,5
330  LOCATE 9,110,9,80
340  AXES .25,.1,0,0,10,10
350  LINE TYPE 2

```

```

360 MOVE 0,0
370 FOR I=1 TO N
380 DRAW T(I),J(I)
390 NEXT I
400 MOVE Tcal(0),Jcal(0)
410 LINE TYPE 1
420 FOR I=1 TO 249
430 DRAW Tcal(I),Jcal(I)
440 NEXT I
450 MOVE 0,-.5
460 LABEL "Differential Temperature (Degrees Centigrade)"
470 MOVE -2,-.5
480 LDIR PI/2
490 LABEL "Current Density, J, in Amps/Meter "
500 LDIR 0
510 MOVE -1.2,-.25
520 LABEL 0
530 MOVE 24,-.25
540 LABEL 25
550 MOVE -1.2,4.9
560 LABEL 5
570 MOVE 3,4.5
580 LABEL USING 590;V1avg
590 IMAGE "V1avg=",SD.DDDE
600 MOVE 12,4.5
610 LABEL USING 620;V2avg
620 IMAGE "V2avg=",SD.DDDE
630 MOVE 4.3,-.25
640 LABEL 5
650 MOVE 9.2,-.25
660 LABEL 10
670 MOVE 14.2,-.25
680 LABEL 15
690 MOVE 19.2,-.25
700 LABEL 20

```

710	MOVE -1.2,.95
720	LABEL 1
730	MOVE -1.2,1.95
740	LABEL 2
750	MOVE -1.2,2.95
760	LABEL 3
770	MOVE -1.2,3.95
780	LABEL 4
790	STOP

```

10  ! THE NAME OF THIS PROGRAM IS 'IRSTAT'---IT READS AND STORES DATA!
20  ! THIS PROGRAM DOES A STATISTICAL ANALYSIS ON THE INITIAL AND FINAL
    IR DATA AND THEN STORES IT IN 'Ir' AND 'Final'!
30  OPTION BASE 1
40  SHORT Ir(64,64),Final(64,64),Dummy(64,64,7)
50  INTEGER I,J,K,L,M,Z,Q,Jj
60  GCLEAR
70  EXIT GRAPHICS
80  INPUT "How many frames are to be averaged (MAX 7)?",M
90  INPUT "Begin at x=",Xmin
100 INPUT "Terminate at x=",Xmax
110 INPUT "Begin at y=",Ymin
120 INPUT "Terminate at y=",Ymax
130 INPUT "Reference Temperature (Centigrade) =",T0
140 INPUT "Enter 2 IF Ref. Temp. is lowest; 1 if highest.",Hi
150 INPUT "Enter Sensitivity.",Sensi
160 PRINT "Push 'CONT' when ready to take data."
170 PAUSE
180 ! !
190 ! NOW WE TAKE M SAMPLES OF RAW ISU DATA !
200 ! !
    FOR K=1 TO M
210     PRINT PAGE
220     PRINT USING 240;K
230     IMAGE " I AM READING DATA SAMPLE ",D
240     OVERLAP
250     WRITE IO 2,5;0
260     READ IO 2,5;A
270     A=BINAND(A,1)
280     IF A=1 THEN 270
290     WRITE IO 2,5;1
300     READ IO 2,5;A
310     A=BINAND(A,1)
320     IF A=0 THEN 310
330     FOR I=Ymin TO Ymax
340

```



```

350 Z=(I-1)*128
360 FOR J=Xmin*2 TO Xmax*2-1 STEP 2
370 JJ=J/2+1
380 Q=J+Z
390 WRITE BIN 2;-Q
400 Dummy(I,J,K)=READBIN(2)
410 NEXT J
420 NEXT I
430 NEXT K
440 !
450 ! WE NOW DO A STATISTICAL ANALYSIS ON 'DUMMY'. WE DELETE ANYTHING OUT OF
    THE RANGE 0-9, CALC. A MEAN AND STD. DEV., DISCARD ANYTHING !
    ! OVER ONE STD. DEV. OUTSIDE OF THE MEAN, THEN CALC. A NEW MEAN !
460 FOR I=Ymin TO Ymax
470 PRINT PAGE
480 PRINT USING 500;I,Ymax-I
490 IMAGE "I AM ON ROW ",DD," I HAVE ",DD," REMAINING ON THE STATISTICAL ANALY
    SIS"
500
510 FOR J=Xmin TO Xmax
520 L=0
530 Dummy=0
540 FOR K=1 TO M
550 Dum=Dummy(I,J,K)
560 IF (Dum<0) OR (Dum>9) THEN 600 ! DISCARD ERRORS !
570 L=L+1 ! L IS THE NUMBER OF VALID READINGS !
580 Dummy=Dummy+Dum ! DUMMY IS THE SUM OF ALL VALID READINGS!
590 Row(L)=Dum ! CONTAINS ONLY VALID IR READINGS !
600 NEXT K
610 IF L=0 THEN 770 ! NO VALID READINGS - GOTO NEXT ELEMENT
    AND LOAD -1 IN IR AS FLAG!
    ! WE CALC. THE FIRST AVERAGE !
    ! WE NOW CALCULATE THE STD. DEV. !
620 Avg=Dummy/L
630 Sumsq=0
640 FOR K=1 TO L
650 Sumsq=Sumsq+(Row(K)-Avg)^2
660 NEXT K
670 Stdev=SQR(Sumsq/(L-.9999)) ! WE DO THE N-1 STD. DEV. ESTIMATE !

```

```

680 Dummy=0
690 N=0
700 FOR K=1 TO L
710 IF (Row(K)<Avg-Stdev) OR (Row(K)>Avg+Stdev) THEN 740
720 N=N+1
730 Dummy=Dummy+Row(K)
740 NEXT K
750 Ir(I,J)=Dummy/N
760 GOTO 780
770 Ir(I,J)=-1
780 Errori=Errori+N
790 MAT Row=ZER
800 NEXT J
810 NEXT I
820 Errori=1-Errori/((Xmax-Xmin+1)*(Ymax-Ymin+1)*M)
830 ! !
840 ! I AM NOW READY TO TAKE THE SECOND SET OF DATA: AFTER IRRADIATION !
850 ! !
860 PRINT PAGE
870 PRINT " I'M FINISHED WITH Ir! Push 'CONT' when ready to proceed...."
880 PAUSE
890 PRINT PAGE
900 MAT Dummy=ZER
910 FOR K=1 TO M
920 PRINT PAGE
930 PRINT USING 940;K
940 IMAGE "I'M READING DATA SAMPLE ",D," FOR THE Final MATRIX."
950 OVERLAP
960 WRITE IO 2,5;0
970 READ IO 2,5;A
980 A=BINAND(A,1)
990 IF A=1 THEN 970
1000 WRITE IO 2,5;1
1010 READ IO 2,5;A
1020 A=BINAND(A,1)
1030 IF A=0 THEN 1010

```

```

1040 FOR I=Ymin TO Ymax
1050 Z=(I-1)*128
1060 FOR J=Xmin*2 TO Xmax*2-1 STEP 2
1070 Jj=J/2+1
1080 Q=J+2
1090 WRITE BIN 2;-Q
1100 Dummy(I,Jj,K)=READBIN(2)
1110 NEXT J
1120 NEXT I
1130 NEXT K
1140 ! !
1150 ! WE ARE NOW READY FOR THE SECOND SET OF STATISTICAL DATA !
1160 ! !
1170 FOR I=Ymin TO Ymax
1180 PRINT PAGE
1190 PRINT USING 1200;I,Ymax-I
1200 IMAGE "I AM WORKING ON ROW ",DD,"; I HAVE ",DD," REMAINING FOR STAT. ANALY
    SIS"
1210 FOR J=Xmin TO Xmax
1220 L=0
1230 Dummy=0
1240 FOR K=1 TO M
1250 Dum=Dummy(I,J,K)
1260 IF (Dum<0) OR (Dum>9) THEN 1300
1270 L=L+1
1280 Dummy=Dummy+Dum
1290 Row(L)=Dum
1300 NEXT K
1310 IF L=0 THEN 1470
1320 Avg=Dummy/L
1330 Sumsq=0
1340 FOR K=1 TO L
1350 Sumsq=Sumsq+(Row(K)-Avg)^2
1360 NEXT K
1370 Stdev=SGR(Sumsq/(L-.9999))
1380 Dummy=0

```

```

1390 N=0
1400 FOR K=1 TO L
1410 IF (Row(K)<Avg-Stdev) OR (Row(K)>Avg+Stdev) THEN 1440
1420 N=N+1
1430 Dummy=Dummy+Row(K)
1440 NEXT K
1450 Final(I,J)=Dummy/N
1460 GOTO 1480
1470 Final(I,J)=-1
1480 Errorf=Errorf+N
1490 MAT Row=ZER
1500 NEXT J
1510 NEXT I
1520 Errorf=1-Errorf/((Xmax-Xmin+1)*(Ymax-Ymin+1)*M)
1530 INPUT "TO STORE PRESENT CALCULATIONS ENTER 1.",Redo
1540 IF Redo<>1 THEN 1790
1550 PURGE "IRDATA"
1560 PURGE "VARIBL"
1570 PURGE "Varib1"
1580 CREATE "IRDATA",5,20000
1590 CREATE "VARIBL",1,500
1600 CREATE "Varib1",1,256
1610 ASSIGN #1 TO "IRDATA"
1620 ASSIGN #2 TO "VARIBL"
1630 MAT PRINT #1;Ir,Final,END
1640 PRINT #2;Xmin,Xmax,Ymin,Ymax,T0,Sensi,M,Errori,Errorf,END
1650 PRINT PAGE
1660 BEEP
1670 PRINT "I AM FINALLY FINISHED TAKING DATA--I MAY BE SICK!!"
1680 PRINT "YOU MUST LOAD 'MEGAIR' TO CONTINUE WITH THE ANALYSIS FOR SURFACE TEMPERATURES AND CURRENTS....GOOD LUCK!!!"
1690 INPUT "FOR SELECTED PROFILE PLOT ENTER 1.",Plot
1700 IF Plot<>1 THEN 1930
1710 EXIT GRAPHICS
1720 INPUT "ENTER 1 FOR Final, 2 FOR Ir.",Mat
1730 INPUT "ENTER THE ROW DESIRED.",Row

```

```
1740 GCLEAR
1750 GRAPHICS
1760 LOCATE 0,110,0,110
1770 SCALE 0,65,0,10
1780 AXES 1,1,0,0,10,10
1790 MOVE Xmin+1,0
1800 FOR J=Xmin+1 TO Xmax
1810 IF Mat=1 THEN Var=ABS(9-Final(Row,J))
1820 IF Mat=2 THEN Var=ABS(9-Ir(Row,J))
1830 DRAW J,Var
1840 NEXT J
1850 PAUSE
1860 LDIR 0
1870 CSIZE 3.3
1880 PEN 1
1890 LETTER
1900 PAUSE
1910 GRAPHICS
1920 GOTO 1890
1930 STOP
```

```

10  ! THE NAME OF THIS PROGRAM IS 'MEGAIR'---IT DOES EVERYTHING!!!!
20  ! IT BEGINS BY READING 'Ir' AND 'Final' FROM THIS DATA TAPE !
30  ASSIGN #1 TO "IRDATA"      !THIS HAS 'Ir,Final,Delta,Dtemp,Curent MATRI
CES!
40  ASSIGN #2 TO "VARIABLE"    !THIS HAS VARIABLES RELATIVE TO Ir AND Final
!
50  ASSIGN #3 TO "Variable"    !THIS CONTAINS CALCULATED VARIABLES!
60  OPTION BASE 1
70  SHORT Ir(64,64),Final(64,64),Delta(64,64),Dtemp(64,64),Curent(64,64),Max(1
40,4),Last(140,4),Slope1(140,4),Slope2(140,4)
80  SHORT Irb(27,27),Finalb(27,27),Deltab(27,27),Tempb(27,27),Crentb(27,27),X(
64,64)
90  INTEGER I,J,K,L,M,Z,Q,Mat,Replot
100 INPUT "For calculation enter I; for a replot a 2.",Replot
110 IF Replot<>1 THEN 140
120 MAT READ #1;Ir(64,64),Final(64,64)
130 READ #2;Xmin,Xmax,Ymin,Ymax,T0,Sensi,M,ErrorI,Errorf
140 IF Replot<>2 THEN 180
150 MAT READ #1;Ir(64,64),Final(64,64),Delta(64,64),Dtemp(64,64),Curent(64,64)
160 READ #2;Xmin,Xmax,Ymin,Ymax,T0,Sensi,M,ErrorI,Errorf
170 READ #3;Dtmax,Curmax,V1avg,V2avg
180 GCLEAR
190 EXIT GRAPHICS
200 Pee=772600.6
210 Que=3102.6
220 PRINT USING 230;M
230 IMAGE "This data is the result of a ",D," frame average."
240 IF Replot=2 THEN 290
250 INPUT "To update P&Q enter 1; 0 otherwise.",Update
260 IF Update=0 THEN 290
270 INPUT "P=",Pee
280 INPUT "Q=",Que
290 PRINT USING 300;Xmin,Xmax,Ymin,Ymax
300 IMAGE "We went from X=",DD," to X=",DD," Y=",DD," to Y=",DD
310 PRINT USING 320;T0
320 IMAGE "The room temperature was ",DD.D," degrees C"

```

```

330 PRINT USING 340;Sensi
340 IMAGE "The camera sensitivity was ",DD
350 IF Replot=2 THEN 760
360 INPUT "Enter V1avg from calibration plot.",V1avg
370 INPUT "Enter V2avg from calibration plot.",V2avg
380 I0=Pee/(EXP(Que/(T0+273.16)))-1)
390 Dtmax=0
400 Curmax=0
410 MAT X=Final-Ir
420 MAT Delta=ABS(X)
430 FOR I=Ymin TO Ymax
440 PRINT PAGE
450 PRINT USING 460;I,Ymax-I
460 IMAGE "I AM ON ROW ",DD,"; I HAVE ",DD," ROWS YET TO COMPLETE."
470 FOR J=Xmin TO Xmax
480 Ii=I0+(-1)^Hi*Sensi*Delta(I,J)*.1
490 Var=ABS(Que/LOG(Pee/Ii+1))-(T0+273.16)
500 IF Var>Dtmax THEN Dtmax=Var
510 Dtemp(I,J)=Var
520 Current(I,J)=(-V2avg+SQR(ABS(V2avg^2+4*V1avg*Var)))/(2*V1avg)
530 IF Current(I,J)>Curmax THEN Curmax=Current(I,J)
540 NEXT J
550 NEXT I
560 ! !
570 ! Dtemp, Delta, AND Curent ARE CALCULATED!
580 ! !
590 INPUT "To store data on data tape enter 1.",Store
600 IF Store<>1 THEN 760
610 PURGE "IRDATA"
620 PURGE "VARIBL"
630 PURGE "Varibl"
640 CREATE "IRDATA",5,20000
650 CREATE "VARIBL",1,500
660 CREATE "Varibl",1,256
670 ASSIGN #1 TO "IRDATA"
680 ASSIGN #2 TO "VARIBL"

```

```

690 ASSIGN #3 TO "Varib1"
700 MAT PRINT #1;Ir,Final,Delta,Dtemp,Curent
710 PRINT #2;Xmin,Xmax,Ymin,Ymax,T0,Sensi,M,Errorri,Errorf
720 PRINT #3;Dtmax,Curmax,V1avg,V2avg,END
730 ! !
740 ! Ir, Final,Delta,Dtemp, AND Curent ARE NOW STORED ON THE DATA TAPE!
750 ! !
760 INPUT "Contour 1; numbers 10; blowup 5; profile 7, row 8",Copy
770 ! !
780 IF Copy=0 THEN 3000
790 INPUT "ENTER: 1-Final; 2-Delta; 3-Temp; 4-Curent; 5-Ir.",Mat
800 IF Copy<>7 THEN 1900
810 INPUT "Enter the no. of lines to step on profile.",Step
820 MAT Max=ZER
830 GRAPHICS
840 GCLEAR
850 LINE TYPE 1
860 LDIR 0
870 CSIZE 2.5,9/15,0
880 LOCATE 15,95,15,95
890 SCALE 0,128,0,128
900 AXES 2,4,0,0,10,10
910 FOR I=Ymax TO Ymin+1 STEP -Step
920 Big=0
930 Sum=0
940 MOVE Xmax+64-I,64-I
950 FOR J=Xmax-1 TO Xmin+1 STEP -1
960 Jj=J+64-I
970 IF Mat<>1 THEN 1010
980 Var=64-I+4*ABS(9-Final(I,J))
990 Varp=64-I+4*ABS(9-Final(I,J+1))
1000 Varm=64-I+4*ABS(9-Final(I,J-1))
1010 IF Mat<>2 THEN 1050
1020 Var=64-I+4*Delta(I,J)
1030 Varp=64-I+4*Delta(I,J+1)
1040 Varm=64-I+4*Delta(I,J-1)

```



```

1050 IF Mat<>3 THEN 1090
1060 Var=64-I+40*Dtemp(I,J)/Dtmax
1070 Varp=64-I+40*Dtemp(I,J+1)/Dtmax
1080 Varm=64-I+40*Dtemp(I,J-1)/Dtmax
1090 IF Mat<>4 THEN 1130
1100 Var=64-I+40*Curent(I,J)/Curmax
1110 Varp=64-I+40*Curent(I,J+1)/Curmax
1120 Varm=64-I+40*Curent(I,J-1)/Curmax
1130 IF Mat<>5 THEN 1170
1140 Var=64-I+4*(9-Ir(I,J))
1150 Varp=64-I+4*(9-Ir(I,J+1))
1160 Varm=64-I+4*(9-Ir(I,J-1))
1170 X1=Jj-1+1E-8
1180 X2=Jj+1E-9
1190 X3=Jj+1+1E-10
1200 Y1=Varm
1210 Y2=Var
1220 Y3=Varp
1230 Det=X1^2*X2+X1*X3^2+X3*X2^2-X2*X3^2-X3*X1^2-X1*X2^2
1240 A=(X2*Y1+X1*Y3+Y2*X3-X2*Y3-Y1*X3-X1*Y2)/Det
1250 B=(X1^2*Y2+Y1*X3^2+Y3*X2^2-Y2*X3^2-Y3*X1^2-Y1*X2^2)/Det
1260 C=(X2*Y3*X1^2+X1*Y2*X3^2+Y1*X3*X2^2-Y1*X2*X3^2-X3*Y2*X1^2-X1*Y3*X2^2)/Det
1270 FOR K=1 TO 4
1280 X=Jj+1-.25*K
1290 Y=A*X^2+B*X+C
1300 IF Y>Big THEN Big=Y
1310 Sum=Sum+Y/(4*(Xmax-Xmin))
1320 Slope2(Jj+1,K)=Slope1(Jj+1,K)
1330 Slope1(Jj+1,K)=2*A*X+B
1340 Last(Jj+1,K)=Max(Jj+1,K)
1350 IF Y>Max(Jj+1,K) THEN 1380
1360 MOVE X,Y
1370 GOTO 1410
1380 Max(Jj+1,K)=Y
1390 IF J=Xmin+1 THEN 1410
1400 DRAW X,Y

```

```

1410 NEXT K
1420 NEXT J
1430 ! HERE IS THE PLACE TO DRAW Y CONTOURS!
1440 FOR J=Xmax TO Xmin+1 STEP -1
1450   Jj=64-I+J
1460   FOR K=1 TO 2
1470     MOVE Jj+1-.5*K,Last(Jj+1,2*K)
1480     IF I=Ymax THEN 1500
1490     IF (Max(Jj+1+Step,2*K)>Last(Jj+1,2*K)) AND (K=2) THEN DRAW Jj+1+Step-.5*K,
Max(Jj+1+Step,2*K)
1500   NEXT K
1510 NEXT J
1520 IF I>Ymax-3*(Ymax-Ymin)/4 THEN 1540
1530 IF Big-Sum<10 THEN 1550
1540 NEXT I
1550 MOVE 25,-4
1560 LABEL "Horizontal (X) Axis"
1570 CSIZE 3.3,9/15,0
1580 MOVE 0,-11
1590 IF Mat=1 THEN LABEL USING 1600;Sensi
1600 IMAGE "FINAL MATRIX AFTER RADIATION: sensitivity=",DDD
1610 IF Mat=2 THEN LABEL USING 1620;Sensi
1620 IMAGE "DIFFERENCE MATRIX, 'DELTA': sensitivity=",DDD
1630 IF Mat=3 THEN LABEL USING 1640;Dtmx
1640 IMAGE "DELTA TEMPERATURE MATRIX (C): Max. Temp. Diff.="",D.DDE
1650 IF Mat=4 THEN LABEL USING 1660;Curmax
1660 IMAGE "CURRENT DENSITY MATRIX (J): Max. Current Diff.="",D.DDE
1670 IF Mat=5 THEN LABEL USING 1680;Sensi
1680 IMAGE "CORRECTION MATRIX: sensitivity=",DD
1690 CSIZE 2.5,9/15,0
1700 LINE TYPE 3
1710 MOVE 0,0
1720 DRAW 64,64
1730 LINE TYPE 1
1740 MOVE 64,0
1750 DRAW 128,64

```

```

1760 LDIR PI/4
1770 MOVE 70,1
1780 LABEL "Vertical (Y) Axis"
1790 LDIR PI/2
1800 MOVE -4,5
1810 IF (Mat=1) OR (Mat=5) THEN LABEL "Z Axis (Isotherm Units)"
1820 IF Mat=2 THEN LABEL "Z Axis (Delta Isotherm Units)"
1830 IF Mat=3 THEN LABEL "Z Axis (Degrees Centigrade)"
1840 IF Mat=4 THEN LABEL "Z Axis (Amp per Square Meter)"
1850 PAUSE
1860 INPUT "For a copy enter a 1; otherwise 0.",Copy
1870 IF Copy=1 THEN DUMP GRAPHICS
1880 EXIT GRAPHICS
1890 GOTO 760
1900 IF Copy<>5 THEN 2130
1910 FOR I=1 TO 27
1920 FOR J=1 TO 27
1930 Finalb(I,J)=9-DROUND(Final(I+18,J+18),1)
1940 Deltab(I,J)=DROUND(Delta(I+18,J+18),1)
1950 Tempb(I,J)=DROUND(10*Temp(I+18,J+18)/Dtmx,1)
1960 Crentb(I,J)=DROUND(10*Current(I+18,J+18)/Curmax,1)
1970 Irb(I,J)=9-DROUND(Ir(I+18,J+18),1)
1980 NEXT J
1990 NEXT I
2000 INPUT "For printout enter 0; otherwise 16.",Print
2010 PRINTER IS Print
2020 IF Mat=1 THEN MAT PRINT Finalb;
2030 IF Mat=1 THEN PRINT "
2040 IF Mat=2 THEN MAT PRINT Deltab;
2050 IF Mat=2 THEN PRINT "
2060 IF Mat=3 THEN MAT PRINT Tempb;
2070 IF Mat=3 THEN PRINT "MAXIMUM DELTA TEMPERATURE = ",Dtmx
2080 IF Mat=4 THEN MAT PRINT Crentb;
2090 IF Mat=4 THEN PRINT "MAXIMUM CURRENT=",Curmax
2100 IF Mat=5 THEN MAT PRINT Irb;
2110 IF Mat=5 THEN PRINT "CORRECTION MATRIX: sensitivity=",Sensi

```

```

2120  PRINTER I: 16
2130  IF (Copy<>1) AND (Copy<>10) THEN 2960
2140  Neg=0
2150  INPUT "For a negative printout enter 9.",Neg
2160  GCLEAR
2170  GRAPHICS
2180  CSIZE 2.2,9/15,0
2190  LDIR 0
2200  LOCATE 0,120,0,110
2210  SCALE 0,65,0,65
2220  AXES 1,1,0,0,10,10
2230  FOR I=Ymin+1 TO Ymax-1
2240  FOR J=Xmin+1 TO Xmax-1
2250  MOVE J,65-I
2260  IF Mat<>1 THEN 2320
2270  Var=DROUND(Neg-Final(I,J),1)
2280  Vp=DROUND(Neg-Final(I-1,J),1)
2290  Vm=DROUND(Neg-Final(I+1,J),1)
2300  V1=DROUND(Neg-Final(I,J-1),1)
2310  Vr=DROUND(Neg-Final(I,J+1),1)
2320  IF Mat<>2 THEN 2380
2330  Var=Delta(I,J)
2340  Vp=Delta(I-1,J)
2350  Vm=Delta(I+1,J)
2360  V1=Delta(I,J-1)
2370  Vr=Delta(I,J+1)
2380  IF Mat<>3 THEN 2440
2390  Var=DROUND(10*Dtemp(I,J),1)
2400  Vp=DROUND(10*Dtemp(I-1,J),1)
2410  Vm=DROUND(10*Dtemp(I+1,J),1)
2420  V1=DROUND(10*Dtemp(I,J-1),1)
2430  Vr=DROUND(10*Dtemp(I,J+1),1)
2440  IF Mat<>4 THEN 2500
2450  Var=DROUND(10*Current(I,J)/Curmax,1)
2460  Vp=DROUND(10*Current(I-1,J)/Curmax,1)
2470  Vm=DROUND(10*Current(I+1,J)/Curmax,1)

```

```

2480 V1=DROUND(10*Current(I,J-1)/Curmax,1)
2490 Vr=DROUND(10*Current(I,J+1)/Curmax,1)
2500 IF Mat<>5 THEN 2560
2510 Var=DROUND(Neg-Ir(I,J),1)
2520 Vp=DROUND(Neg-Ir(I-1,J),1)
2530 Vm=DROUND(Neg-Ir(I+1,J),1)
2540 V1=DROUND(Neg-Ir(I,J-1),1)
2550 Vr=DROUND(Neg-Ir(I,J+1),1)
2560 IF Ir(I,J)=-1 THEN 2580
2570 GOTO 2600
2580 LABEL "X"
2590 GOTO 2830
2600 IF Copy=10 THEN 2810
2610 IF Var<.5 THEN Var=0
2620 MOVE J,66-I
2630 IF (Var<>Vp) AND (Var<>Vr) THEN DRAW J+1,65-I
2640 MOVE J,65-I
2650 IF (Var<>Vm) AND (Var<>V1) THEN DRAW J+1,66-I
2660 IF (Var<>Vp) AND (Var<>Vr) THEN 2730
2670 IF Var=Vp THEN 2700
2680 MOVE J,66-I
2690 DRAW J+1,66-I
2700 IF Var=Vr THEN 2740
2710 MOVE J+1,65-I
2720 DRAW J+1,66-I
2730 IF (Var<>Vm) AND (Var<>V1) THEN 2830
2740 IF Var=Vm THEN 2770
2750 MOVE J,65-I
2760 DRAW J+1,65-I
2770 IF Var=V1 THEN 2830
2780 MOVE J,65-I
2790 DRAW J,66-I
2800 GOTO 2830
2810 IF (1<Var) AND (Var<10) THEN LABEL Var
2820 IF (Var>.5) AND (Var<1) THEN LABEL 1
2830 NEXT J

```

```

2840 NEXT I
2850 IF Mat<>3 THEN 2880
2860 MOVE 2,0
2870 LABEL "MAXIMUM TEMPERATURE=",Dtmax
2880 IF Mat<>4 THEN 2910
2890 MOVE 2,0
2900 LABEL "MAXIMUM CURRENT=",Curmax
2910 INPUT "For a paper copy enter 1.",Paper
2920 IF Paper=1 THEN DUMP GRAPHICS
2930 CSIZE 3.3,9/15,0
2940 GCLEAR
2950 EXIT GRAPHICS
2960 IF Copy<>8 THEN 3190
2970 PRINT "Xmin=",Xmin," Xmax=",Xmax
2980 PRINT "Ymin=",Ymin," Ymax=",Ymax
2990 INPUT "Enter the row desired.",Row
3000 GCLEAR
3010 GRAPHICS
3020 LOCATE 0,110,0,110
3030 SCALE 0,65,0,10
3040 AXES 1,.1,0,0,10,10
3050 MOVE Xmin,0
3060 FOR J=Xmin+1 TO Xmax
3070 IF Mat=1 THEN Var=ABS(9-Final(Row,J))
3080 IF Mat=2 THEN Var=Delta(Row,J)
3090 IF Mat=3 THEN Var=10*Dtemp(Row,J)/Dtmax
3100 IF Mat=4 THEN Var=10*Current(Row,J)/Curmax
3110 IF Mat=5 THEN Var=ABS(9-Ir(Row,J))
3120 DRAW J,Var
3130 NEXT J
3140 PAUSE
3150 LDIR 0
3160 CSIZE 3.3
3170 LETTER
3180 PAUSE
3190 GOTO 760
3200 STOP

```

```

10 ! THE NAME OF THIS PROGRAM IS 'PDISC' !
20 ! IT COMPUTES CURRENTS ON PEC DISCS THROUGH (Rho/RADIUS)^6 !
30 GCLEAR
40 EXIT GRAPHICS
50 OPTION BASE 1
60 ! RADIUS IS NORMALIZED TO 1 !
70 R=1
80 INPUT "ENTER KAPPA: WAVE NUMBER (K=2*PI/LAMBDA) X RADIUS",K
90 SHORT Jt1(13)
100 FOR I=1 TO 13
110 Y=1/13*2*A-A/13
120 X=0
130 IF SQR(X^2+Y^2)>=A THEN 260
140 IF Y=0 THEN Y=1E-12
150 Rho=SQR(Y^2+Y^2)
160 R=Rho/A
170 Cos2=(X^2-Y^2)/(X^2+Y^2)
180 Sin2=2*X*Y/(X^2+Y^2)
190 Ra=4/9*PI*K^3*(2-R^2)-2*PI*K^5/675*(-296+192*R^2-15*R^4)
200 Ia=1/3*(-4+3*R^2-K^2/90*(56-40*R^2+5*R^4))+K^4/12600*(-2656+2408*R^2-448*R
    ^4+21*R^6)
210 Rb=- (4*PI*K^3*R/9)-2*PI*K^5*R^2/675*(134-15*R^2)
220 Ib=R^2/3-K^2*R^2/30*(-8+R^2)+K^4*R^2/2520*(200-68*R^2+3*R^4)
230 Jx=K*80573/SQR(1-R^2)*SQR((Ra+Rb*Cos2)^2+(Ia+Ib*Cos2)^2)
240 Jy=K*Sin2*80573/SQR(1-R^2)*SQR(Rb^2+Ib^2)
250 Jt1(I)=SQR(Jx^2+Jy^2)
260 NEXT I
270 FOR I=1 TO 13
280 PRINT USING 290;Jt1(I)
290 IMAGE D.DDE," ",D.DDE," ",D.DDE," ",D.DDE," ",D.DDE,"
    ",D.DDE," ",D.DDE," ",D.DDE," ",D.DDE," ",D.DDE
300 NEXT I
310 STOP

```

```

10 ! THE NAME OF THIS PROGRAM IS 'DISK' !
20 GCLEAR
30 EXIT GRAPHICS
40 OPTION BASE 1
50 INPUT "Enter '1' FOR .38, '2' FOR .50, '3' FOR 1.0, '4' FOR 1.3",J
60 INPUT "Enter vertical height of scan in meters",V
70 INPUT "Enter radius of the disk in meters",D
80 INPUT "Enter minimum calculated 'x' in meters",Xmin
90 INPUT "Enter maximum calculated 'x' in meters",Xmax
100 SHORT Jx(4,201),Jy(4,201),Xinc(4,201),Jtot(4,201)
110 FOR I=1 TO 201
120 Jx(J,I)=0
130 Jy(J,I)=0
140 Jtot(J,I)=0
150 Xinc=D/100
160 Xinc(J,I)=I*Xinc-(D+Xinc)
170 C=ABS(Xinc(J,I))
180 IF C<Xmin THEN 410
190 IF C>Xmax THEN 410
200 X=SQR(Xinc(J,I)^2+V^2)
210 IF X>Xmax THEN 410
220 Cos=V/SQR(Xinc(J,I)^2+V^2)
230 Sin=ABS(Xinc(J,I)/SQR(Xinc(J,I)^2+V^2))
240 IF J<>1 THEN 270
250 Jt=(-10076*X^3+87.09*X^2-13.52*X+3.403)*Cos
260 Jp=(950222*X^4-78558*X^3+2361*X^2-26.38*X+3.395)*Sin
270 IF J<>2 THEN 300
280 Jt=-3694*X^3-76.17*X^2-9.941*X+3.808
290 Jp=2389217*X^5-126591*X^4-4184*X^3+454.7*X^2-10.78*X+3.775
300 IF J<>3 THEN 330
310 Jt=4536*X^3-883.7*X^2-8.268*X+3.194
320 Jp=903319000*X^6-130549100*X^5+7448120*X^4-203306*X^3+2264*X^2-17.25*X+3.1
76
330 IF J<>4 THEN 360

```



```

340 Jt=-418320*X^4+60469*X^3-2844*X^2+22.52*X+3.008
350 Jp=5907612*X^5-883402*X^4+51274*X^3-1620*X^2+9.621*X+3.060
360 GOTO 370
370 Jx(J,I)=Jt*Sin+Jp*Cos
380 Jy(J,I)=Jt*Cos+Jp*Sin
390 Jtot(J,I)=SQRT(Jt^2+Jp^2)
400 ! CURRENTS HAVE NOW BEEN CALCULATED !
410 NEXT I
420 GRAPHICS
430 LINE TYPE 1
440 LOCATE 5,112,0,44
450 SCALE -D,D,0,5
460 AXES .01,1,0,0,10,10
470 MOVE Xinc(J,I),Jx(J,I)
480 LINE TYPE 3
490 FOR I=1 TO 201
500 DRAW Xinc(J,I),Jx(J,I)
510 NEXT I
520 MOVE Xinc(J,I),Jy(J,I)
530 LINE TYPE 8
540 FOR I=1 TO 201
550 DRAW Xinc(J,I),Jy(J,I)
560 NEXT I
570 MOVE Xinc(J,I),Jtot(J,I)
580 LINE TYPE 1
590 FOR I=1 TO 201
600 DRAW Xinc(J,I),Jtot(J,I)
610 NEXT I
620 PAUSE
630 LDIR 0
640 CSIZE 3.3
650 LETTER
660 PAUSE
670 GOTO 20
680 STOP

```

APPENDIX E

HORIZONTAL MAGNETIC FIELD PROBE RESULTS

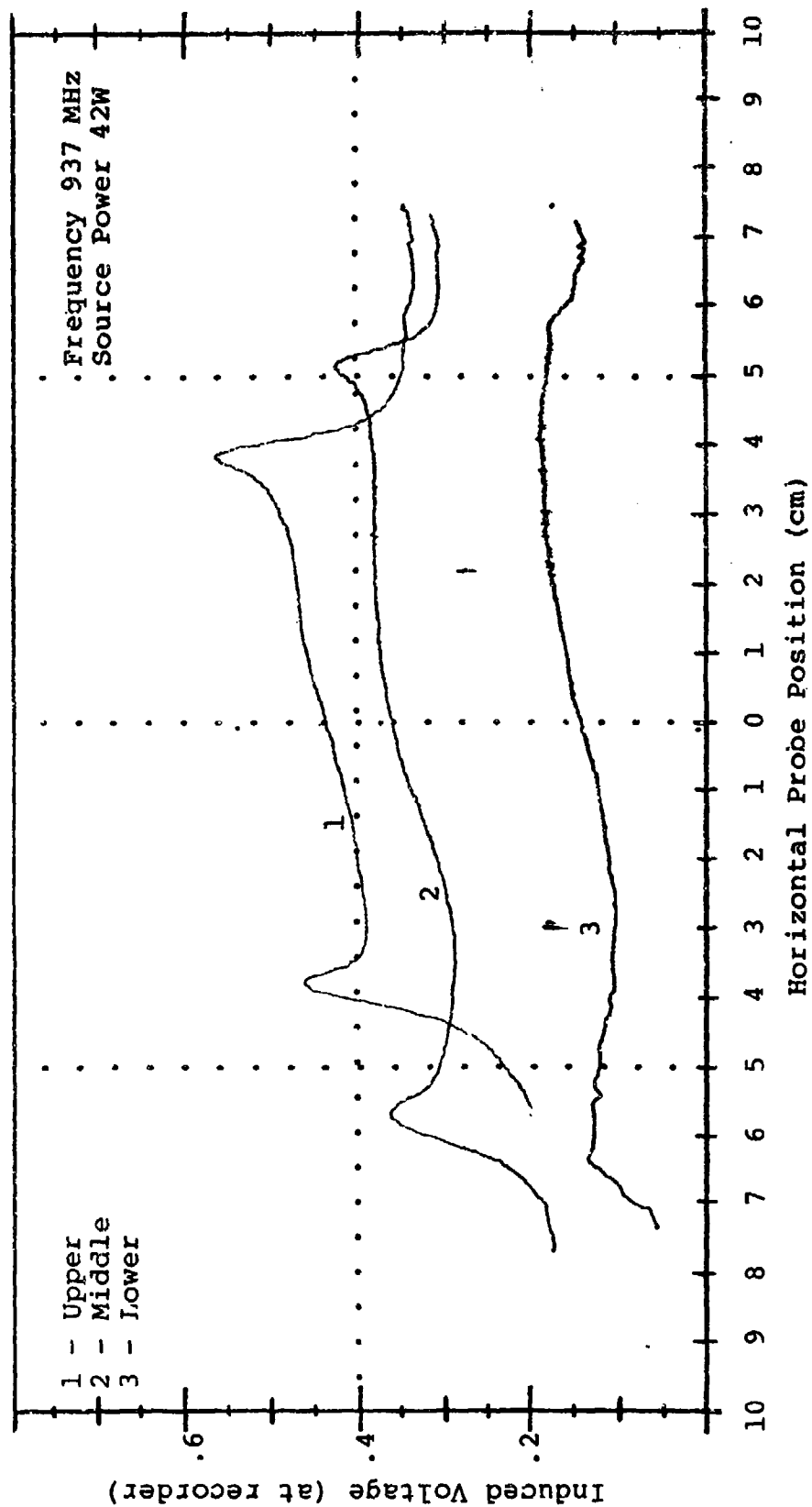


Figure E1: Horizontal Magnetic Field Probe Measurements for the .38 wavelength circular disk.

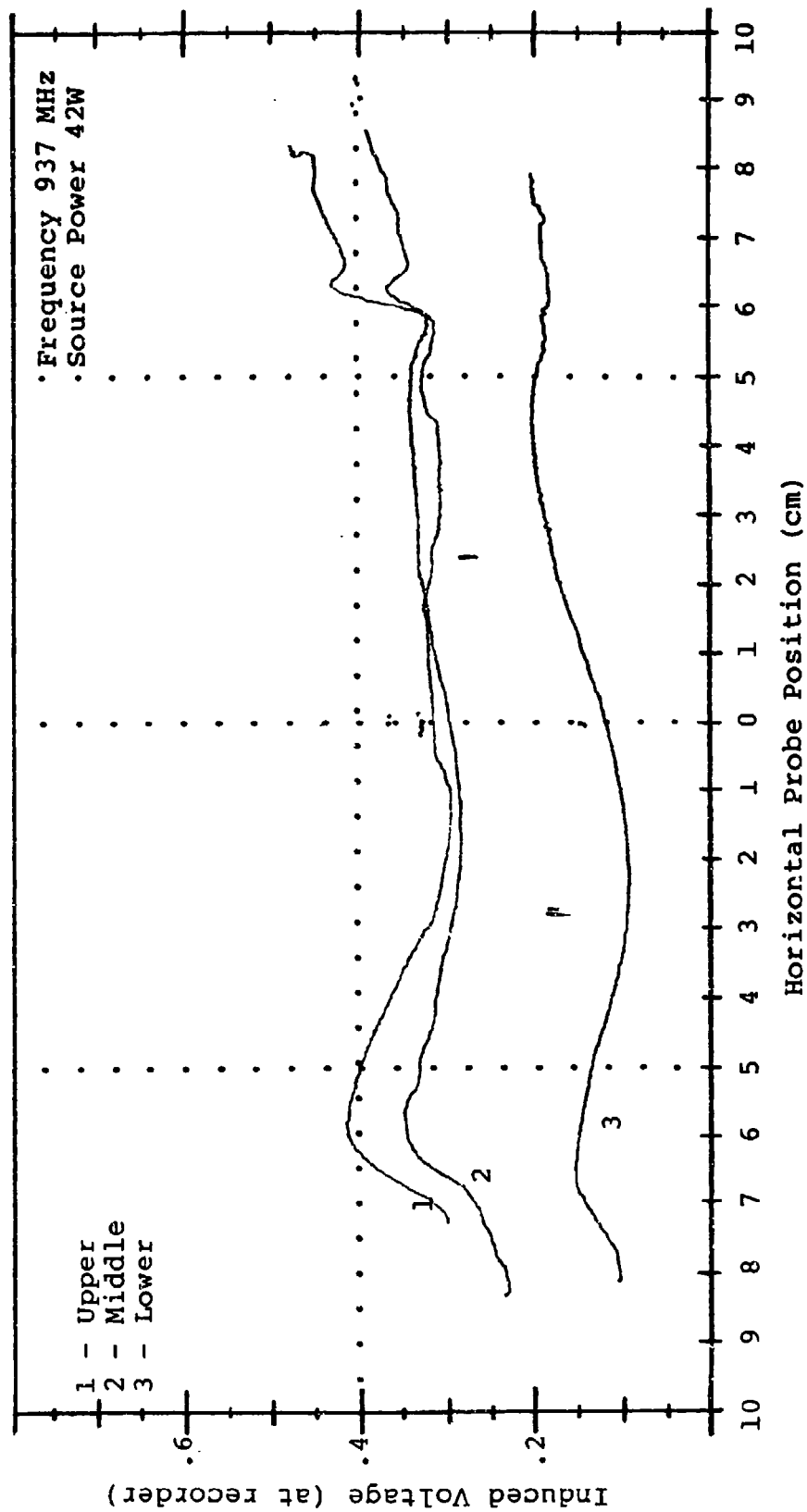


Figure E2: Horizontal Magnetic Field Probe Measurements for the .38 wavelength square plate.

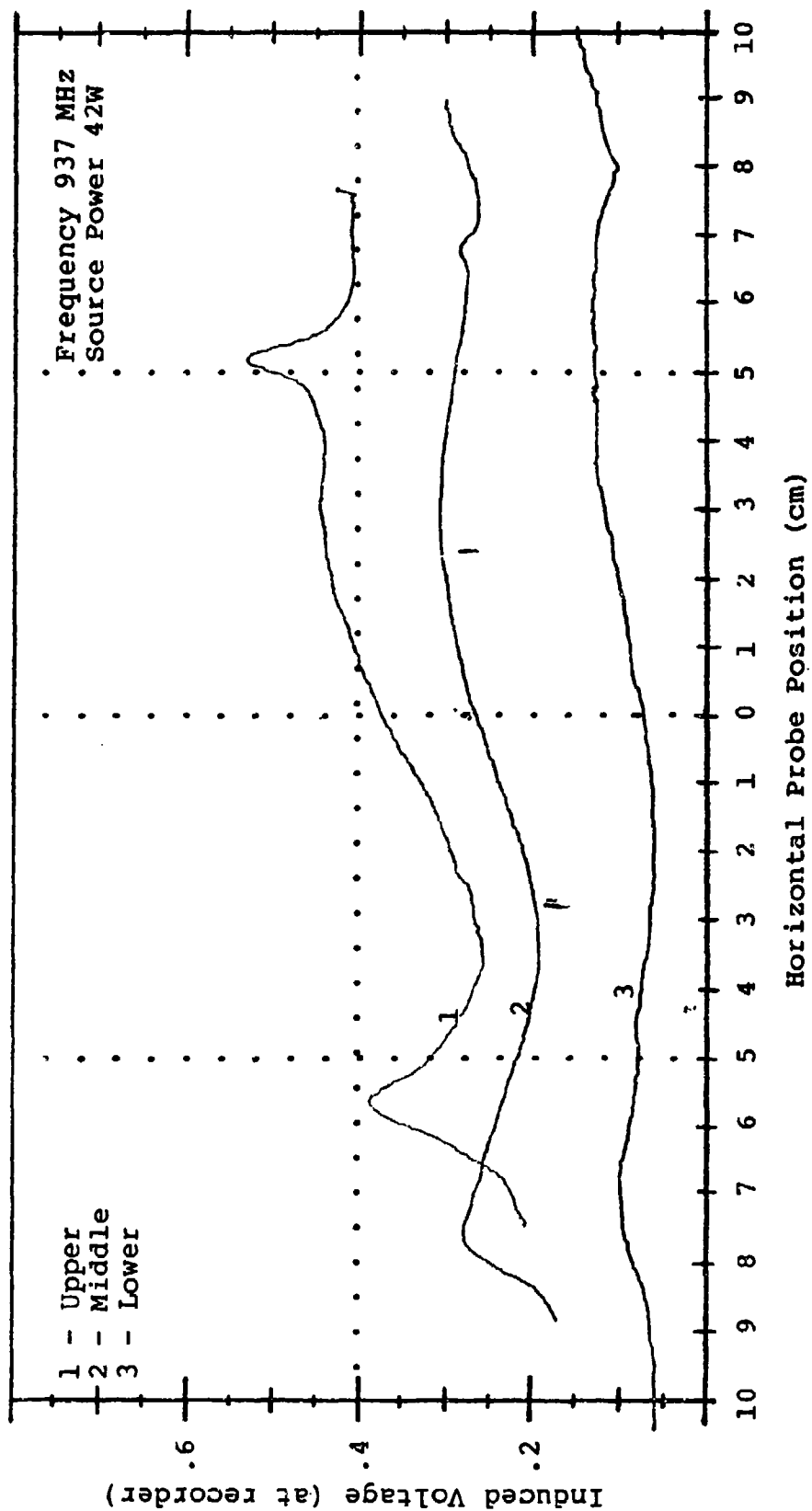


Figure E3: Horizontal Magnetic Field Probe Measurements for the .50 wavelength circular disk.

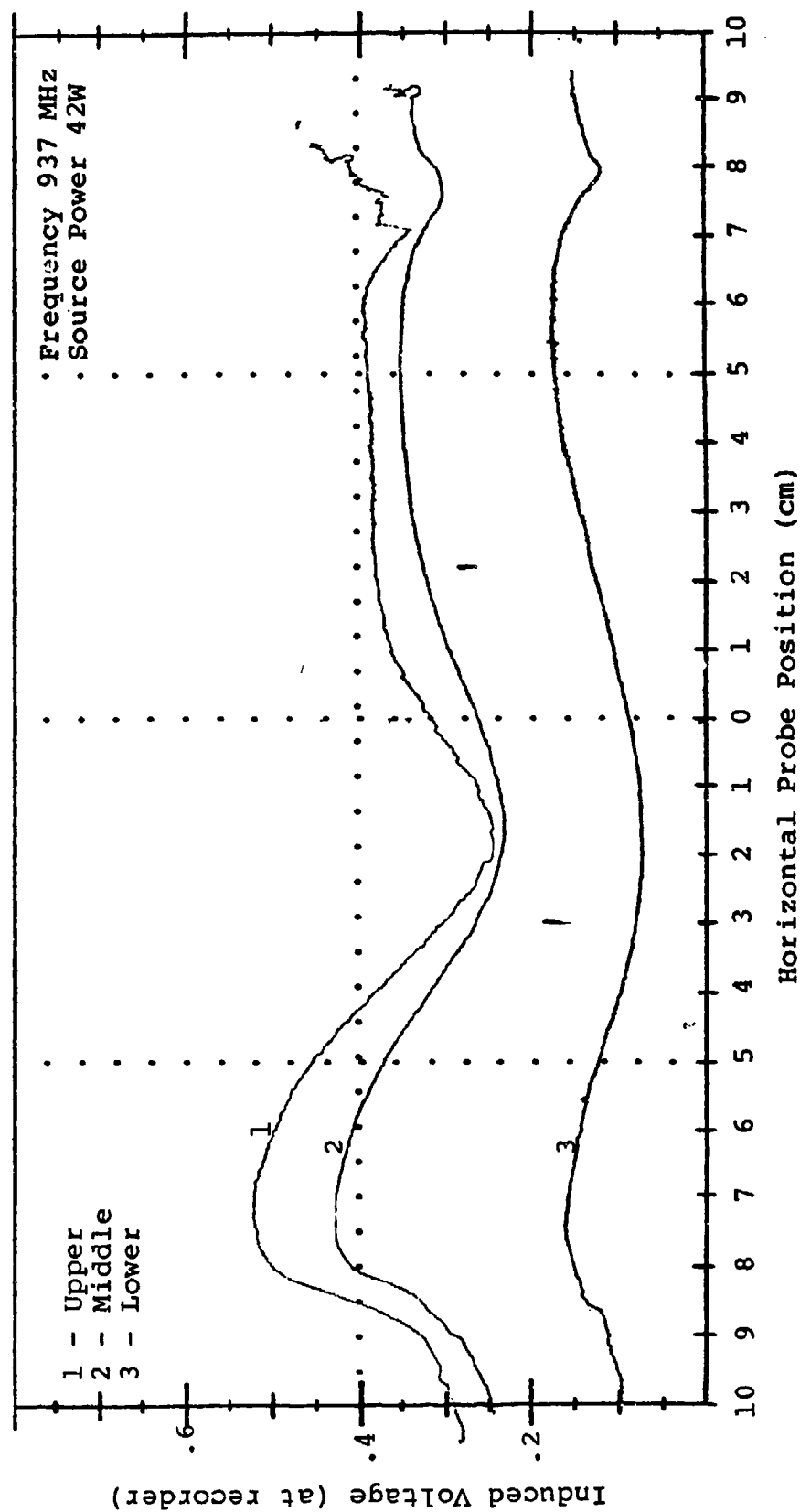


Figure E4: Horizontal Magnetic Field Probe Measurements for the .50 wavelength square plate.

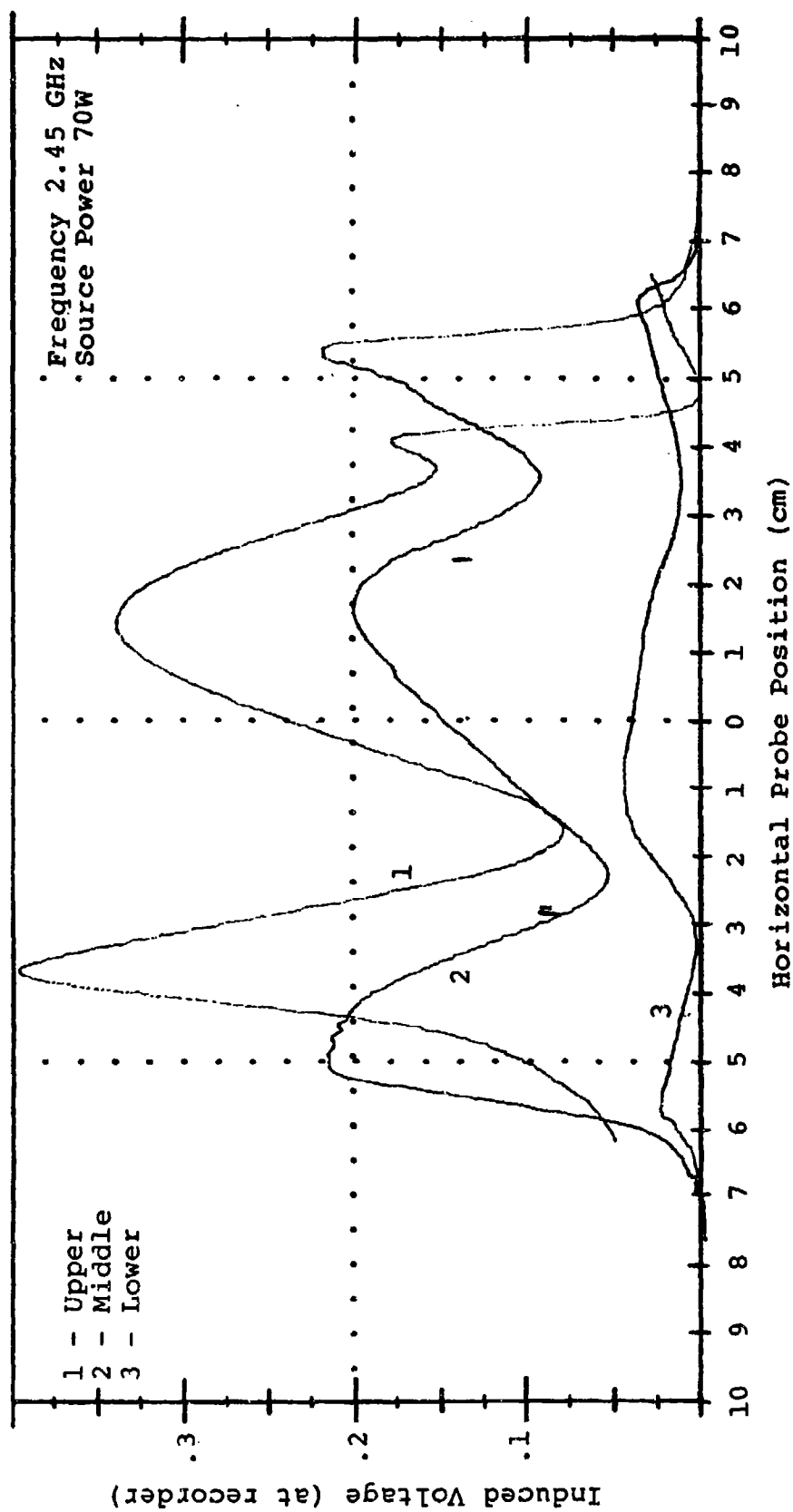


Figure E5: Horizontal Magnetic Field Probe Measurements for the 1.0 wavelength circular disk.

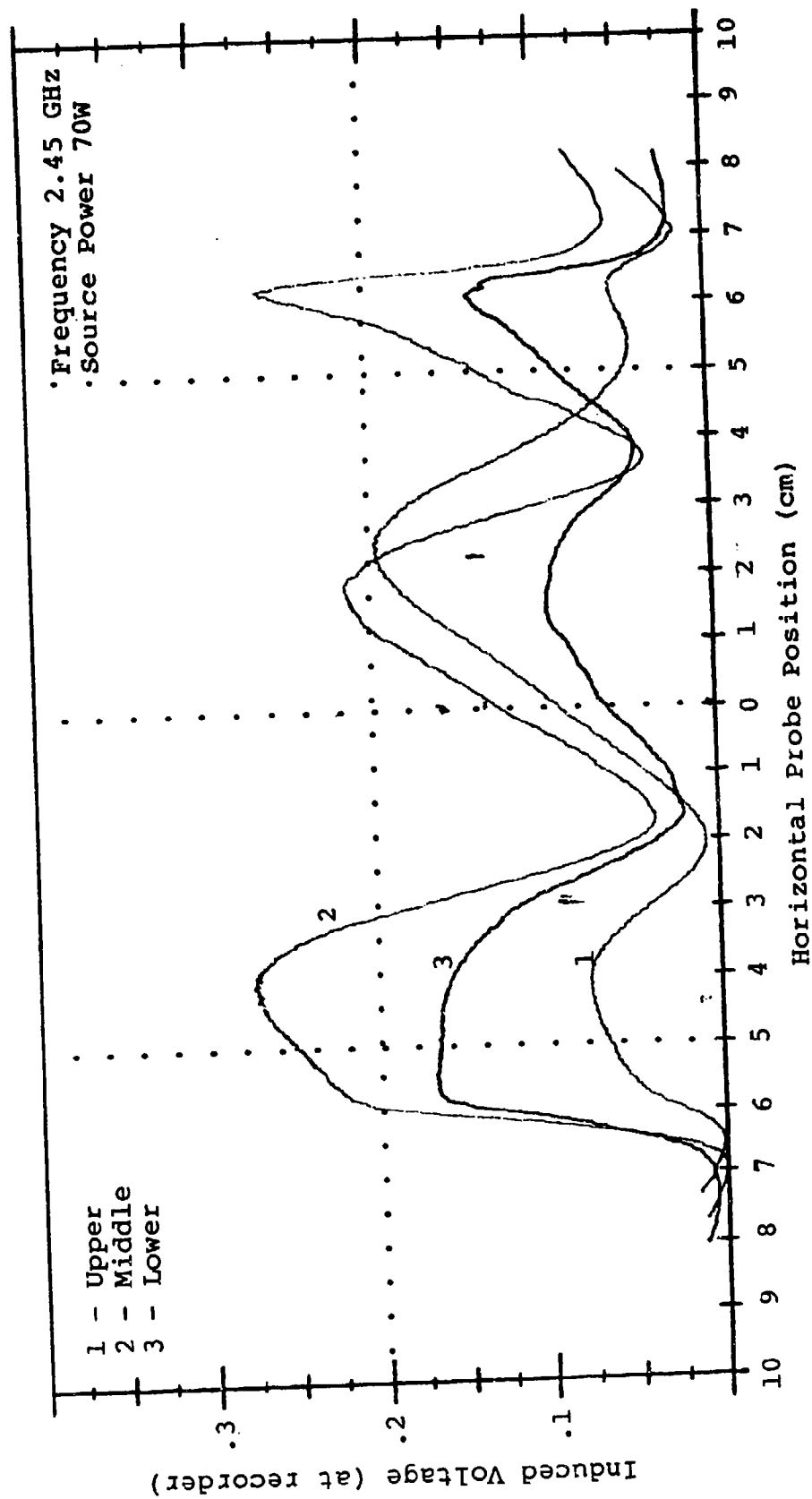


Figure E6: Horizontal Magnetic Field Probe Measurements for the 1.0 wavelength square plate.

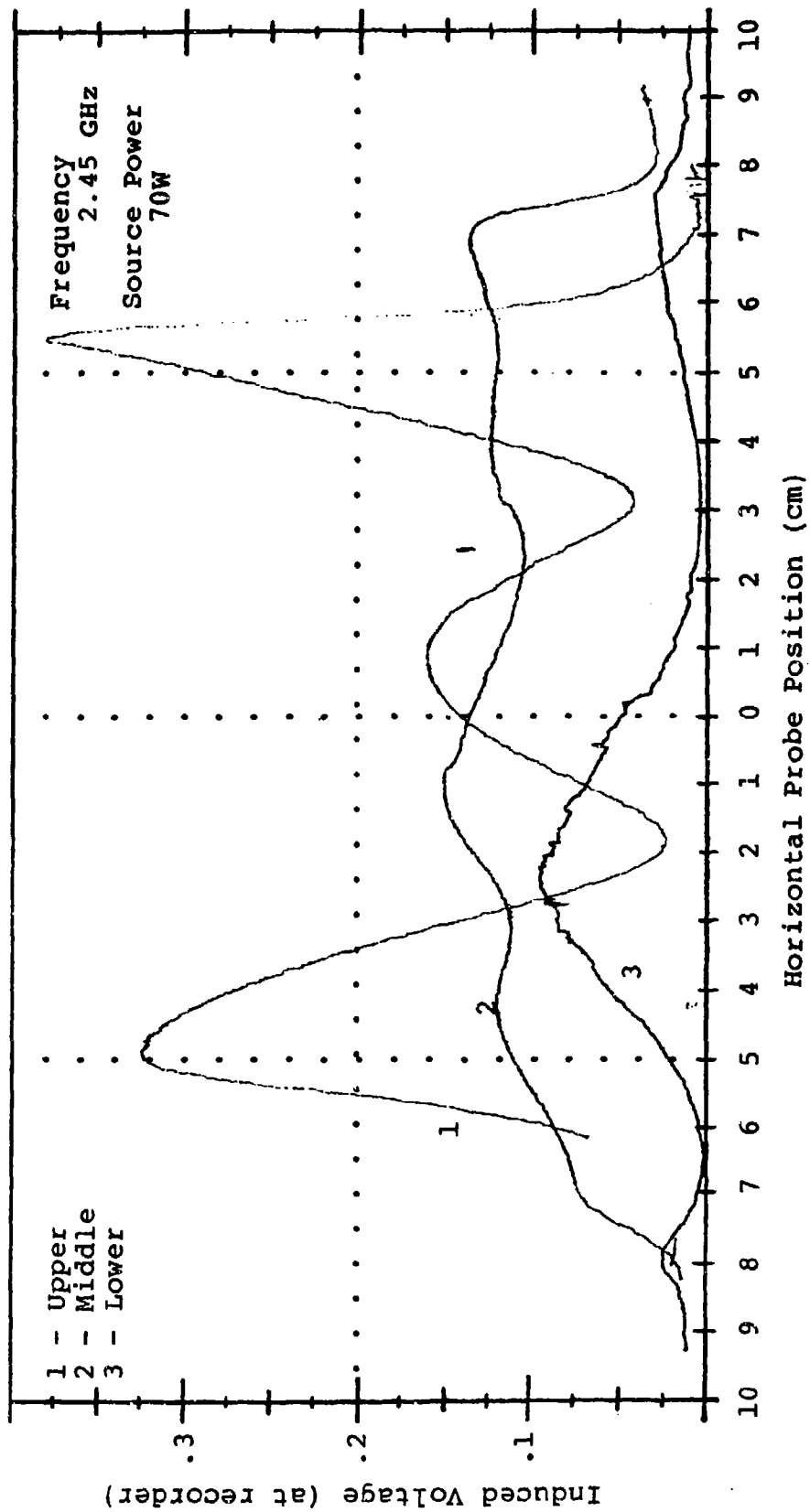


Figure E7: Horizontal Magnetic Field Probe Measurements for the 1.3 wavelength circular disk.

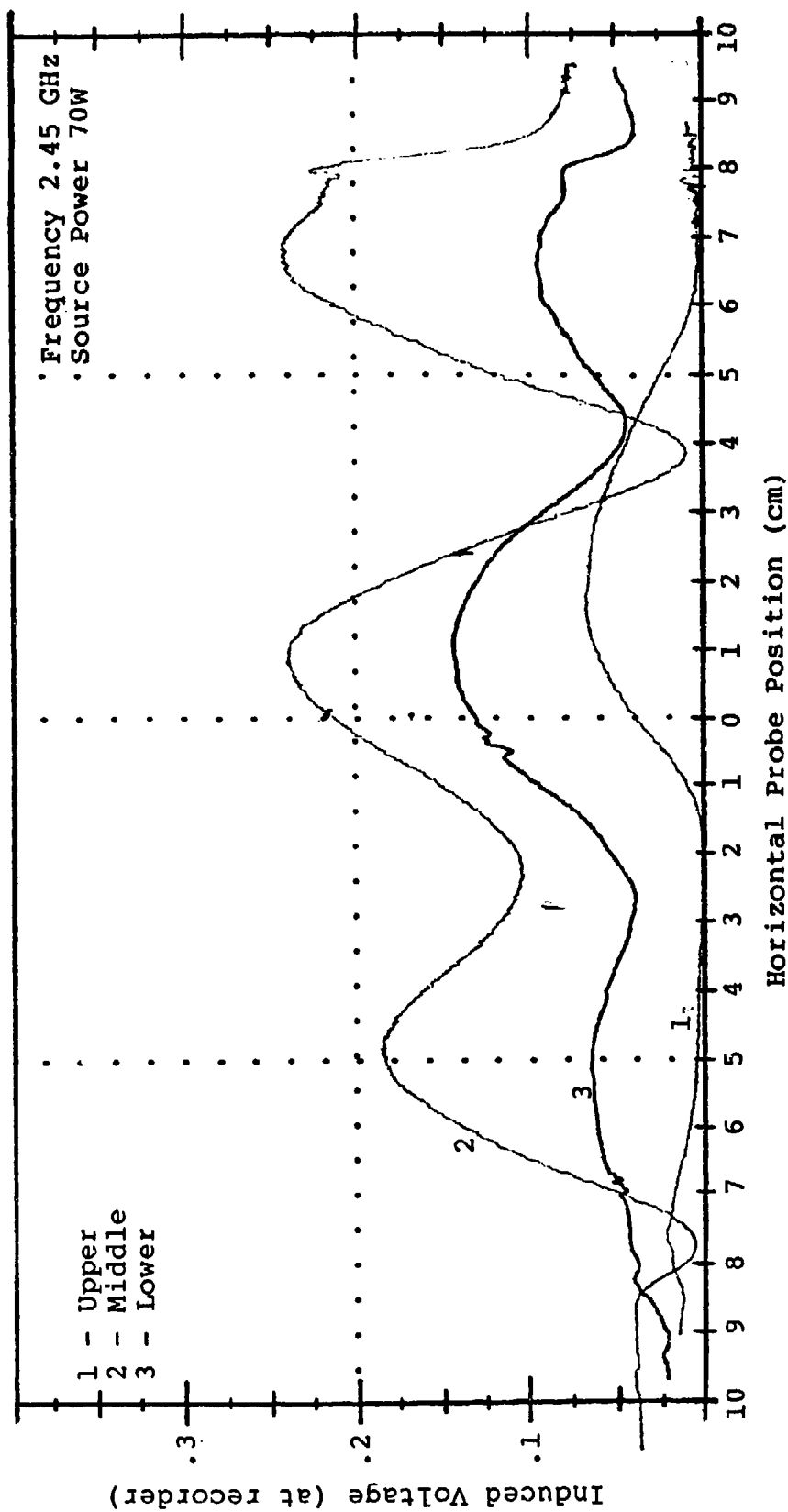


Figure E8: Horizontal Magnetic Field Probe Measurements for the 1.3 wavelength square plate.

APPENDIX F

EMISSIVITY DEPENDENCE ON ANGLE

Emissivity is the absorption/emission properties of a substance as compared to the isotropic and perfectly absorbing/emitting properties of a black body radiator. To determine the true temperature of an elemental area on an object surface using an infrared system, the directional nature of the IR photon emission was investigated. A simple point by point correction using a stored object matrix taken in an ambient temperature, non-illuminated state was found to be effective with temperature elevations up to 5° K above ambient. This work was reported through presentations and publications to SPIE - The International Society for Optical Engineering (4) and the IEEE (5). It represents an important gain in knowledge that is most applicable for viewing angles that are other than normal incidence.

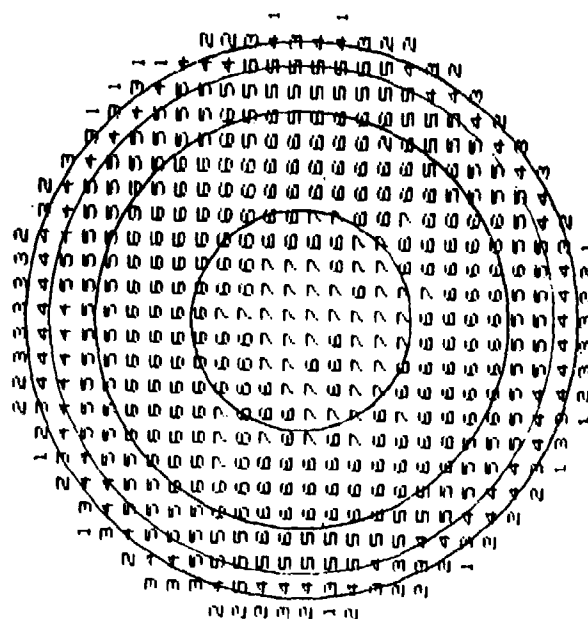
Experimentally Determined Emissivities

In determining the surface temperature distribution of three dimensional objects by thermographic analysis, the problem of directional emissivity--

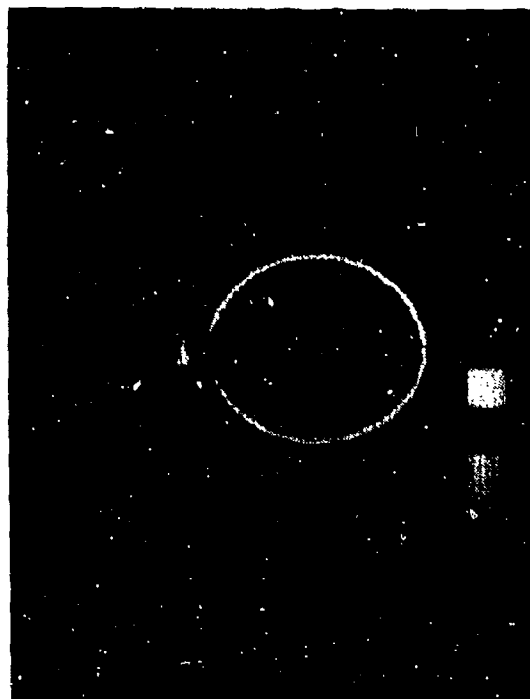
angular and material dependence of infrared emission from varying surfaces--must be accounted for. At a given temperature, different materials emit differing intensities of infrared radiation, and the intensity is also directionally dependent. This could cause problems with correlating the thermographic output from an infrared camera with actual surface temperatures on objects of various material coatings or complex geometries. A simple experiment was conducted using a hollow aluminum sphere coated with a carbon base paint and maintained at a constant temperature with an interior water bath held at the boiling point. The arrangement is seen in Figure (F1). The Thermovision, depicted the sphere in ten colors, each representing 1°C , as nine concentric rings around a center circle, Figure (F2). The Thermovision depiction of a ten degree temperature range contrasted with the nearly uniform temperature profile actually present. This demonstration clearly indicated the requirement to correct for geometry to obtain accurate results. The influence of the emissivity dependence on thermographically determined temperature distributions was also noted by Hsieh and Ellington (2) in 1977. Idealized plots of emissivity and angular dependence can be found in several sources (6). However, because



Figure F1: Experimental arrangement for the heated sphere.



(b) Digitized
Sphere.

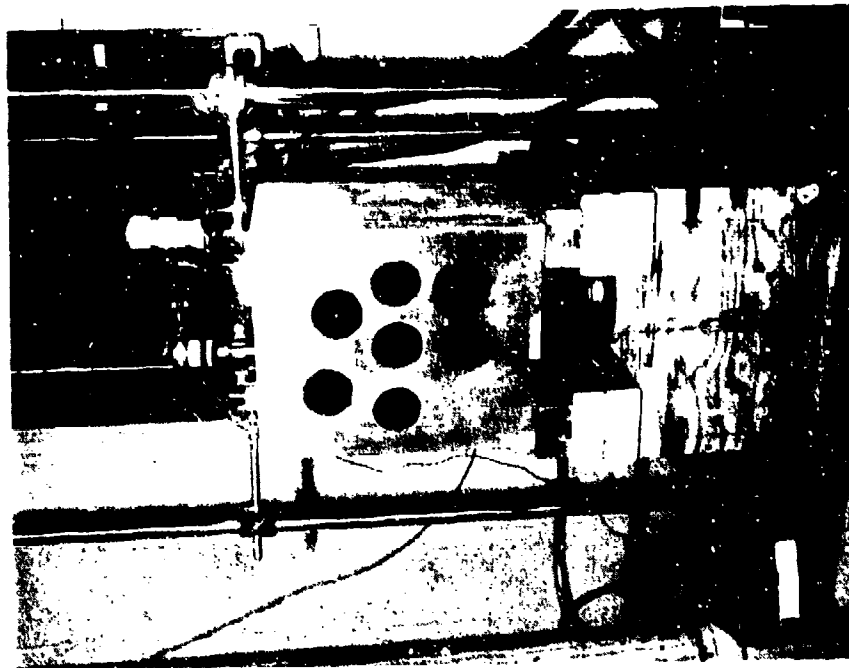


(a) Thermogram.

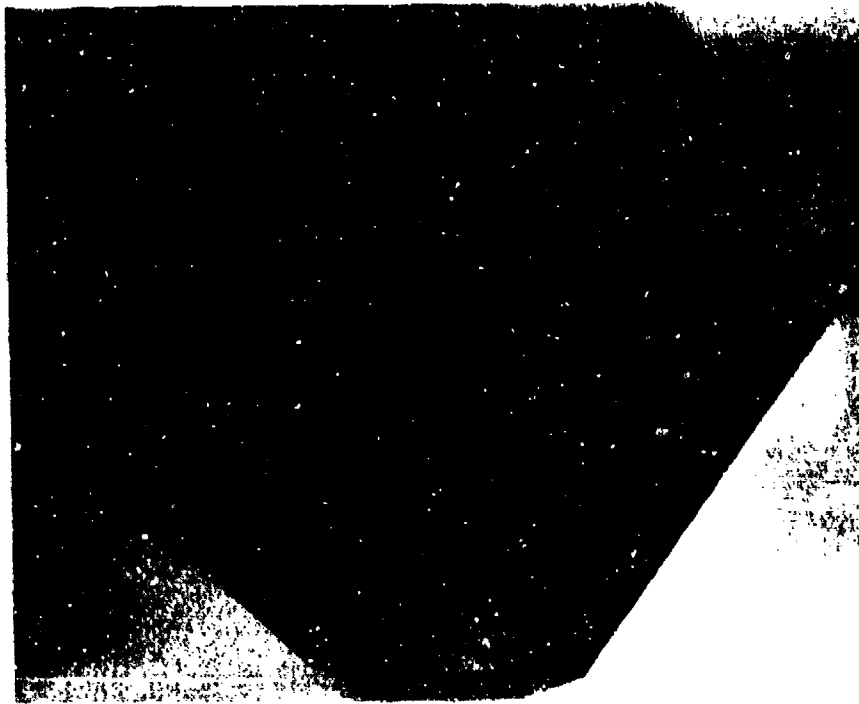
Figure F2: Uniformly heated sphere.

various coating preparations were to be used in the thermographic analysis, it was felt necessary to experimentally determine the directional emissivity of various potential coating materials.

For this determination, an apparatus to determine emissivity at various viewing angles for several different materials and coatings was built, and is shown in Figure (F3). Patches of different resistive coatings which could be used in our analysis were applied to the side of a water-filled aluminum box. A 15 cm diameter spherical aluminum chamber coated inside with lampblack and welded into the side of the box with a 5 cm diameter circular opening at the front of the box served as a simulated blackbody radiator, with which the emissivities of the various coating patches could be compared. The emissivity of the blackbody reference was taken as $\epsilon_r=1$, and verified to be isotropic by viewing the blackbody with the Thermovision camera at angles between 0° and 70° to the normal of the face of the box (the detected IR radiation from the blackbody simulator did not vary with angle until the camera could not longer see inside the lip of the simulator opening at 70° from the normal). The water was maintained at boiling (about 92° C), and thermographic



(a) Experimental arrangement.
Figure F3: Blackbody Simulator.



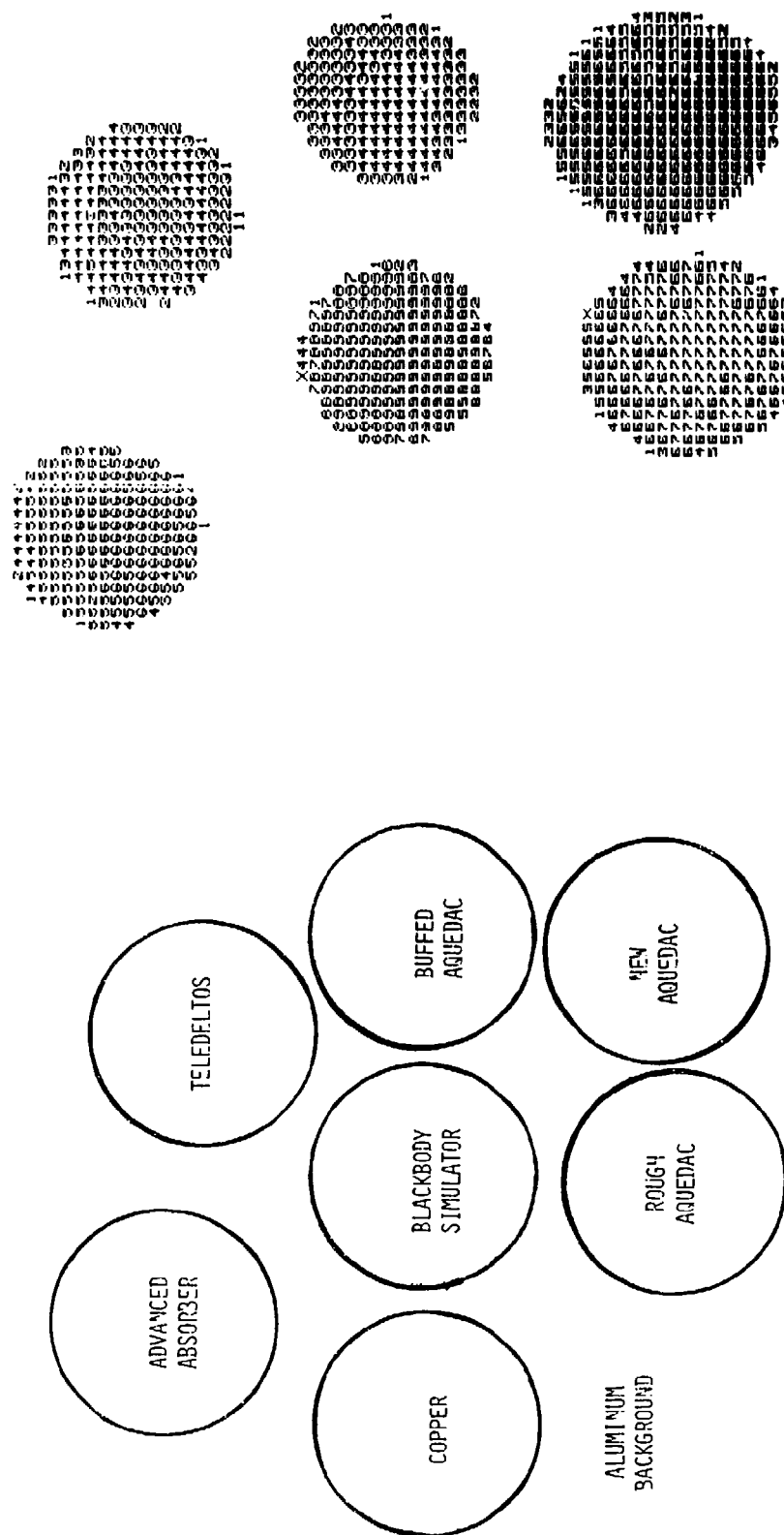
(b) Interior view.

data was taken at angles between 0° and approximately 90° from the normal to the box face with an AGA Thermovision 680 interfaced with a HP 9845B mini-computer described in the previous section. The emissivities as a function of angle were calculated using the following formula, explained in the AGA Thermovision 680 Operating Manual (1):

$$\epsilon(\theta) = \frac{\Delta i + \epsilon_r (I_r - I_a)}{I_o - I_a}$$

where Δi is the difference in isotherm levels on the Thermovision between the test material (varying with angle θ) and the blackbody reference, and I_r , I_a , and I_o are the isotherm levels of the blackbody reference, ambient, and test material temperatures, respectively.

Figure (F4) shows the position of the material on the simulator face and a digital printout at 10° from normal incidence. Only the center portion was used to determine coverage isotherm readings used in the calculations.



(a) Identification of surface patches.

(b) Digitized thermovision output at 10° from normal incidence.

Figure F4: Blackbody facing surface.

Figure (F5) depicts experimental results from the emissivity test apparatus for teledeltos paper and smooth/rough surface preparations of aquadac. Teledeltos is a resistive paper, and aquadac is also available resistive coating, discussed earlier. Also shown for comparison are the results for a typical dielectric (wood) and aluminum, on which the samples were attached. Curves for wood and aluminum are taken from the literature. The dielectric nature of the coating appeared to account for the decreasing IR emittance from the normal to tangential viewing angles.

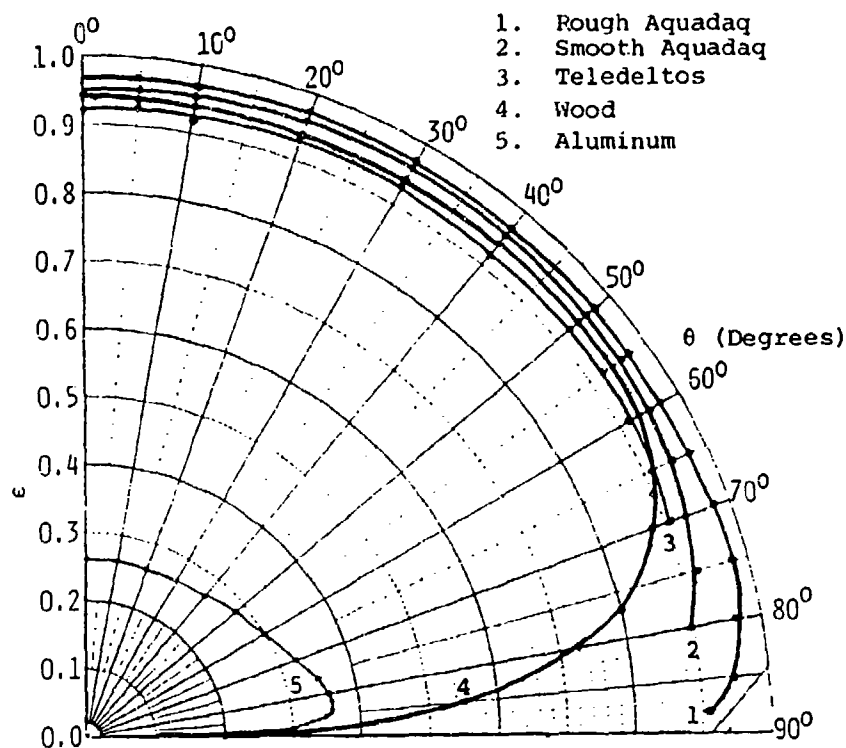
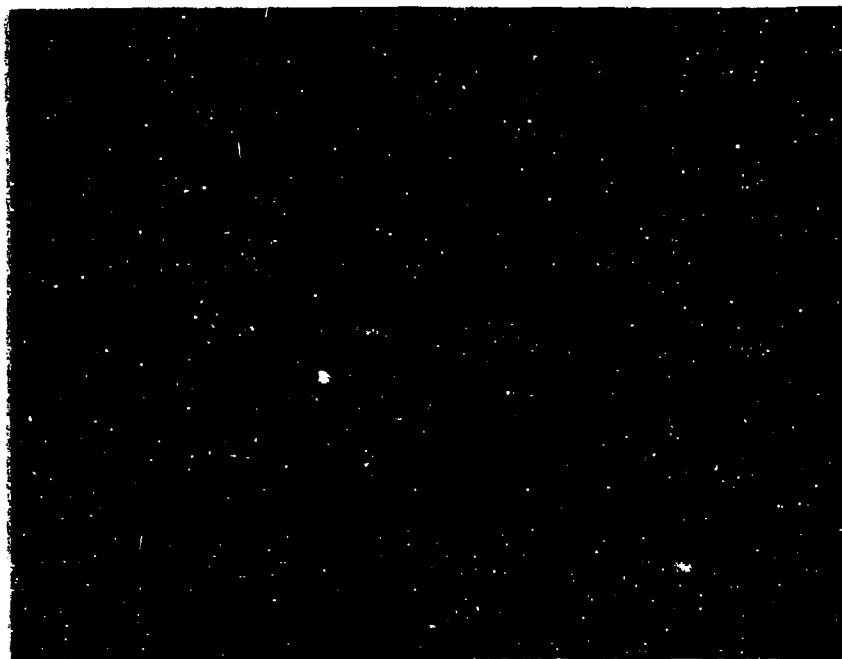
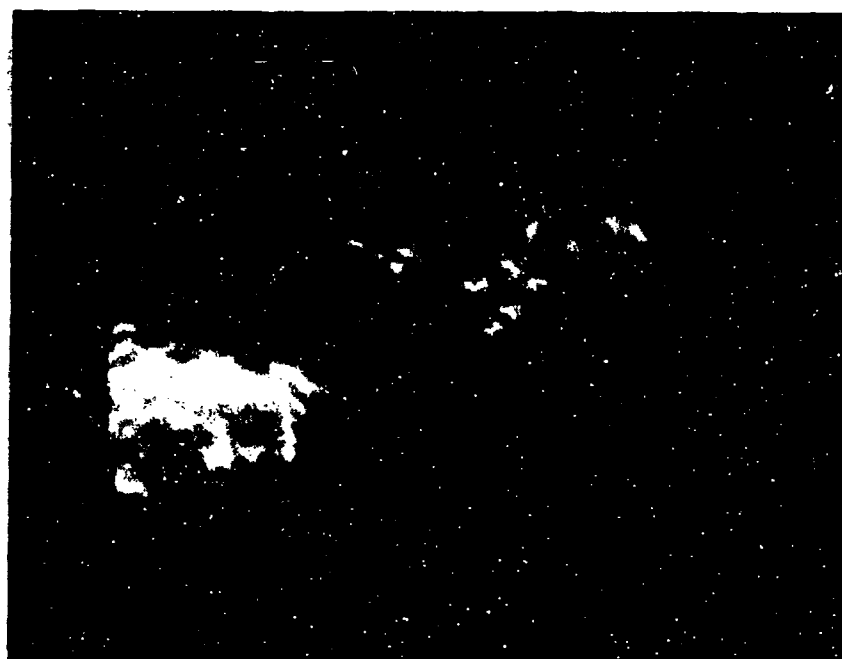


Figure F5: Total Directional Emittance Distributions

It was interesting that roughness appeared to be a factor for material emissivity and this prompted a brief Scanning Electron Microcroscope observation of the coating surfaces to be used in the IR detection of surface currents. The results are seen in Figures (F6) and (F7).

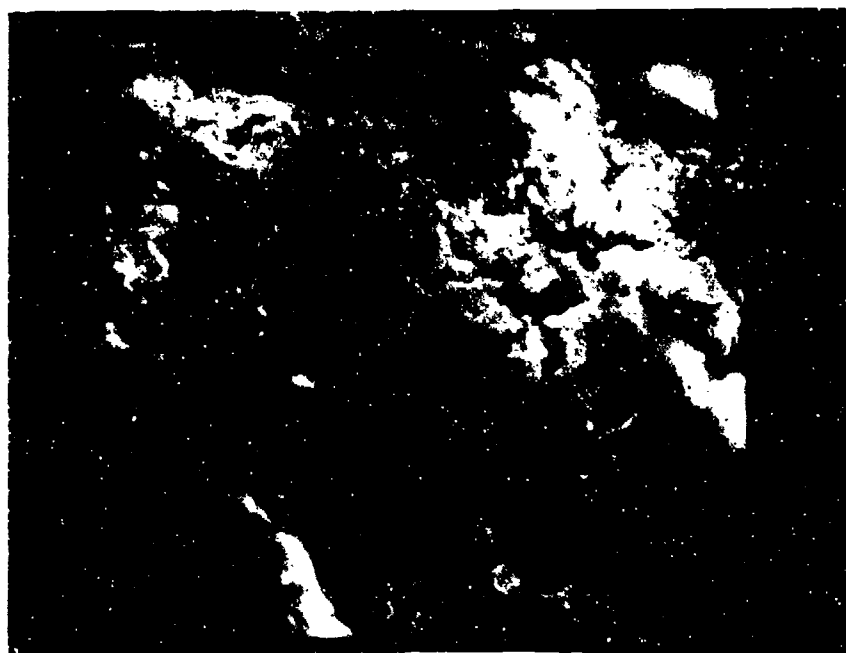


(a) Aquadac (1300X).

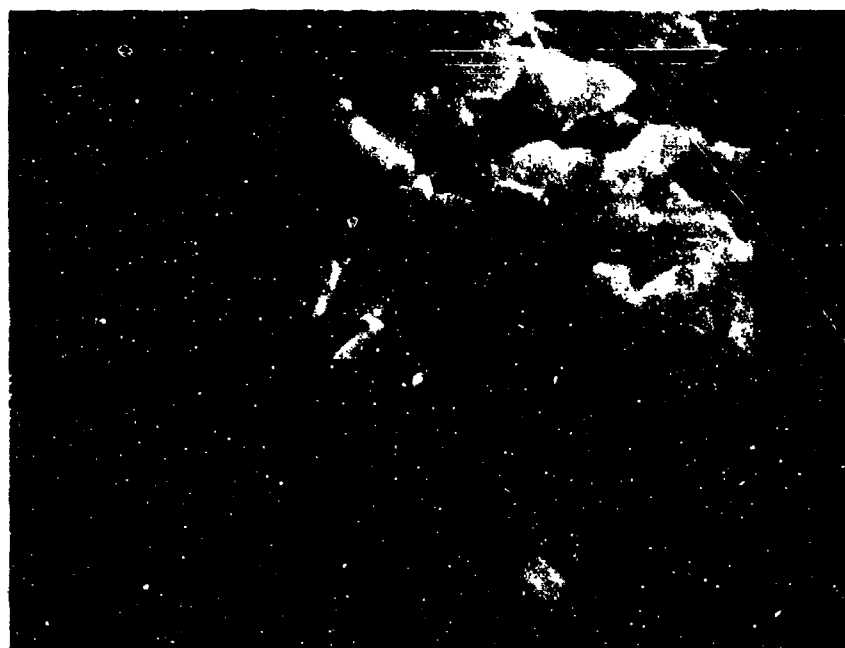


(b) Aquadac (5200X).

Figure F6: Micrographs of the aquadac coating.



(a) Carbon/paraffin (1300X).



(b) Carbon/paraffin (5200X).

Figure F7: Micrographs of the carbon/paraffin coating.

As was discussed, a correction was necessary since an accurate determination of surface temperature was a prerequisite for obtaining surface current information. The emissivity variation with viewing angle was determined to be the needed correction. The theoretical, mathematical approach was presented (3) and later replaced by a simpler experimental one, summarized here. For temperature variations that typically do not exceed 5°C it was found that a matrix of temperature values taken of the object at a steady state ambient temperature condition prior to irradiation by microwave, could be used effectively for emissivity correction for geometry. Experimental verification of the validity of the correction for angular dependence of emissivity by simple subtraction of the correction matrix from a final "heated" temperature matrix was carried out over a range of temperatures above ambient for the hollow sphere.

The procedure for determining currents on complex shapes would involve storage of a correction matrix obtained from an average of several frames taken of the object at ambient temperature. A several frame average of an illuminated or "final" matrix is stored. The correction matrix is then

subtracted from the illuminated to yield a difference matrix in ISU units which now has accounted for emissivity variation with angle. The standard conversions to temperature and current are then made. The following five figures depicts this procedure applied to an early aquadac/plexiglass flat plate.

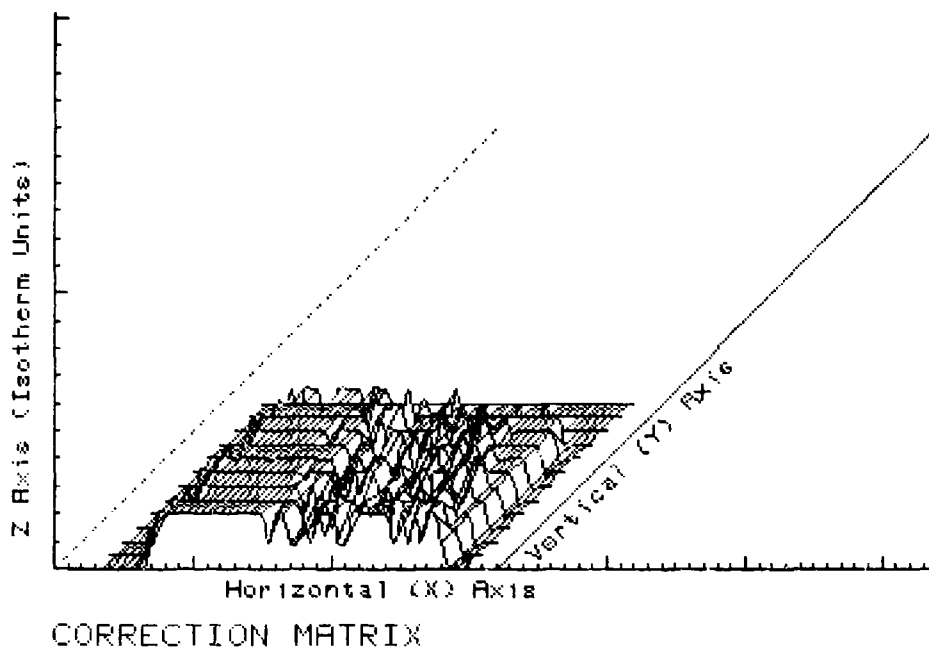


Figure F8: Correction Matrix.

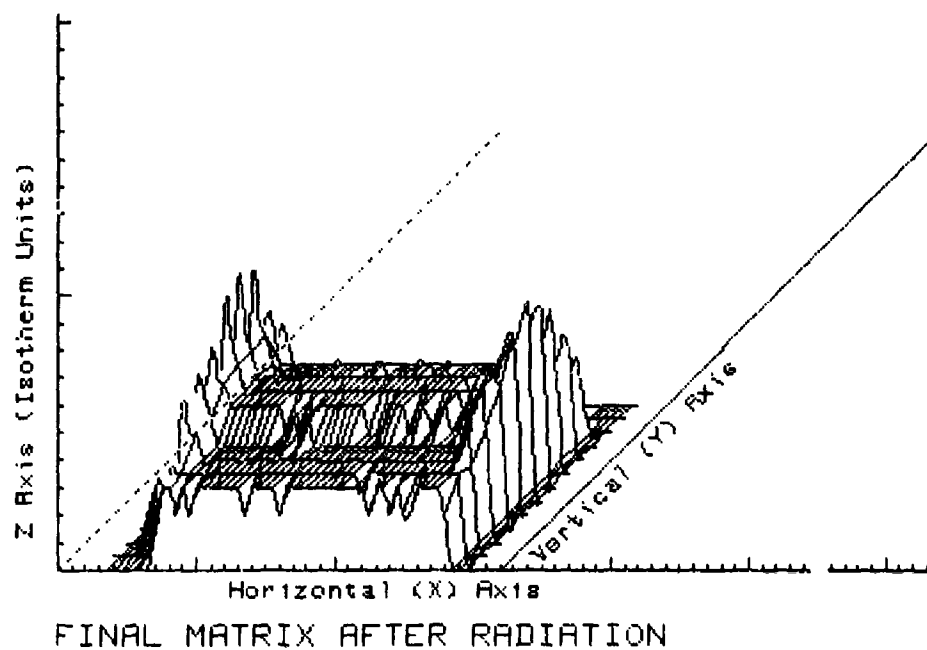


Figure F9: Illuminated Matrix.

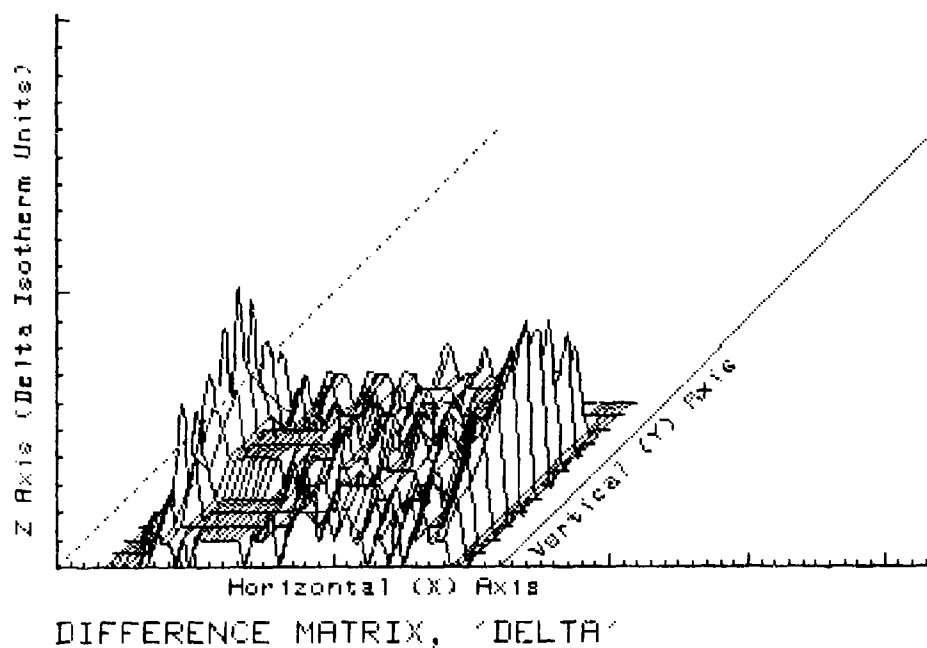


Figure F10: Difference Matrix (ISU).

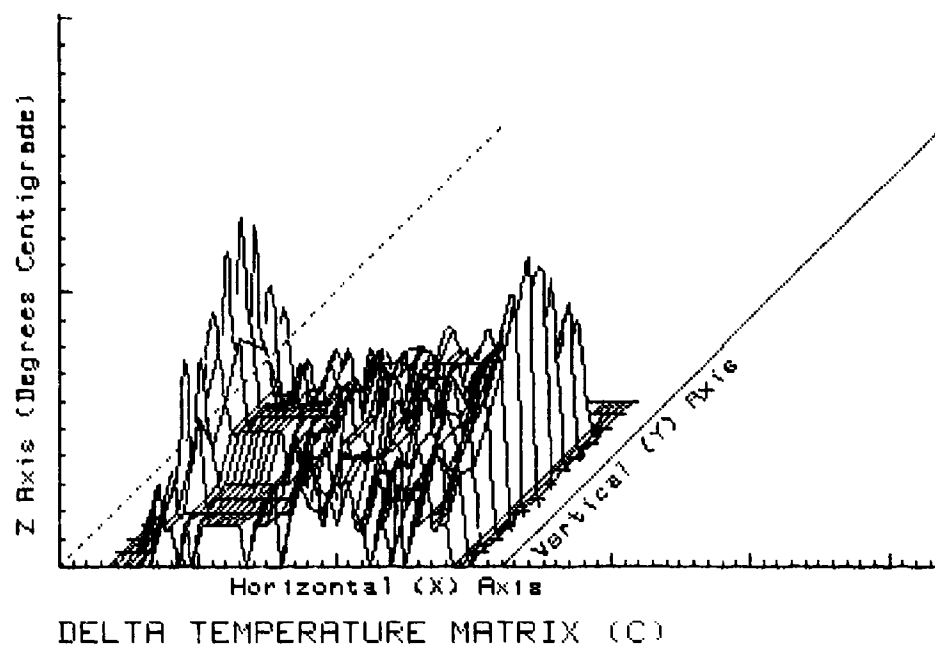


Figure F11: Difference Matrix (degrees C).

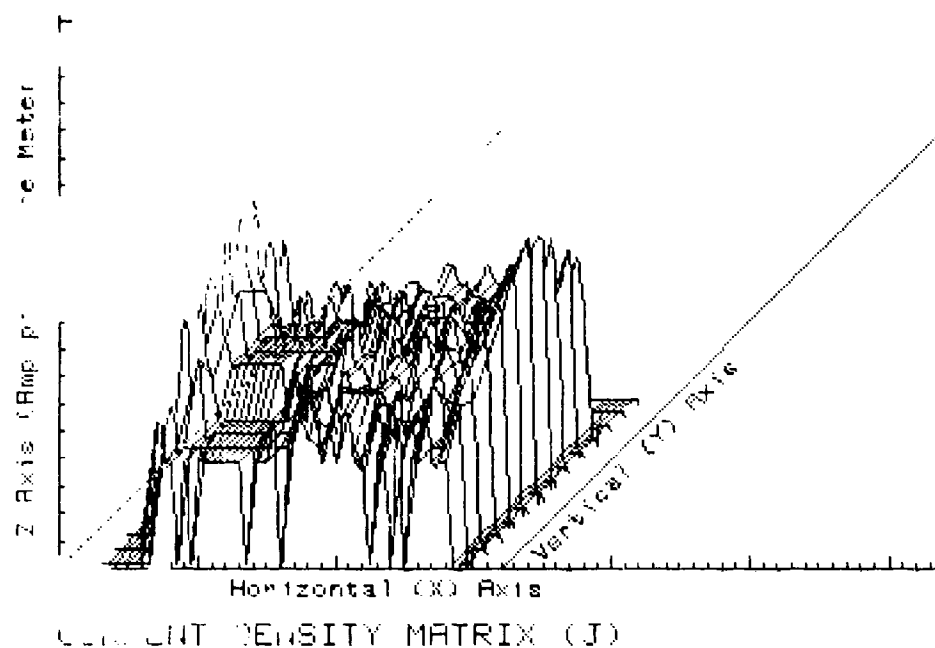


Figure F12: Current Matrix.

Copy available to DTIC does not
 permit fully legible reproduction

References

1. AGA Thermovision 680 Operating Manual, AGA Infrared Systems AB, 5-81 Lidingo, Sweden, 1975.
2. Hsieh, C. K. and Ellingson, W. A., "A Quantitative Determination of Surface Temperatures Using an Infrared Camera," Modern Utilization of Infrared Technology III, SPIE, Vol. 124, 1977, pp 228-235.
3. Martin, V. M., Sega, R. M., Stewart, C. V., and Burton, R. W., "Application of Infrared Thermography in the Analysis of Induced Surface Currents due to Incident Electromagnetic (EM) Radiation on Complex Shapes," Infrared Systems, Vol. 256, Society of Photo-Optical Instrumentation Engineers (SPIE), September 1980.
4. Sega, R. M., Martin, V. M., Warmuth, D. B., and Burton, R. W., "An Infrared Application to the Detection of Induced Surface Currents," Modern Utilization of Infrared Technology VII, Vol. 304, SPIE-The International Society for Optical Engineering, August 1981.
5. Sega, R. M., Martin, V. M., and Burton, R. W., "Microwave Induced Surface Current Measurement via Infrared Detection," 1982 International Symposium Digest-Antennas and Propagation (IEEE), Albuquerque, NM, May 1982.
6. Sparrow, E. M. and Cess, R. D., Radiation Heat Transfer, Augmented Edition, McGraw-Hill Book Company, New York, NY, 1978.